New insight into the drivers, magnitude and sources of fluvial CO_2 efflux in temperate and arctic catchments

Hazel Elizabeth Long

MPhysGeog

Submitted in fulfilment of the requirements for the degree of Doctor of Philosophy

School of Geographical and Earth Sciences

College of Science and Engineering

University of Glasgow

December 2016

Abstract

Freshwater systems are generally found to be sources of CO_2 to the atmosphere and evasion of CO_2 from fluvial systems is now recognised to be a significant component of the global carbon cycle. However detailed understanding of fluvial carbon dynamics and controls on the system is lacking and global coverage of published data is sparse, but thorough understanding across a broad range of locations is crucial if global carbon budgets are to be refined. This research addresses this lack of understanding by investigating the magnitude, controls and sources of CO_2 efflux across five catchments with different catchment characteristics, global locations and climate-change sensitivities. In doing so new understanding is used to explore a novel method for large-scale upscaling of CO_2 efflux, time series reconstruction of the source and magnitude of CO_2 efflux and incorporation of an Arctic region into the global fluvial carbon budget.

The magnitude of and controls on CO_2 efflux are not well understood, although it has been suggested that increased flow velocity and turbulence can enhance CO_2 efflux rates. This research uses direct and contemporaneous measurements of CO_2 efflux (range: -3.53 to 107 $\mu mol\, CO_2\, m^{-2}\, s^{-1}$), flow hydraulics (e.g. mean velocity range: 0.03 to 1.39 m s^{-1}; shear Reynolds number range: 350 to 174000), and water chemistry (e.g. pCO_2 range: 388 to 4660 ppm), at sites in three UK catchments to assess whether flow intensity (a term which is used to describe one or more measures of flow strength and turbulence) is a primary control on CO_2 efflux. These field sites have been chosen as they have contrasting size and land use: Drumtee Water (DW), 5.7 km^2 and rural, the River Kelvin (RK), 335 km^2 and urban, and the River Etive (RE), remote and snow-melt influenced. At the more soil-dominated sites DW and RK, a strong positive logarithmic relationship exists between CO_2 efflux and measures of flow intensity (e.g. shear Reynolds number, overall $R^2 = 0.69$), but this relationship is strengthened by including pCO_2 (overall $R^2 = 0.72$). Flow intensity may have a key influence on CO_2 influx, although data are limited. A method using visual classification of flow intensity shows promise for supporting large-scale upscaling of fluvial CO_2 efflux, if classification of water surface state can be standardised.

Movement of dissolved inorganic carbon (DIC) through the hydrological cycle is an important component of global carbon budgets, and how they may respond to changing climatic conditions. However uncertainty remains about the hydrological and biogeochemical controls on DIC transmission through a catchment. Using contemporaneous measurements of DIC concentration ([DIC]) and stable carbon isotope composition of the DIC pool ($\delta^{13}C_{DIC}$), fluvial DIC at more soil dominated sites, DW and RK, is found to vary considerably in response to changes in catchment hydrology. At low flow groundwater dominates, and has similar composition in both systems ([DIC]: 1.5 mmol L^{-1} DW, 2.0 mmol L^{-1} RK; $\delta^{13}C_{DIC}$: -9 ‰ DW and RK) indicating a common hydrogeological inheritance in DIC, that is comparable to that of other temperate and tropical locations. Differences in composition at high flow ([DIC]: 0.1 mmol L^{-1} DW, 1.0 mmol L^{-1} RK;

$\delta^{13}C_{DIC}$: -23 ‰ DW, -14 ‰ RK) reflect catchment land use, and a lower contribution of soil water to the DIC pool in the more urban catchment (RK). Measured diel cycles in DIC pool composition at DW indicate biological processes modify the pool, and time series reconstructions of pool composition and CO_2 efflux at DW reveal seasonal- and flow-related patterns in this biological activity. Time series reconstructions also reveal that at DW terrestrial-aquatic-atmospheric carbon cycling is rapid during event flows, with large amounts of CO_2, of soil-origin, effluxed to the atmosphere in relatively short periods of time. Conversely, at low flows, CO_2 efflux is of smaller magnitude and primarily fuelled by groundwater, and terrestrial-aquatic-atmospheric carbon cycling is slower. The reconstructions allow for inter-year comparisons which are useful in assessing for behaviours in CO_2 source and feedback that might be typical under climate change-induced changes in hydrology (e.g. wetter winters, drier summers, more frequent large flow events).

Global ice melt and permafrost thaw are increasing due to climate change, effects of melting ice and thawing permafrost on the global carbon cycle, and carbon cycling dynamics of the melt/thaw waters are not well understood. Data from the River Etive has few similarities to that of DW and RK and indicates that snow- and ice- dominated systems may behave very differently to more soil-dominated systems in terms of magnitude and controls on efflux and sources and mixing of the DIC pool. This is confirmed by data collected from the melt/thaw waters of two cryospheric systems in Greenland: a Greenland Ice Sheet (GrIS) drainage river (Akuliarusiarsuup Kuua River, or AR) and the local permafrost-landscape surface-drainage systems (PLST). CO_2 efflux appears independent of flow controls in both systems, and instead seems to be pCO_2 limited (average pCO_2: 115 ppm AR, 596 ppm PLST), with spatial variation in AR (efflux decreases downstream) and temporal variation in PLST (efflux decreases with melt season progression). The frequent occurrence of CO_2 influx (measured in 64% and 14% of cases in AR and PLST respectively), which has rarely been reported from other rivers globally, reveals that Arctic fluvial systems can periodically act as net sinks of CO_2 and this should be incorporated into global carbon budgets. The occurrence of CO_2 influx, and dominance of air-water CO_2 exchange in these low pCO_2 systems, is reflected in the DIC pool composition which is ^{13}C-enriched and approaches isotopic equilibrium with the atmosphere (~0 ‰), and indicates that soil and ground water contributes little to the DIC pool under frozen ground conditions. Radiocarbon analysis gives further insight into the source of carbon in these systems, revealing that the GrIS is releasing old DOC (~5200 to 6600 yrs BP) upon melting, which is considered to be highly biolabile and may prime bacterial activity and feedback to climate change, and meltwaters are returning old carbon (800 to 960 yrs BP) to the atmosphere via CO_2 efflux. Thus it appears that climate change (via melting ice sheets) may be a driver of the age of atmospheric carbon composition. The effluxed CO_2 being less old than the DOC indicates the source of CO_2 efflux is a mixed pool of respired/UV-oxidised old DOC and modern atmospheric CO_2 from drawdown. In contrast to GrIS meltwaters, and the permafrost of other global locations (e.g. the Siberian Yedoma deposits), the permafrost landscape of the

Kangerlussuaq region of Greenland is cycling modern carbon and appears not to be degrading, as old carbon is not found in, or degassed from, the fluvial systems.

In summary this research contributes to a greater understanding of fluvial carbon dynamics and the processes controlling the return of CO_2 to the atmosphere via efflux, across an array of catchment types, sizes, land uses and global locations, and makes contributions of novel data to a number of areas of fluvial carbon cycling research where there are scarcities. Marked differences in the fluvial carbon cycling dynamics of cryospheric and snow-melt dominated systems compared to soil-dominated terrestrial systems are uncovered, novel upscaling attempts made using new findings of the research, and a number of exciting new research directions and opportunities that could enhance the findings of this work are identified. Overall, this research takes steps towards a greater understanding of fluvial carbon cycling dynamics on a global scale and improved projections of the likely response of fluvial systems to climate change, ultimately aiding the community to be more prepared for what our shifting climate will bring.

This work has been funded by the UK Natural Environment Research Council (NERC), and undertaken and supported at the University of Glasgow within the College of Science and Engineering (CoSE), as part of activities within the Carbon Landscape and Drainage (CLAD) research group, led by Prof. Susan Waldron, in the School of Geographical and Earth Sciences (GES). Additional funding for the field campaign to Greenland was provided by the Sir Alwyn Williams Postgraduate Scholarship in Geographical and Earth Sciences, the CoSE Graduate School Mobility Funding, SAGES (Scottish Alliance for Geoscience, Environment and Society) Theme 2 Research Enabling Funding for field research support and the Dudley Stamp Memorial Award (Royal Geographical Society with Institute of British Geographers). The Scottish Universities Environmental Research Centre helped support the stable isotope analysis and radiocarbon measurements were funded by NERC Radiocarbon Analysis award Number 1790.0414.

Table of Contents

List of Tables

List of Figures

Acknowledgements

Without the contributions and support of the following people, this piece of work would not have been possible. I am very fortunate to have had this network of people behind me over the course of my Ph.D.

Thank you to NERC for providing the funding to make this research possible. The Greenland field campaign would not have been possible without the additional funding provided by the Sir Alwyn Williams Postgraduate Scholarship in GES, the CoSE Graduate School Mobility Funding, SAGES (Scottish Alliance for Geoscience, Environment and Society) Theme 2 Research Enabling Funding for field research support and the Dudley Stamp Memorial Award (Royal Geographical Society with Institute of British Geographers). The trip was an amazing experience and I am very grateful for this financial aid. Thanks go to the Scottish Universities Environmental Research Centre who helped support the stable isotope analysis which was a vital part of this research, and again to NERC who funded (Radiocarbon Analysis award) radiocarbon measurements, which added an exciting novel element to the Arctic research.

I have had a wonderful supervisory team – Prof. Susan Waldron, Prof. Trevor Hoey and Dr Jason Newton – who all deserve a huge thank you. Jason, for his assistance with and training in stable isotope analysis, and for the many hours spent helping with data processing. Trevor, for his support and help throughout the PhD, particularly his statistical guidance, his incredible proof reading skills, his assistance in Greenland (including keeping me calm through a missing equipment shipment and a vehicle sunk in a bog) and for always making mountains seem like molehills with his calm and patience. Finally, Susan, who has been an incredible support throughout, and a constant source of help and guidance. Her high expectations and dedication to helping me achieve my potential have kept me on track and motivated and I have learned such vast amount over the four years. Her drive and enthusiasm for scientific research has been inspiring to see, and she has gone beyond what I believe is expected of a Ph.D supervisor… including keeping me supplied with excellent home-made jam. Susan, thank you, I would not be here without you.

I must also mention Dr. Leena Vihermaa, whose help and advice throughout my Ph.D has been invaluable, particularly in the early stages when, after six years out of academia, even simple concepts and tasks sometimes felt like a mystery. Thank you for your patience with my constant questions, your assistance with the 24-hour field campaign at Drumtee Water (including protection from the cows and forcing me back out into the cold and midges at 4am), and for your friendship.

Fieldwork has been integral to this research, so my gratitude goes to the many people that assisted me in collection of data and samples: Dr. Leena Vihermaa, Dr. Hu Ding, Dr. Ben Smith, Hemanth Pasumarthi, Sofia Daouadji, Amy Childs, Dr. Andrew Singleton, Emilie Lepretre and David

Fisher. A special mention must go to Martin Coleman who I worked with regularly in the field for two years. Martin was always extremely willing to help and good company despite the often challenging Scottish weather conditions… which only frayed our tempers once. An additional special mention goes to Crystal Smiley for a huge amount of field help in Greenland. She cheerfully tolerated long walks with heavy equipment, hours among the mosquitoes and staying up all night without ever complaining. You were great company Crystal, thank you. Finally, I would like to thank Mr Kenny Roberts for being the best field and laboratory technician a person could ask for, quickly and willingly solving any issue and regularly going above and beyond his duty. Thank you for keeping me calm through shipping 85 kg of equipment to Greenland and for the many cups of tea and chats about the world. I could not have done this research without your help.

Thank you to Dr. Mark Garnett for his assistance in applying for the NERC Radiocarbon Analysis award, for subsequent training in the field sampling procedure, and for his helpfulness in answering my Radiocarbon-related queries. Thank you also to Mr David Riggans for his enormous efforts with the difficult process of shipping large amounts of equipment to and from a remote location in Greenland. Thank you to all the members of Carbon Landscape Research Group, past and present, for being a great group to work with. The valuable advice and constructive feedback on my work was always appreciated and you provided a great forum for bouncing and discussing ideas.

To my parents Mrs Margaret Long and Mr Tony Long, thank you for your support and encouragement throughout this PhD. Thank you for always supporting my education and the choices I have made that have lead me here. Thank you also to my siblings Andrew Long and Heather Long for your encouragement, particularly in the last few months. I am lucky to have you all.

I could not have asked for better officemates than Dr. Ben Smith, Ying Zheng and Dr. Roger Grau Andres. Ben, thank you for being a constant source of banter, advice and support through the highs and lows of Ph.D life, and for your company and enthusiasm at Swim Club and out on the hills. Ying, thank you for keeping me calm with your cheerful company and conversation through the write-up period, and for never getting angry that I always left the water bottles empty. Roger, thank you for the daily check-ins during our coinciding write-up period and some great hill-walks.

Thank you to my friends and fellow PhD students: Jill McColl and Kirsty Hill, for the laughs, support and wine; Eric Portenga, for the chats and excellent hill walks; Ruth Olden, for being a wonderful friend throughout, for the support, advice, the many many cups of tea and homemade currys, for keeping me rational and for always being there. Thank you to my friends at GLUG dive club for being so welcoming and for the excellent diving, which was a great break from my studies. I could not have done it without you all.

Author's Declaration

I declare that the work outlined and described in this thesis has been carried out by myself unless otherwise acknowledged. This thesis is completely my own composition and has not, in whole or part, been submitted for any other degree at this or any other university.

Hazel E. Long

September 2016

Thesis Citation: Long, H. E. (2016) New insight into the drivers, magnitude and sources of fluvial CO_2 efflux in temperate and arctic catchments. Ph.D. thesis, University of Glasgow, School of Geographical and Earth Sciences, Glasgow, UK.

Abbreviations

AMS	Accelerator Mass Spectrometer
AR	Akuliarusiarsuup Kuua River
C	Carbon
CBL	Concentration boundary layer
CO_2	Carbon dioxide
CO_3^{2+}	Carbonate ion
$\delta^{13}C$	Stable carbon isotope ratio
DIC	Dissolved inorganic carbon
DOC	Dissolved organic carbon
DW	Drumtee Water
Fr	Froude number
GrIS	Greenland Ice Sheet
HCO_3^-	Bicarbonate ion
IC	Inorganic carbon
IPCC	Intergovernmental Panel on Climate Change
ISO-CADICA	Isotopic, continuous, automated dissolved inorganic carbon analyser
mmol L^{-1}	Milimoles per litre
mg L^{-1}	Miligrams per litre
m s^{-1}	Meters per second
NEP	Net ecosystem productivity
NOAA	National Oceanic and Atmospheric Administration

OC	Organic carbon
OM	Organic matter
Pg	Petagrams = 10^{15} g
PIC	Particulate inorganic carbon
PLST	Permafrost-landscape surface-thaw
POC	Particulate organic carbon
ppm	Parts per million
Q	Stream discharge ($m^3\ s^{-1}$)
R^*	Shear Reynolds' number
Re	Reynolds' number
RE	River Etive
RK	River Kelvin
s.e.	Standard errors of residuals
SEPA	Scottish Environment Protection Agency
SUERC	Scottish Universities Environmental Research Centre
τ	Shear stress ($Kg\ m^{-1}\ s^{-2}$)
$\bar{u}$	Mean velocity ($m\ s^{-1}$)
u^*	Shear velocity
µmol CO_2 m^{-2} s^{-1}	Micromoles of carbon dioxide per meter squared per second
Yrs BP	Years before present, where present is 1950 A.D.
[ ]	Square brackets are used to indicate concentration

1 Introduction

1.1 Thesis Aims

Freshwater systems have generally been found to be sources of carbon dioxide (CO_2) to the atmosphere and CO_2 evasion from fluvial systems is now recognised as a significant component of the global carbon cycle (e.g. Hope *et al*., 2001; Cole *et al*., 2007; Waldron *et al*., 2007; Billett and Moore, 2008; Rasera *et al*., 2008; Tranvik *et al*., 2009; Alin *et al*., 2011; Aufdenkampe *et al*., 2011; Wallin *et al*., 2011; Polsenaere *et al*., 2013; Raymond *et al*., 2013; Long *et al*., 2015). However, although knowledge is increasing in temperate soil-dominated catchments, the magnitude, controls and sources of CO_2 efflux are not thoroughly understood, particularly in high-latitude locations for which there is little published data (Raymond *et al.*, 2013). Further, knowledge of the specific mechanisms controlling CO_2 efflux is lacking for all global locations (Zappa *et al.*, 2007; Alin *et al.*, 2011; Raymond *et al*., 2013). There have been limited attempts to upscale CO_2 efflux at a global scale due to the incomplete global coverage of published CO_2 efflux data and a scarcity of accurate global river surface area data and, as a result, those attempts are subject to large uncertainties (Raymond *et al.*, 2013). Sources and movement of carbon through the hydrological cycle is another important component of carbon budgets, however uncertainty remains here too about the controls on carbon transmission through a catchment (Tobias and Böhlke, 2011). The age of carbon in, and effluxing from, fluvial systems can give insight into whether a system is degrading (releasing old carbon), or stable (just cycling new carbon), and although studies applying ^{14}C dating to fluvial carbon dynamics are emerging (e.g. Vonk *et al.*, 2013; Leith *et al.*, 2014; Vihermaa *et al.*, 2014) this is a relatively new application of the technique and such studies are not abundant.

The overall objective of this study is to fill some of these gaps in our understanding of fluvial carbon cycling dynamics and the return of carbon to the atmosphere via CO_2 efflux. Specifically this study aims to:

1. Improve current knowledge of the magnitude and primary controls on riverine CO_2 loss via efflux from a variety of fluvial systems with different catchment types, global locations and climate-change sensitivities, and assess whether: (i) controls on and magnitude of efflux are similar or different across this range of catchments; (ii) whether fluvial systems always behave as sources of CO_2 to the atmosphere; and, (iii) whether the magnitude and control mechanisms can potentially be used to upscale CO_2 efflux on a regional or global scale.

2. Improve current knowledge of the source of carbon in the dissolved inorganic carbon (DIC) pool of fluvial systems and determine whether there is an influence of internal processing of the DIC pool in the fluvial systems studied here. Subsequently assess

whether this knowledge can be used to reconstruct DIC source and CO_2 efflux over time and the relationship between the two, to aid predictions of how fluvial carbon dynamics may respond to a climate-induced changing hydrological cycle.

3. Investigate the age of the carbon returned to the atmosphere in fluvial systems particularly vulnerable to climate change and assess whether carbon stores in these systems are being lost such that this loss may render these systems positive feedbacks to climate change.

To address these aims, it is crucial to first understand the importance of this area of research and the functioning of the fluvial carbon system. The following sections will detail why CO_2 is important, the process of CO_2 efflux from fluvial systems, the origins of carbon in the water, and the workings of the carbonate system which is fundamental to DIC pool dynamics.

1.2 The Significance of Carbon Dioxide

CO_2 is a radiatively-forcing gas that is 240 times more abundant than the next most abundant greenhouse gas, methane (CH_4), and thus is a major component of the greenhouse effect (Lutgens and Tarbuck, 2001). Global climate has warmed over the 20th century as a result of rising levels of atmospheric CO_2 and other GHGs (IPCC, 2007; Lu *et al.*, 2013), causing changes in seasonality, altered rainfall patterns, frozen regions to begin thawing and sea level rise (IPCC, 2007; IPCC, 2013; Pithan and Mauritsen, 2014). The climate continues to warm, and is projected to increase by up to 4.8 $^{\circ}$C over the 21st century (IPCC, 2013). High latitude and high altitude regions are warming more, and at a greater rate, than the global mean (IPCC, 2007 and 2013; Oberbauer *et al.*, 2007; Lu *et al.*, 2013; Schuur *et al.*, 2015).

Raised mean global temperatures could impact global carbon cycling considerably, causing positive (CO_2 release to the atmosphere) or negative (carbon sequestration) feedbacks to global climate change (Doctor *et al.*, 2008; Lin *et al.*, 2011; IPCC, 2013). Under a changing climate, the understanding of carbon cycling (the pathways and mechanisms by which carbon moves from one pool to another) and how it might be altered by a warming climate, is therefore of vital importance. In the global aquatic carbon cycle (Figure 1) CO_2 is returned to the atmosphere through efflux from water surfaces and thus efflux has the potential to provide a positive feedback to a changing climate (Doctor *et al.*, 2008).

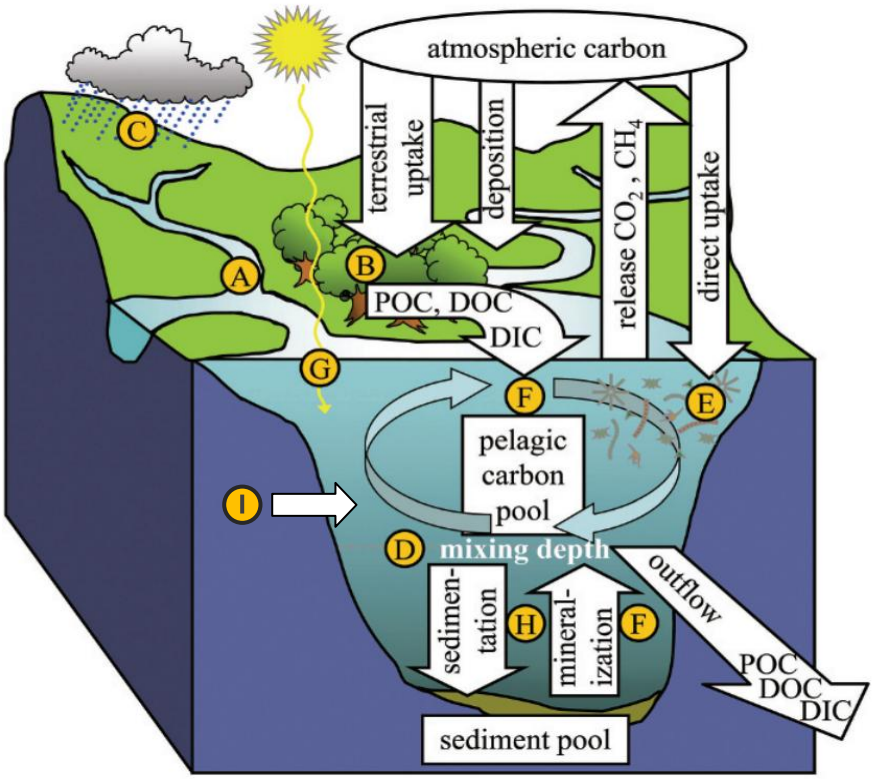

Figure 1: Schematic diagram of carbon cycling in terrestrial waters

A = rivers and lakes (water flux and residence time), B = vegetation (photosynthesis, respiration and decay), C = precipitation (flushes soil/litter C into waters), D = seasonality and lake condition (ice cover, flushing, stratification, permanency), E = autochthonous C production (littoral vegetation, phytoplankton, benthic algae), F = microbial degradation of dissolved organic matter, G = UV oxidation of organic matter to CO_2, H = sedimentation (caused by salinity, pH, cations), I = Lithology (weathering and dissolution). Adapted from Tranvik *et al*. (2009).

1.3 CO_2 Efflux from Fluvial Systems

CO_2 efflux is the export of CO_2 from a water body to the atmosphere, and can also be referred to as CO_2 evasion or degassing (Wallin *et al.*, 2011). Intensive research has been undertaken on CO_2 efflux from lakes, estuaries and oceans, but much less attention has been given to river systems, especially lower order streams (Butman and Raymond, 2011; Melack, 2011; Wallin *et al.*, 2011), and existing research is predominantly focused on temperate locations (Raymond *et al.*, 2013). River systems are often over-saturated with CO_2 (e.g. 1.2 – 7.9 and 1.9 – 16.5 times atmospheric equilibrium, Hope *et al.* (2001) and Wallin *et al.* (2011) respectively) and thus have the capacity to degas CO_2 to the atmosphere (Billett *et al.*, 2006; Butman and Raymond, 2011; Melack, 2011; Polsenaere *et al.*, 2013). Oversaturation of a water body creates a gradient in the partial pressure of CO_2 (pCO_2) across the air-water interface, which causes the movement of CO_2 from the water into the atmosphere (Billett and Moore, 2008). Thus river systems have typically been found to be sources of CO_2 to the atmosphere (e.g. Hope *et al.*, 2001; Cole *et al.*, 2007; Waldron *et al.*, 2007; Billett and Moore, 2008; Rasera *et al.*, 2008; Alin *et al.*, 2011; Aufdenkampe *et al.*, 2011; Wallin *et al.*, 2011; Polsenaere *et al.*, 2013; Long *et al.*, 2015).

Rivers contain varying amounts of inorganic and organic carbon (IC and OC) in dissolved (DIC and DOC) and particulate (PIC and POC) form and are a chief transport medium of continental carbon to the oceans (Aucour *et al.*, 1999; Polsenaere *et al.*, 2013; Khadka *et al.*, 2014). Rivers have previously been considered to be inert conduits carrying this terrestrial carbon to the oceans. However, recent studies have shown that the role of rivers in the global carbon cycle is not limited to passive transport but a significant amount of carbon is reprocessed within fluvial systems in a series of transformations and losses (Aucour *et al.*, 1999; Cole *et al.*, 2007; Tranvik *et al.*, 2009; Aufdenkampe *et al.*, 2011; Polsenaere *et al.*, 2013; Khadka *et al.*, 2014). Carbon in transit can be lost to the atmosphere as CO_2 or sequestered in sediments, sometimes first through biological fixation (Figure 2) (Cole *et al.*, 2007; Tranvik *et al.*, 2009; Aufdenkampe *et al.*, 2011; Khadka *et al.*, 2014).

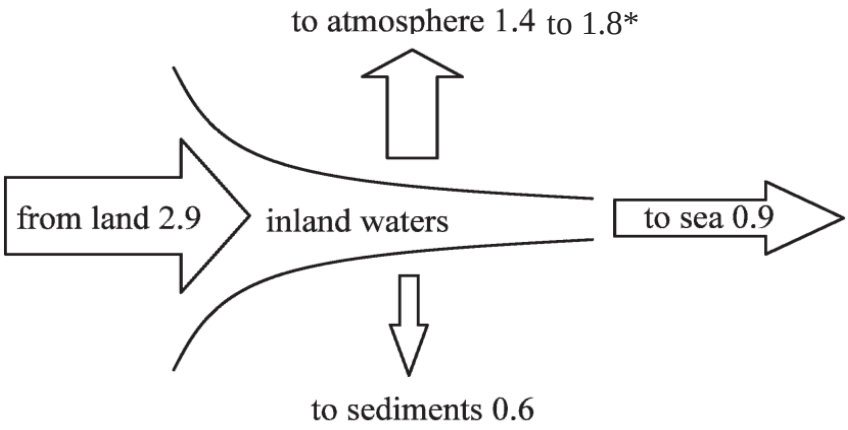

Figure 2: Simplified schematic of the role of inland aquatic systems in the global carbon balance
From Tranvik *et al.* (2009). A revision of the 'active pipe' hypothesis advanced by Cole et al. (2007). *updated from 1.4 in Tranvik et al. (2009) to 1.8 by Raymond et al. (2013). Values in Pg C yr^{-1}.

Fluvial evasion of CO_2 is now recognised to be a major component of regional and global carbon cycles, currently estimated at a rate of 1.8 ± 0.25 petagrams of carbon per year (Raymond *et al.*, 2013; Figure 2), and its omission from carbon budget calculations may account for some of the imbalance in global estimates of carbon reservoir size and rate of transfer (Richey *et al.*, 2002; Billett *et al.*, 2006; Doctor *et al.*, 2008; Aufdenkampe *et al.*, 2011). It has been estimated that 48% of land carbon received by inland waters is returned to the atmosphere as CO_2 (Tranvik *et al.*, 2009), but this proportion could be higher. For example, more recently CO_2 degassing was found to account for up to 73% of total catchment carbon export in the Archachon Lagoon catchment (Polsenaere and Abril, 2012). Thus if CO_2 degassing is not taken into account the portion of the DIC that is exported by river waters is underestimated (Cole *et al.*, 2007; Tranvik *et al.*, 2009; Butman and Raymond, 2011; Polsenaere and Abril, 2012).

Whilst efflux estimates are becoming more precise (e.g. Raymond *et al.*, 2013), the specific controls on CO_2 efflux and its exact magnitude remain poorly understood and quantified (Zappa *et*

al., 2007; Alin *et al.*, 2011; Butman and Raymond, 2011; Rasera *et al.*, 2013) and fluvial CO_2 evasion may still be underestimated (Alin et al., 2011; Raymond et al., 2013) or overestimated (Hunt et al, 2011, Abril et al 2015). Better quantification and understanding of the controls on aquatic CO_2 degassing are therefore needed, particularly in systems, such as lower order streams and high latitude rivers, for which data are still sparse (Butman and Raymond, 2011; Melack, 2011; Wallin *et al.*, 2011; Raymond et al., 2013). Additionally, climate change is projected to change regional hydrology, including seasonality (e.g. Gloor *et al.*, 2013; Charlton and Arnell, 2014), thus understanding the magnitude, controls and origins of fluvial CO_2 efflux is vital to assessing the impact of climate change on this potential CO_2 feedback process.

1.4 Origins of Carbon in Fluvial Systems

CO_2 efflux is fuelled by the DIC pool which comprises dissolved CO_2 ($CO_{2(aq)}$), carbonic acid (H_2CO_3), bicarbonate (HCO_3^-) and carbonate (CO_3^{2-}). The primary sources of DIC in freshwaters are bedrock/mineral dissolution, biogenic CO_2 and atmospheric CO_2 (Yang *et al.*, 1996; Butman and Raymond, 2011; Melack, 2011; Wallin *et al.*, 2011; Sand-Jensen and Staehr, 2012; Polsenaere *et al.*, 2013; Khadka *et al.*, 2014).

DIC in freshwater can be differentiated into two fractions with distinct origins and behaviours: carbonate alkalinity (which is predominantly in the form of HCO_3^-) and $CO_{2(aq)}$ (which is predominantly of biogenic origin) (Polsenaere and Abril, 2012). HCO_3^- originates from weathering and dissolution of bedrock and soil minerals (Yang *et al*. 1996; Aucour *et al*., 1999; Polsenaere and Abril, 2012) and contributes to the riverine DIC pool via surface flow and groundwater discharge (Aucour *et al.*, 1999; Barth *et al.*, 2003). $CO_{2(aq)}$ can be contributed to the DIC pool from: (i) root respiration and bacterial oxidation (aerobic respiration) of organic matter (OM) within the soils, which enters the river by flushing of the soil or via the groundwater discharge; (ii) respiration of OM within the river itself; and, (iii) atmospheric equilibrium CO_2 exchange at the air/water interface (Yang *et al.*, 1996; Aucour *et al.*, 1999; Polsenaere and Abril, 2012; Polsenaere *et al.*, 2013; Khadka *et al.*, 2014).

DOC can also fuel efflux, but indirectly. DOC is found in aquatic systems in forms that range in size from simple amino acids to large complex molecules (e.g. humic and fulvic acids) with high molecular weights and generation is linked to biological decomposition of OM (Stumm and Morgan, 1996; Neff and Asner, 2001). DOC cannot degas from water to the atmosphere directly, however UV-oxidation and/or microbial respiration of DOC produces CO_2 (and other greenhouse gases) which can be dissolved into the water and contribute to the DIC pool, thus DOC is a primary intermediary to global carbon cycling (Cole *et al.*, 2007; Waldron *et al.*, 2007; Battin *et al.*, 2008; Vonk *et al.*, 2013).

1.5 The Carbonate System

The aquatic DIC pool, consisting of the species $CO_{2(aq)}$, H_2CO_3, HCO_3^- and CO_3^{2-}, is governed by the carbonate system, a weak acid/base natural buffer system that dominates the Earth's fresh and marine waters (Rose and Long, 1989; Atekwana and Krishnamurthy, 1998; Hofmann and Schellnhuber, 2010; Brezonik and Arnold, 2011; Pedersen *et al.*, 2013). H_2CO_3 (true carbonic acid) is the product of hydration of CO_2, and so it and $CO_{2\ (aq)}$ are commonly expressed simultaneously as H_2CO_3*or CO_2* (Stumm and Morgan, 1996; Brezonik and Arnold, 2011; Polsenaere and Abril, 2012). Total dissolved carbonate (TC) is given by Equation 1 and the equilibria among the components can be written as Equation 2 (Hofmann and Schellnhuber, 2010; Brezonik and Arnold, 2011).

Equation 1 $TC = [H_2CO_3^*] + [HCO_3^-] + [CO_3^{2-}]$

Equation 2 $CO_{2(aq)} + H_2O \rightleftharpoons HCO_3^- + H^+ \rightleftharpoons CO_3^{2-} + 2H^+$

Speciation of DIC is governed by the following well-known equilibria (Equation 3 - 5) (Rose and Long, 1989; Stumm and Morgan, 1996):

Equation 3 $CO_2 + H_2O \rightleftharpoons CO_2^*$

Equation 4 $H_2CO_3 \rightleftharpoons H^+ + HCO_3^-$

Equation 5 $HCO_3^- \rightleftharpoons H^+ + CO_3^{2-}$

The relative proportion of each DIC species in a solution is a function primarily of pH (Figure 3) (Stumm and Morgan, 1996; Hofmann and Schellnhuber, 2010; Pedersen *et al.*, 2013), and understanding the chemistry of dissolved DIC and the proportional changes of the constituents in response to pH is essential because it determines the availability of free CO_2 for efflux (Pedersen *et al.*, 2013). At pH < 6.3 CO_2 (CO_2*) dominates, at pH 6.3 – 10.3 HCO_3^- dominates, and at pH > 10.3 CO_3^{2-} dominates (Pedersen *et al.*, 2013). CO_2 can exist in aqueous or gaseous form whereas HCO_3^- and CO_3^{2-} can only exist in aqueous form, thus in waters with pH < 6.3 a greater fraction of the DIC is present as free CO_2 and available for degassing than in waters with pH > 6.3 where a decreasing fraction of the DIC is in a form available for degassing (Hofmann and Schellnhuber, 2010). The pH of temperate streams is typically 4 – 7 (Ingvarsson, 2008), and much of the dissolved carbon is available for degassing in this range.

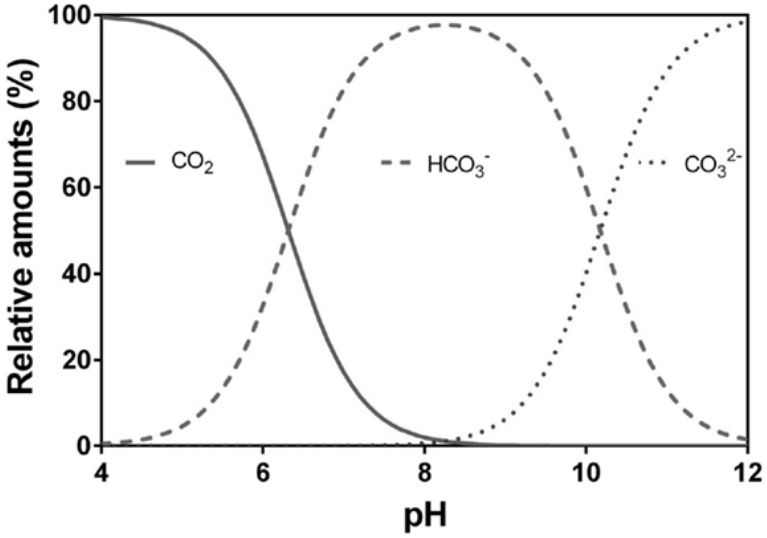

Figure 3: Relative amount of the components of the aquatic carbonate system as a function of pH
For conductivity 250 µS cm^{-1} and temperature 20°C. From (Pedersen *et al.*, 2013).

Alkalinity, defined as the capacity of water to accept hydrogen ions (H^+), is also important to the carbonate system (Manahan, 1993). Alkalinity serves as a buffer to pH with HCO_3^-, CO_3^{2-} and hydroxide ions (OH^-) being the main species responsible (Manahan, 1993). As alkalinity is generally dominated by the presence of HCO_3^- and CO_3^{2-} ions in a solution (Rose and Long, 1989; Hofmann and Schellnhuber, 2010), it can be used as an indicator of the size of the inorganic carbon pool in the water.

1.6 Tracing the Carbon Pool

Concentration of DIC ([DIC]) and the carbon stable isotopic composition of the DIC ($\delta^{13}C_{DIC}$) are particularly useful tracers of the DIC pool and have been used to evaluate the sources, sinks and fluxes of carbon in fluvial systems (e.g. determining proportional contributions of carbon from groundwater vs. terrestrial sources (Waldron *et al.*, 2007); identifying seasonal contribution of snow melt (Doctor *et al.*, 2008); tracing carbon inputs from the urban environment (Glaser *et al.*, 2005); calculating the export of DIC to the oceans (Meybeck, 1993; Aufdenkampe *et al.*, 2011)), as well as the biogeochemical processes that affect the $\delta^{13}C_{DIC}$ composition of the DIC pool (e.g. biological mediation (Parker et al., 2010; Waldron et al., 2007; Gammons et al., 2011) and CO_2 efflux (Doctor *et al*., 2008; Polsenare and Abril, 2012)).

DIC concentrations and loads in surface waters represent the net effect of catchment inputs, outputs and in-situ processes (Finlay, 2003; Tobias and Böhlke, 2011). The primary sources of DIC in freshwaters (atmospheric CO_2, biogenic CO_2 and bedrock/mineral C) have widely varying $\delta^{13}C_{DIC}$ in fluvial systems (Polsenaere *et al*., 2013; Yang *et al*., 1996; Khadka *et al*., 2014), because fractionation (the partitioning of isotopes between two substances or two phases of the same substance) (Hoefs, 1997; Criss, 1999; see Appendix A) imparts specific isotopic signatures on the

carbon compounds. This $\delta^{13}C_{DIC}$ can sometimes be used to determine the relative contributions of each source to the DIC pool, and/or any biogeochemical processes the DIC pool has subsequently undergone (e.g. Waldron *et al*., 2007; Khadka *et al*., 2014). The range of $\delta^{13}C$ usually measured in a number of natural carbon-containing compounds is shown in Figure 4.

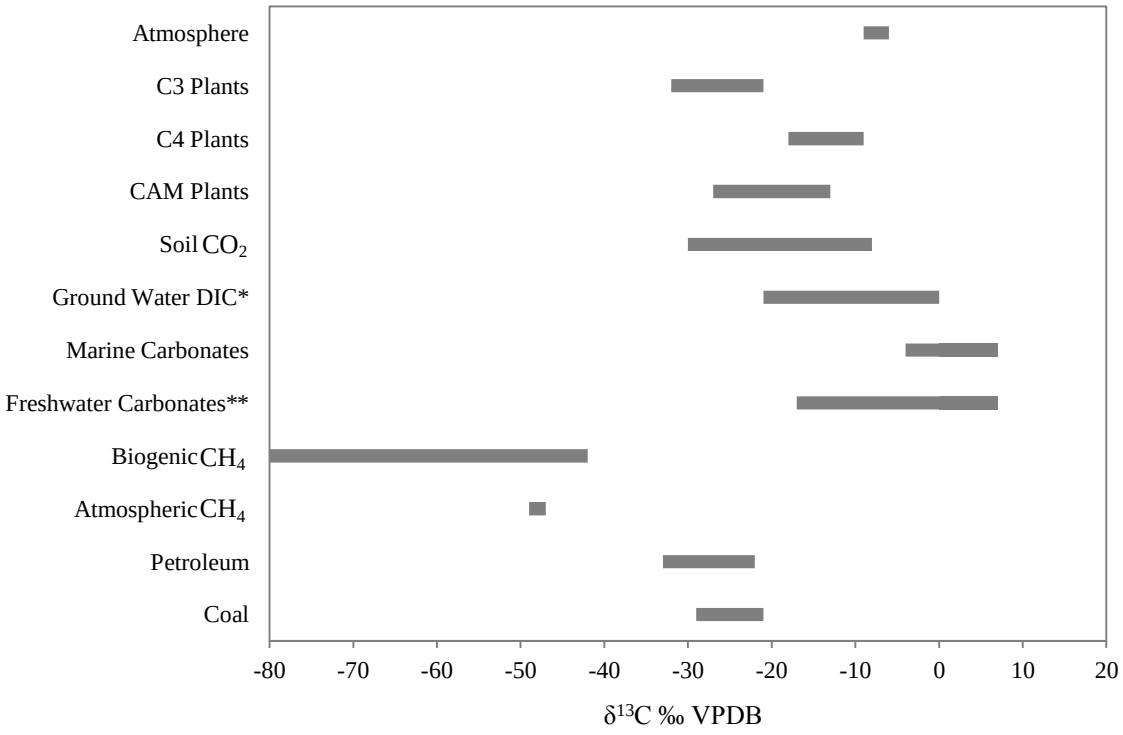

Figure 4: Usual ranges of $\delta^{13}C$ in carbon-containing natural compounds
* Can be as high as +14 ‰. ** Can be -32 to +18 ‰. Adapted from Clark and Fritz (1997).

The processes involved in the internal cycling of DIC in fluvial systems and the resultant DIC mass balance and isotopic signature of the DIC are discussed in Chapter 4, and detail on isotope fractionation and notation is provided in Appendix A.

1.7 Thesis Contents

This thesis comprises three individual pieces of research detailed below, that together address the aims of the Thesis (section 1.1):

Chapter 3, "Hydraulics as a control on CO_2 Efflux", investigates the magnitude of and controls on CO_2 efflux across three contrasting (size, land use, characteristics) UK catchments, using direct contemporaneous measurement of CO_2 efflux and hydraulic and environmental parameters, and suggests a new approach for large-scale upscaling of CO_2 efflux using visual classification of water surfaces.

Chapter 4, "Isotope systematics and sensor technology provide insight into the source and cycling of fluvial DIC and CO_2", uses stable carbon isotope and DIC concentration measurements to investigate whether the source and internal processing of the DIC pool varies across the three contrasting UK catchments. The relationships of DIC source and CO_2 efflux with logged hydrochemistry parameters are explored for use in reconstructing temporal variation in DIC source and CO_2 efflux to understand the origin of effluxed carbon and how this may respond to a climate-induced changing hydrological cycle.

Chapter 5, "Greenland Ice Sheet meltwaters are a pathway for the return of old carbon to the atmosphere and potentially a sink for CO_2", investigates the magnitude of and controls on CO_2 efflux, and the source(s) of carbon in two cryospheric systems in a region (arctic Greenland) that is particularly vulnerable to climate change, and where the DIC pool is not dominated by terrestrial soil inputs (as it tends to be in temperate regions), but by ice-sheet and ground-ice melt. Carbon-source investigations are extended to include determination of the age of fluvial and effluxed carbon, using radio-carbon dating, to assess whether old, highly biolabile carbon is being released and returned to the atmosphere and potentially feeding back to climate change. Spatial patterns of efflux and draw-down are used to upscale the contribution of a high-latitude region to the global CO_2 efflux budget.

The appropriate literature for each piece of research will be drawn upon within the chapter. The three studies are linked and their findings and implications will be pulled together in the final chapter, Chapter 6, "Discussion and Conclusions". A general methods chapter, Chapter 2, "Methods", follows this introduction, and outlines field and laboratory methods used throughout the thesis. Methods specific to a chapter will be outlined in the chapter methodology.

2 Methods

This chapter details the methods that apply to more than one subsequent chapter. Any methods specific to only one chapter will be detailed within the methods section of that chapter. Work from Chapter 3 of this Thesis has been published – Long *et al*., 2015, Appendices B and C – and so much of the methodological information herein is similar to that in the paper.

2.1 Field Sites

This study incorporates five contrasting field sites that vary in location, size and catchment characteristics. At each site, sampling was carried out over a minimum of several months to a maximum of two years, in order to capture a range of seasons and hydrological conditions. Within each field site, sampling locations were chosen to ensure that a range of flow intensities were included.

Measurements were made in three catchments in the UK – Drumtee Water (DW), the River Kelvin (RK) and the River Etive (RE) – and two catchments in Greenland – the Akuliarusiarsuup Kuua River (AR) and permafrost-landscape surface-thaw systems in the vicinity (PLST). Below is an overview of each field site and further detail, including the reasons for the choice of each site, is contained within the relevant chapter.

2.1.1 UK Field Sites

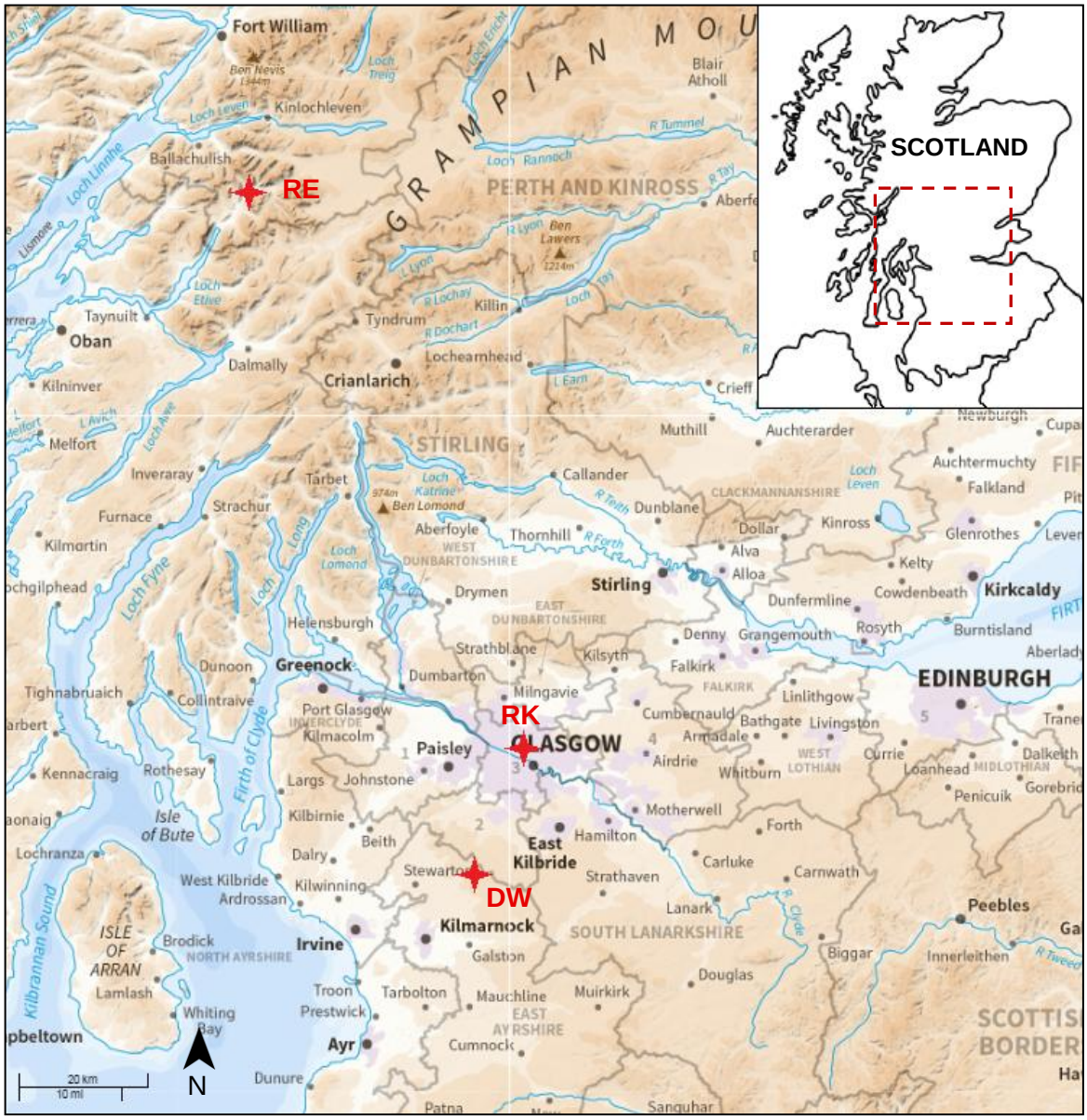

Figure 5: UK field sites location map

Red stars show the general location of sampling sites. Base map taken from Digimap 2016, contains OS data © Crown copyright and database right 2015. For educational use only.

2.1.1.1 Drumtee Water, Scotland

Figure 6: Drumtee Water sampling site
The image shows the stream in low flow conditions, the arrow shows flow direction. Photograph taken in June 2013.

Located in central Scotland, 30 km south of Glasgow, Drumtee Water (sampling site 55º41'16"N 4º23'37"W, 197 m.a.s.l.) is a headwater, 5.7 km^2, peat-dominated catchment where the land use is rough grazing and maximum elevation within the catchment is 260 m (Figure 6). The climate is temperate; mean annual temperature is 8 – 9 ^oC, mean annual rainfall is 1250 – 1500 mm and on average there are 10 to 20 days of snow lying per year (1981 – 2010; Met Office, 2016). The bedrock is mainly sandstone and lava with no carbonates (Digimap, 2016). Measurements were made in a 19 m reach, where the stream is 3rd order, the channel is 4 – 5 m wide, and bed sediment is a mixture of pebbles, boulders and soft sediment. Fieldwork was carried out between July 2012 and May 2014 (number of full- and part-sampling occasions: 100).

2.1.1.2 River Kelvin, Scotland

Figure 7: River Kelvin sampling site
The image shows the river in low flow conditions, the arrow shows flow direction. Photograph taken in July 2013.

Located in central Scotland, in the city of Glasgow, the River Kelvin (sampling site 55º52'06"N 4º17'16"W, 18 m.a.s.l.) is a 335 km^2 (SEPA, 2012) semi-urban (23%) catchment, containing agricultural land (70%) and some forestry (6%), with a maximum elevation within the catchment of 510 m (Figure 7). The climate is temperate; mean annual temperature is 9 – 10 $^{\circ}$C, mean annual rainfall is 1000 – 1250 mm and on average there are 0 to 20 days of snow lying per year (1981 – 2010; Met Office, 2016). The bedrock is mainly sandstone, lava and silicalastics with no carbonates (Digimap, 2016). Measurements were made within a 30 m reach, where the river is 5th order, 1.2 km upstream of the confluence with the River Clyde Estuary and approximately 9 km downstream of the Scottish Environmental Protection Agency (SEPA) Killermont gauging station (station reference NS 55828 70516). Bankfull width is 15 – 20 m and bed sediment is gravel, large pebbles and patches of exposed bedrock. Fieldwork was carried out between June 2012 and May 2014 (number of full- and part-sampling occasions: 99).

2.1.1.3 River Etive, Scotland

Figure 8: The River Etive
The image is from the mid-reaches and shows the river at moderate flow in spring 2015. The arrow shows flow direction. Image taken from: www.lochplus.com, 2016.

Located in the West Highlands of Scotland, the River Etive (56º37'00"N 4º56'30"W, sampling section 5 – 240 m.a.s.l.) is a small rural catchment (in the order of 50 km^2) draining Rannoch Moor (peatland) and mountainous terrain (maximum elevation >1000 m) (Figure 8). The climate is temperate; mean annual temperature is 8 – 9 $^{\circ}C$, mean annual rainfall is >3000 mm and on average there are 30 to 60+ days of snow lying per year (1981 – 2010; Met Office, 2016). The bedrock is mainly granitic with some lavas and no carbonates (Anderson, 1937). The river is approximately 30 km in length and drains into Loch Etive. Measurements were made within the lower 20 km reach of the river, the furthest downstream sampling point being 500 m upstream of the head of the loch (sea level). The bankfull width varies between approximately 8 and 200 m in this section, and was between 10 and 50 m at the sampling locations of this study. The bed sediment is gravel to large boulders and in places the channel is partially braided. The catchment is partially to fully snow-covered each winter. Fieldwork was carried out in April and May 2014 and between February and June 2015 (number of full- and part-sampling occasions: 21).

2.1.2 Greenland Field Sites

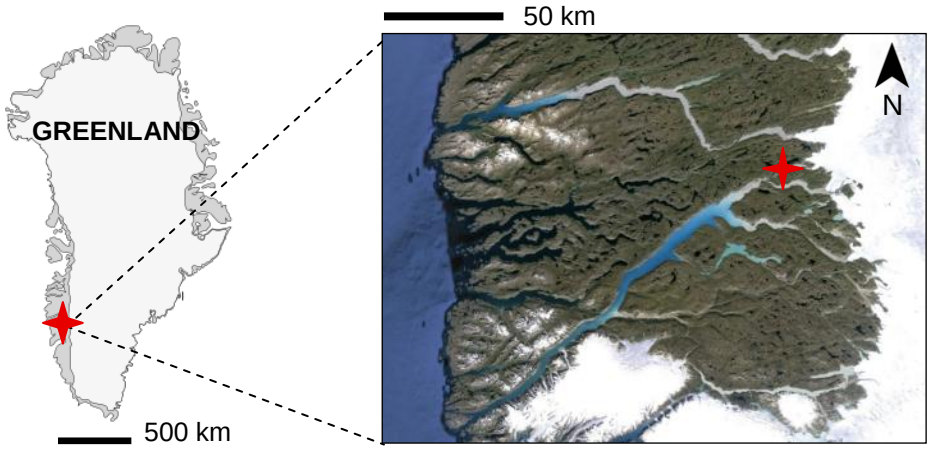

Figure 9: Greenland site location map

The red star shows general location of AR and surrounding PLST sites. Image from Google Earth, 2016: Imagery ©2016 U.S. Geological Survey, IBCAO, Map Data ©2016.

Both Greenland field sites were located in the Kangerlussuaq region of West Greenland (Figure 9). Located just north of the Arctic circle, the Kangerlussuaq region is an area of continuous ice-free land adjacent to the GrIS (Willemse, 2002). Since the last major glaciation the ice margin has retreated, with frequent pauses and re-advances, from beyond the current coastline to its present location, which has been relative stability since 1500 BP (Ten Brink and Weidick, 1974; Storms *et al.*, 2012). During the late Holocene the ice margin here, as well as other parts of west Greenland, re-advanced over Quaternary deposits containing fresh organic matter, soils and vegetation (Bhatia *et al.*, 2010; Lawson *et al.*, 2014).

Kangerlussuaq settlement (population 499; Statbank Greenland, 2016) is located in a 2-3 km wide proglacial river valley with a surrounding landscape of mountains (400-600 m.a.s.l.) and numerous predominantly closed basin lakes and pools (Eisner *et al.*, 1995; Jørgensen and Andreasen, 2007; Aebly and Fritz, 2009). The bed rock in the region is predominantly reworked and metamorphosed gneisses (Ryu and Jacobson, 2012) and the soils are continuous permafrost (Eisner *et al.*, 1995; Jørgensen and Andreasen, 2007; Wallroth *et al.*, 2010). In winter the entire soil profile is frozen, but summer active layer thickness ranges from 0.15 and 5.0 m (Van Tatenhove and Olesen, 1994). Active layer thickness can vary over short distances due to due to differences in vegetation, snow cover, soil types and thermal properties of the subsurface (Wallroth *et al.*, 2010).

Precipitation and winds in the area are heavily influenced by the GrIS (3000 m.a.s.l.) with the resulting climate sub-arctic and arid (Jørgensen and Andreasen, 2007), and continental despite proximity to the coast (Eisner *et al.*, 1995). Mean annual precipitation is low, 150 – 160 mm yr^{-1} (Russell, 2007; Aebly and Fritz, 2009; Ryu and Jacobson, 2012). Winds are katabatic and strong, and decrease in strength with distance from the GrIS margin (Eisner *et al.*, 1995). Mean annual

temperatures have risen by 2 – 3 °C since the beginning of the 1990s (Jørgensen and Andreasen, 2007) to -5 °C (Ryu and Jacobson, 2012) and daily average temperatures range from -43 °C in the winter to +24 °C in the summer (Russell, 2007).

2.1.2.1 Akuliarusiarsuup Kuua River

Figure 10: Akuliarusiarsuup Kuua River

Left image = upper reaches, photograph taken 08/06/2014. Right image = lower reaches and the confluence of the Akuliarusiarsuup Kuua River (left channel) with the Qinnguata Kuussua River (right channel), photograph taken 21/06/2014. The arrows show the flow direction.

The Akuliarusiarsuup Kuua River (67°02'N, 50°35'W, sampling section 8 – 450 m a.s.l.) is situated in a proglacial valley and drains the Greenland Ice Sheet (GrIS) via the Russell and Insunnguata Glaciers (Ryu and Jacobson, 2012) (Figure 10). AR is 38.4 km in length, and joins the more southerly Qinnguata Kuussua River to become the Watson River <3 km upstream of the settlement of Kangerlussuaq (67°01'N 50°42'W, 90 m a.s.l.) where it discharges into Søndre Strømfjord (Rennermalm *et al.*, 2012; Ryu and Jacobson, 2012). The river varies in channel type and bed sediment along its length from single channel and braided sand/silt bed reaches to highly-braided pebble-/boulder-bed reaches. The bankfull width is also highly variable from a few meters to a few 100 meters, and there are a number of lakes within the reach. The river is seasonal flowing typically between late May/early June to mid/late September (Bartholomew *et al.*, 2011; van As *et al.*, 2012; Hasholt *et al.*, 2013) and the lake surfaces (both the lakes within AR and hydrologically disconnected lakes in the surrounding permafrost landscape) are typically frozen from October to June (Russell, 2007). Fieldwork was carried out at the beginning of the melt season of 2014 (4th June – 4th July) (number of full- and part-sampling occasions: 46).

2.1.2.2 Permafrost-Landscape Surface-Thaw Waters

Figure 11: Permafrost-landscape surface-thaw waters
Left image = small pool, photograph taken 01/07/2014. Right image = large lake outlet stream, photograph taken 11/06/2014, the arrow shows the flow direction.

Measurements were made within a range of surface-thaw waters among the permafrost-landscape (Figure 11) in the region; small pools (55 – 130 m wide), medium lakes (1200 m length) and large (5.5 km length) lake systems were sampled. Lake surfaces and pools are frozen for ~9 months of the year: they are generally ice-free by mid June and refreeze mid to late September (Anderson *et al.*, 2001). Many lakes/pools have no direct surface inflow, except between lakes/pools in close proximity, and outflows are generally seasonal, flowing in the early melt season but dry by the end of the summer (Anderson *et al.*, 2001). Fieldwork was carried out at the beginning of the melt season of 2014 (4^{th} June – 1^{st} July) (number of full- and part-sampling occasions: 25). During the early melt period there is greatest potential for carbon pools trapped during the winter to be released upon thaw (e.g. Kling *et al.*, 1992), thus this period was chosen with the aim of capturing this release.

2.2 Field Methods

A full set of field measurements and samples comprises: CO_2 efflux, flow velocity profile, water chemistry parameters (pH, alkalinity, [DIC] and $\delta^{13}C$), environmental parameters (air and water temperatures, wind speed, humidity, light intensity) and a visual assessment of water surface state (see Table 1). Each method is outlined below, with further detail of some methods and additional methods specific to a chapter included in the relevant results chapter.

Table 1: Full set of field measurements and samples, and their purpose

Type of Measurement	Unit	Purpose
CO_2 efflux	µmol CO_2 m^{-2} s^{-1}	The rate of transfer of carbon to the atmosphere – the focus of this research
Flow velocity profile	m s^{-1}	For calculation of hydraulic parameters and subsequent assessment of their control on CO_2 efflux
pH	unitless	An indicator of the DIC pool size and CO_2 availability. Used for calculation of pCO_2.
Alkalinity	mg L^{-1}	A broad indicator of the DIC pool size and groundwater inputs
[DIC]	mmol L^{-1}	A direct measure of the DIC pool size. Used for calculation of pCO_2.
$\delta^{13}C_{DIC}$	‰	A tracer for the source of DIC
Air temperature	˚C	An indicator of catchment productivity which can influence DIC delivery to, and reprocessing in, fluvial systems. Used for CO_2 efflux rate calculations.
Water temperature	˚C	An indicator of in-stream productivity which can influence DIC delivery to, and reprocessing in, fluvial systems. Used for calculation of hydraulic parameters.
Wind speed	m s^{-1}	Measured to assess for control on CO_2 efflux
Humidity	%	Measured to assess for differences between field sites
Light intensity	lux	A broad indicator of light available for catchment/in-stream productivity
Water surface state	smooth, medium or rough	Classified to assess for a relationship with CO_2 efflux

2.2.1 CO_2 Efflux

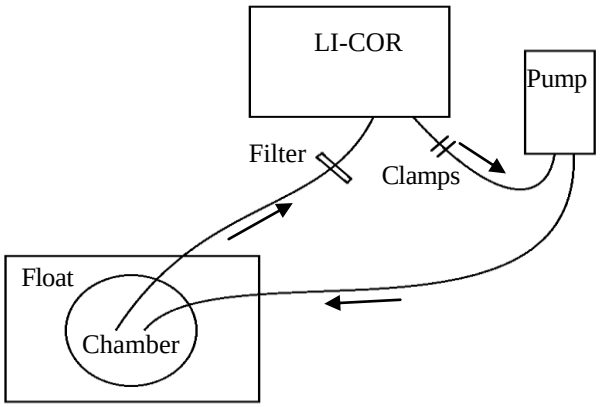

Figure 12: Schematic diagram of the closed-loop floating chamber system

Diagram not to scale. Pump (Schego Optimal) is to ensure internal air circulation. Arrows show the direction of air flow. Filter is in place to protect Licor from water/particles that may enter the tubing. Clamps are to maintain the circulating airflow at a speed of 0.3 – 1.0 L m^{-1}. From (Long *et al.*, 2015).

CO_2 efflux was measured, using the floating chamber method (Frankignoulle, 1988), at all sites on all sampling occasions, except where there was equipment failure, or flow conditions rendered measurement unsafe. A Licor (LI-840A) infrared CO_2/H_2O gas analyzer was used to measure the rate of CO_2 accumulation in a floating chamber of known volume (0.0029 m^3) (Frankignoulle, 1988) (for configuration see Figure 12). The cylindrical chamber had a polystyrene float and a lip of 50 mm that penetrated the water surface below, closing the system. CO_2 accumulation was measured over four minutes (the chamber was anchored) and repeated a minimum of three times, with atmospheric CO_2 levels recorded before and after each repeat by venting the chamber to the atmosphere (Figure 13). The gradient of CO_2 accumulation was used to calculate the CO_2 flux rate (see 2.4.1).

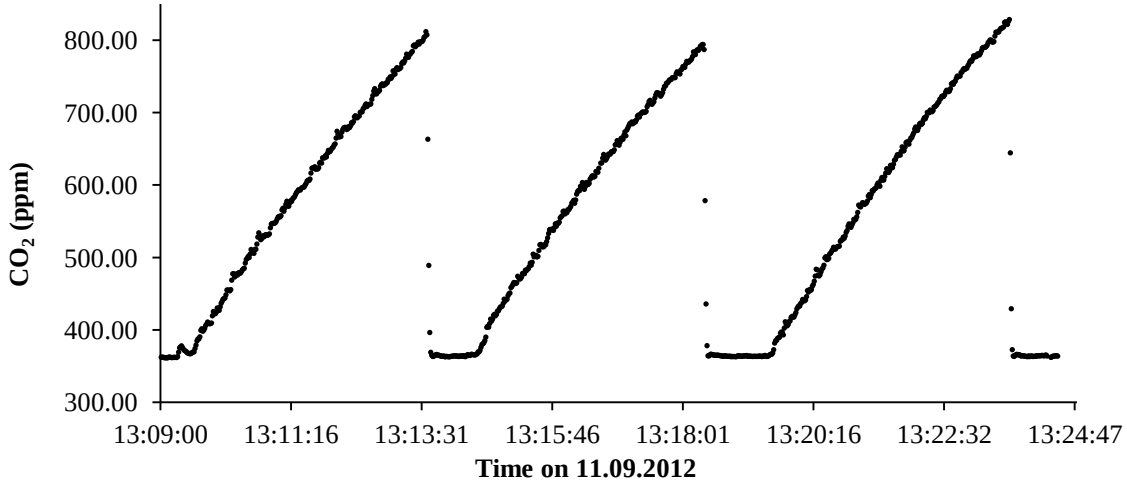

Figure 13: Example chamber air pCO_2 profile over a measurement cycle

CO_2 accumulation in the floating chamber at DW on 11.09.2012. Each slope represents one float repeat, with atmospheric CO_2 level recorded before, between, and after repeats to ensure all accumulations begin from background atmospheric CO_2 concentration.

Although widely used (e.g. Frankignoulle, 1988; Billet *et al*., 2006; Billet and Moore, 2008; Rasera *et al*., 2008; Alin *et al*., 2011; Wallin *et al*., 2011; Neu *et al*., 2011; SandJensen and Staehr, 2012; Striegl *et al*., 2012; Rasera *et al*., 2013), there are concerns that floating chambers may under- or over-estimate the CO_2 efflux. Underestimation may occur due to the removal of the effect of wind at the water surface and subsequent reduction of water surface turbulence (e.g. Wallin *et al*., 2011; Billet & Moore, 2008), or chambers may overestimate CO_2 efflux by disrupting the water surface, causing artificial turbulence and thus affecting gas exchange (Kremer et al., 2003; Vachon et al., 2010; Lorke et al., 2015). It has been argued that, in flowing waters, anchored chambers overestimate CO_2 efflux compared to drifting chambers (Lorke et al., 2015), however the authors omit that a drifting chamber will spend proportionally more time in the slower flowing reaches of the river where gas fluxes are lowest (e.g. Long et al., 2015).

Alternative methods of direct CO_2 efflux measurement exist, e.g., the eddy-covariance technique (e.g. Baldocchi, 2014) and volatile gas tracer experiments (e.g. Hope *et al*., 2001). However, eddy-covariance requires a large open water surface fetch around the point of measurement, thus is unsuitable for most rivers and streams (Wallin *et al*., 2011; Lorke *et al*., 2015), and gas tracers can only practically be applied to small streams (Lorke et al., 2015) and are susceptible to microbubbles which may cause overestimated gas fluxes (Beaulieu et al., 2012). Although concerns exist regarding the absolute accuracy of CO_2 fluxes generated using floating chambers, they can be used across a wide size-range of fluvial systems, they are uncomplicated, inexpensive, easy to transport, measurements can be easily spatially and temporally replicated, and they are widely used thus results generated here will be comparable to numerous published studies.

2.2.2 Flow Velocity Profiles

Flow velocity profiles were constructed for each sampling occasion from measurements of stage height and flow velocity at various increments of the flow depth, at one point of the channel width, except where there was equipment failure, or flow conditions rendered measurement unsafe.

Stage height (flow depth) was measured manually with a meter stick while standing downstream of the stick to minimise disturbance of the water at the point of measurement. Corresponding stage height values were obtained for RK from the SEPA Killermont gauging station, 9 km upstream of the measurement site of this study, and for DW from the in-situ pressure transducer (within the MP TROLL 9000 sonde). No corresponding stage height information was available for RE.

Flow velocity was measured using a Valeport flowmeter, with an impeller diameter of 50 mm, set to 60 second averaging, at a minimum of 5 depth increments through the water column. Measurements were taken while standing downstream of the flow meter and with the impeller aligned with the direction of the flow.

Hydraulic parameters (Froude number, Reynolds number, mean velocity, shear stress, shear velocity and shear Reynolds number), which are descriptors of flow turbulence and/or structure, were calculated from each flow velocity profile and associated water temperature (see Chapter 3, section 3.3.4).

2.2.3 Water Chemistry

Water chemistry was measured at the time of CO_2 flux measurement to allow calculation of pCO_2 and exploration of data for explanatory variables for CO_2 flux models.

2.2.3.1 pH

Methods of pH measurement varied across the four different field sites due to logistics and practicalities, however, at all sites except RK pH was measured in-situ. This was to eliminate the possibility of a delay (e.g. transportation of water samples to the laboratory, or storage of samples before testing) enabling microbial action that alters sample pH (Abril *et al.*, 2015) or compromise sample integrity through laboratory processes e.g. stirring can alter sample pH through artificial degassing (Herczeg and Hesslein, 1984; Abril *et al.*, 2015).

Drumtee Water: pH was logged continuously at 30 minute resolution using an In-Situ Inc. MP TROLL 9000 water chemistry sonde, installed within 20 m upstream of the sampling locations of this study. The Troll 9000 was calibrated approximately every 4 to 6 weeks using a two-point calibration from freshly prepared pH 4 and pH 7 buffer solutions, and ensuring the manufacturers specified acceptable values for slope and intercept were reached. Measuring pH continuously met the manufacturer's pH probe minimum equilibration time specification of 20 minutes.

River Kelvin: pH was originally measured from an unfiltered water sample, taken at the time of chamber deployment, using a Mettler Toledo G20 Titrator immediately upon return to the University. This was 0.5 – 4 hours after sample collection; the short turnaround keeping alteration of pH through possible metabolic activity of microbes to a minimum. As the samples had low particulate content they were unfiltered to avoid alteration of pH through additional artificial degassing. However, this pH data was later considered questionable due to titrator malfunction caused by a lack of maintenance of the pH probe, and so pH was calculated from a linear relationship ($n = 10$; $R^2 = 0.72$) between discharge and pH at Killermont monitoring station. For details see Appendix C: Long *et al*., 2015, supporting information.

River Etive, Akuliarusiarsuup Kuua River and Permafrost-Landscape Surface-Thaw Waters: pH was measured directly from the river using handheld pH meters, as no in-situ loggers existed at these sites. The handheld probes were left to equilibrate for a minimum of 45 minutes to meet recommendations for low conductivity/ionic strength waters (e.g. Ryu and Jacobson, 2012). At RE, pH was measured at the time of chamber deployment using a Hanna HI98127 pHep®4 pH Tester (accuracy +/- 0.1 pH). A two-point calibration using laboratory prepared pH 4 and pH 7 buffer solutions was carried out prior to each field trip. At AR and PLST, pH was measured at the time of CO_2 flux measurement using a Hanna HI98127 pHep®4 pH Tester (accuracy +/- 0.1 pH) or a Hanna HI98103 Checker® pH Tester (accuracy +/-0.2 pH). The Hanna HI98127 probe was used for all measurements until 19th June 2014 when it was lost in a melt surge, and the Hanna HI98103 probe was for all subsequent measurements. In laboratory tests these probes were found to agree to within 0.3 pH in low conductivity waters (12 – 40 μS cm^{-1}) typical of the proglacial rivers in the area (Bartholomew *et al.*, 2011). A two-point calibrations (pH 7 and pH 10 Hanna Calibration Buffer Sachet solutions) was carried out on both hand held probes at least once a week.

2.2.3.2 Alkalinity

Alkalinity was measured in the laboratory from water samples taken at the time of CO_2 flux measurement (see section 2.3.1 for details of laboratory procedure). Water samples were collected from within the water column in 100 ml air-tight plastic pots which were rinsed three times with stream water prior to collection of the sample. Pot lids were replaced below the water surface to ensure no air was trapped within the sample bottle, thus avoiding creating a headspace into which gas would degas.

The alkalinity data is subject to some uncertainty due to the problem with the laboratory pH probe that would determine end-points. However the data correlates very well with discharge, Troll pH and SEPA/Troll stage height implying that broad trends are being captured (Appendix G). As there is a wealth of alkalinity measurements in hydrological research and it is a useful parameter to understand broadly a dominance of catchment flow by groundwater and different sources of groundwater (e.g. Rodgers *et al.*, 2004), this data has been included in the thesis as an indicator of broad trends.

2.2.3.3 DIC and $\delta^{13}C$ of the DIC

At all sites, within 15 minutes of the flux measurement, water samples were collected for determining dissolved inorganic carbon concentration ([DIC]) and stable carbon isotope ratio of the DIC ($\delta^{13}C_{DIC}$) using a headspace method (Waldron *et al.*, 2014). Using a 10ml plastic syringe and disposable needle (size: 23G 1¼", 0.6 x 30 mm) (both rinsed three times with stream water), 10 ml or 9 ml of stream water was introduced into a 12 ml exetainer, pre-washed for 24 hours in 5 molar nitric acid (to remove any contaminants) and pre-evacuated for 1 h (to remove all air), by piercing the lid septum with the needle. This was done under water to prevent air ingress during insertion and removal of the needle. Upon piercing the septum, due to pre-evacuation of the exetainer, the syringe barrel was sucked in and the stream water sample sucked from the syringe into the exetainer. Strong sucking in of the syringe barrel (< 1 min) indicated exetainers had retained vacuum and atmospheric CO_2 contamination was minimal (Waldron *et al.*, 2007). Any samples collected in exetainers where the suction time exceeded 1 min and/or any sample remained in the syringe or the vacuum failed entirely, were rejected, though this was rare. Exetainers were pre-acidified with an excess of degassed phosphoric acid (150 µL, 103%) to convert any DIC in the water to CO_2 gas which evades from the water into the headspace. The exetainer was shaken thoroughly after injection of the stream water to ensure full mixing of the sample and acid, and thus conversion of the entire DIC pool to free $CO_{2(g)}$, then stored upside down to prevent air escape/ingress via the lid or septa. The headspace was later analysed for [DIC] and $\delta^{13}C$ using an Isotope Ratio Mass Spectrometer (IRMS) (see section 2.3.2). Samples were low in particulates thus not filtered; they were collected in triplicate for statistical integrity, and collected from 20th June 2013 onwards only as techniques had to be learned prior to this.

2.2.3.4 pCO_2

Partial pressure of CO_2 (pCO_2) was calculated from the [DIC] using pH and water temperature (Rebsdorf *et al.*, 1991; Stumm and Morgan, 1996). Where pH was measured using a TROLL 9000 (DW) or a Hanna HI98127 pHep®4 pH Tester (RE, AR and PLST) uncertainty in pH is +/- 0.1 pH unit according to the manufacturers specifications. Where a Hanna HI98103 Checker® pH Tester was used (AR and PLST) uncertainty is +/- 0.2 pH according to the manufacturers specifications. For RK uncertainty in pH is 1.3%, indicated by the percent residuals of the relationship between pH and discharge (for further details see Appendix C: Long *et al*., 2015, supporting information).

pCO_2 was calculated from 20th June 2013 onwards as DIC was not measured prior to this (see 2.2.3.3 above). EpCO_2 was calculated from the pCO_2 and atmospheric CO_2 level (ppm) from 20th June 2016 onwards, as [DIC] and pCO_2 were not measured prior to this (see 2.2.3.3 above).

2.2.3.5 Discharge

River Kelvin: discharge data was obtained from SEPA, and was measured at the Killermont gauging station.

Drumtee Water: the nearest SEPA gauging station is Newmilns (station reference: NS 53252 37188) which is located on the River Irvine. DW makes up part of the River Irvine catchment thus discharge data from Newmilns may be representative of discharge at Drumtee water, however timing and magnitude of events may differ. To avoid this concern, discharge at DW was calculated from a relationship between discharge measured by an ISCO logger installed at the site on 5th Novmber 2013 (thus does not cover the full period of this study) and stage height measured by the Troll 9000 water chemistry sonde (covers the full period of this study and 5 years previous). Both instruments were installed within 20 m of each other and of the sampling locations of this study. Continuously logged stage height data was converted to discharge using a strong polynomial relationship between the two parameters (N = 3758, $R^2 = 0.99$).

River Etive, Akuliarusiarsuup Kuua River and Permafrost-Landscape Surface-Thaw Waters: discharge data was not available.

2.2.4 Environmental Parameters

Environmental parameters were recorded during each sampling occasion to allow calculation of pCO_2 and hydraulic parameters and exploration of data for explanatory variables for CO_2 flux models.

2.2.4.1 Air and Water Temperature

Air and water temperature were measured in the shade using a Lilipop®, Traceable®, handheld digital thermometer.

2.2.4.2 Wind Speed, Humidity and Light Intensity

Wind speed, humidity and light intensity were measured using a Lutron LM-8000A combined anemometer, humidity meter and light meter.

2.2.4.3 Visual Water Surface Classification

A qualitative visual assessment of the water surface state was made at the time of each CO_2 flux measurement. The degree of surface disturbance was estimated as "smooth" (a flat water surface), "medium" (ripples/waves with no white water) or "rough" (ripples and waves with white water). For examples of these states see Figure 14 taken from Long et al., 2015, supporting information (Appendix C). Visual classification of water surface state incorporates the effect of wind at the water surface.

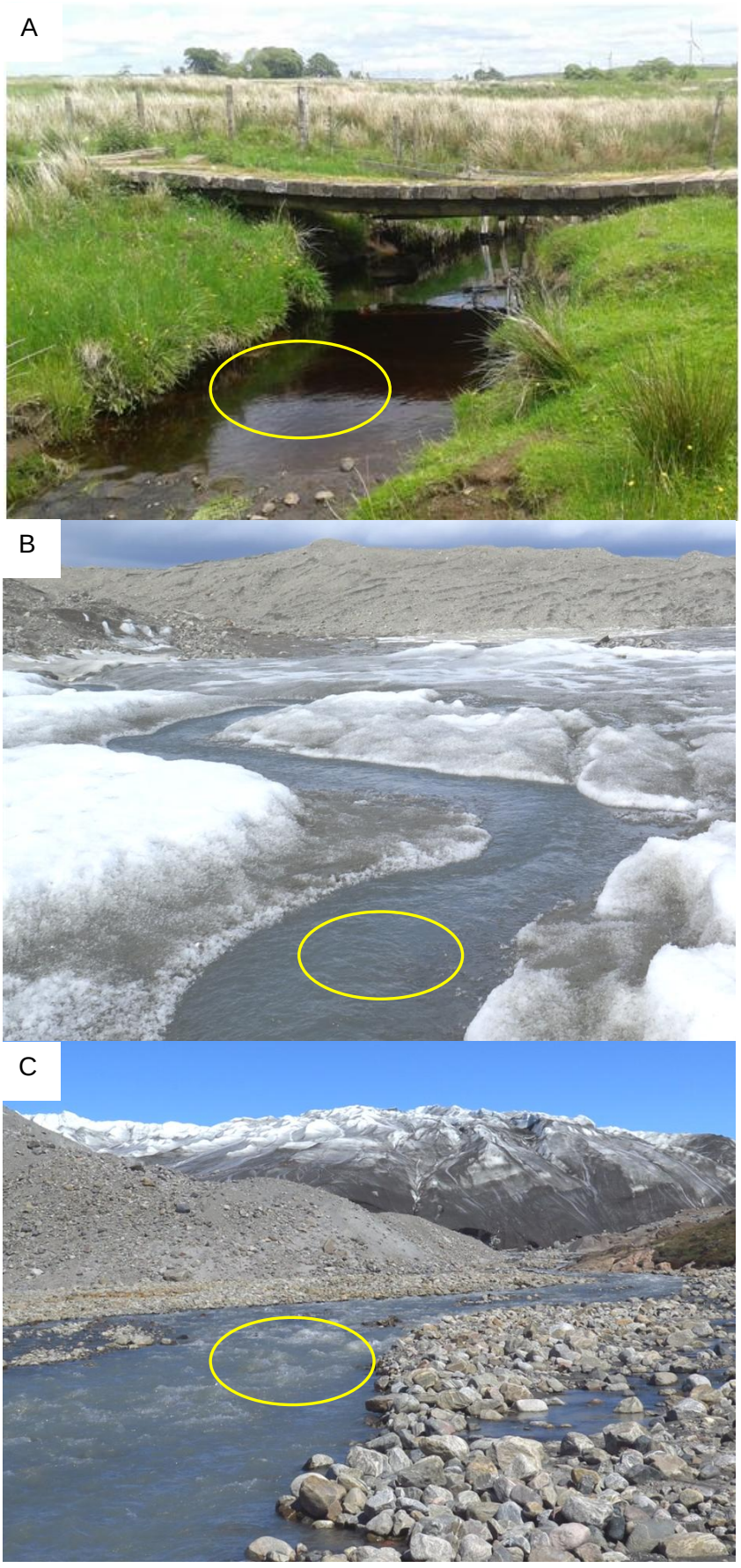

Figure 14: Photographic examples of water surface state classifications

Example water surface highlighted with yellow oval. A, smooth = a flat water surface; B, medium = ripples, with no white water; C, rough = ripples with white water.

2.3 Laboratory Methods

The following tests were carried out on water samples collected during, or within 15 minutes of, CO_2 measurements.

2.3.1 Alkalinity

Alkalinity was measured from unfiltered water samples using a Mettler Toledo G20 Titrator immediately upon return to the University. This was 0.5 – 5 hours after sample collection. As the samples had low particulate content they were unfiltered to avoid additional artificial degassing which can increase pH and alter alkalinity (Herczeg and Hesslein, 1984; Abril *et al.*, 2015).

2.3.2 DIC and $\delta^{13}C$ of the DIC

Stream water samples for [DIC] and $\delta^{13}C_{DIC}$ measurement (see section 2.2.3.3 above) were stored upside down to reduce air ingress/egress, and upon return to the university refrigerated and stored in the dark to reduce alteration of the carbon chemistry by metabolic activity of microbes (the acidification of the sample also inhibits microbial activity). [DIC] and $\delta^{13}C$ in the headspaces of samples were analysed at Scottish Universities Environmental Research Centre (SUERC) AMS Laboratory on a Thermo-Fisher-Scientific Gas Bench/Delta V Plus automated continuous-flow Isotope-Ratio Mass Spectrometer (IRMS), as Waldron *et al*, (2014).

Aqueous DIC standards were prepared and tested with the samples to allow for calibration of $\delta^{13}C$ through linear regression (in case of non-linearity of the mass spectrometer). These ranged in DIC concentration and were of three isotopically distinct sources of inorganic carbon (one $NaHCO_3$ and two $CaCO_3$ from Fisher Scientific and BDH Chemicals). The range of the $\delta^{13}C$ and [DIC] of the standards was greater than that of the samples to allow construction of calibration lines that spanned the sample range. To check for instrumental drift, one of the inorganic carbon standards (varied per run) was measured after every 7^{th} sample. Detailed laboratory procedures are available in Waldron *et al.* (2007). Uncertainty in [DIC] is 0.027 nM; the error quantification approach is reported extensively in Waldron *et al*. (2014).

Duplicate samples were often measured. The third replicate was only measured if previous replicates unexpectedly fell out with the range of standards, if there was large disagreement between sample pairs (this was rare), or if there were problems with the run such as needle/ capillary blockages. Because the accuracy and precision of the method is very high (Waldron et al., 2014), results from single samples where there were no issues with the run and the sample fell within range of the standards could be relied upon. Often duplicate samples were run to provide assurance (particularly in the early stages of learning the laboratory analysis procedure) or if initial sample results were not trust worthy.

2.4 Data Processing

2.4.1 CO_2 Efflux Rate Calculations

CO_2 flux was calculated using Equation 6 (Frankignoulle, 1988; Rasera *et al.*, 2008):

Equation 6: $$F_{CO2} = \left(\frac{\delta CO_2}{\delta t}\right)\left(\frac{V}{RTS}\right)$$

where F_{CO2} is the flux (µmol CO_2 m^{-2} s^{-1}), $\delta CO_2/\delta t$ is the slope of CO_2 accumulation in the chamber (µatm s^{-1}), V is the chamber volume (m^3), R is the gas constant (m^3 atm K^{-1} mol^{-1}), T is air temperature (K), and S is surface area of the chamber at the water surface (m^2).

For each sampling occasion, individual flux rates were calculated for each float repeat, and mean CO_2 efflux calculated as average of these. Data from the repeats was not pooled as there was mostly no overlap in the 95% confidence levels of the CO_2 accumulation slopes.

Equation 6 requires $\delta CO_2/\delta t$ is linear (Frankignoulle, 1988). However, many of the CO_2 accumulation slopes began to curve within a four minute chamber float (Figure 15 and Figure 16) as the chamber air progressed towards equilibrium with the stream water. As CO_2 evades from the stream water into the chamber, the concentration gradient between the two progressively reduces, thus the rate at which CO_2 can outgas is gradually reduced, causing the profile to curve. A curved profile means that a simple linear equation *(max CO_2 value – min CO_2 value)/number of seconds* of a four minute float is not appropriate for calculating $\delta CO_2/\delta t$. Instead, the linear part of each CO_2 accumulation slope was selected by eye (typically 0 – 100 sec) and linear regression carried out on only the linear section (Figure 17). The m value from the equation ($CO_2 = mt + c$) was used as an estimate for $\delta CO_2/\delta t$.

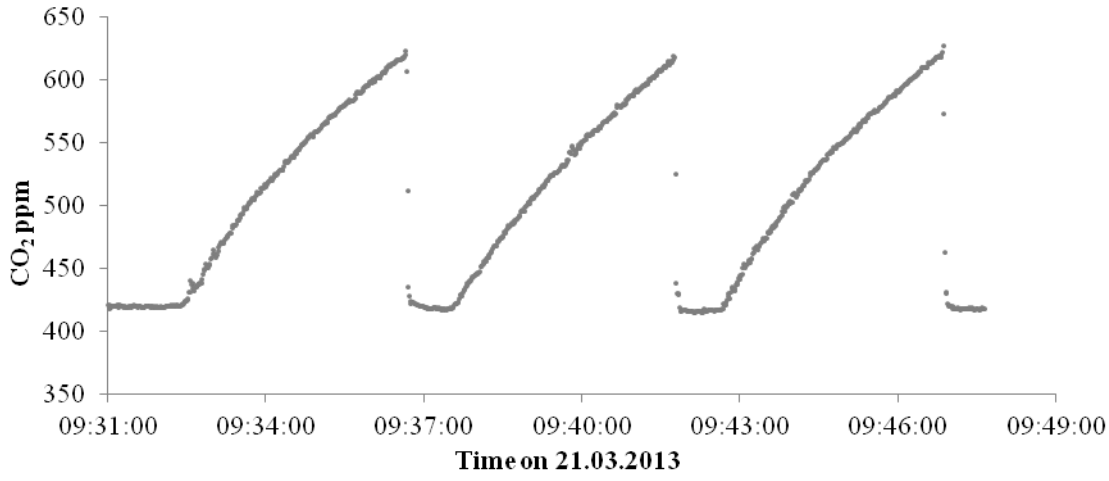

Figure 15: Example of chamber CO_2 accumulation profile
For RK 1 on 21.03.2013 showing curved CO_2 accumulation slopes

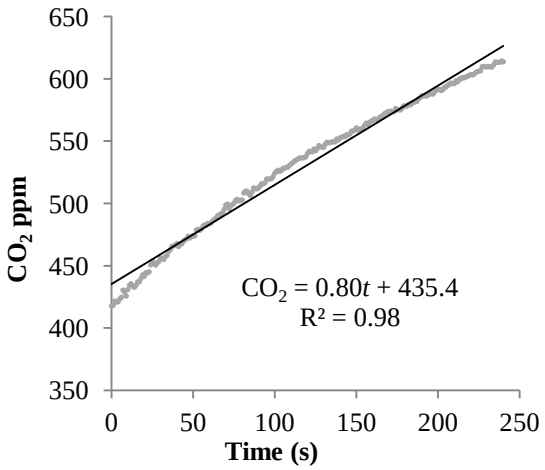

Figure 16: Whole accumulation slope
For repeat 3 at RK 1 on 21.03.2013

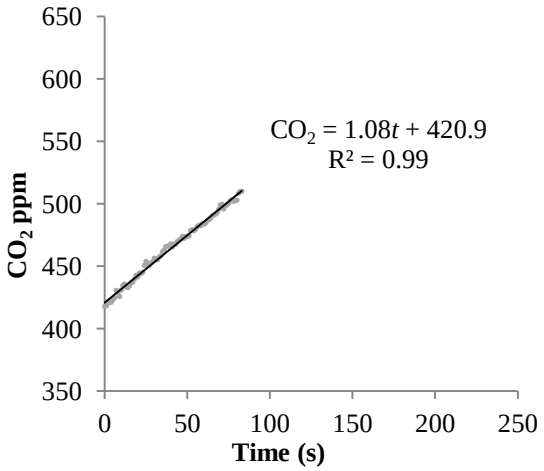

Figure 17: Cropped accumulation slope
For repeat 3 at RK 1 on 21.03.2013

2.5 Data Analysis

All data was stored in Microsoft Excel. CO_2 efflux, hydraulic, and aquatic carbon data associated with the publication Long *et al*., 2015, are lodged with the NERC-Environmental Information Data Centre hosted by the Centre for Ecology and Hydrology, doi: 10.5285/02d5cea7-10aa-4591-938a-a41e1c5bc207. Minitab 16 Statistical Software was used for some regression analysis, ANOVA, calculation of p-values, f-values and s.e. values and creation of histograms. Microsoft Excel was used for some regression analysis, calculation of confidence intervals and creation of all line, scatter and box plots. QGIS 2.12.1 was used for the creation of Figure 53 (Kangerlussuaq site map).

3 Hydraulics as a control on CO_2 efflux

3.1 Abstract

Using direct contemporaneous CO_2 efflux, hydraulic, and environmental measurements from sites in three distinct UK catchments with varied catchment characteristics and sizes, I assess whether flow intensity (a generic term which describes one or more of the measures of flow strength including mean flow velocity, bed shear stress, turbulence intensity and flow state) is a primary control on CO_2 efflux. A strong positive relationship is found between CO_2 efflux and flow intensity, and the relationship is strengthened by including pCO_2. Limited influx data indicate that flow intensity also has a key influence on CO_2 influx. A visual classification method explored as an approach for supporting large-scale (catchment, regional or larger) upscaling of fluvial CO_2 efflux, shows potential if subjectivity in interpreting water surface state can be overcome.

This chapter is an expanded version of Long *et al*. (2015), thus themes and discussion herein are similar to those in the publication, which is referenced herein as appropriate. However, this chapter does not include data collected by co-authors, and focuses only on the data collected by H. E. Long during this PhD, and includes data additional to the publication. Data analysis carried out by co-authors for the publication is excluded and all data analysis herein was carried out by H. E. Long.

3.2 Introduction

It has been observed that fluvial CO_2 evasion rates are enhanced by high turbulent energy during high river flow (Hope *et al.*, 2001; Billett *et al.*, 2006; Billett and Moore, 2008; Butman and Raymond, 2011; Wallin *et al.*, 2011; Rasera *et al.*, 2013; Raymond *et al.*, 2013), and some of the lowest evasion rates from fluvial systems have been observed in low velocity flows (Hope *et al.*, 2001; Billett *et al.*, 2006). Aquatic CO_2 evasion may also be influenced by the pressure of CO_2 in the water (pCO_2); data are not abundant, but in non-flowing water, where the effects of flow and turbulence are limited, elevated pCO_2 has been found to enhance CO_2 evasion (Billett and Moore, 2008). However, pCO_2 appears of less importance to CO_2 evasion than flow, and, there is limited understanding of the specific mechanisms by which turbulence leads to advection of gas within the water body and transfer to the atmosphere (e.g. Moog and Jirka, 1999).

Given the strong rationale that turbulence and high flows are important to the rates of gas evasion, this chapter will test the hypothesis:

"Flow intensity controls gas transfer within the water column and water surface disturbance, and so CO_2 efflux correlates with flow intensity"

The influence of turbulence on riverine CO_2 evasion was assessed by direct, contemporaneous measurements of hydraulic flow characteristics, and CO_2 efflux. As climate change is projected to change regional hydrology, including seasonality (Gloor *et al.*, 2013; Charlton and Arnell, 2014), understanding whether flow characteristics exert a physical control on efflux rate is crucial to measuring the impact of climate change on CO_2 feedback processes. Given there is indication that pCO_2 may also influence CO_2 efflux, water chemistry parameters (pH and [DIC] for calculation of pCO_2) will be assessed alongside flow hydraulics for secondary control on CO_2 efflux.

3.2.1 Water Turbulence

Water flow can be laminar or turbulent. In laminar flow, mixing occurs between the layers by molecular diffusion (Gordon *et al.*, 2004). Laminar flow in natural streams/rivers, where mixing occurs by molecular diffusion between the layers, is usually only found within the laminar sub layer ($<10^{-4}$ m) close to the channel boundary (Knighton, 1998; Gordon *et al.*, 2004). In turbulent flow, the fluid elements follow irregular flow paths and, although molecular diffusion still occurs, mixing is dominated by turbulent eddies which exist at all scales and continuously form and break down (Knighton, 1998; Gordon *et al.*, 2004). An important consequence of turbulence for CO_2 transfer is that mixing due to eddies is much faster than by molecular diffusion alone (Knighton, 1998). Because of a high degree of spatial and temporal variability, turbulence is difficult to measure or simulate (Knighton, 1998; Banerjee, 2007), and predictive modelling can be speculative. There remains a lack of consensus on the physical aspects of turbulent structures and their contribution to momentum and mass transfer (Nezu *et al.*, 1994; Gordon *et al.*, 2004).

3.2.2 Turbulence as a Control on CO_2 Efflux

Studies of convection in lakes and turbulent mixing in streams have found that eddies, both in the water and adjacent atmosphere, greatly enhance the transfer of gasses across the air-water interface (Moog and Jirka, 1999; Eugster *et al.*, 2003; Jonsson *et al.*, 2008). These mechanisms act on both sides of this boundary, but cannot cross it; gas transfer across the air-water interface occurs by molecular diffusion (Moog and Jirka, 1999), the rate of which is controlled by the gas concentration gradient between the air and water. The rate of diffusion is also controlled by the thickness of the surface concentration boundary layer (CBL) (Broecker and Peng, 1974; Moog and Jirka, 1999; D'Asaro *et al.*, 2014). As gases diffuse from the water to the atmosphere, their concentration decreases immediately below the interface; the mean distance over which the gas concentration varies from the surface to nearly the bulk value is called the CBL (Moog and Jirka, 1999). Thicker CBLs therefore reduce the rate of diffusion. Turbulent eddies and convection cells disrupt the boundary layer and renew the surface zone with gas-rich water from lower in the water column (Moog and Jirka, 1999; Jonsson *et al.*, 2008); these processes, that control the thickness of the CBL and exchange with the adjacent water column, facilitate faster diffusion and so greater gas efflux (Jonsson *et al.*, 2008).

Although similar processes affect gas exchange in oceans, lakes and rivers, the relative influence of these processes is largely determined by the scale of the water body (Long *et al.*, 2015). Research on gas exchange in oceans and lakes has been more extensive than that in rivers. On these larger water bodies wind has a large influence on gas exchange. Earlier studies used empirical relationships between wind speed and gas transfer velocity to explain air-water gas exchange in oceans and lakes (Liss, 1973; Broecker and Siems, 1984; Liss and Merlivat, 1986; Wanninkhof, 1992). However, the influence of wind speed on gas exchange is indirect, and other environmental parameters influence the rates of exchange (Bock *et al.*, 1999). Wind drag on a water surface creates surface waves and in turn turbulence in the upper layer of the water body; the resultant increased water surface area and surface disturbance enhance diffusion through the larger area for diffusion and disruption of the CBL, and thus increase gas fluxes (Bock *et al.*, 1999; Wanninkhof and McGillis, 1999; Eugster *et al.*, 2003; D'Asaro *et al.*, 2014; Long *et al.*, 2015). Fetch may increase gas transfer: larger waves (and thus greater turbulence and/or surface area for diffusion) are created at a given wind speed if the fetch is longer (Jonsson *et al.*, 2008). White water also increases efflux; when waves break, subsurface turbulence is enhanced (Jonsson *et al.*, 2008) and spray and bubbles are produced which increase the surface area for gas exchange and can entrain air into the water (Thackston and Dawson, 2001; Jonsson *et al.*, 2008), all of which further increase gas exchange (Wanninkhof and McGillis, 1999; Thackston and Dawson, 2001; Eugster *et al.*, 2003; Jonsson *et al.*, 2008). Conversely, surface films (e.g. DOM of natural and anthropogenic origin, and petroleum seeps/spills), can impede gas transfer (Wanninkhof, 1992; Bock *et al.*, 1999; Wanninkhof and McGillis, 1999).

In estuaries and large rivers, wind-generated waves can be the dominant physical control on gas exchange, but in smaller channels, such as those measured in this study, where the effect of wind is spatially and temporally restricted, stream characteristics which control the hydraulic properties of the flow are more significant controls over gas exchange (Alin *et al.*, 2011). The interaction of the down-slope flow of water and the channel bed roughness controls the velocity of the water, generates turbulence within the water column, and energy dissipation in the form of surface waves when the flow reaches a critical state (Gordon *et al.*, 2004) disrupting the surface boundary layer. Additionally, turbulence gives rise to flow events called sweeps and ejections which act towards and away from the bed, respectively (Best, 1992; Knighton, 1998; Reidenbach *et al.*, 2010; Bomminayuni and Stoesser, 2011), and likely have important implications for transport of dissolved gasses through the water column.

A range of hydraulic factors, including velocity, depth and channel slope, have been found to have statistically significant relationships that can be used to calculate the capacity for fluvial systems to absorb gas from the atmosphere (Moog and Jirka, 1998; Thackston and Dawson, 2001; Palumbo and Brown, 2013). While these studies provide understanding of gas fluxes, none are specific to CO_2 and no single reaeration equation works adequately under all hydraulic conditions and so there

is a range of forms of the predictive relationships (Thackston and Dawson, 2001; Palumbo and Brown, 2013). There is recognition that existing approaches are restricted by the range of flow depths, velocities and slopes for which gas transfer data are available, and by the quality of the overall database (such as whether slope/wind/water surface state were taken into account) (Moog and Jirka, 1998; Thackston and Dawson, 2001; Palumbo and Brown, 2013).

3.2.3 Flow Hydraulics

Many hydraulic parameters can be used to describe the mean and time-varying properties of flow in a moving water body. Mean velocity ($\bar{u}$), either across a river cross-section or in a single vertical, is an indicator of averaged hydraulic conditions, but flow characteristics can be explored in more detail by considering a range of hydraulic parameters. This study considers Froude number (*Fr*), Reynolds number (*Re*), bed shear stress (τ), shear velocity (u_*) and shear Reynolds number (R_*) each of which can be calculated from a flow velocity profile (Chapter 2) (e.g. Bergeron and Abrahams, 1992; Smart, 1999).

Fr (Equation 7) represents the ratio of inertial to gravitational forces in the flow, and thus the resistance to flow due to gravitational effects (Gordon *et al.*, 2004). *Fr* indicates the amount of water surface deformation, such as waves and ripples, that are produced (Thackston and Dawson, 2001; Gordon *et al.*, 2004; Allen, 2009) and so can act as a proxy for the interaction and degree of gas exchange between a water surface and the atmosphere (Long *et al.*, 2015). Generally as *Fr* rises, the more disturbed a water surface appears, and the more gas exchange with the atmosphere occurs (Thackston and Dawson, 2001). Flows with *Fr* of <1 are classified as subcritical and surface waves do not break, or partially break as *Fr* approaches 1. *Fr* = 1 is defined as critical flow, and at *Fr* >1 flows are classified as supercritical and have full breaking waves (Gordon *et al.*, 2004; Allen, 2009).

Equation 7

$$Fr = \frac{\bar{u}}{\sqrt{gH}}$$

where $\bar{u}$ is mean velocity (m s^{-1}), g is acceleration due to gravity (m s^{-2}) and H is water depth (m) (Leopold and Maddock Jr, 1953; Smart, 1999).

Re (Equation 8) represents the ratio of inertial forces to viscous forces in the flow and is an index for the degree of turbulence and hence mixing in the water column (Gordon *et al.*, 2004). *Re* is thus an indicator of the potential transfer of CO_2-enriched water from lower in the water column and hyporheic zone (e.g. Peter *et al.*, 2014) to the water surface. When *Re* is >2000, flows are fully turbulent and *Re* is used here in assessing the magnitude of the turbulence/mixing and whether this impacts on CO_2 evasion.

Equation 8

$$Re = \frac{\bar{u}H}{\nu}$$

where ν is kinematic viscosity (m^{-2} s^{-1}) (Gordon *et al.*, 2004). ν is temperature dependent and has thus been corrected for temperature (Heggen, 1983).

Bed shear stress (τ) is the stress exerted by the water parallel to the stream bed (Wilkinson, 1984). Shear velocity (u*) (Equation 9) is derived from the bed shear stress, has the units of velocity (m s^{-1}) for mathematical convenience, and describes shear-related motion in flows. Shear Reynolds number (R*) (Equation 10) provides an assessment of turbulence intensity with reference to the shear stress (Moog and Jirka, 1999); it is a measure of the fluid forces and energy that create turbulence.

Equation 9

$$u* = \sqrt{\frac{\tau}{\rho}}$$

where ρ is the water density (kg m^{-3}) (Smart, 1999; Waterman *et al.*, 2016).

Equation 10

$$R_* = \frac{u*H}{\nu}$$

(Moog and Jirka, 1999). For further details of calculation of hydraulic parameters see section 3.3.4.

3.3 Methods

3.3.1 Field Site Description

Three contrasting UK catchments were used to assess hydraulic controls on CO_2 efflux: Drumtee Water (DW), the River Kelvin (RK) and the River Etive (RE). Chapter 2 contains an overview of each study area and detail on catchment and channel characteristics; information on specific sampling points and sampling regimes is provided here.

3.3.1.1 Choice of Field Sites

Drumtee Water is a small (5.7 km^2), moorland catchment which contrasts with the large (335 km^2), 23 % urbanised catchment of the River Kelvin, allowing for comparisons of the controls on CO_2 efflux to be made across catchment scale and levels of anthropogenic influence. Both sites are local to the University of Glasgow enabling regular sampling over a two-year period. Furthermore, long-term, high-resolution water chemistry and hydrological data are available for both sites, which supplements collected spot-data and enables reconstruction of hydraulic/water chemistry conditions and efflux over time. The River Etive provides further contrasts with both DW and RK as, at the times of sampling, it is a snow melt-influenced, remote rural system. RE provides an 'intermediate scenario' between the temperate, soil-dominated systems of central Scotland (DW and RK) and the Arctic, cryospheric, icemelt-dominated systems of Greenland, which are the focus of Chapter 5. RE is included for comparison and sampling frequency is low, and the data is exploratory serving as a pilot study for investigations into intermediate scenario catchments.

3.3.1.2 Drumtee Water

Four measurement points were used with contrasting water surface characteristics. Two instruments were installed at DW in 2007 and 2012, respectively, each taking readings at 30 minute intervals. The first is an In-situ Inc. MP TROLL 9000 water chemistry sonde (pH range 0 – 12 pH, pH resolution 0.01 pH, conductivity range 0.3 µS mm^{-1} to 5000 µS mm^{-1}) with pressure transducer (range 0-21 m, resolution 1nm). The second is a S::CAN Spectrolyser (Messtechnik GmbH), a portable ultraviolet-visible spectrometer, measuring absorbance of the water (range 200 – 735 nm, in 2.5nm increments) for reconstruction of dissolved organic carbon concentrations (DOC) (e.g. Langergraber *et al.*, 2003; Bass *et al.*, 2011). The instrument has exceptional stability and DOC is generally calculated using absorption at 254 nm, but other wavelengths can be used (Bass *et al.*, 2011); for DW 255nm was selected. The Spectrolyser was cleaned monthly and has an internal Global Calibration (Bass *et al.*, 2011) which was used along with calibrations using local samples from streams in Scotland. Due to the narrow (4-5 m), shallow channel, all measurement points were located close channel centre.

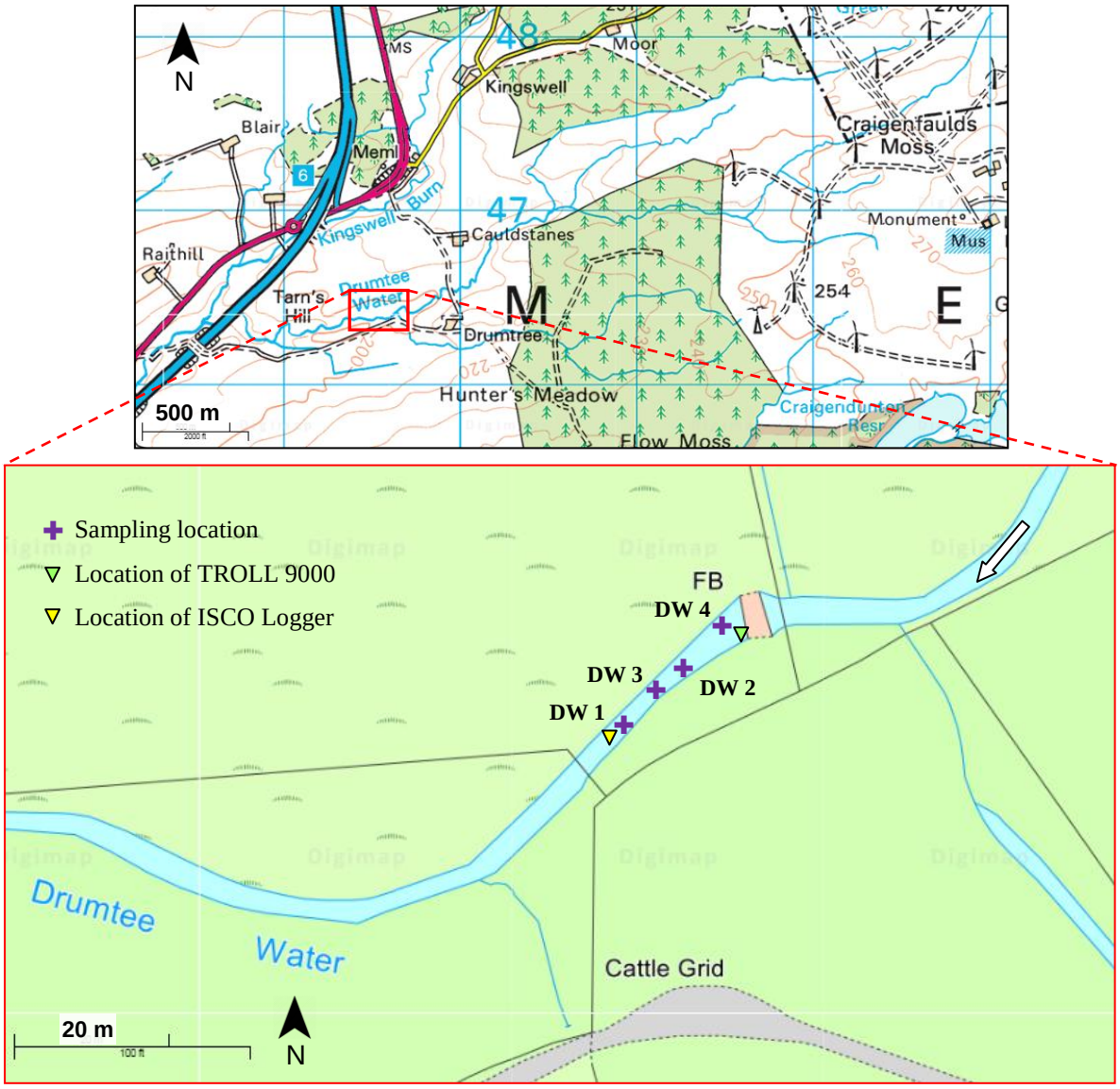

Figure 18: Map of DW field site and measurement point locations

Arrow shows flow direction. Images taken from Digimap: ©Crown copyright and database rights 2016 Ordinance Survey (Digimap Licence). For Educational use only.

DW 1: Can be accessed in any flow conditions, water surface was generally smooth.

DW 2: Can be accessed in any flow conditions, water surface was generally moderately disturbed.

DW 3: Can be accessed in any flow conditions, water surface was generally disturbed, with breaking waves under high flow conditions.

DW 4: Can be accessed in any flow conditions, water surface was generally smooth.

3.3.1.3 River Kelvin

Three measurement points were chosen with contrasting water surfaces. Due to the width (15-20 m) and depth of the river, and the equipment configuration (3.5 m maximum range from the channel bank), measurement points are located off-centre close to the right bank. The site has a pebble bar attached to the right-hand bank, which becomes submerged when stage height (at SEPA Killermont gauging station, ~9 km upstream) reaches 0.8 m. At Killermont gauging station, the average stage height is 0.6 m and range in stage height is 3.7 m (0.1 – 3.8 m) (SEPA, 2016). When stage height is over 1.3 m none of the measurement points can be accessed due to safety requirements.

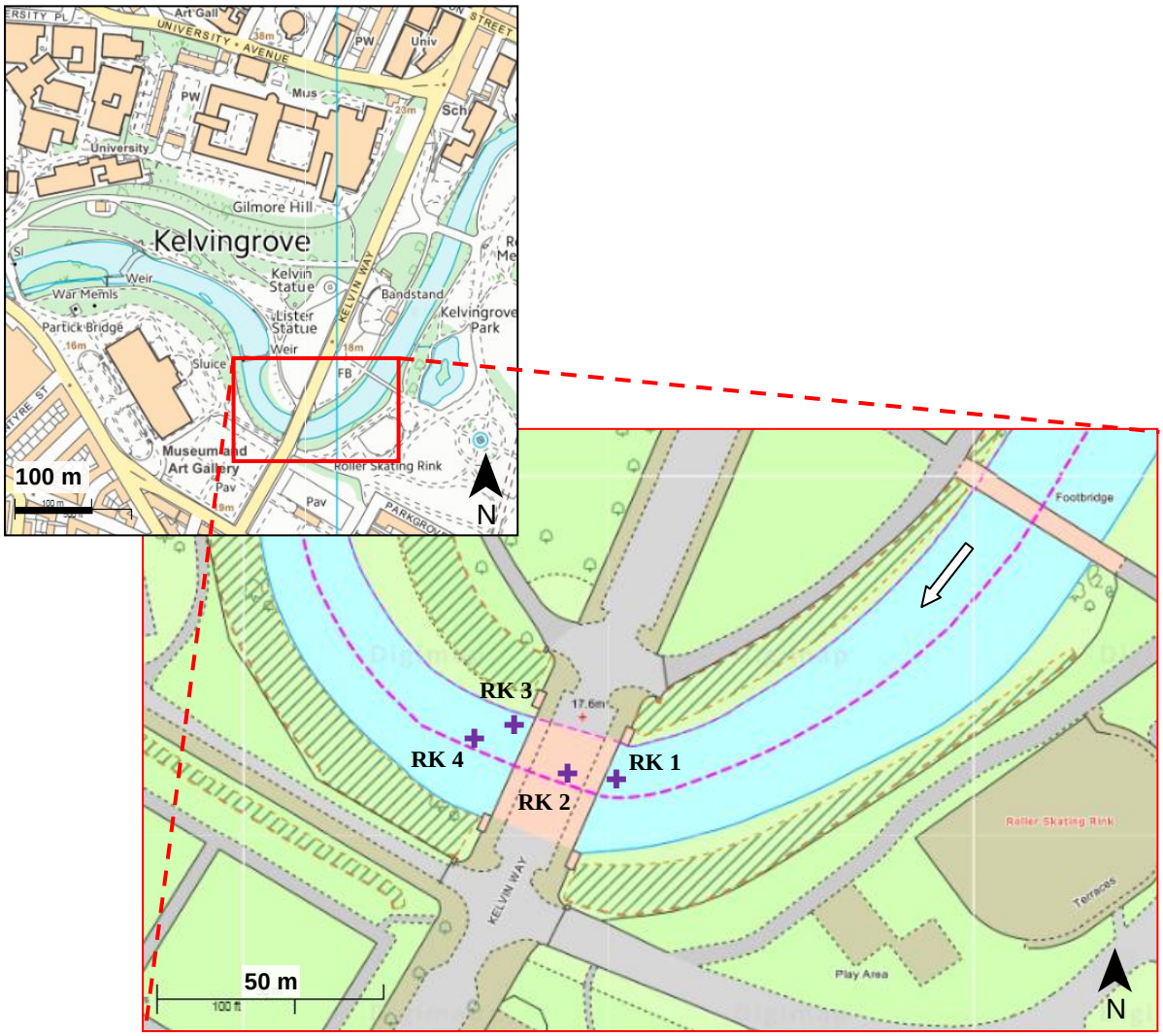

Figure 19: Map of RK field site and measurement point locations

Channel shown at bankfull, arrow shows flow direction, ✚ = measurement point. Images taken from Digimap: ©Crown copyright and database rights 2016 Ordinance Survey (Digimap Licence). For Educational use only.

RK 1: Only accessible in low-moderate flow conditions (stage height < 0.8 m). Water surface was generally smooth.

RK 2: 8 m downstream of RK 1. Only accessible in low-moderate flow conditions. Water surface was generally mildly disturbed.

RK 3: Located on the gravel bank, so can only be measured in high flow conditions when the stage height is 0.9 m – 1.3 m. Water surface was generally disturbed.

RK 4: 30 m downstream of RK 1. Only accessible in low-moderate flow conditions. Water surface was generally disturbed.

3.3.1.4 River Etive

Five measurement points were chosen with contrasting water surfaces. Due to the width (8 – 200 m) and depth of the channel and equipment range, measurement points were located closer to the right bank than the centre of the channel. There is no gauging information available for this site. At the times of measurement the catchment was partially snow-covered and thus snow-melt contributed a proportion of the discharge.

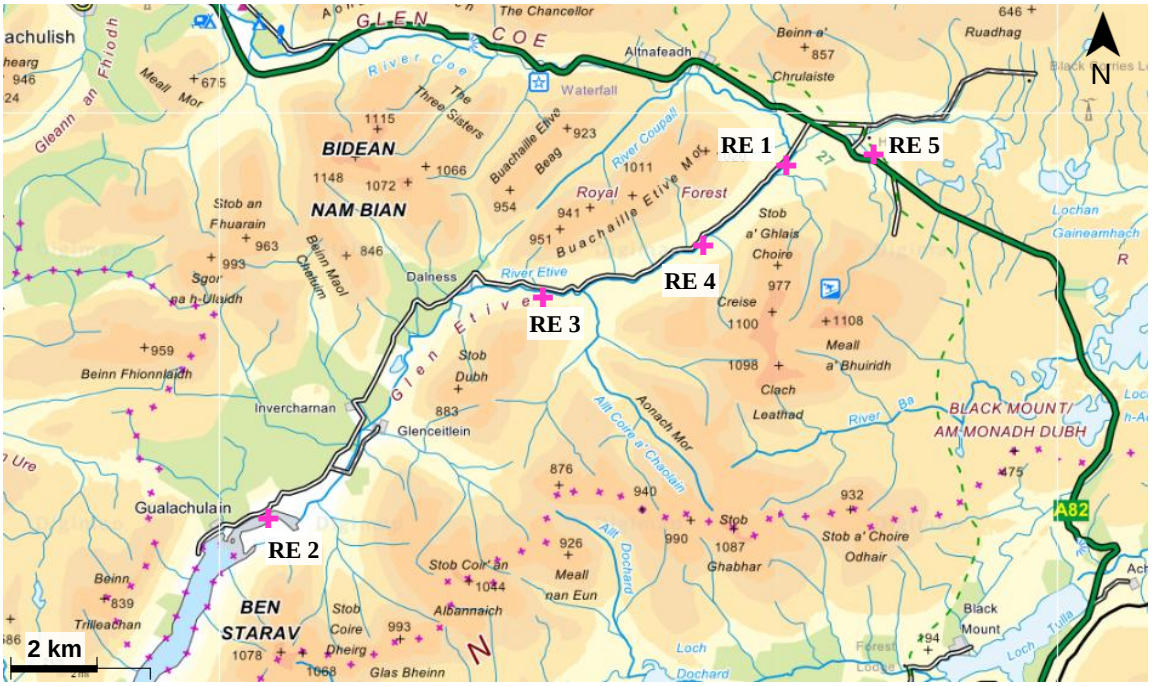

Figure 20: Map of RE field site and measurement point locations

Flow direction = top right to bottom left, ✚ = measurement point. Images taken from Digimap: ©Crown copyright and database rights 2016 Ordinance Survey (Digimap Licence). For Educational use only.

RE 1: One-off test measurement point. Water surface was moderately disturbed.

RE 2: Accessible in all flow conditions. Water surface was generally mildly disturbed.

RE 3: Accessible in all flow conditions. Water surface was generally disturbed.

RE 4: Accessible in all flow conditions. Water surface was generally disturbed.

RE 5: Accessible in all flow conditions. Water surface was generally moderately disturbed.

3.3.2 Sampling Regime

Sampling was carried out over two years at the two main field sites (DW for 23 months; RK for 24 months), and during two consecutive spring periods at the River Etive pilot site (Table 2)

Table 2: Efflux-hydraulics sampling regime at each field site

Site	Sampling Period	Sampling Frequency						Exceptions (no sampling)
		Individual days per month			Times per given day			
		Usual	Min	Max	Usual	Min	Max	
DW	Jul-12 to May-14	2	1	4	2	1	3*	Aug-12 & Dec-12
RK	Jun-12 to May-14	2 - 3	1	7	2	1	4	Aug-12
RE	Apr to May-14 Feb to Jun-15	1	-	-	3 - 4	1	4	

*with the addition of a 24 hour sampling campaign (27-28th Aug-13) where 12 consecutive sets and part-sets of measurements were made

3.3.3 Field Measurements

On each sampling occasion, CO_2 efflux, a flow velocity profile, pH and environmental parameters (air and water temperature, wind speed, humidity, light intensity, weather observations) were measured, and water samples collected for measurement of further water chemistry parameters (alkalinity, [DIC]). A qualitative visual assessment of the water surface state was made at the time of each CO_2 flux measurement. Where possible a full set of these measurements were made but on occasion, flow conditions, time constrains and/or equipment malfunction meant a sub-set of measurements were taken. Full details of these methods can be found in Chapter 2.

3.3.4 Hydraulic Parameters

Froude number, Reynolds number, mean velocity, shear stress, shear velocity and shear Reynolds number were calculated from flow velocity profiles (Figure 21) (e.g. Wilkinson, 1984; Bergeron and Abrahams, 1992). These are all descriptors of the flow properties, and so may influence evasion of CO_2, and are auto-correlated by definition.

3.3.4.1 Velocity Profile

Flow velocity was measured at 20% and 80% of the depth to allow depth-averaged mean calculations, and a minimum of three other depths to allow identification of any outliers. Velocity measurements were taken at depths throughout the water column, but concentrated in the semi-logarithmic lower part of the flow profile (Nezu *et al.*, 1994), where depth and channel dimensions allowed. A set of measurements typically took <15 minutes. Velocity profiles were constructed by

plotting velocity against height above the channel bed, on a semi-logarithmic plot (Figure 21). Outliers from the semi-logarithmic relationships may reflect local flow conditions (such as cross-stream flow initiated by obstacles) or measurement errors. Outliers were eliminated from the data as with small data sets they would influence the resulting calculations excessively. The measurement of distance above the bed is difficult as the bed is uneven and so the base of the measurement pole may not be exactly the same as the zero level of the velocity profile. Following convention, a zero-plane displacement is added to all measurement heights (Biron *et al.*, 1998). The value of this displacement is chosen to maximise the R^2 of the velocity-depth line, and the hydraulic parameters calculated from this amended profile.

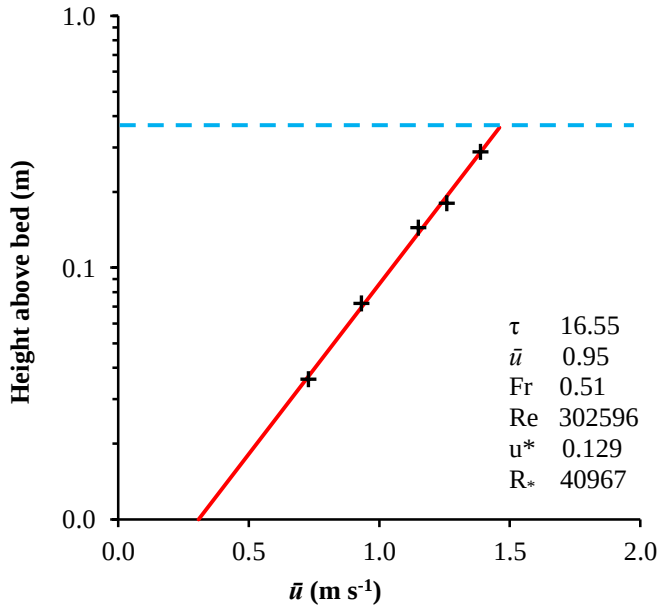

Figure 21: Example flow velocity profile

Flow measured at 10, 20, 40, 50 and 80 % of the water depth (0.36 m) at a RK measurement point on 21.08.2013. Blue dashed line represents the water surface.

3.3.4.2 Derived Parameters

Measurements of $\bar{u}$ (m s^{-1}) in turbulent flow require to be time-averaged (Gordon *et al.*, 2004), and here 60 second averaging was used. Each velocity measurement in the flow velocity profile was weighted according to its spacing in the vertical, and a depth-averaged estimate of the mean calculated (See example Figure 21). *Fr* is a depth-averaged, dimensionless quantity that was calculated from the flow velocity profile using Equation 7. *Re* number is a depth-averaged, dimensionless quantity that was calculated according to Equation 8. τ (N m^{-2}) was calculated from the gradient of the velocity profile and universal von Karman's constant (κ 0.4) (Wilkinson, 1984; Cudden and Hoey, 2003). u^* has the dimensions of velocity (m s^{-1}) and was calculated via Equation 9. R^* is dimensionless and calculated via Equation 10.

3.4 Results

The tables and figures below summarise the important carbon pools (Table 3; Figure 22) and hydraulic conditions (Table 4; Figure 23) at each site. The following sections (3.4.1 to 3.4.4) provide more detailed explanation of the magnitudes of, and relationships between, the parameters. Hydrographs for DW and RK, showing the timing of all full- or part-sampling occasions, are available in Appendix E.

Table 3: Comparison of important carbon pools and environmental parameters that influence or represent the size of the carbon pool (e.g. pH, alkalinity) at each site*

	CATCHMENT		
CARBON POOL	**Drumtee Water**	**River Kelvin**	**River Etive**
CO_2 efflux (µmol CO_2 m^{-2} s^{-1})	8.11 [2.66] 0.07:107 *98*	8.41 [4.76] -3.53:50.7 *95*	0.28 [0.23] -0.12:0.81 *20*
***n* efflux:*n* influx:*n* equilibrium**	98:0:0	92:3:0	18:2:0
[DIC] (mmol L^{-1})	0.37 [0.25] 0.08:1.57 *58*	1.28 [1.16] 0.44:2.03 *39*	0.06 [0.06] 0.04:0.09 *4*
pH	6.8 [6.8] 5.3:7.8 *97*	7.7 [7.8] 6.3:7.9 *95*	6.3 [6.4] 5.4:7.1 *19*
Alkalinity (mg L^{-1})	30.0 [21.4] 5.11:91.0 *78*	92.3 [87.4] 32.4:146 *70*	11.4 [11.2] 9.05:16.8 *21*
***p*CO_2 (ppm)**	1299 [1226] 612:2677 *57*	1294 [1097] 645:4660 *39*	817 [817] 388:1245 *2*
E*p*CO_2 (ppm)	899 [826] 212:2277 *57*	894 [697] 245:4260 *39*	435 [453] 5:864 *2*

*Mean [median] minimum:maximum *n*. *n* = number. CO_2 flux considered at equilibrium when efflux <0.01 or influx >-0.01

Table 4: Comparison of hydraulic conditions at each site*

	CATCHMENT		
HYDRAULIC PARAMETER	**Drumtee Water**	**River Kelvin**	**River Etive**
Mean velocity (m s^{-1})	0.32 [0.20] 0.03:1.08 *98*	0.59 [0.61] 0.10:1.39 *98*	0.46 [0.41] 0.04,0.81 *19*
Froude number	0.16 [0.14] 0.02:0.61 *95*	0.29 [0.28] 0.04:0.57 *98*	0.26 [0.24] 0.13:0.44 *18*
Reynolds number	113000 [54000] 6000:599000 *95*	211000 [180000] 23000:750000 *98*	104000 [100000] 23000:191000 *18*
Shear Reynolds number	21000 [10000] 350:174000 *95*	26000 [18000] 1800:124000 *98*	19000 [16000] 6800:69000 *20*
Visual classification ratio (smooth : medium : rough (*n*))	2.3 : 1 : 1 (*92*)	2.4 : 1.8 : 1 (*89*)	1 : 6 : 3 (*20*)

*Mean, [median] (minimum:maximum; *n*).

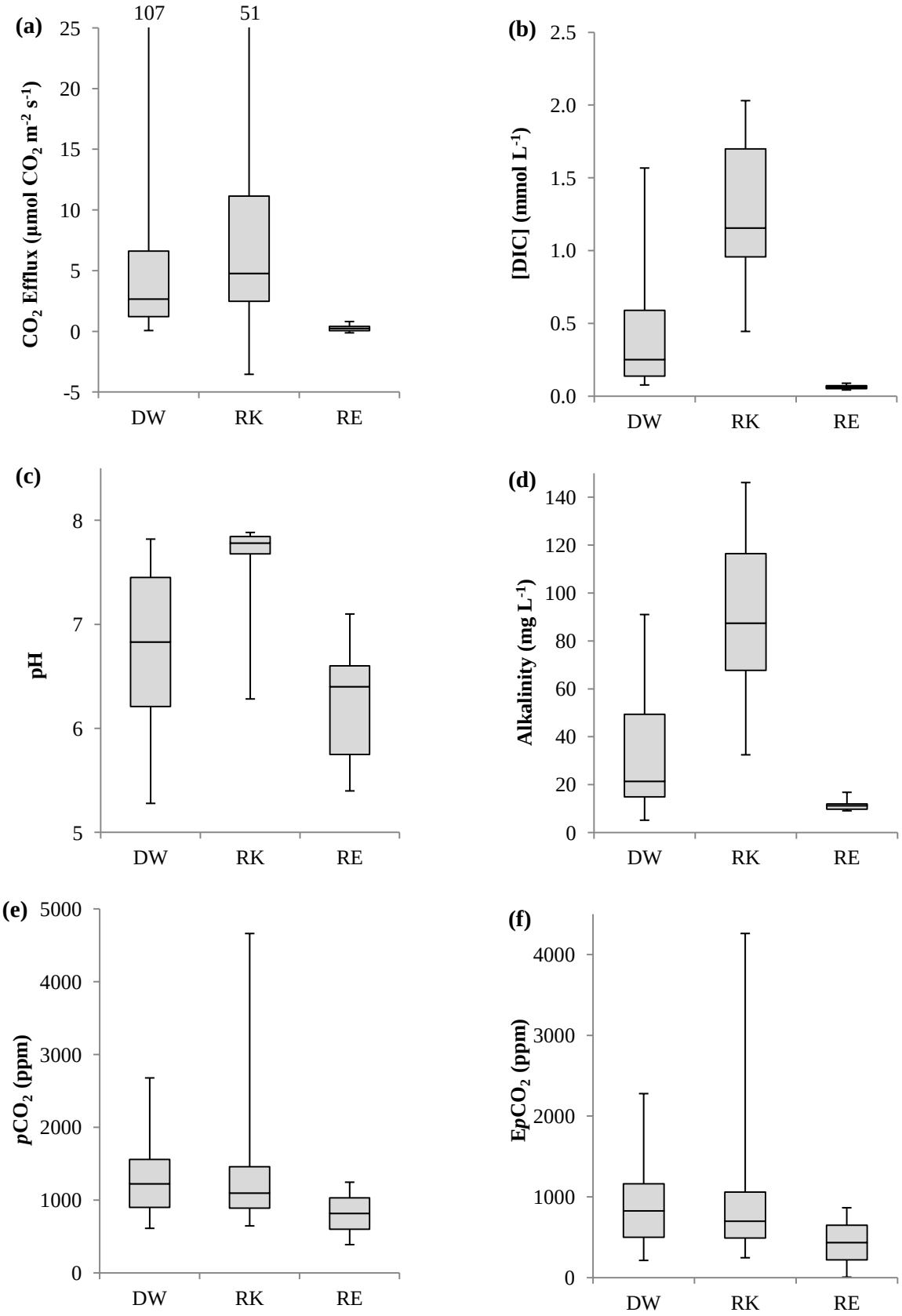

Figure 22: Box plots of important carbon pools and environmental parameters that influence or represent the size of the carbon pool

Boxes represent the interquartile range, horizontal bars within the boxes are the median values, and vertical bars represent maximum and minimum values. (a) DW and RK max values are 107 and 51 respectively.

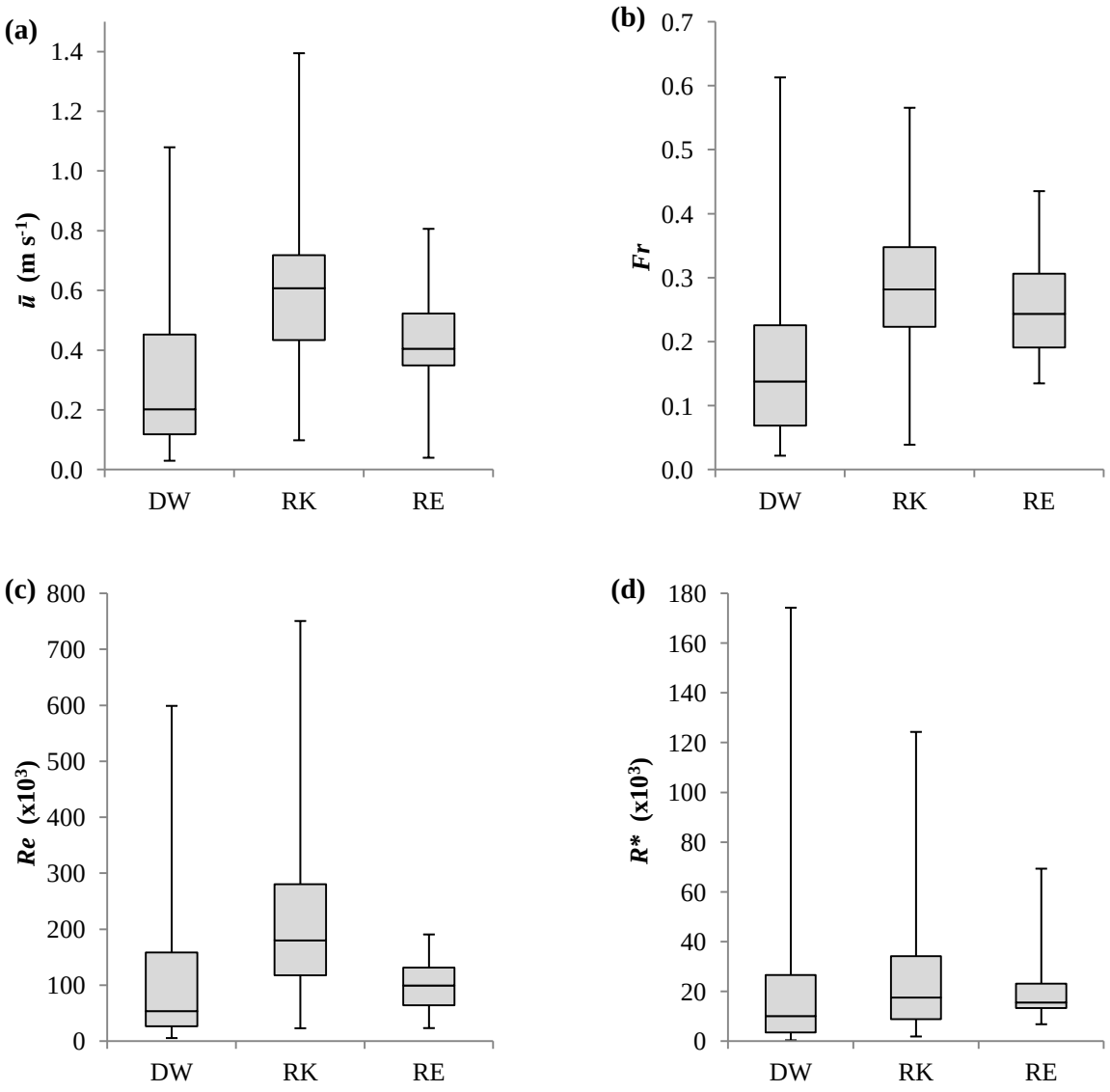

Figure 23: Box plots of hydraulic conditions

Boxes represent the interquartile range, horizontal bars within the boxes are the median values, and vertical bars represent maximum and minimum values.

3.4.1 Magnitude of CO_2 Efflux

Overall, CO_2 efflux rates ranged between -3.53 and 107 µmol CO_2 m^{-2} s^{-1} at the three sites, overall mean CO_2 efflux was 7.51 and median 3.02 µmol CO_2 m^{-2} s^{-1} (n = 213, s.d. = 12.18). The main field sites, DW and RK, had similar CO_2 efflux ranges but the range extended further at the upper end at DW, and no influx was measured at DW, which was measured on three occasions (on the same day) at RK (Figure 22a, Table 3). DW and RK had very similar mean CO_2 effluxes (8.11 and 8.41 µmol CO_2 m^{-2} s^{-1} respectively) but RK has a higher median CO_2 efflux than DW (4.68 µmol CO_2 m^{-2} s^{-1} and 2.66 µmol CO_2 m^{-2} s^{-1} respectively) (Figure 22a, Table 3). The pilot site, RE, had a much smaller range, and magnitude of CO_2 efflux than DW and RK (range: -0.12 to 0.81, mean: 0.28, median: 0.23 µmol CO_2 m^{-2} s^{-1}, n = 20) and influxed on two occasions (separate days) (Figure 22a, Table 3). Ranges and means of CO_2 efflux at all sites lie within the range of previously reported values (Appendix B – Long et al., 2015).

3.4.2 Flow Intensity

Average hydraulic conditions at all three sites are comparable (Table 4). Mean $\bar{u}$ (m s^{-1}), *Fr*, *Re* and R* were respectively: DW 0.32, 0.16, 113000, 21000; RK 0.59, 0.29, 211000, 26000; RE 0.46, 0.26, 104000, 19000. The highest mean values of all hydraulic parameters were measured at RK showing that flow intensity (a generic term which describes one or more of the measures of flow strength including mean flow velocity, bed shear stress, turbulent stress and flow state; Long *et al*., 2015) was greatest here at the points and occasions measured. At DW and RK the ranges in all hydraulic parameters were very similar, but at RE a noticeably narrower range of flow intensities was measured (Figure 23). This was due to the river being overall faster and more turbulent; smooth, calm, slow flowing sites were rarely available to measure (only 2 of 20 measurement occasions), and the water surface was generally very uneven. At flow velocities greater than those measured, a seal could not be maintained between the floating chamber and the water surface and water entered the tubing which could damage the equipment, so measurement was not possible.

3.4.2.1 CO_2 Efflux Data

In 208 of 213 measurements (98%) CO_2 evaded from the water to the atmosphere; other possibilities are equilibrium between the water and the atmosphere or CO_2 invasion/influx into the water from the atmosphere. Both the CO_2 efflux and hydraulic parameters are positively skewed (Figure 22a, Figure 23), so relationships between these variables are best considered as power functions ($CO_2 = a.X^b$, where a,b are obtained from ordinary least squares regression of log-transformed data, and *X* refers to any of the set of measured hydraulic variables).

Table 5: Statistics of correlations between CO_2 efflux and hydraulic parameters at each site*

Site	Parameter correlated with efflux					
	$\bar{u}$	*Fr*	*Re*	*R**	τ	*u**
DW	0.82	0.77	0.74	0.79	0.74	0.74
	0.000	0.000	0.000	0.000	0.000	0.000
	1.91	2.00	2.09	1.92	2.08	2.08
RK	0.66	0.56	0.47	0.49	0.53	0.54
	0.000	0.000	0.000	0.000	0.000	0.000
	1.89	2.06	2.22	2.18	2.10	2.10
RE	0.23	0.35	0.04	0.01	0.05	0.05
	0.042	0.015	0.482	0.759	0.423	0.423
	2.80	2.59	3.20	0.325	3.18	0.318

* Relationships are considered as power-functions due to positive skew of hydraulic parameters (Figure 23). R^2 obtained from regression models fitted to the data (see equations of Figure 24 and Figure 25). Top row = R^2, middle row = p-value, bottom row = s.e.

Data from DW and RK show significant positive correlation between CO_2 efflux and all hydraulic parameters (Table 5, Figure 24). Discussion will focus on $\bar{u}$, *Fr*, *Re*, and *R** as these are the most relevant to gas exchange between the water and the atmosphere. $\bar{u}$ is a good bulk indicator of hydraulics and is commonly measured, however is not a good indicator of the specifics of the flow structure, and so *Fr*, *Re* and *R** are also considered as they are more physically meaningful. *Fr* is a proxy for the interaction between the water surface and the atmosphere, *Re* is an index for turbulence within the water column and *R** is a measure of the fluid forces and energy that create turbulence. τ and *u** were included for integrity, but are not considered in further discussion as they both represent force exerted on the bed parallel to the bed, and so are less directly involved in gas transfer within the water column or behaviour of the water-atmosphere interface (see Appendix D for plotted data).

Data from DW and RK overlap indicating similar controls on efflux at the sites, although there are some differences in the gradients and significance levels of the relationships (Figure 24, Table 5). Efflux rates are slightly higher (indicated by the vertical position of the trend lines), curves slightly steeper (indicated by the exponent values), and relationships slightly stronger (indicated by R^2 and s.e. values) at DW than at RK for all four flow parameters (with the only exception being the s.e. for efflux-$\bar{u}$ at RK). All relationships were highly significant at $p = < 0.001$. Standard errors of the residuals (s.e.) values indicate that the relationship between $\bar{u}$ and efflux is strongest at both DW and RK, and *Re* and efflux relationships the weakest, but all are strong with R^2 values 0.47 – 0.82. The overall relationships of all parameters with efflux at DW and RK show fanning at the upper end, although the density of data points is much reduced. Data from DW and RK have also been found to overlap with data from 3 out of 4 sites in the Peruvian Amazon, which share the same relationship between CO_2 efflux and flow intensity as the UK sites (Appendix B: Fig. 3 of; Long et al, 2015).

The similarity of relationships involving $\bar{u}$, *Fr*, *Re* and *R** with efflux occurs by definition (Table 6); while $\bar{u}$ has the highest correlation with CO_2 efflux, turbulence (*Re* and *R**) and water surface disturbance (*Fr*) are responsible for gas transfer within the water column and at the water-atmosphere boundary, respectively. All are considered important to CO_2 efflux and so for generality, the term flow intensity is used to encompass the combined effects of velocity, turbulence and water surface conditions on gas transfer and exchange (Long *et al.*, 2015).

Table 6: Matrix of the R^2 of correlations between the hydraulic parameters*

	$\bar{u}$	*Fr*	*Re*	τ	*u**	*R**
$\bar{u}$	-	0.93	0.89	0.58	0.58	0.67
Fr	0.93	-	0.69	0.58	0.58	0.55
Re	0.89	0.69	-	0.46	0.46	0.71
τ	0.58	0.58	0.46	-	1.00	0.89
*u**	0.58	0.58	0.46	1.00	-	0.89
*R**	0.67	0.55	0.71	0.89	0.89	-

*Relationships are considered as power-functions due to positive skew of hydraulic parameters (Figure 23)

Data from the pilot site, RE, does not overlap with that from DW and RK as efflux magnitudes remain very low regardless of the flow intensity (Figure 24). It has therefore not been added to the pooled DW and RK dataset (of Figure 24 and Figure 25). However, when the data are displayed with a log-CO_2 efflux scale (Figure 25) the shape of the relationships at RE are very similar to those of DW and RK, but are set lower on the efflux scale. Efflux does increase with flow intensity, but at a lower gradient, and efflux is much less at a given flow than at DW and RK. Additionally, R^2 is noticeable lower for RE, which reflects the greater scatter in the data, but this is likely to be a result of there being significantly fewer data points for this site.

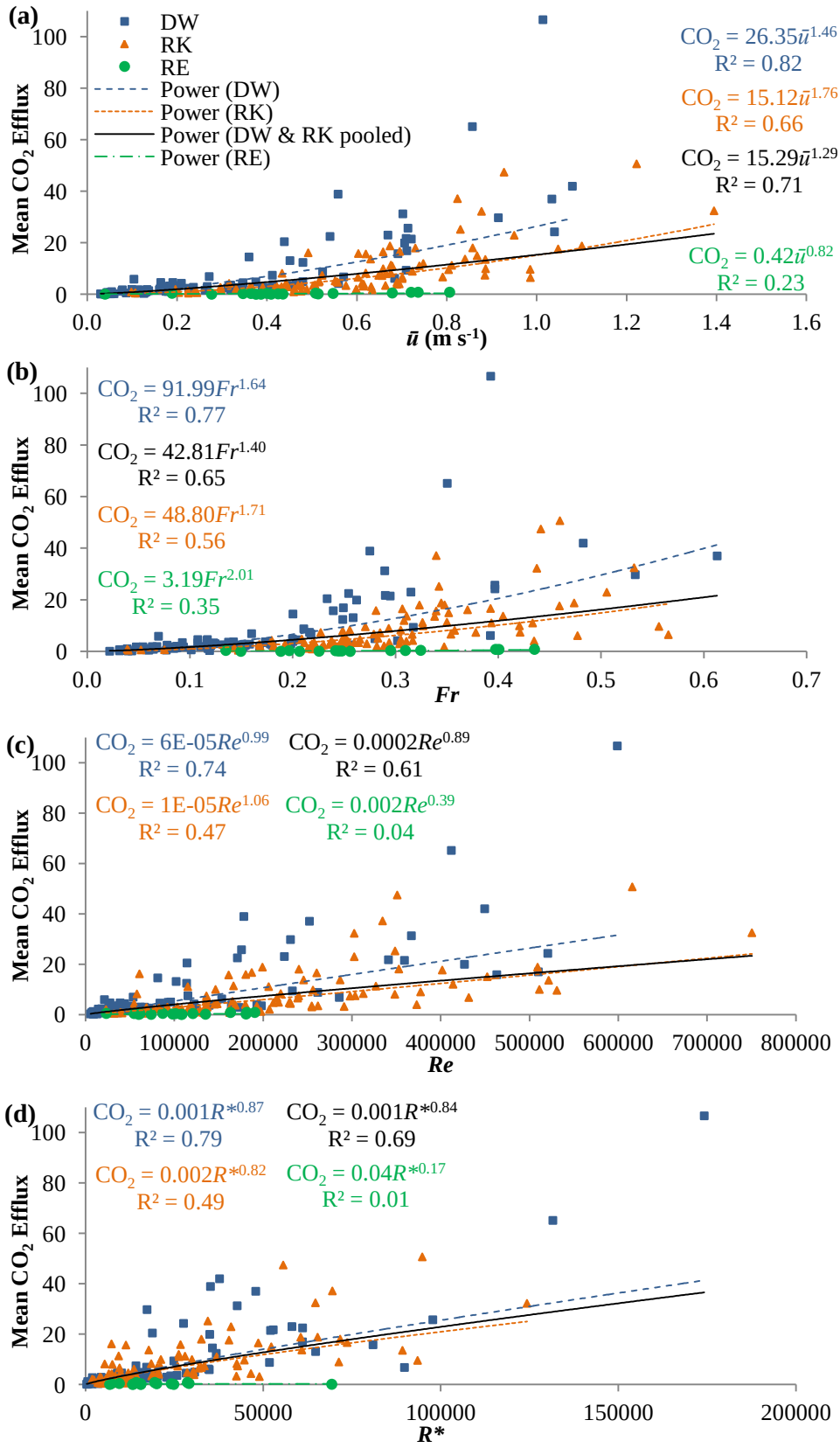

Figure 24: Relationship between CO_2 efflux and hydraulic parameters

CO_2 efflux (µmol CO_2 m^{-2} s^{-1}) against (a) mean velocity ($\bar{u}$); p = <0.001, s.e. = 2.08, (b) Froude number (*Fr*); p = <0.001, s.e. = 2.32, (c) Reynolds number (*Re*); p = <0.001, s.e. = 2.25 and (d) Shear Reynolds number (*R**); p = <0.001, s.e. = 2.05. p- and s.e. values are for DW and RK pooled data, p- and s.e. values for individual sites are reported in Table 5. Legend is the same for all plots. Strong positive relationships are seen with CO_2 efflux at DW and RK. Influx values have not been plotted here, as gas transfer processes act in the opposite direction and trendlines used here cannot incorporate negative values. Influx was measured on three occasions at RK and two occasions at RE. Influx values are considered separately (3.4.2.2).

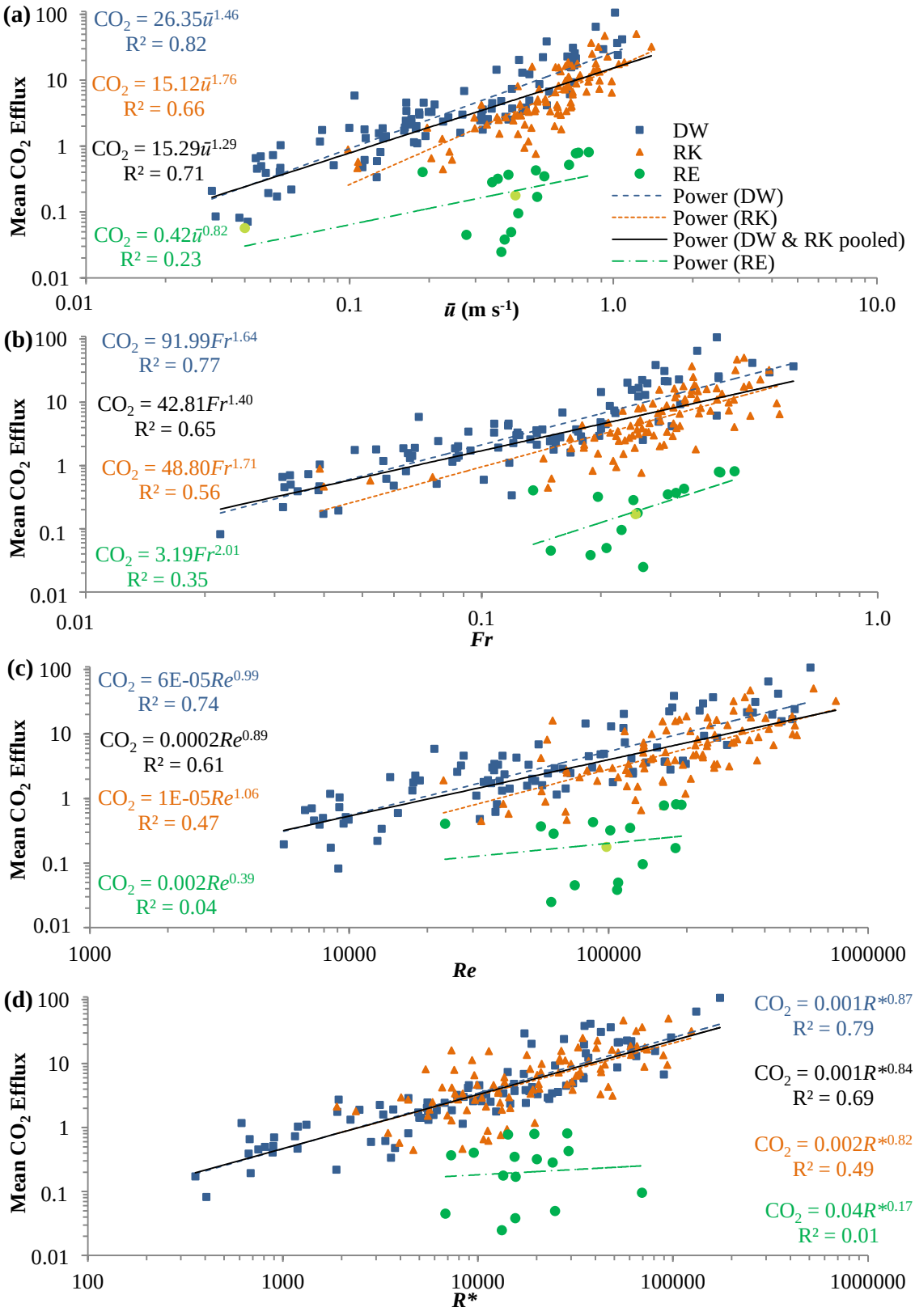

Figure 25: Log-log plot of relationship between CO_2 efflux and hydraulic parameters

CO_2 efflux (in µmol CO_2 m^{-2} s^{-1}) is plotted on a logarithmic scale against (a) mean velocity ($\bar{u}$), (b) Froude number (*Fr*), (c) Reynolds number (*Re*) and (d) Shear Reynolds number (*R**), all on a logarithmic scale. p- and s.e. values are for DW and RK pooled data are as Figure 24, p- and s.e. values for individual sites are reported in Table 5. Legend is the same for all plots. Strong positive relationships are seen with CO_2 efflux at DW and RK. Influx values have not been plotted here, as gas transfer processes act in the opposite direction and trendlines used here cannot incorporate negative values. Influx was measured on three occasions at RK and two occasions at RE. Influx values are considered separately (3.4.2.2). The RE data points in brighter green are the points that feature on Figure 27a and b.

3.4.2.2 CO_2 Influx Data

In 5 of 213 measurements (2%) CO_2 influx, a process where CO_2 is absorbed into the water from the atmosphere due to CO_2 under-saturation of the water, occurred. Data from the influx occasions has been considered separately as the direction of gas transfer is opposite and trendlines used for CO_2 efflux cannot incorporate negative values. Although sample size is very small (N = 5), influx values show very strong correlations with three out of four measures of flow intensity, with an increase in flow intensity causing an increase in CO_2 influx, and R^2 of linear relationships between influx and $\bar{u}$, *Fr* and *Re* all being >0.8 (Figure 26). From this small dataset, flow intensity appears to have a comparable influence on CO_2 influx as it does on efflux, but because of the direction of gas movement, acts in the opposite direction.

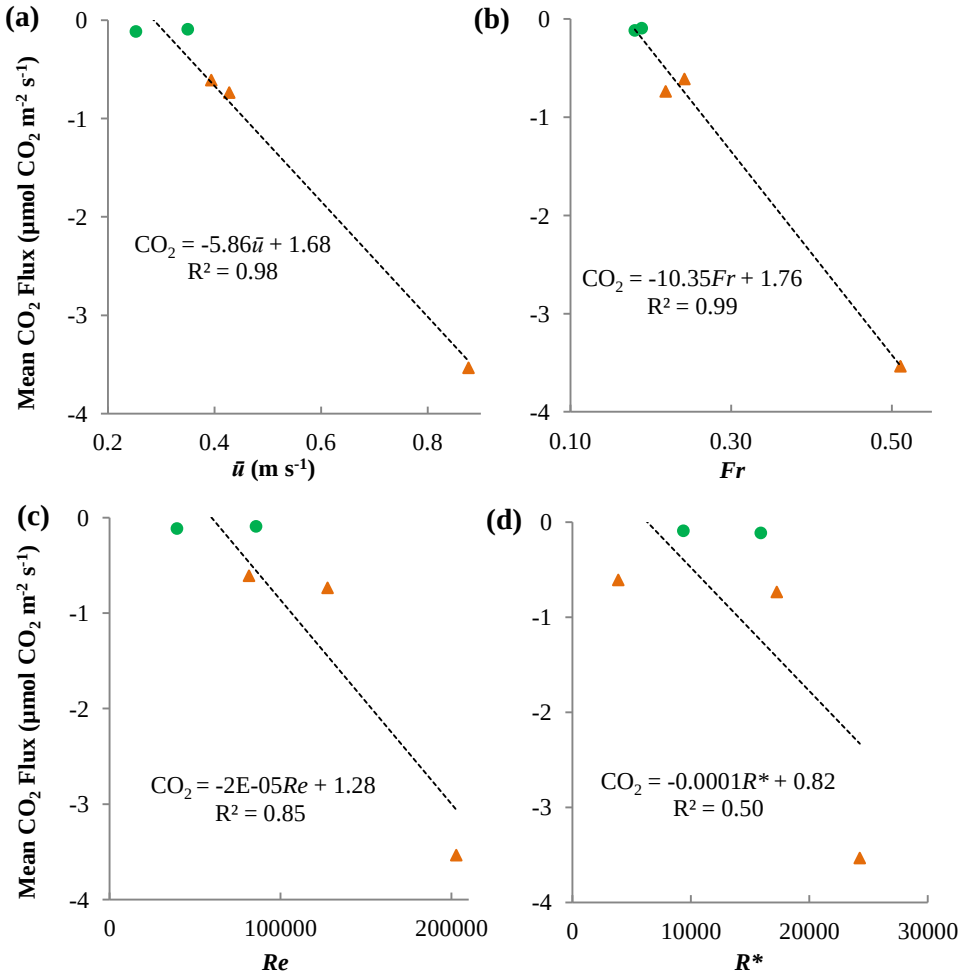

Figure 26: Relationship between CO_2 influx and hydraulic parameters

CO_2 influx data from RK (orange triangles) and RE (green circles) is plotted against (a) mean velocity ($\bar{u}$), (b) Froude number (*Fr*) and (c) Reynolds number (*Re*). Strong correlations are seen with influx increasing with all parameters.

3.4.3 *p*CO_2

Dissolved inorganic carbon concentration [DIC] varied between sites (Figure 22b, Table 3). RK had the highest mean [DIC] (1.28 mmol L^{-1}), this being 3 times that of DW (0.37 mmol L^{-1}). The minimum [DIC] at RK (0.44 mmol L^{-1}) was an order of magnitude higher than the minimum at DW (0.08 mmol L^{-1}) and higher than the mean and median at DW. The maximum [DIC] at RK (2.03 mmol L^{-1}) was ~30% larger than that of DW (1.57 mmol L^{-1}). At the pilot site, RE, only four measurements of [DIC] were made, but results show that [DIC] is far lower at this site, with the mean and median [DIC] one and two orders of magnitude higher at DW and RK, respectively, and the maximum [DIC] at RE (0.09 mmol L^{-1}) is only slightly higher than the minimum at DW (0.08 mmol L^{-1}) and an order of magnitude lower than that at RK (0.44 mmol L^{-1}).

pH varied between sites (Figure 22c, Table 3). Mean and median pH at DW (6.8, 6.8) was ~1 pH unit lower than at RK (7.7, 7.8), and so an order of magnitude lower as the pH scale is logarithmic. At RE, the pilot site, the mean (6.3) and median (6.4) pH were the lowest of any of the sites.

Water temperature varied with season at all three sites in a very similar manner as all are within the same climatic zone. Ranges and means were very similar across all three sites, but slightly lower at RE as the summer months were not measured. DW: -0.5 – 18.5, 9.5 (*98*); RK: 0.9 – 21.5, 10.8 (*99*); RE: 2.3 – 13.4, 7.9 (*21*) (all in ^{o}C: min – max, mean (*n*))

pCO_2 varied between sites (Figure 22e, Table 3), and all were within previously reported ranges (Raymond *et al*., 2013; Long *et al*., 2015). Maximum *p*CO_2 at RK (4660 ppm) was almost twice that of DW (2677 ppm), however mean and median *p*CO_2 were similar at the two sites, being higher at DW than at RK (DW 1299, 1226 ppm; RK 1294, 1097 ppm). At RE only two *p*CO_2 values could be calculated due to limited [DIC] measurements and problems with the pH measurement, however the results show that *p*CO_2 was low (388 ppm) and similar (1245 ppm) on these two measurement occasions to both RK and DW *p*CO_2.

When pCO_2 is considered alone there is a general increase in efflux with *p*CO_2 at DW and RK (insufficient data points at RE) but the relationship is weak (Figure 27a). When the influence of pCO_2 is included in the flow intensity-efflux relationship, by plotting CO_2 efflux against the product of mean flow velocity and *p*CO_2 ($\bar{u}$**p*CO_2), the data from DW and RK overlap more closely than in the flow intensity-efflux relationship (Figure 24a, Figure 25a) and the data from RE (although only 2 data points) are brought closer to, and within the maximum scatter of, that of the other sites. The overall relationship is improved from R^2 = 0.71 and s.e. = 2.08 for DW and RK pooled data (Figure 24a) to R^2 = 0.74 and s.e. = 2.26 even when including RE data in the pooled dataset (Figure 27b). Flow intensity-efflux relationships are also improved at 3 out of 4 sites in the Peruvian Amazon by including the influence of *p*CO_2, and data from DW and RK overlap with this

Amazonian data (Appendix B: Fig. 4 of Long *et al*., 2015). When the influence of pCO_2 is included in the relationship between R^* and efflux, by plotting CO_2 efflux against the product of R^* and pCO_2 ($R^*.pCO_2$), the data overlap more closely than the R^*-efflux relationship (Figure 24d, Figure 25d), and inter-site variation in the relationship is reduced, with all trendlines collapsing onto one line. The gradients of $\bar{u}^*pCO_2$ do not overlap (1.234 ± 0.084 for DW and 1.706 ± 0.236 for RK) but the gradients of $R^*.pCO_2$ do overlap (0.801 ± 0.049 for DW and 0.733 ± 0.172 for RK). The overall relationship is improved from $R^2 = 0.69$ and s.e. = 2.05 for DW and RK pooled data (Figure 24) to $R^2 = 0.74$ and s.e. = 2.17 even when including RE data in the pooled dataset (Figure 27c).

No [DIC] measurements were made for the five CO_2 influx occasions, and thus no pCO_2 data is available and the influence of pCO_2 in the flow intensity-influx relationship cannot be considered.

3.4.4 Summary of Regression Models

Table 7: Summary of regression models

Log CO_2 efflux vs. Log $\bar{u}^*pCO_2$	**Log CO_2 efflux vs. Log R^*pCO_2**
DW	**DW**
$\log(CO_2 \text{ efflux}) = -2.51 + 1.23 \log(\bar{u}^*pCO_2)$	$\log(CO_2\text{efflux}) = -5.13 + 0.80 \log(R^*pCO_2)$
s.e. residuals: 2.15; $p < 0.001$	s.e. residuals: 1.94; $p < 0.001$
Gradient (+/- 1 s.e.): 1.15 - 1.32	Gradient (+/- 1s.e.): 0.75 - 0.85
RK	**RK**
$\log(CO_2 \text{ efflux}) = -4.03 + 1.71 \log(\bar{u}^*pCO_2)$	$\log(CO_2\text{efflux}) = -4.68 + 0.73 \log(R^*pCO_2)$
s.e. residuals: 1.97; $p < 0.001$	s.e. residuals: 2.40; $p < 0.001$
Gradient (+/- 1s.e.): 1.47 - 1.94	Gradient (+/- 1s.e.): 0.56 - 0.91
Pooled (DW, RK and RE)	**Pooled (DW, RK and RE)**
$\log(CO_2 \text{ efflux}) = -2.58 + 1.22 \log(\bar{u}^*\text{pCO}_2)$	$\log(CO_2\text{efflux}) = -5.12 + 0.80 \log(R^*\text{pCO}_2)$
s.e. residuals: 2.26; $p < 0.001$	s.e. residuals: 2.17; $p < 0.001$
Gradient (+/- 1s.e.): 1.15 - 1.30	Gradient (+/- 1s.e.): 0.74 - 0.85

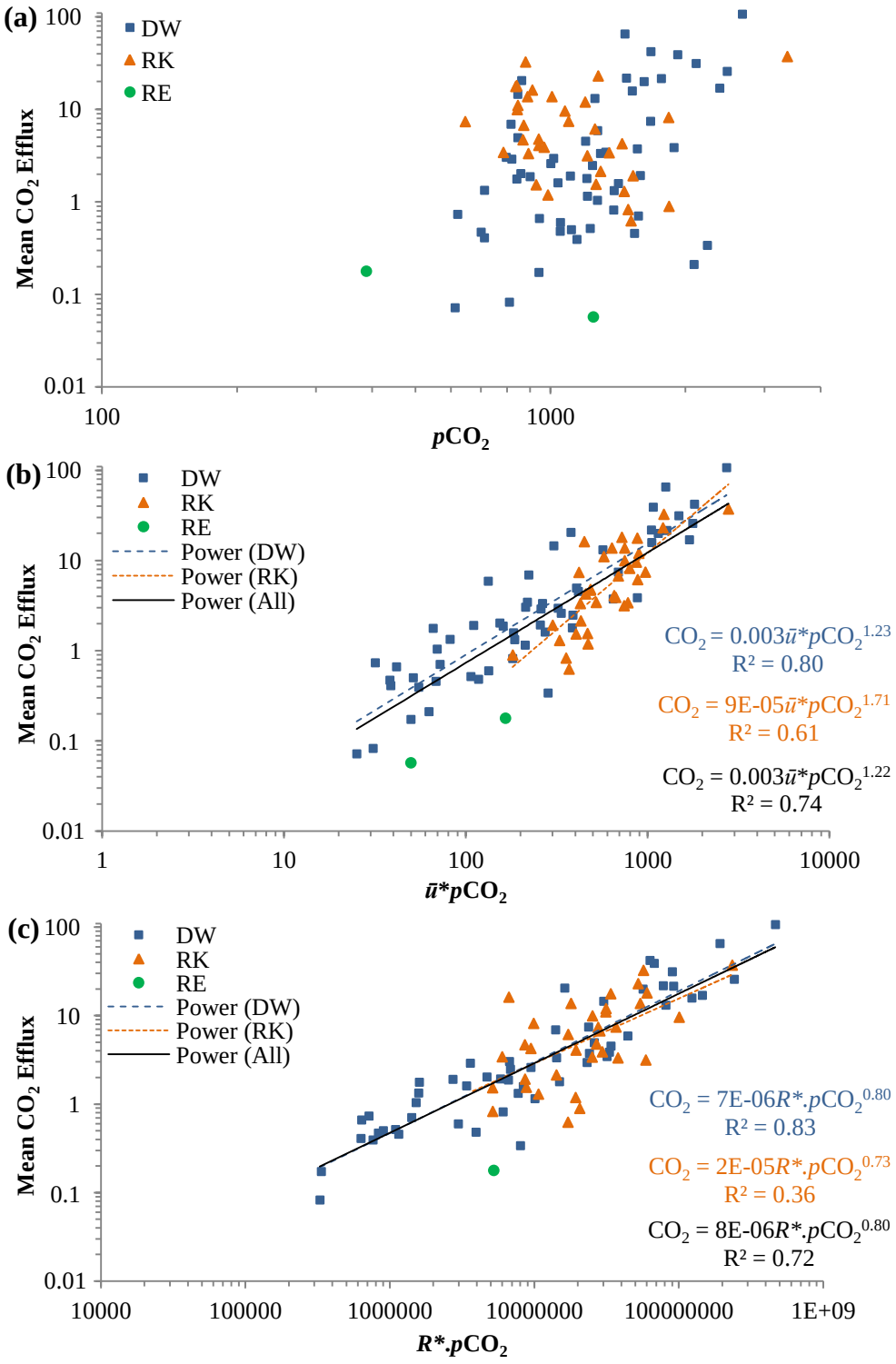

Figure 27: Relationship between pCO_2 and efflux, $\bar{u}$ *pCO_2 and efflux, and R*.pCO_2 and efflux

Relationship between CO_2 efflux (µmol CO_2 m^{-2} s^{-1}) and (a) pCO_2; there is a general increase in CO_2 efflux with pCO_2, but the relationship is weak so trendlines are not shown (R^2 = 0.09, p = 0.004, s.e. = 4.60), (b) the product of flow velocity ($\bar{u}$) and pCO_2; R^2 = 0.74, p = <0.001, s.e. = 2.26, (c) the product of R* and pCO_2; R^2 = 0.72, p = <0.001, s.e. = 2.17. When pCO_2 is included in the relationship between flow and efflux the relationship is improved, data from DW and RK overlap closely and RE is brought much closer to DW and RK. When pCO_2 is included in the relationship between R* and efflux the data collapse onto one line.

3.4.5 Visual Water Surface Classification

At DW and RK, sampled sites included more smooth water surfaces than either medium or rough surfaces, whereas at RE more medium and rough surfaces were measured than smooth (Table 3). All categories are represented well overall, with smooth, medium and rough water surfaces constituting 44%, 30%, and 21% of total CO_2 efflux measurements respectively (n = 93, 64, 44). For the remaining <6% of efflux measurements water surface was not recorded (n = 12).

Without direct measurement of hydraulic properties, water surface classification data offers the potential for rapid upscaling based on suitable imagery (e.g. low level aerial photographs taken from a drone). When water surface state is added to the logarithmic relationships between CO_2 efflux and hydraulic variables, the data separate according to the visual characterisation of the water surface (Figure 28). At all field sites there is only a little separation between the medium and rough datasets, but more noticeable separation of the smooth datasets from the medium and rough datasets at DW and RK. This is less apparent at RE because of the unavailability of smooth water surfaces in the dataset.

A similar trend as for effluxing conditions appears to exist when water surface state is added to the relationships between CO_2 influx and hydraulic variables, however there was insufficient influx data to draw strong conclusions. Plots were created for integrity (Figure 29).

The distribution of efflux across all water surface classification categories is positively skewed; the ranges of CO_2 efflux within each category overlap, but the range extends at the upper end from smooth, through medium to rough water surface state (Figure 30). Additionally, the proportion of low efflux observations reduces as the water surface state becomes rougher: the CO_2 efflux rate was < 5 µmol CO_2 m^{-2} s^{-1} in 96 %, 53% and 32% of cases for smooth, medium and rough water surfaces, respectively.

When water surface state is categorised by Froude number (*Fr*), water surfaces classified as ‘smooth’ separate by *Fr* from those classified as ‘medium’ and ‘rough’ which themselves display significant separation (p = <0.001) (Figure 31).

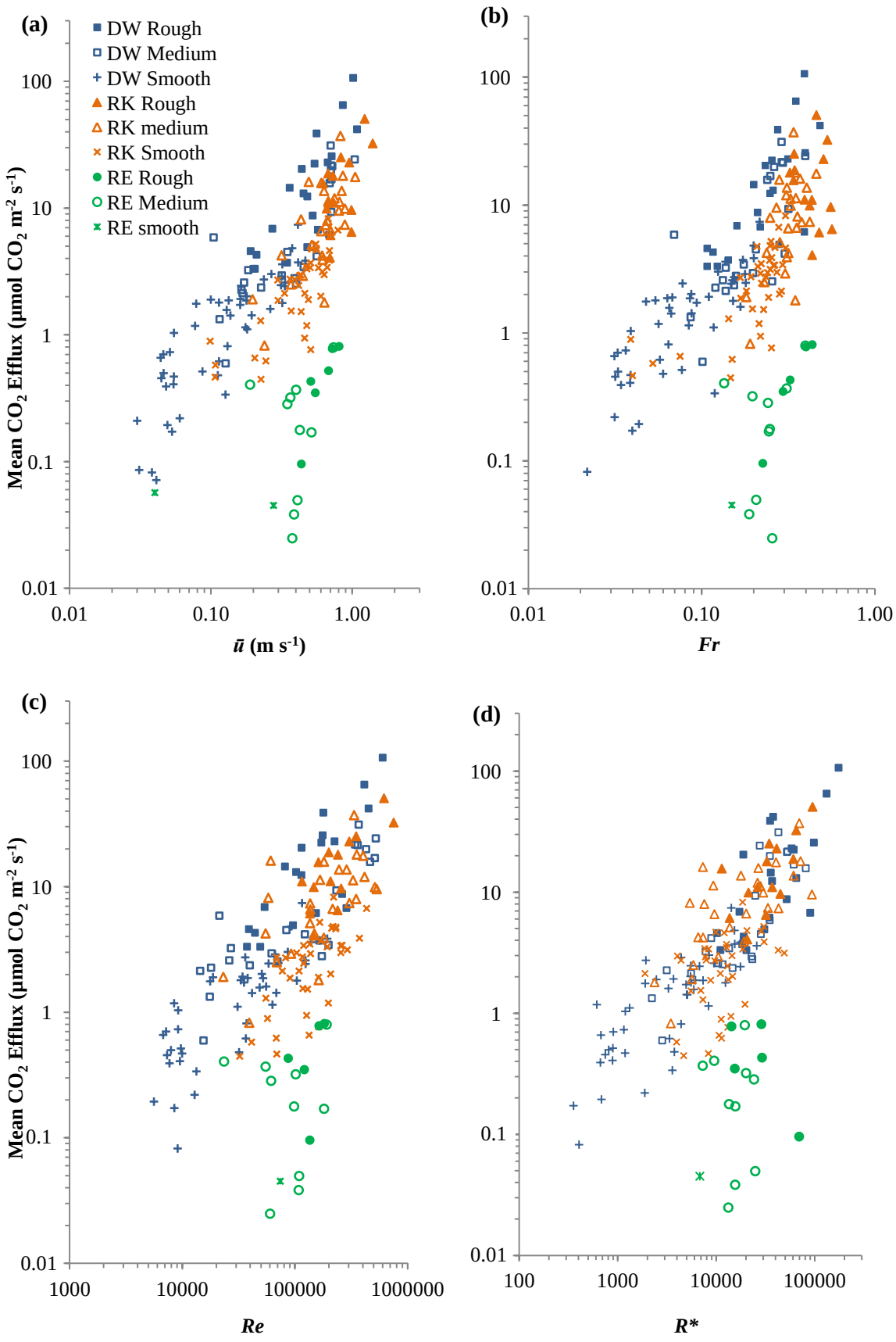

Figure 28: Separation of CO_2 efflux data by visually determined flow state

When water surface state is considered in the log-log relationships between CO_2 efflux and (a) mean velocity, (b) Froude number, (c) Reynolds number and (d) Shear Reynolds number, data separate according to the visual classification.

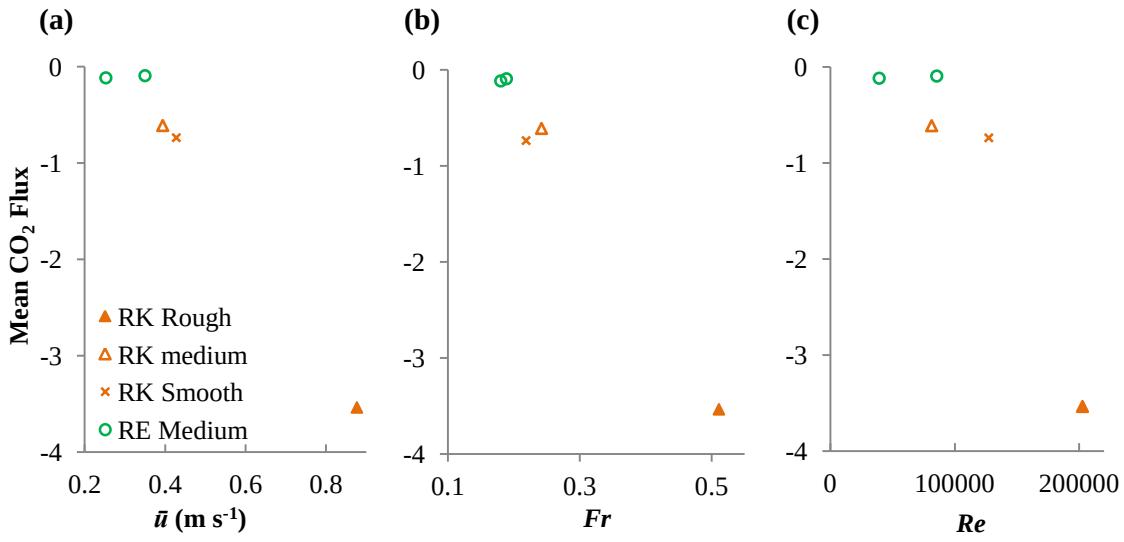

Figure 29: Separation of CO_2 influx data by visually determined flow state

When water surface state is considered in the log-log relationships between CO_2 influx and (a) mean velocity, (b) Froude number and (c) Reynolds number, 'rough' data separate from the 'medium' and 'smooth' data which overlap. With so few points (n = 5) this trend is not conclusive, but suggests that gas influx increases with water surface disturbance as gas efflux does (Figure 24b, Figure 25b). Mean CO_2 flux in µmol CO_2 m^{-2} s^{-1}.

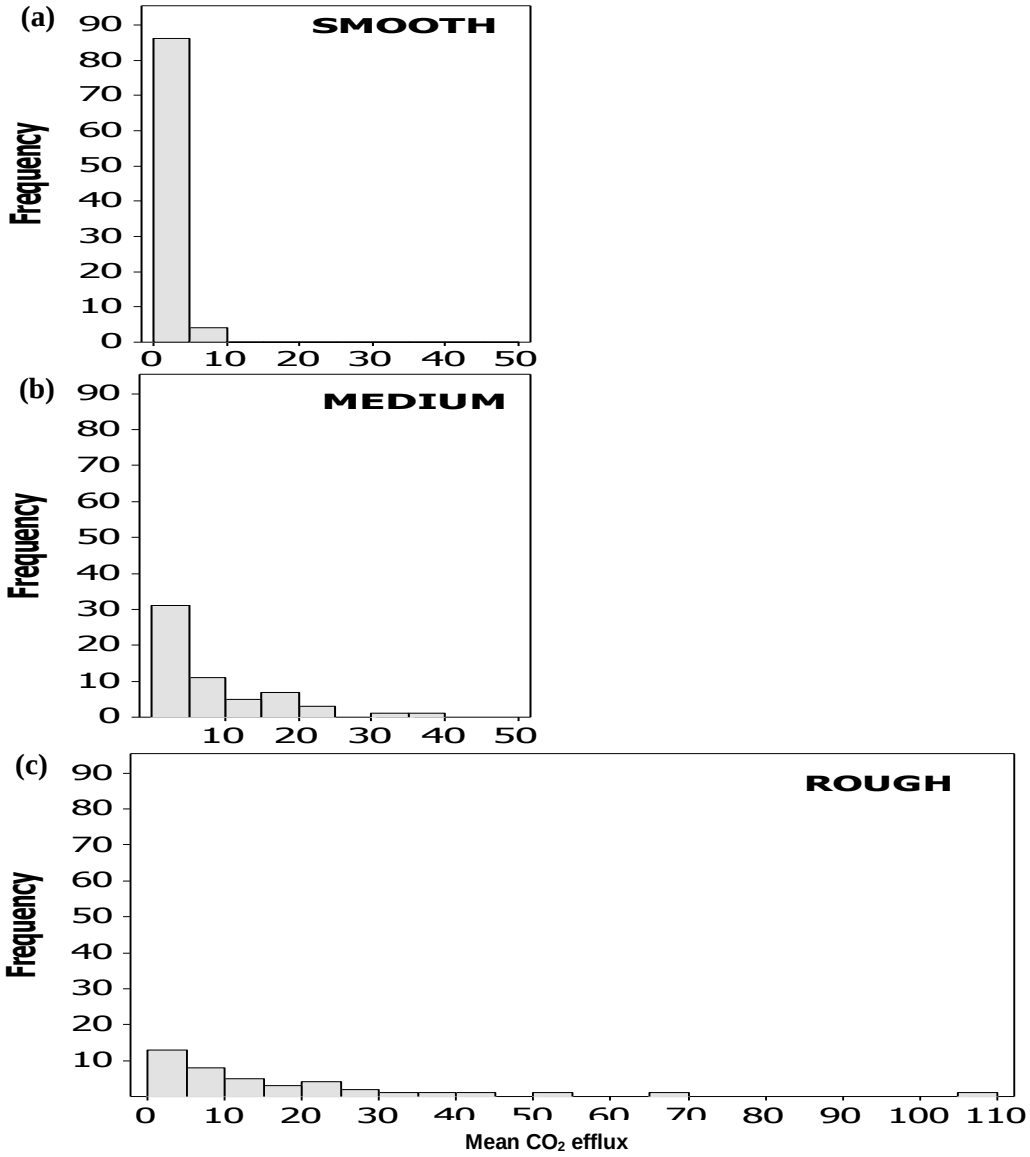

Figure 30: Distribution of CO_2 efflux for each water surface state classification

Mean CO_2 efflux in µmol CO_2 m^{-2} s^{-1}. Percentage of CO_2 efflux measurements < 5 µmol CO_2 m^{-2} s^{-1}: (a) smooth = 96 %, (b) medium = 53 %, and (c) rough = 32%.

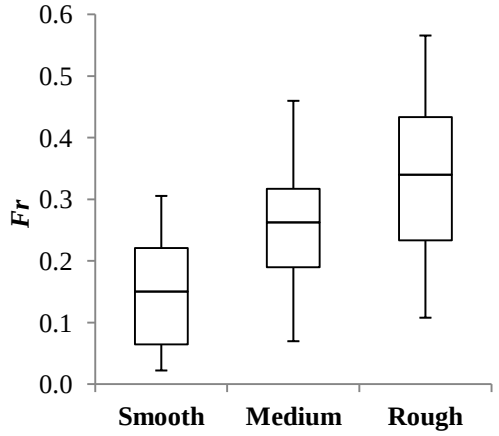

Figure 31: Separation of visual water surface classification data by Froude number

Water surfaces classified as 'smooth' separate by *Fr* from those classified as 'medium' and 'rough'. Boxes represent interquartile range with the intersecting horizontal line as the median, and upper and lower bars represent maximum and minimum values respectively. One-way ANOVA, with smooth, medium and rough categories, confirmed that the differences between classes are significant ($F = 55.14$; $p = <0.001$).

3.5 Discussion

3.5.1 Controls on CO_2 Efflux

3.5.1.1 Latitude and Net Ecosystem Productivity

Magnitude and ranges of CO_2 efflux from the three contrasting catchments used in this study fall within previously reported CO_2 efflux ranges from a wide latitudinal extent (Appendix B: Fig. 1 and Table 1 of Long *et al.*, 2015). Greater catchment productivity has been linked to increased riverine CO_2 concentrations and associated CO_2 efflux (Maberly *et al.*, 2013) and catchment biological productivity has been found to be greater in warmer environments, provided that moisture is not a limiting factor (Lauerwald *et al.*, 2013; Maberly *et al.*, 2013). However, these published CO_2 efflux data from a wide latitudinal range show no consistent pattern with latitude (Long *et al.*, 2015), thus net ecosystem productivity (NEP) (e.g. Cramer *et al.*, 1999) appears not to be a primary control on CO_2 efflux. This is perhaps not surprising as drivers of the fluvial $CO_{2(aq)}$ pool size, such as soil type, geology, temperature and river water pH, that have been found to explain variation in CO_2 efflux rates (Rebsdorf *et al.*, 1991; Aufdenkampe *et al.*, 2011; Lauerwald *et al.*, 2013; Long *et al.*, 2015), can vary greatly across a given latitude.

3.5.1.2 Stream Order

An overall decreasing trend in dissolved CO_2 and CO_2 efflux has been found with increasing stream order, and thus stream size (Hope *et al.*, 2001; Alin *et al.*, 2011; Butman and Raymond, 2011; Wallin *et al.*, 2011). It has been postulated that small streams contribute the largest proportion of CO_2 outgassed to the atmosphere by a river system due to their tendency to be more over-saturated with CO_2, more turbulent due to steeper topography, and to comprise a higher proportion of total stream surface area than larger rivers (Bishop *et al.*, 2008; Butman and Raymond, 2011; Wallin *et al.*, 2011). The two main catchments of this study (DW and RK) are of significantly different sizes and stream orders, the smaller stream (DW, stream order 3, catchment 5.7 km^2), was sampled in the headwaters and the larger river (RK, stream order 5, catchment 335 km^2) was sampled in the lower reaches, and the catchment/river sizes of Peruvian Amazon data (Long *et al.*, 2015) are more varied still (Appendix A), yet the ranges and means of CO_2 efflux at all sites were of very similar magnitudes. This suggests that the controls on CO_2 efflux can be consistent across rivers of different scales and that the controls on efflux are more complex than stream order.

3.5.1.3 Flow intensity

When pooled CO_2 efflux data from all three sampling sites were plotted against hydraulic parameters ($\bar{u}$, *Fr*, *Re* and *R**) an increase in CO_2 efflux occurred with flow intensity regardless of catchment characteristics (Figure 24, Figure 25). The same relationship is found in data from the

Amazon Basin in Peru, showing that flow intensity is a control on CO_2 efflux across different climatic zones (Long et al., 2015 – Appendix B). CO_2 efflux should be enhanced by flow intensity because convection and turbulent mixing associated with eddies (represented by *Re* and *R**) and surface waves (represented by *Fr*) greatly enhance gas transfer across the air-water interface (Moog and Jirka, 1999; Eugster *et al.*, 2003; Palumbo and Brown, 2013) by repeatedly renewing the surface boundary layer with $CO_{2(aq)}$-rich water. These processes maintain a steep water-atmosphere CO_2 concentration gradient, which causes CO_2 to diffuse across the interface into the atmosphere (Moog and Jirka, 1999; Eugster *et al.*, 2003; Jonsson *et al.*, 2008). There has been debate whether large or small scale eddies are most important to interfacial gas transfer in channel flow (O'Connor and Dobbins, 1958; Fortescue and Pearson, 1967; Lamont and Scott, 1970), and a more recent suggestion that it is a combination of both scales (Moog and Jirka, 1999). Numerical simulations (Komori *et al.*, 1993) have shown that higher frequency small-scale eddies are embedded within larger eddies at a range of Reynolds numbers (Moog and Jirka, 1999). The notion that large-scale eddies carry the small eddies to the surface where they renew the concentration boundary layer, transferring gas from the bed (where available), has been termed the "chainsaw model" (Moog and Jirka, 1999). Both the speed of the small eddies (or chainsaw teeth) and frequency of the large eddies (or chainsaw blade) dictate the rate of gas transfer (or cutting) (Moog and Jirka, 1999). It should be noted that this model may not apply beyond the point of riverbank breach, when both water surface area and flow velocity (parameters that highly impact CO_2 flux rates, e.g. Raymond *et al*., 2013 and Long *et al*., 2015) can alter vastly from channelised flow.

Although limited to only five measurements, CO_2 influx data was also highly correlated with flow intensity, with higher flow intensities associated with greater influx. This relationship is controlled by the same flow processes, turbulent eddies and mixing, as the efflux-flow intensity relationship, but the gas moves in the opposite direction as with oxygen reaeration (Palumbo and Brown, 2013). Influx requires a reversal of the concentration gradient between the atmosphere and the water; CO_2 must be under-saturated in water with respect the atmosphere. Unfortunately no pCO_2 data exists to confirm under-saturation, however the pH was at the upper end of the range for each site on the influxing occasions (RK: 7.9, RE: 6.6 – 6.7), suggesting that less of the DIC pool was available as $CO_{2(aq)}$ than on many other occasions.

Fanning at the upper end of the relationship between CO_2 efflux and all measures of flow intensity ($\bar{u}$, *Fr*, *Re* and *R**) (Figure 24) indicates that more data are needed at high flow and efflux, and may suggest that factors not considered in this study contribute to variation in CO_2 efflux; for example the interaction of stream water with the river bed (Peter *et al.*, 2014), dissolved organic carbon concentration (as a contributor through respiration or UV oxidation to CO_2; Cole *et al.*, 2007) or seasonality (controlling allochthonous inputs and as a proxy for temperature, autochthonous and secondary production, e.g. Billett and Moore, 2008, Dawson *et al*., 2009).

3.5.1.4 pH, [DIC] and pCO_2

pH can limit CO_2 efflux through its influence on speciation of the DIC pool (Hofmann and Schellnhuber, 2010) (Chapter 1, section 1.5). At high pH, a greater proportion of the DIC pool is in the form of carbonate and bicarbonate ions, which only exist in aqueous form, and so are not available for degassing. Thus it is possible that at higher pH the CO_2 pool size may be smaller; however the size of the CO_2 pool is also dependent on the total DIC concentration, as it is a proportion of this. pCO_2 is calculated to incorporate the combined effects of pH and [DIC] on availability of CO_2 for degassing. Although data are not abundant, elevated pCO_2 has been previously reported to enhance CO_2 evasion (Billett and Moore, 2008), due to a greater availability of CO_2 for degassing and a steeper water-atmosphere CO_2 concentration gradient (Billett *et al.*, 2006).

At all sites, pCO_2 levels show over-saturation of the water with respect to atmospheric CO_2 concentration (Table 3). No pCO_2 data is available for the influxing occasions but under-saturation with respect to atmospheric CO_2 would be expected, with the reversal of the concentration gradient causing atmospheric CO_2 to diffuse into the water. Mean and median pCO_2 was highest at DW thus it seems likely that the higher concentration of CO_2 in the water resulted in the greater efflux rates at a given flow intensity. Efflux and pCO_2 are similar at DW and RK, despite RK having much higher [DIC]. pCO_2 and efflux are limited at RK by the influence of the higher pH on speciation of the carbon pool. RE has lower efflux rates at a given velocity, however mean pH is the lowest of the three sites and so not limiting efflux; availability of CO_2 appears limited by low DIC concentrations.

When pCO_2 is included in the mean velocity-efflux relationship, data from DW and RK align more closely, and the two data points from RE are brought within the maximum scatter of the other two sites (Figure 27b). Mean velocity is a good bulk indicator of flow characteristics, and useful because it is commonly measured, however Shear Reynolds number is more physically meaningful as it measures the fluid forces and energy that create turbulence. When including R^* instead of $\bar{u}$ in the model between efflux, flow hydraulics and pCO_2 the model is improved; inter-site variation is removed with data from DW and RK collapsing onto one line, and overlapping entirely (Figure 27c) (confirmed by the s.e. of the gradient coefficients; sections 3.4.3 and 3.4.4). pCO_2 alone does not have a strong relationship with efflux (Figure 27a), but it enhances an already strong relationship between flow intensity and efflux, indicating that flow intensity is the primary control on efflux and pCO_2 a secondary control. Additionally, pCO_2 was found to align the outlying Peruvian Amazon site with data from DW and RK and the three other Peruvian Amazon sites showing that pCO_2 acts as a secondary control on efflux across climatic zones (see Appendix B: Fig. 4 of Long et al, 2015). A relationship between CO_2 efflux, slope and flow velocity has been reported previously (Butman and Raymond, 2011) where the gas transfer velocity (kCO_2) (which correlates with efflux, e.g. Richey et al, 2002 and Alin et al., 2011) increased with the product of slope and flow velocity (which correlate with turbulence, e.g. Gordon et al., 2004). However this

relationship (R^2 = 0.55, p<0.0001, n = 563) does not explain data from DW and RE as well as the R*.pCO_2 model proposed here (R^2 = 0.72, p<0.001, n = 98) (Appendix J).

These data suggest that at DW, RK and the Peruvian Amazon sites of Long *et al.* (2015) CO_2 efflux can be considered to be hydraulically-limited for the range of pCO_2 values sampled. This is analogous to transport-limited solute transport in rivers (Allen, 2009), i.e. the flux of CO_2 to the atmosphere is primarily determined by turbulence and water surface disturbance which respectively supply CO_2 to the water surface and facilitate its evasion to the atmosphere. Where the supply of CO_2 is limited (supply-limited in solute or material transport terms), for example in high pH or low [DIC]/pCO_2 streams, the relative significance of hydraulic conditions will likely be reduced, and the dominant control on efflux shift towards availability of CO_2. At the times of sampling, the flow in RE was at least partly produced by snow-melt, and, although confirmation is needed, initial results suggest that both [DIC] and pCO_2 were low, as would be expected in a snow-melt dominated stream, due to reduced connectivity with bedrock and soils compared to a groundwater dominated system (Chapter 4). The relationship of efflux with measures of flow intensity are consistently significantly weaker at RE than at the other sites which are not CO_2 limited, supporting the idea that the importance of hydraulic conditions will reduce under CO_2 supply limited scenarios. However confirming this requires more rigorous data collection and investigation.

3.5.2 Visual Classification

As yet there is no simple sensor technology to directly measure CO_2 efflux from a stream or river surface, so we need to explore proxy approaches to enable rapid and/or large-scale spatial and temporal upscaling. When considering the water surface state in the relationship between CO_2 efflux and log $\bar{u}$, log *Fr*, log *Re* and log *R** the data separate according to the visual characterisation of the water surface (Figure 28). That there is little separation between the medium and rough data sets, implies that moderate disturbance of the water surface disrupts the surface boundary layer enough to enhance gas exchange. The relationship between water surface state and Froude number is well known (Gordon *et al.*, 2004), with Froude number increasing with the degree of disturbance of a water surface (see section 3.2.3). When water surface state is categorised by Froude number (*Fr*), water surfaces classified as 'smooth' separate by *Fr* from those classified as 'medium' and 'rough' which themselves display some separation (Figure 31), and because *Fr* is correlated with other measures of flow intensity by definition, this corroborates the separation by surface state observed in CO_2 efflux-hydraulic parameter relationships. Further testing is required, with a greater number of datasets and firm standardisation of visual classifications to ensure repeatability between observers, and it is imperative visual classification be carried out during or just prior to the flux measurement to avoid bias. However, with the collection of such suitable calibration data sets, visual classification data could provide estimates of *Fr* where direct measurement is not possible. Water surface state can be measured from aerial imagery (Cox and Munk, 1954; Preisendorfer and Mobley, 1986; Gordon, 2005) and so if this visual classification method can be refined, there may

be potential for using remote-sensing techniques to estimate *Fr*, and thus include more accurate estimates of CO_2 evasion from low-order and/or inaccessible streams in catchment scale or global estimates of riverine CO_2.

3.6 Conclusions

Direct measurements of flow intensity with CO_2 efflux rates at three sites with contrasting catchment characteristics, as well as four sites in a contrasting climatic region (Long *et al.*, 2015) show that flow intensity is a primary control on CO_2 efflux. Thus the hypothesis *"Flow intensity controls gas transfer within the water column and water surface disturbance, and so flow intensity correlates with CO_2 efflux"* remains supported. Flow intensity also appears to be a primary control on CO_2 influx rates, however further data is required to strengthen this observation. Mean velocity has the highest correlation with CO_2 efflux, but is less physically meaningful and less likely to be applicable across scales than *Fr*, *Re* and *R**, so instead the term 'flow intensity' is used to encompass multiple measures of flow strength. The relationship between flow intensity and CO_2 efflux is refined when pCO_2 is included in the model, correcting for inter-site variability, and indicating pCO_2 is a secondary control on CO_2 efflux. To determine whether this is the case for CO_2 influx, collection and analysis of substantial pCO_2 and CO_2 influx data is needed. The highest CO_2 effluxes were measured when both flow velocity and pCO_2 were high. However the highest effluxes occur over a range of velocities, suggesting that additional controls, for example diurnal or seasonal responses or the impact of hydrological events (Peter *et al.*, 2014) also influence CO_2 efflux rates. The model could be refined by quantifying these and incorporating such controls empirically into the model.

Having confirmed the significance of hydraulic controls over CO_2 efflux, there is potential for improving both the coverage and accuracy of CO_2 efflux estimates from surface waters, overcoming limitations in understanding that support upscaling. The model describes less-well CO_2 efflux rates at the highest flows and so further data are required in high flow conditions to refine the model. Additionally knowledge is lacking of CO_2 recharge from the interaction of the water column with the benthic and hyporheic zones (Peter *et al.*, 2014), and how this influences the capacity to degas CO_2 needs to be considered, with a view to comparison with models that estimate CO_2 degassing at the catchment scale (Abril *et al.*, 2014). Further this model is unlikely to apply in conditions where CO_2 efflux is supply limited e.g. high-pH systems and/or low [DIC] systems, such as glacial-melt (Thomas and Raiswell, 1984; Brown, 2002) or tufa systems (Chen *et al.*, 2004; Pedley *et al.*, 2009) where speciation and/or availability of DIC can limit efflux, but flow velocity may still be high. Limited data collected at a snow-melt dominated system implies this, but extensive data collection and analysis is needed for confirmation. To support upscaling, visual classification of water surface state shows promise but requires development and rigorous testing to reduce subjectivity and variation in the estimates.

4 Isotope systematics and sensor technology provide insight into the source and cycling of fluvial DIC and CO_2

4.1 Abstract

Detailed understanding of the hydrological and biogeochemical processes, and mechanisms, that control the transmission of DIC through fluvial systems is required to improve accurate predictions of how these systems, which may act as a feedback to climate change through CO_2 efflux, will respond to changing environmental conditions. Using contemporaneous measurements of DIC concentration ([DIC]) and stable carbon isotope composition of the DIC pool ($\delta^{13}C_{DIC}$) in three distinct UK catchments with varied catchment characteristics and sizes (DW, RK, RE), it is found that the DIC pool composition at DW and RK is comparable to that of other temperate and tropical systems globally, and has a strong hydrological response. Groundwater dominates at low flow in both DW and RK and is of similar composition ([DIC]: 1.5 mmol L^{-1} DW, 2.0 mmol L^{-1} RK; $\delta^{13}C_{DIC}$: -9 ‰ DW and RK) indicating a common lithology. Differences in pool composition at high flow ([DIC]: 0.1 mmol L^{-1} DW, 1.0 mmol L^{-1} RK; $\delta^{13}C_{DIC}$: -23 ‰ DW, -14 ‰ RK) reflect catchment land use, and a lower contribution of soil water to the DIC pool in the RK urban-influenced catchment. Data from RE indicate snow- and ice-melt dominated systems may have very different carbon pool dynamics, and that multiple-end-member mixing models may be required for such systems.

Measured diel (24-hour) cycles in DIC pool composition at DW reveal biological processes modify the pool, while time series reconstructions of pool composition and CO_2 efflux at DW reveal detail in carbon pool dynamics e.g. the duration, magnitude and seasonal pattern of diel variation, that manual sampling can easily omit. Time series reconstructions also reveal that terrestrial-aquatic-atmospheric carbon cycling is very rapid over event flows, degassing large amounts of terrestrially-sourced CO_2 to the atmosphere over a relatively short duration. At base flow, efflux is of small magnitude and groundwater origin. This first known reconstruction of CO_2 efflux at high resolution over a number of years enables inter-year comparison and projection that under a drier climate with fewer and/or smaller magnitude event flows, fluvial systems will return less CO_2 to the atmosphere from a terrestrial source than under a wetter climate.

4.2 Introduction

The fluvial DIC pool contains dissolved CO_2 that fuels CO_2 efflux (Chapter 3). The source and cycling of fluvial DIC therefore has a direct influence on the type (e.g. terrestrial, atmospheric) and amount of carbon returned to the atmosphere via CO_2 efflux. Although movement of DIC through the hydrological cycle is an important component of global carbon budgets, uncertainty remains about the controls on DIC transmission through a catchment (Tobias and Böhlke, 2011). Increasing understanding of the hydrological and biogeochemical processes, and mechanisms, that influence

the inputs, outputs and mediation of the DIC pool in fluvial systems will aid prediction of how these systems will respond to changing environmental conditions and anthropogenic impacts. This is important as natural aquatic environments have the potential to feedback to climate change through CO_2 efflux (Parker *et al.*, 2010; Tobias and Böhlke, 2011).

Because the carbon dynamics of fluvial systems are closely linked to river-hydrochemistry, hydrochemical parameters can be useful and powerful tracers of the carbon dynamics in a catchment (Chapter 3; Yang *et al.*, 1996; Atekwana and Krishnamurthy, 1998; Finlay, 2003; Doctor *et al.*, 2008; Polsenaere *et al.*, 2013). Sensor technology can provide continuous long-term time series of relevant hydrochemical parameters that can be used to reconstruct DIC pool dynamics (Waldron *et al.*, 2007) and CO_2 efflux potential (Elayouty *et al.*, 2016) and further aid understanding and predictions of response under a changing climate, hydrological cycle and associated hydrochemical river regime.

Fluvial carbon pool models are beginning to be developed, but are in their early stages and are scarce. An approach to quantify CO_2 degassing from headwater bodies using pCO_2, [DIC] and $\delta^{13}C_{DIC}$ has been devised (Polsenaere and Abril, 2012) and is effective for low pH systems (e.g. Polsenaere *et al.*, 2013), but generates large uncertainties and unrealistic values of efflux at high pH and/or high pCO_2, and so further improvement and validation of the model is still required (Polsenaere and Abril., 2012). Additionally, to reconstruct efflux over time using this model would require long-term, high-resolution [DIC] and $\delta^{13}C_{DIC}$ data which is not commonly available due to the difficulties in manually sampling/measuring these parameters at high intensity. An instrument capable of continuous automated measurement of oceanic DIC exists (Sayles and Eck, 2009) but due to its large size, its use in rivers/streams and remote terrestrial locations is highly impractical. Additionally the ~6 h sampling frequency may cause events to be missed entirely in hydraulically responsive catchments (Bass *et al.*, 2012a). An isotopic, continuous, automated dissolved inorganic carbon analyser (ISO-CADICA), capable of sub-hourly measurement of [DIC] and $\delta^{13}C_{DIC}$ from a liquid water source (e.g., ocean, river, lake, ground water), has recently been developed (Bass *et al.*, 2012b), but as yet has not been deployed over long time scales (e.g. months or years).

Hydrochemical sensors are commonly used to collect time series pH, alkalinity, stage height, conductivity and temperature data, thus if sufficiently strong relationships exist between $\delta^{13}C_{DIC}$ and efflux and these parameters, they can be used to model and reconstruct $\delta^{13}C_{DIC}$ (integrated signal of the source and transformations of the DIC) and efflux (return of carbon to the atmosphere) over any time period for which hydrochemical time series data are available. For example, [DIC] and $\delta^{13}C_{DIC}$ have been reconstructed from pH data (Waldron *et al*. 2007) to ascertain the proportion of DIC from weathering and soil respiration, however they did not reconstruct efflux. Reconstructions of $\delta^{13}C_{DIC}$ and efflux could subsequently be used to assess for behaviours in source and CO_2 feedback that might be typical under climate change-induced changes in hydrology (e.g. wetter winters, drier summers, more frequent large flow events).

4.2.1 Aims

This chapter will investigate the DIC pool size and $\delta^{13}C_{DIC}$ of the waters of Drumtee Water (DW), the River Kelvin (RK) and the River Etive (RE) to determine the source of the DIC, the stability of the DIC pool and transport pathways and processes that amend the DIC pool. Additionally, contemporaneous changes in $\delta^{13}C_{DIC}$ and CO_2 efflux time series reconstructions will be used to consider the origin of effluxed carbon and how the carbon pool and CO_2 efflux may be affected by a climate change-induced shifting hydrological cycle. Specifically, the aims of this chapter are to:

(1) Use isotopic measurement to provide insight to systematic processes controlling the inputs and outputs of carbon in the fluvial systems of this study (DW, RK, RE), the carbon pool composition and pool reprocessing in the fluvial system.

(2) Explore whether there are relationships with logged hydrochemistry that can be used to develop models to reconstruct temporal variation in the source of fluvial DIC ($\delta^{13}C_{DIC}$) and CO_2 efflux, and:

   a. use this to help understand where the carbon that is effluxed originates, and

   b. consider contemporaneous changes of $\delta^{13}C_{DIC}$ and CO_2 efflux with hydrology, to identify behaviours that may be typical of flow under changing climates.

However, before expanding further on the research, a brief overview of isotope systematics in the terrestrial-aquatic-atmospheric C cycle is provided to contextualise the data that will come later.

4.3 Overview of Isotope Systematics

4.3.1 Sources of and Controls on the Fluvial DIC Pool

[DIC] and $\delta^{13}C_{DIC}$ are useful tracers of the DIC pool (see Chapter 1 and Appendix A for detail). A number of processes control the internal cycling of DIC in fluvial systems and the resultant DIC mass balance through input and output of carbon and changes to the carbon biogeochemistry. These processes are: air-water CO_2 exchange at the air-water interface, photosynthesis, respiration, geochemical reactions, groundwater discharge and evaporation (Atekwana and Krishnamurthy, 1998; Tobias and Böhlke, 2011). Each process can exert variable control on the DIC budget of a system, and shifting dominance of these processes results in variation in both the concentration and $\delta^{13}C$ of the DIC pool over diel (24-hour) to seasonal timescales (summarised in Figure 32) (Atekwana and Krishnamurthy, 1998; Waldron et al., 2007; Tobias and Böhlke, 2011). Thus quantification of changing [DIC] and $\delta^{13}C_{DIC}$ can aid identification of the dominating process(es) (Tobias and Böhlke, 2011).

Changes in [DIC] result from addition or removal of carbon to/from the DIC pool by the above processes, while changes in $\delta^{13}C_{DIC}$ occur as a result of carbon isotopic fractionation during transformation of carbon or due to mixing of carbon from different sources (Figure 32; Atekwana & Krishnamurthy, 1998). $\delta^{13}C_{DIC}$ is a non-conservative tracer and different sources of DIC may share the same isotopic signature (e.g. Figure 4), thus $\delta^{13}C_{DIC}$ alone does not definitively indicate a particular source or transformation of the DIC and should ideally be used in conjunction with a conservative tracer. Here, $\delta^{13}C_{DIC}$ is used together with [DIC] and CO_2 efflux to reduce uncertainty.

The potential sources and processing of DIC, and how they influence $\delta^{13}C_{DIC}$ are discussed in more detail in the following sections.

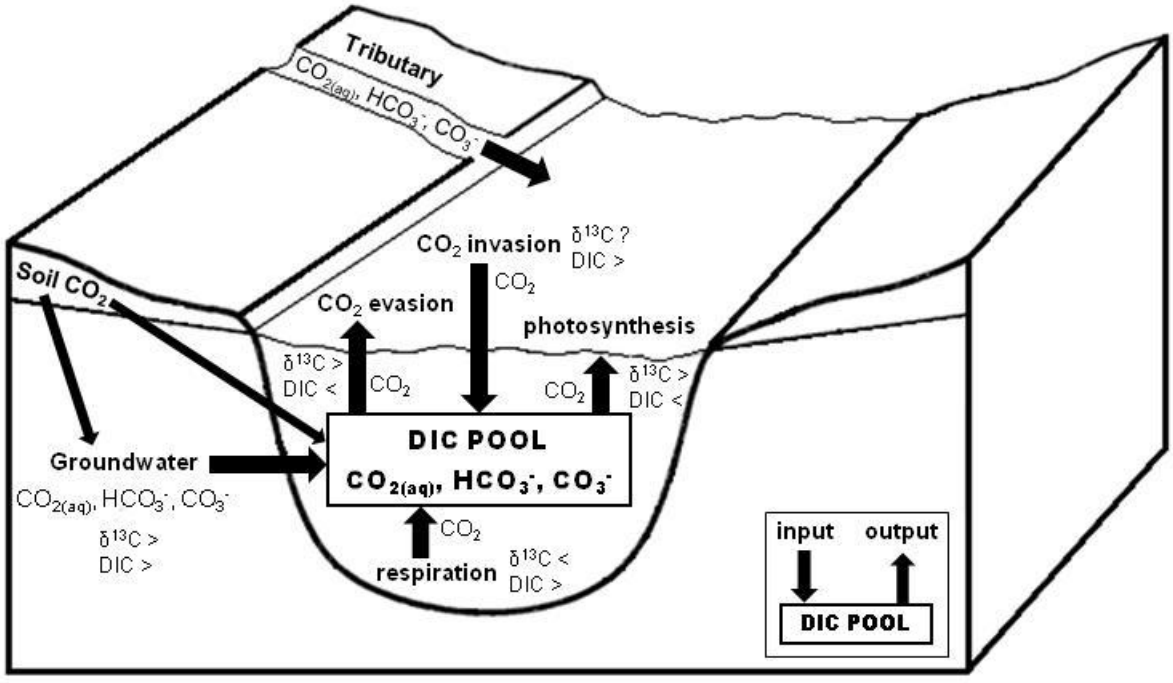

Figure 32: Changes in $\delta^{13}C_{DIC}$ and [DIC] in relation to processes that control fluvial DIC pool dynamics
Adapted from Atekwana & Krishnamurthy (1998). Direction of change in $\delta^{13}C_{DIC}$ and [DIC] are shown by > (increase) and < (decrease).

4.3.1.1 Air-Water CO_2 Exchange

Atmospheric CO_2 is the smallest global reservoir of carbon, controlled by tectonism, weathering, and biological activity (Clark and Fritz, 1997). Current atmospheric levels are ~404 ppm (NOAA, 2016). The evolution of DIC begins with atmospheric CO_2, which has a typical $\delta^{13}C$ of -11 to -6 ‰ (Stuiver and Polach, 1977) and an average between -7 ‰ and -8 ‰ (Clark and Fritz, 1997; Doctor *et al.*, 2008; Parker *et al.*, 2010; Polsenaere and Abril, 2012; Khadka *et al.*, 2014) (See 1.6 of Chapter 1), but which is gradually decreasing due to the release of ^{13}C-depleted CO_2 from the burning of fossil fuels (Clark and Fritz, 1997). At an atmosphere-water body interface, air-water CO_2 exchange occurs (regardless of the net direction of CO_2 movement), and, with it, isotopic equilibrium fractionation (Appendix A) of the CO_2 molecules, whereby the ^{13}C-containing

molecules tend to accumulate in the phase with the strongest inter-molecular bonds (usually the densest phase), i.e. the water. As a result, both invasion and evasion of CO_2 from and to the atmosphere isotopically-enrich the DIC pool (Yang *et al.*, 1996; Atekwana and Krishnamurthy, 1998). Air-water CO_2 exchange has been postulated to contribute to increasing downstream $\delta^{13}C_{DIC}$ enrichment (Yang *et al.*, 1996; Atekwana and Krishnamurthy, 1998; Aucour *et al.*, 1999) and is assumed to be more influential in systems with long water residence times (Atekwana and Krishnamurthy, 1998). Air-water exchange will modify the $\delta^{13}C_{DIC}$ towards the equilibrium value with the atmosphere of $\delta^{13}C_{DIC}$ of ~ 1 ‰. Where the air-water concentration gradient is steep, significant efflux or influx of CO_2, beyond isotopic equilibrium exchange, can occur; drawdown of atmospheric CO_2 will cause $\delta^{13}C_{DIC}$ enrichment towards ~0 ‰ (Deuser and Degens, 1967; Waldron *et al.*, 2007). CO_2 efflux has been found to cause 1 – 4 ‰ ^{13}C-enrichment over a distance of a few tens of meters of stream flow (Doctor *et al.*, 2008), and $\delta^{13}C_{DIC}$ shifts up to 5 ‰ at carbonate springs (Michaelis *et al.*, 1985).

4.3.1.2 Biological influence on fluvial DIC

Diffusive fractionation (Appendix A) occurs during photosynthetic uptake of atmospheric CO_2 due to the preferential incorporation of lighter ^{12}C-bearing CO_2 molecules into the plant (Criss, 1999; Clark and Fritz, 1997). This effect is amplified by subsequent metabolic reactions, the combined effect being 5 – 25 ‰ ^{13}C-depletion with respect to the atmosphere (Clark and Fritz, 1997). Photosynthetic pathways differ among plant types: C3 (Calvin cycle), C4 (Hatch-Slack cycle) or CAM (Crassulacean acid metabolism) (see Appendix A for more detail). All result in plants having low $\delta^{13}C$, and this is passed up the food chain and into the soils (Criss, 1999; Clark and Fritz, 1997). The natural vegetation of temperate and high-latitude regions is almost exclusively C3 (Clark and Fritz, 1997), and so this pool is most relevant here. The $\delta^{13}C$ of C3 plants ranges from -23 to -34 ‰ with an average of about -27 ‰ (Faure, 1986; Vogel, 1993; Clark and Fritz, 1997; Doctor *et al.*, 2008).

Degradation of plant matter is key to soil-forming processes, and soil and plant organic matter (OM) can be broken down into DOC, POC and DIC which can enter a river via runoff and erosion (Clark and Fritz, 1997). Thus $\delta^{13}C$ of the catchment soil OM and fluvial DOC, POC and DIC are generally very similar to that of the catchment vegetation (Clark and Fritz, 1997).

Soil CO_2 is produced by plant root respiration and heterotrophic respiration of soil OM (Doctor *et al.*, 2008; Khadka *et al.*, 2014). Neither of these processes cause significant fractionation of the CO_2 produced, thus initially soil CO_2 $\delta^{13}C$ is the same as that of the OM/vegetation (Lin and Ehleringer, 1997; Khadka *et al.*, 2014). Bacterial respiration raises the concentration of soil CO_2 by one to three orders of magnitudes, and as this degasses to the atmosphere diffusive fractionation (Appendix A) of ~ 4.4 ‰ occurs, causing ^{13}C-enrichment of the soil CO_2 to ~ -23‰ in C3 vegetation soils (Cerling *et al.*, 1991; Clark and Fritz, 1997; Khadka *et al.*, 2014). Exchange with relatively-enriched atmospheric CO_2 (~ -8 ‰) can also enrich $\delta^{13}C$ of soil CO_2 (Doctor *et al.*, 2008;

Khadka *et al*., 2014). ^{13}C-enrichment of soil CO_2 is thus dependent on the rate of soil respiration and the concentration gradient of CO_2 in the soil (Doctor *et al*., 2008). In C3-dominated catchments, when soil CO_2 is transported into a river system as DIC, it can influence the $\delta^{13}C_{DIC}$, generally causing ^{13}C-depletion (Yang *et al*., 1996; Atekwana and Krishnamurthy, 1998).

In-stream photosynthesis and respiration can also influence the DIC pool. The preferential uptake of $^{12}CO_2$ during photosynthesis by aquatic plants renders the remaining fluvial DIC pool ^{13}C-enriched, and photosynthesis simultaneously decreases the [DIC]. Conversely, respiration of OM in the water column produces CO_2 of $\delta^{13}C$ similar to that of the dominant vegetation (~ -27 ‰ for C3) which causes ^{13}C-depletion of the riverine DIC pool and an increase in [DIC] (Yang *et al*., 1996; Atekwana and Krishnamurthy, 1998; Waldron *et al*., 2007; Parker *et al*., 2010; Gammons *et al*., 2011; Khadka *et al*., 2014). Like many in-stream biogeochemical processes, photosynthesis and respiration respond to the solar photocycle and so occur on diel timescales (Nimick *et al.*, 2011). As such, diel sampling of [DIC] and $\delta^{13}C_{DIC}$ has been used in a number of studies of riverine carbon dynamics to determine the importance of biological processes in fluvial systems. These studies reveal that in the absence of competing reactions, biological processes tend to increase $\delta^{13}C_{DIC}$ and decrease [DIC] during the day when photosynthesis dominates, and decrease $\delta^{13}C_{DIC}$ and increase [DIC] at night when respiration dominates (Parker *et al.*, 2005; Waldron *et al.*, 2007; Parker *et al.*, 2010; Gammons *et al.*, 2011; Tobias and Böhlke, 2011), including in high-pH karst systems where precipitation of $CaCO_3$ accompanies daytime photosynthetic removal of CO_2 (De Montety *et al.*, 2011).

Biological processes can influence the DIC pool over longer time scales, and have been found to superimpose seasonal patterns of [DIC] and $\delta^{13}C_{DIC}$ on a groundwater baseline, with photosynthesis dominating in the summer months and respiration/decay in the autumn (Atekwana and Krishnamurthy, 1998). In high DIC systems, such as tropical river floodplains and heavily sewage-polluted rivers with copious plant growth, biological processes can dominate the DIC pool dynamics, and some of the largest reported amplitudes of diel $\delta^{13}C_{DIC}$ cycles occur (~7 ‰ Bass *et al*., 2013, up to 5 ‰ Parker *et al*, 2010; Gammons *et al*., 2011). Conversely, where in-stream photosynthesis is weak, inputs from terrestrial soil CO_2 may dominate the DIC pool (Polsenaere *et al*., 2013).

4.3.1.3 Weathering influence on DIC

A number of rock weathering reactions can release HCO_3^- and thus contribute DIC (via the groundwater) to a river system (Barth *et al.*, 2003). Silicates do not release IC upon weathering, and so silicate weathering does not significantly influence $\delta^{13}C$ of the DIC pool (Wachniew, 2006). In silicate-dominated bedrock, the DIC pool is dominated by ^{13}C-depleted DIC inputs from the soil (Khadka *et al*., 2014). In carbonate-dominated bedrock dissolution of the carbonate is a source of DIC to a river system, and can dominate the DIC pool dynamics (Khadka *et al*., 2014). Carbonates are generally enriched in ^{13}C, e.g. marine carbonates with $\delta^{13}C$ ~0 ‰, and so have a large ^{13}C-enriching effect on $\delta^{13}C_{DIC}$ (Clark and Fritz, 1997).

Groundwaters are typically a source of DIC to fluvial systems and are generally more ^{13}C-enriched than soil CO_2 and C3 vegetation (Fig. 1), but $\delta^{13}C_{DIC}$ can vary broadly, between -21 ‰ and 0 ‰ (Clark and Fritz, 1997; Tobias and Böhlke, 2011). The $\delta^{13}C_{DIC}$ composition of groundwater depends on the proportional inputs from bedrock weathering and soil CO_2; the greater the input from the bedrock, the more ^{13}C-enriched the groundwater (Aucour *et al*., 1999). Groundwater generally dominates the DIC pool dynamics under low flow conditions (Atekwana and Krishnamurthy, 1998; Waldron *et al*., 2007; Tobias and Böhlke, 2011; Polsenaere *et al*., 2013).

4.3.2 Fluvial Carbon Dynamics are Hydrologically Linked

Hydrochemical parameters and DIC pool dynamics are strongly influenced by river hydrology, and a number of studies find [DIC] and $\delta^{13}C_{DIC}$ to vary directly with the flow state of the system. Generally [DIC] reduces and $\delta^{13}C_{DIC}$ becomes more ^{13}C-depleted under high flow conditions; conversely [DIC] increases and $\delta^{13}C_{DIC}$ becomes more ^{13}C-enriched at base/low flow (Yang *et al*., 1996; Atekwana and Krishnamurthy, 1998; Finlay, 2003; Waldron *et al*., 2007; Doctor *et al*., 2008; Polsenaere *et al*., 2013; Khadka *et al*., 2014). Low flows are generally groundwater-dominated so the fluvial DIC pool will generally have similar [DIC] and $\delta^{13}C_{DIC}$ to the groundwater (Atekwana and Krishnamurthy, 1998; Waldron *et al*., 2007; Tobias and Böhlke, 2011; Polsenaere *et al*., 2013). Precipitation events, which cause high flows and/or flood events flush the soils and transport soil CO_2 to a river system, which introduces ^{13}C-depleted CO_2 (~ -23 ‰) to the fluvial DIC pool causing a decrease in $\delta^{13}C_{DIC}$ (Waldron *et al.*, 2007; Polsenaere *et al.*, 2013, Khadka *et al*., 2014). The simultaneous decrease in [DIC] is typically due to the diluting effect of large volumes of rainwater which cause the high flows (Akekwana and Kryshnamurthy, 1998; Waldron *et al*., 2007). However the extent of dilution will depend on the concentration of CO_2 in the catchment soils and the extent to which the soils were previously flushed (Waldron et al, 2007). Some exceptions to these relationships have been found, for example in the seasonal tropics. Here, during periods of high discharge, it has been found that [DIC] and $\delta^{13}C_{DIC}$ increase as a result of increased proportional subsurface inflow from the savanna plains relative to that from the rainforest (Tweed *et al.*, 2015), and, during very high rainfall events, $\delta^{13}C_{DIC}$ can initially be very ^{13}C-enriched (~ -1‰) due to large inputs of ^{13}C-enriched rainwater (close to atmospheric equilibrium) to the river via rapid overland flow (Bass *et al.*, 2014a).

4.4 Methods

4.4.1 Field Site Description

The same field sites as Chapter 3 were used for this chapter: Drumtee Water (DW), the River Kelvin (RK) and the River Etive (RE) with contrasting catchment characteristics. Chapter 2 contains an overview of each study site and Chapter 3 contains more detailed information on specific sampling points.

4.4.2 Field Measurements and Laboratory Analyses

On each sampling occasion (post 20th June 2013) samples were collected for determination of $\delta^{13}C_{DIC}$ and [DIC] alongside the set of field measurements/samples listed in Chapter 3: CO_2 efflux, flow velocity profile, pH, alkalinity, environmental parameters and a visual assessment of the water surface state. Full details of these methods can be found in Chapters 2 and 3.

4.4.2.1 Sampling Regime

Sampling was carried out over one year at the two main field sites (DW for 11 months; RK for 10 months), and during one spring period (Apr-May 2014) at the River Etive. Samples were not collected for the entire field sampling period (Jun-12 to May-14), but from 20th June 2013 onwards, as prior to this the sampling and analysis techniques were still being learned (Table 8).

Table 8: $\delta^{13}C$ sampling regime at each field site*

Site	Sampling Period	Sampling Frequency						Exceptions (no sampling)*
		Individual days per month			Times per given day			
		Usual	Min	Max	Usual	Min	Max	
DW	Jun-13 to May-14	2	1	4	2	1	3**	
RK	Jul-13 to May-14	2	1	6	2	1	3	Dec-13$^{\alpha}$
RE	Apr to May-14	1	-	-	-	1	3	Feb to Jun-15

* Does not include the period prior to 20th Jun-13 when sampling technique had not been learned. **With the exception of a 24-hour field campaign (27-28th Aug-13) where 9 consecutive sets of measurements were made. $^{\alpha}$ Samples were taken but dropped and smashed before analysis.

4.4.2.2 Diel Sampling

A 24-hour sampling campaign was carried out at Drumtee water at DW 4 (see
Figure 18) on 27-28th August 2013, to assess for the influence of biological processes on the fluvial DIC pool. During the 24-hour sampling period flow was low and stable after recent dry weather, ranging by only 0.011 m s^{-1} (between 0.044 and 0.055 m s^{-1}). Nine full sets of field measurements/samples were made/collected between 10:30 on 27-Aug-13 and 10:30 on 28-Aug-13, with the initial measurement time repeated as the final measurement to ensure a complete sampling cycle. Measurements were made/samples taken between 1h 15min and 4h 45min apart, though usually between 2h 30min and 4h apart. Ideally measurements/sample collection would have been evenly spaced over the 24-hour period (i.e. 3 hours apart), however equipment malfunction and field logistics deemed precise sampling times hard to control. Diel sampling was not carried out at RK and RE, for logistical reasons.

4.4.2.3 $\delta^{13}C_{DIC}$ and [DIC] Sampling

Samples for $\delta^{13}C$ and [DIC] analysis were collected using a headspace method following (Waldron *et al.*, 2014), within 15 minutes of, but usually at the same time as, the flux measurement, to ensure $\delta^{13}C$ and [DIC] corresponded as closely as possible to the efflux rate. For full field procedure see Chapter 2. $\delta^{13}C$ and [DIC] were analysed from the same water sample. No $\delta^{13}C_{DIC}$ or [DIC] data exists for the five influx occasions at the sites because either it occurred before sampling techniques had been learned (RK), or collected samples could not be tested (RE).

4.4.2.4 $\delta^{13}C_{DIC}$ and [DIC] Measurement and Notation

$\delta^{13}C$ and [DIC] were measured at the Scottish Universities Environmental Research Centre (SUERC) Stable Isotope Laboratory, using an isotope-ratio mass-spectrometer (IRMS), within 15 weeks of collection. Uncertainty in [DIC] is 0.027 nM (Waldron *et al*., 2014) (see Chapter 2 for detail).

Gas source mass spectrometry is a standard tool to determine stable isotope abundance, and abundance is reported as the ratio of the two most abundant isotopes of a given element (Criss, 1999; Clark and Fritz, 2007). The isotopic differences between materials are extremely small, so isotopic composition is measured and reported as the relative difference between an internationally accepted standard, and the sample (Michener and Lajtha, 2008). The standard for carbon is the hypothetical V-PDB (for further information see Appendix A).

The relative difference between the sample and the standard is expressed using the delta (δ) notation and by the equation:

$$\delta(‰) = \left(\frac{R_x}{R_{std}} - 1\right) \times 1000$$

where R is the ratio of heavy to light isotope, R_x is the isotope ratio of the sample, and R_{std} is the ratio of the standard. As variations in isotope concentration are extremely small, the δ-value is expressed in parts per thousand (‰ or permil) difference from the reference, by multiplying by 1000 (Michener and Lajtha, 2008).

Carbon isotopes ratios of inorganic materials are measured from CO_2 gas, which is usually produced by acidification with 100% phosphoric acid (H_3PO_4) at 25°C. Because in the reaction $CaCO_3 + 2H^+ \rightarrow CO_2 + H_2O + Ca^{2+}$ all the carbon is converted to CO_2, there is no fractionation of the ^{13}C, and $\delta^{13}C$ of the CO_2 is the same as the carbonate (Clark and Fritz, 1997).

4.4.2.5 Modelling and reconstructing $\delta^{13}C$ and CO_2 Efflux

Relationships of $\delta^{13}C_{DIC}$ and CO_2 efflux with other sampled/measured parameters were explored for use as predictive models for $\delta^{13}C_{DIC}$ and CO_2 efflux. Relationships with pH and stage height were used for modelling $\delta^{13}C_{DIC}$ and efflux as they had strong relationships with $\delta^{13}C_{DIC}$ and efflux.

Additionally, both pH and stage height are routinely measured by hydrochemistry sondes and so it is likely there would be good data availability globally for similar analysis in other studies. 95% confidence intervals were calculated for the models.

Using the relationships between $\delta^{13}C_{DIC}$ and CO_2 efflux (dependent variables) and pH and stage height (independent variables), $\delta^{13}C$ and CO_2 efflux were estimated from measured pH and stage height data and then compared to corresponding measured $\delta^{13}C_{DIC}$ and CO_2 efflux to check for agreement. The pH and stage height models for $\delta^{13}C_{DIC}$ and the pH model for CO_2 efflux were used to reconstruct $\delta^{13}C_{DIC}$ and CO_2 efflux at 30 minute resolution over the three hydrological years (HY) covering the period of this study (01-Oct-2011 to 30-Sep-2012; 01-Oct-2012 to 30-Sep-2013; 01-Oct-2013 to 30-Sep-2014). Efflux was reconstructed from the pH model only as pH is a more direct representation of the DIC pool and CO_2 availability than stage height, which is hydrologically, not directly, linked to DIC pool size and availability. For the $\delta^{13}C_{DIC}$ reconstructions, the models were capped at -27 ‰ at low pH and high stage height to prevent highly unrealistic $\delta^{13}C_{DIC}$ values being generated under high flow conditions (when low pH and high stage height occur), as here there is a lack of data. -27 ‰ was chosen as this is the average $\delta^{13}C$ of C3 vegetation, and of soil CO_2 before diffusive fractionation, thus in a system dominated by soil water at high flow this is the typically the most ^{13}C-depleted $\delta^{13}C_{DIC}$. Capping was achieved by identifying the pH and stage height that generates -27 ‰ using the models (here pH 4.94 and stage height 0.951 m), and subsequently assigning -27 ‰ as the output for all data in the time series with a lower pH than 4.94 or higher stage height than 0.951 m. CO_2 efflux reconstructions were not capped at high flow as no theoretical maximum efflux can be ascertained from previous studies. 90% confidence intervals were calculated and added to the reconstructions.

Data modelling and reconstruction was only carried out for DW as several years of accurate, high-resolution pH and stage height data are available from a Troll 9000 water chemistry sonde installed very close to the sampling locations of this study (within 20m upstream). For RK and RE, long-term, high-resolution hydrochemistry data from close proximity to the sampling locations are not available to explore such modelling

Reconstructed efflux data was used to calculate total annual efflux, for one m^2 of river at the location of the Troll, for each hydrological year. As efflux was reconstructed at 30 minute resolution, it was assumed each efflux rate represented the succeeding 30 minutes, and so each rate was multiplied by 1800 seconds (30 minutes). These rates were summed for each hydrological year to obtain CO_2 efflux totals in µmol CO_2 m^{-2} y^{-1}, converted to mol CO_2 m^{-2} y^{-1} by dividing by 1000000, and finally to kg CO_2 m^{-2} y^{-1} by multiplying by 0.04401, the molar mass of CO_2 in kg.

4.5 Results

4.5.1 Pool Magnitude

Ranges and averages of $\delta^{13}C_{DIC}$ and [DIC] at the three field sites (DW, RK and RE) are compared in Table 9 and Figure 33 below:

Table 9: Ranges and averages of $\delta^{13}C_{DIC}$ and [DIC] at each field site*

Site	Min	Max	Average		n
			Mean	Median	
DW	-23.2 0.08	-9.3 1.57	-14.1 0.37	-12.4 0.25	58
RK	-14.0 0.44	-7.9 2.03	-11.3 1.28	-11.2 1.16	39
RE	-14.8 0.04	-0.7 0.09	-6.6 0.06	-5.3 0.06	4

*Top values = $\delta^{13}C_{DIC}$ in permil (‰), bottom values = [DIC] in mmol L^{-1}. For other corresponding water chemistry data see Chapter 3 section 3.4.

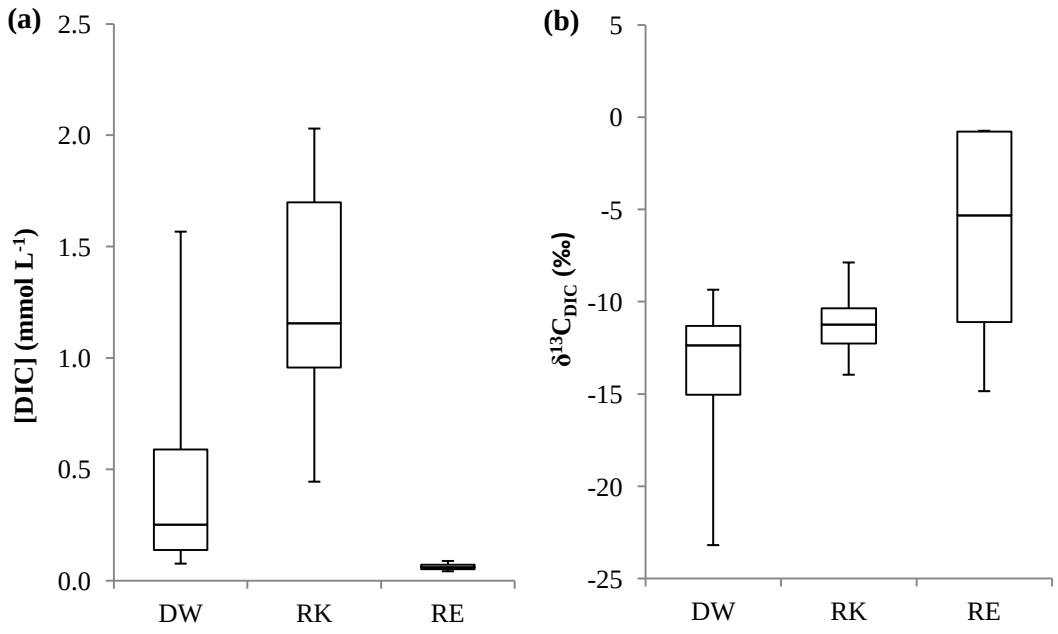

Figure 33: Box plot of $\delta^{13}C_{DIC}$ and [DIC] range at each site

(a) [DIC]; One-way ANOVA, with DW, RK and RE categories, confirmed that the differences between sites are significant ($F = 63.31$; $p = <0.001$). (b) $\delta^{13}C_{DIC}$; One-way ANOVA, with DK, RK and RE categories, confirmed that the differences between sites are significant ($F = 12.81$; $p = <0.001$). For other corresponding water chemistry and hydraulic parameter box plots see Chapter 3 section 3.4.

The ranges in [DIC] are statistically different at each site (Table 9, Figure 33a). RE has limited data points (n = 4), but has a much narrower range in [DIC] (0.05 mmol L^{-1}) than DW (1.49 mmol L^{-1}) and RK (1.59 mmol L^{-1}), which have relatively broad, and similar magnitude, ranges. RE has the lowest [DIC] of the three sites, the mean and median (0.06 and 0.06 mmol L^{-1}) being one and two orders of magnitude smaller than that of DW (0.37 and 0.25 mmol L^{-1}) and RK (1.28 and 1.16 mmol L^{-1}) respectively. Although RK and DW have similar magnitude ranges, the minimum, maximum, mean and median [DIC] are all greater at RK, with mean and median at RK one order of magnitude higher than those of DW, and minimum values at RK higher than the mean and median at DW, and the maximum at RE (Table 9). Maximum values at RK (2.03 mmol L^{-1}) are 23% and 96% higher than those of DW (1.57 mmol L^{-1}) and RE (0.09 mmol $L^{-1)}$ respectively. Minimum values are similar at DW and RE (0.08 and 0.04 mmol L^{-1} respectively) and one order of magnitude smaller than that of RK (0.44 mmol L^{-1}).

The ranges in $\delta^{13}C_{DIC}$ are statistically different at each site (Table 9, Figure 33b). RK has the narrowest range, which falls between that of the other two sites. DW and RK have similar maximum (DW -9.3 ‰, RK -7.9 ‰) and median (DW -12.4 ‰, RK -11.2 ‰) $\delta^{13}C_{DIC}$, but $\delta^{13}C_{DIC}$ at RK are all more ^{13}C-enriched and so the mean compositions are different (DW -14.0 ‰, RK -11.3 ‰). At DW the range of $\delta^{13}C_{DIC}$ extends lower than at RK (and RE), with DW having the most ^{13}C-depleted minimum $\delta^{13}C_{DIC}$ (-23.2 ‰) of all three sites, ~ 8 to 10 ‰ more depleted than the minimum at RK (-14.0 ‰) and RE (-14.8 ‰), which have similar minima. Although data is limited for RE, it has the largest range and most enriched $\delta^{13}C_{DIC}$ of all three sites, with 3 of 4 measurements being more ^{13}C-enriched than the maximum at DW and RK.

4.5.2 Catchment Controls on DIC Pool Composition

4.5.2.1 Identification of End-Members

Hydrochemical parameters (including [DIC] and $\delta^{13}C_{DIC}$) have been found to scale with measures of flow (see 4.3.2). Here [DIC] and $\delta^{13}C_{DIC}$ are plotted against the inverse of a measure of flow (specific discharge) as this approach allows the high-flow end-members to be estimated from where the relationships approach the y-axis. Specific discharge (discharge/catchment area) is used to enable direct comparison between DW and RK which have very different catchments sizes. Data are not available for RE as no gauging information is available at the site.

At DW and RK [DIC] and $\delta^{13}C_{DIC}$ correlate strongly with inverse specific discharge (Q_{sp}^{-1}) (Figure 34). At both sites [DIC] increases with Q_{sp}^{-1}, i.e. as discharge increases, [DIC] decreases (Figure 34a). $\delta^{13}C_{DIC}$ becomes less-depleted with increasing Q_{sp}^{-1}, i.e. as discharge increases, $\delta^{13}C_{DIC}$ becomes increasingly depleted (Figure 34b).

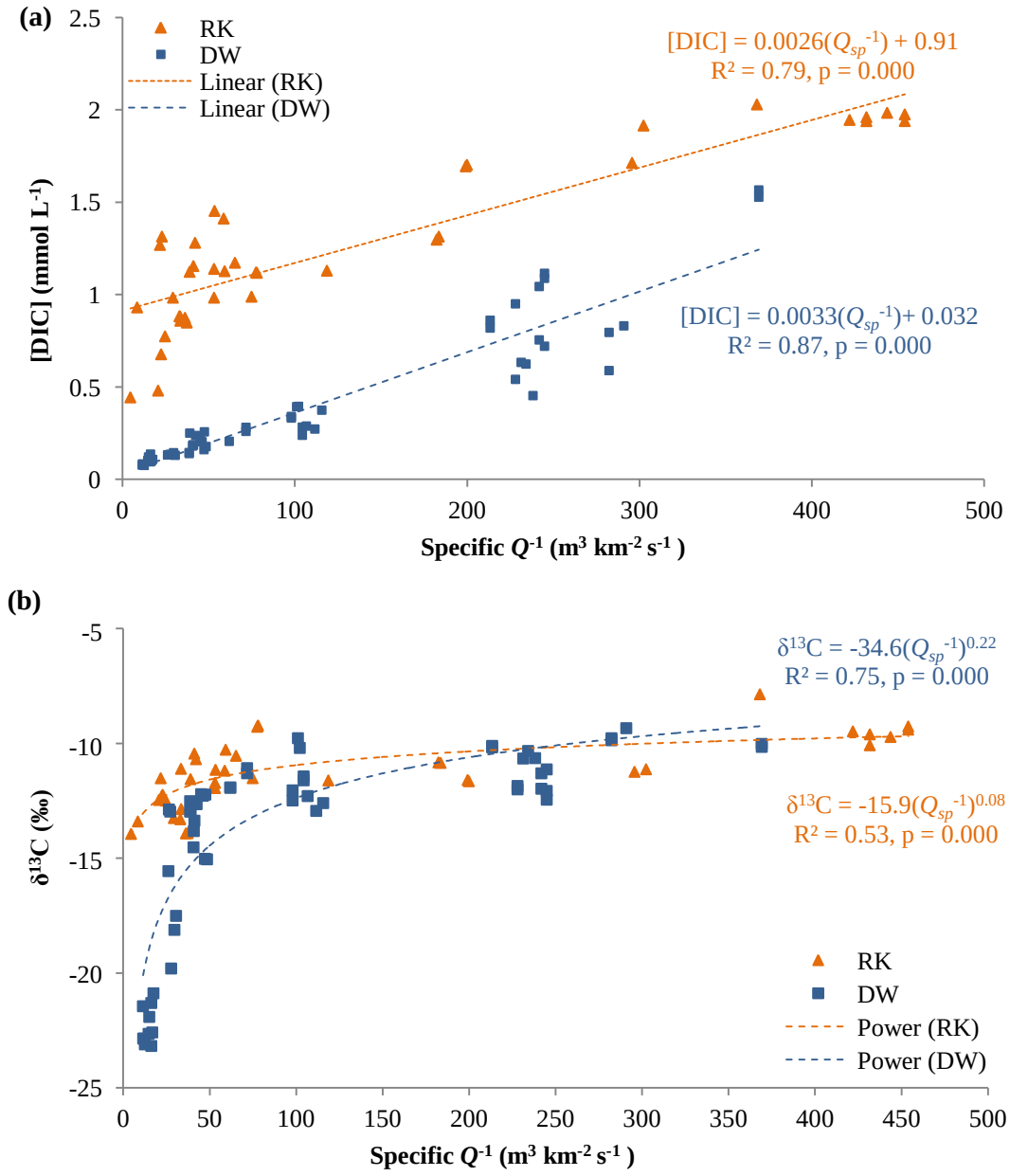

Figure 34: Relationships between inverse specific discharge and [DIC] and $\delta^{13}C_{DIC}$

Strong, highly significant, positive relationships exist at both sites between (a) inverse specific discharge and [DIC], and (b) inverse specific discharge and $\delta^{13}C_{DIC}$. Specific discharge = Q/catchment area. Q_{sp}^{-1} is used as an abbreviation for inverse specific discharge in the equations.

At low discharge (high Q_{sp}^{-1}), the relationships between [DIC] and specific discharge at DW and RK move close together, with [DIC] of similar magnitude at the two sites at the lowest sampled discharge. However, relationships and data do not overlap. The relationships between $\delta^{13}C_{DIC}$ and specific discharge at DW and RK converge at low flows at ~ -10 ‰, and data overlap.

At high discharge (low Q_{sp}^{-1}) the relationships at DW and RK diverge for both [DIC] and $\delta^{13}C_{DIC}$ relationships. The relationships are steeper at DW than at RK, with a greater decrease in [DIC] and $\delta^{13}C_{DIC}$ for a given increase in discharge at DW. At the highest sampled specific discharge [DIC] is an order of magnitude lower at DW than RK, with relationships approaching the y-axis at ~0.03 and ~0.9 mmol L^{-1} respectively. $\delta^{13}C_{DIC}$ is ~ 10 ‰ more depleted at DW than RK, with minimum measured values being ~ -23 ‰, and ~ -14 ‰ respectively.

Another method to consider end-member composition is the Keeling plot (Keeling, 1961). Keeling plots allow the $\delta^{13}C_{DIC}$ of groundwater to be estimated from where the relationships intercept the y-axis (Waldron *et al.*, 2007). Here a Keeling plot (Figure 35) reveals $\delta^{13}C_{DIC}$ correlates with the inverse of [DIC], ($[DIC]^{-1}$), at the main field sites, but not at RE where data points, although few, are widely spread and no relationship with $[DIC]^{-1}$ is apparent. Relationships at DW and RK are both linear and highly significant, at p = <0.001, but differ in strength and gradient. At DW the relationship is stronger (R^2 = 0.81 DW, 0.43 RK) and the gradient shallower (m = -1.13 DW, -2.48 RK) than at RK. Data from DW and RK overlap at the lower (y-axis) end, but data from RE are distinct. The relationships at the two sites converge at the y-axis with the intercept (thus ground water $\delta^{13}C_{DIC}$) being ~ 9 ‰ at DW and RK.

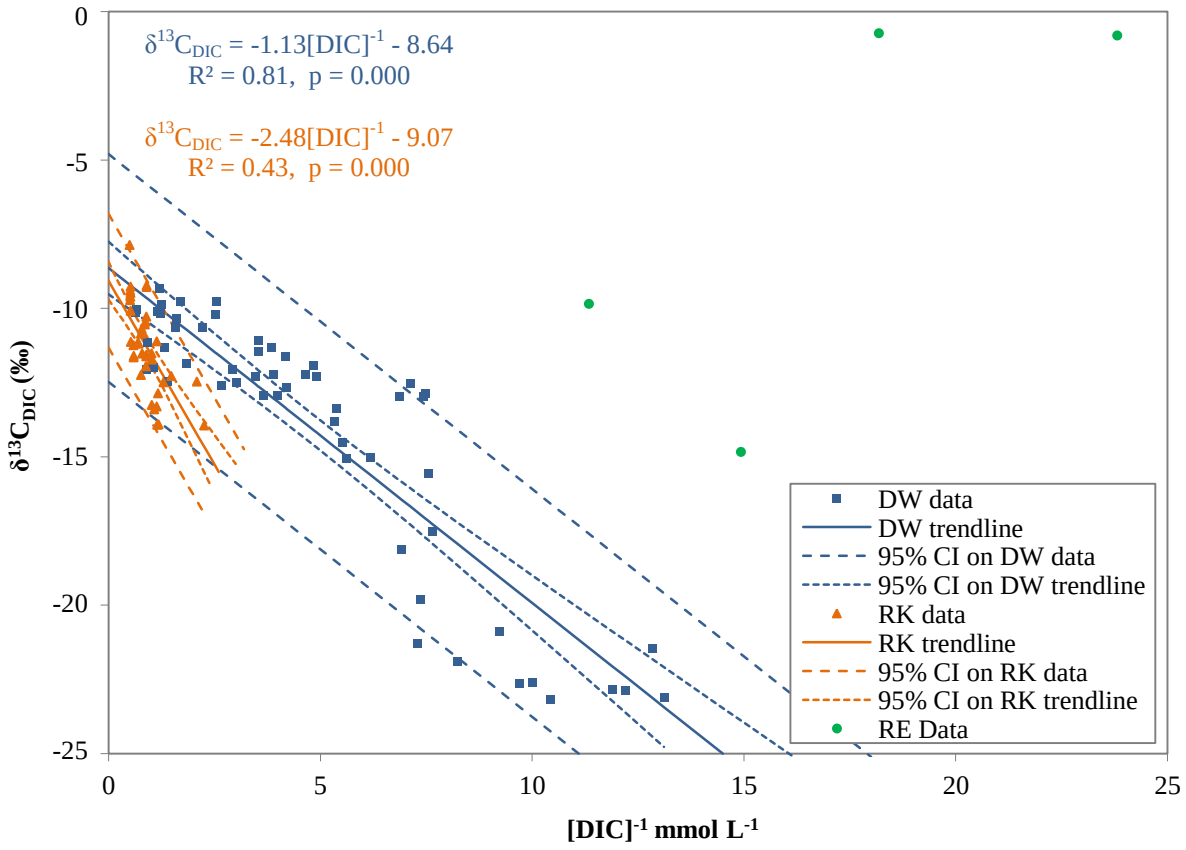

Figure 35: Keeling plot showing the relationship between the $[DIC]^{-1}$ and $\delta^{13}C_{DIC}$ at DW and RK
Strong, highly significant, linear relationships exist at DW and RK, but no relationship is apparent at RE.

4.5.2.2 End-Member Mixing

The mixing of carbon-pool end-members has been investigated by considering the relationship between $\delta^{13}C_{DIC}$ and [DIC] (Waldron *et al*, 2007). DW and RK $\delta^{13}C_{DIC}$ data correlate with [DIC] (Figure 36). The relationship is positive, and hyperbolic in shape, with $\delta^{13}C_{DIC}$ becoming more ^{13}C-enriched with an increase in [DIC], a result of both parameters interacting with flow (Figure 34) rather than a direct interaction. The limited data available for RE do not show a relationship between $\delta^{13}C_{DIC}$ and [DIC].

The low [DIC], ^{13}C-depleted component that occurs at high flow can be considered the high-flow end-member (HFEM), and the high [DIC], ^{13}C-enriched component that occurs at low flow can be considered the low-flow end-member (LFEM) (as in Waldron *et al*., 2007, and observed in Khadka *et al*., 2014). The hyperbolic shape of the relationship indicates mixing of the two end-members (e.g. Waldron et al., 2007). The LFEMs are very similar at the two sites, however the full hyperbolic shape is only apparent at DW.

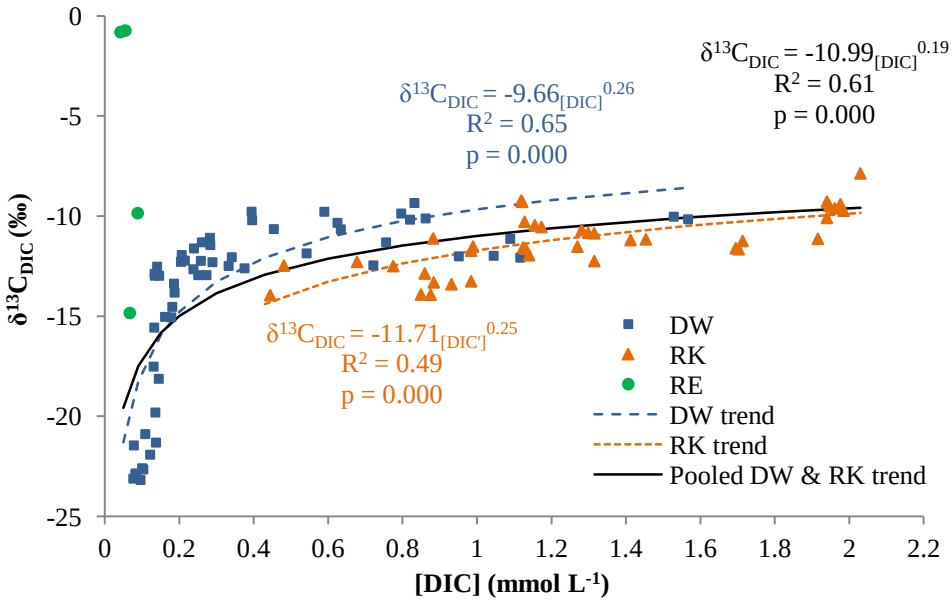

Figure 36: Relationship between $\delta^{13}C_{DIC}$ and [DIC]

Strong, highly significant positive relationships exist between $\delta^{13}C_{DIC}$ and [DIC] at DW and RK. Because data overlap well, the relationship of pooled DW and RK data has been included. No relationship is apparent between $\delta^{13}C_{DIC}$ and [DIC] at RE.

4.5.3 In-River Processes that Amend DIC Pool Composition

4.5.3.1 Diel Variation

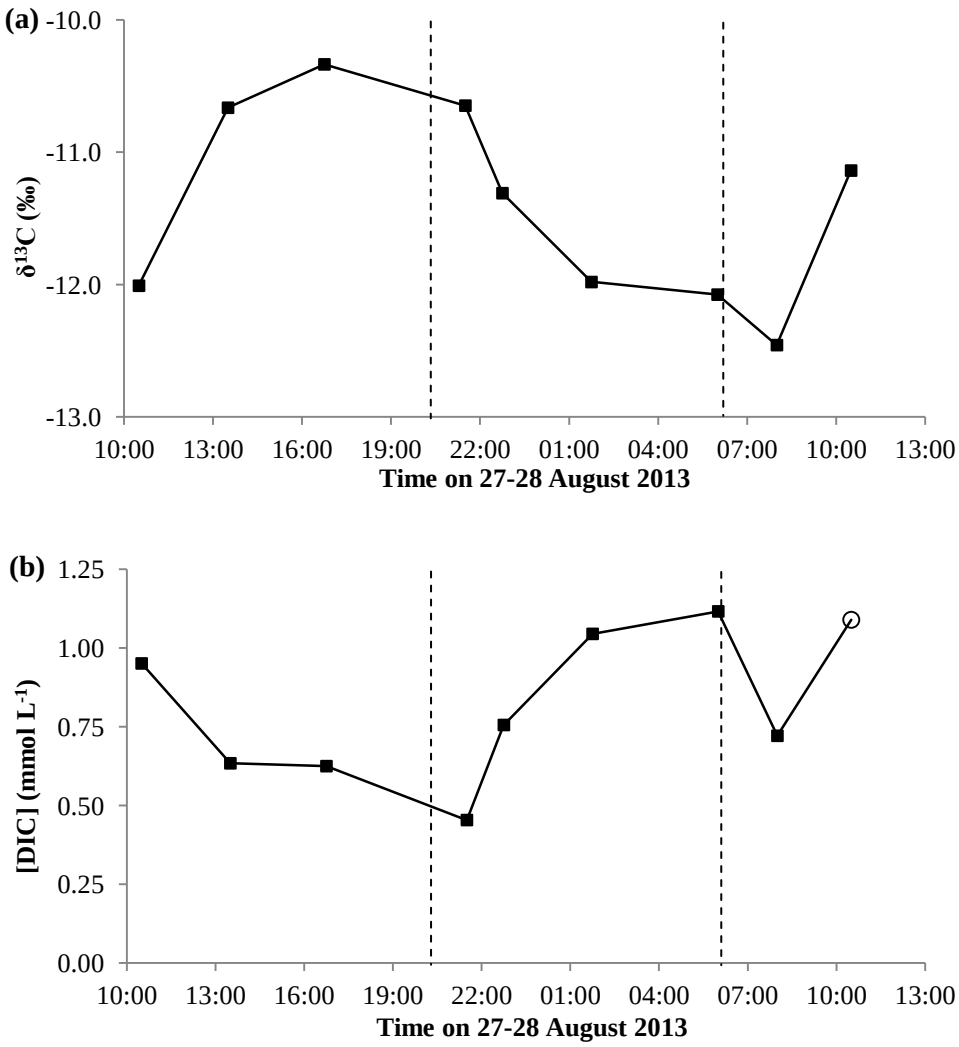

Figure 37: Diel variation in $\delta^{13}C_{DIC}$ and [DIC] at DW

Variation in (a) $\delta^{13}C_{DIC}$ and (b) [DIC] on 27th-28th August 2013, under stable and low flow conditions. The initial sampling time was repeated at the end of the 24-hour sampling regime to complete the cycle. Dashed lines represent sunset on 27th Aug-13 at 20:24 and sunrise on 28th Aug-13 at 06:14. The hollow circular data point does not fit the trend, but overall there is strong diel variation in (a) and (b).

$\delta^{13}C_{DIC}$ ranged by 2.1 ‰, between -12.5 ‰ and -10.3 ‰, and [DIC] ranged by 0.7 mmol L^{-1}, between 0.45 and 1.12 mmol L^{-1}, over a 24-hour period of stable flow (Figure 37). The most enriched $\delta^{13}C_{DIC}$ was at 16:45, and most depleted $\delta^{13}C_{DIC}$ was at 08:00. The highest [DIC] was at 06:00, and lowest [DIC] was at 21:30. A diel pattern is apparent in $\delta^{13}C_{DIC}$ and [DIC] data. $\delta^{13}C_{DIC}$ becomes ^{13}C-enriched over the daylight hours, then ^{13}C-depleted as the sun sets and during darkness, until soon after sunrise when $\delta^{13}C_{DIC}$ becomes ^{13}C-enriched again. [DIC] concentration decreases over the daylight light hours, then begins to increase after the sunsets and during darkness, until sunrise when [DIC] begins to fall again. The hollow circular data point does not fit the trend, but overall there is strong diel variation.

4.5.3.2 CO_2 Efflux

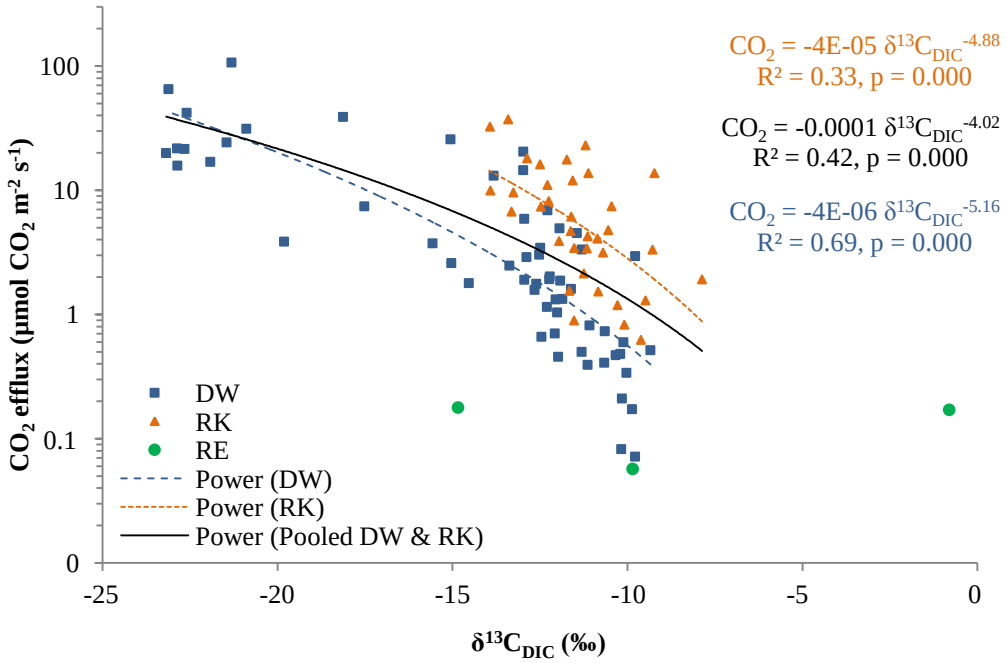

Figure 38: Relationship between $\delta^{13}C_{DIC}$ and CO_2 efflux

Significant relationships exist between $\delta^{13}C_{DIC}$ and CO_2 efflux at DW, and RK, individually or pooled but no relationship is apparent at RE.

Data from DW and RK show a negative correlation between $\delta^{13}C_{DIC}$ and CO_2 efflux, (Figure 38) indicating $\delta^{13}C_{DIC}$ becomes increasingly ^{13}C-depleted with increasing efflux rates. The correlation is stronger at DW (R^2 = 0.69 at DW and 0.33 at RK), but highly significant at both sites with p-values of <0.001, but the relationships are similar at the two sites with data partly overlapping. However the gradient of the relationship is steeper at DW and the $\delta^{13}C_{DIC}$ pool is more ^{13}C-depleted for a given efflux rate, particularly the higher efflux rates. Although there are limited data points, data from RE show no correlation between $\delta^{13}C_{DIC}$ and efflux, and a broad range of $\delta^{13}C_{DIC}$ at the low effluxes measured.

4.5.4 Modelling $\delta^{13}C_{DIC}$ and CO_2 Efflux

Strong and highly significant relationships exist at DW and RK between $\delta^{13}C_{DIC}$ and measures of flow and water chemistry that are pertinent to the inorganic carbon pool and commonly logged by hydrochemical sensors (summarised in Table 10, Figure 39, Figure 40). Such correlations can thus be used for modelling the source of carbon in a system. Hydrochemical parameters also have strong relationships with efflux at DW and RK (Table 10, Figure 41). Modelled efflux can be compared to modelled $\delta^{13}C_{DIC}$ to assess the relationship of the source of carbon to CO_2 efflux, and contemporaneous behaviour with hydrological variation. For RE either no data is available (Figure 39a, Figure 39b, Figure 41b, Figure 41c) or the limited data do not correlate with $\delta^{13}C_{DIC}$ and flow (Figure 39c, Figure 40a, Figure 40b, Figure 41a).

Table 10: Statistics of correlations between $\delta^{13}C_{DIC}$ and flow parameters and water chemistry at the main field sites*

Site	Correlations with $\delta^{13}C_{DIC}$					Correlations with Efflux	
	Q	Stage Height	$\bar{u}$	pH	Alkalinity	pH	Stage Height
DW	0.75 0.000	0.89 0.000	0.79 0.000	0.89 0.000	0.74 0.000	0.62 0.000	0.64 0.000
RK	0.53 0.000	0.53 0.000	0.36 0.000	0.28 0.000	0.60 0.000	0.29 0.000	0.49 0.000

*Top row = R^2, bottom row = p-value. All relationships, except $\bar{u}$, are considered as power-functions due to positive skew of parameters. $\bar{u}$ is not skewed and a linear relationship is the best fit for the data. RE not included as either insufficient data points or no correlation existed.

4.5.4.1 Relationships Between $\delta^{13}C_{DIC}$ and Flow Parameters

$\delta^{13}C_{DIC}$ data from DW and RK correlates with a number of measures of flow: discharge, stage height and flow intensity (for which mean velocity is used as a proxy; Long et al., 2015 and Chapter 3) (Table 10, Figure 39). The measures of flow are auto-correlated (Appendix F), but included to demonstrate the relationship with $\delta^{13}C_{DIC}$ across scales. In all instances: (i) relationships are negative, with $\delta^{13}C_{DIC}$ becoming more ^{13}C-depleted with increasing flow; (ii) data from the three sites has little overlap; and, (iii) relationships are stronger and gradients steeper at DW.

Convergence of stage height (Figure 39b) and mean velocity (Figure 39c) relationships at the two sites at low flow (as observed in Figure 34), supports the interpretation $\delta^{13}C_{DIC}$ pool in the two rivers has a similar composition at the lowest flows. Similarly increasing divergence in $\delta^{13}C_{DIC}$ between rivers with increasing flow indicates that the high flow end-member has a different composition.

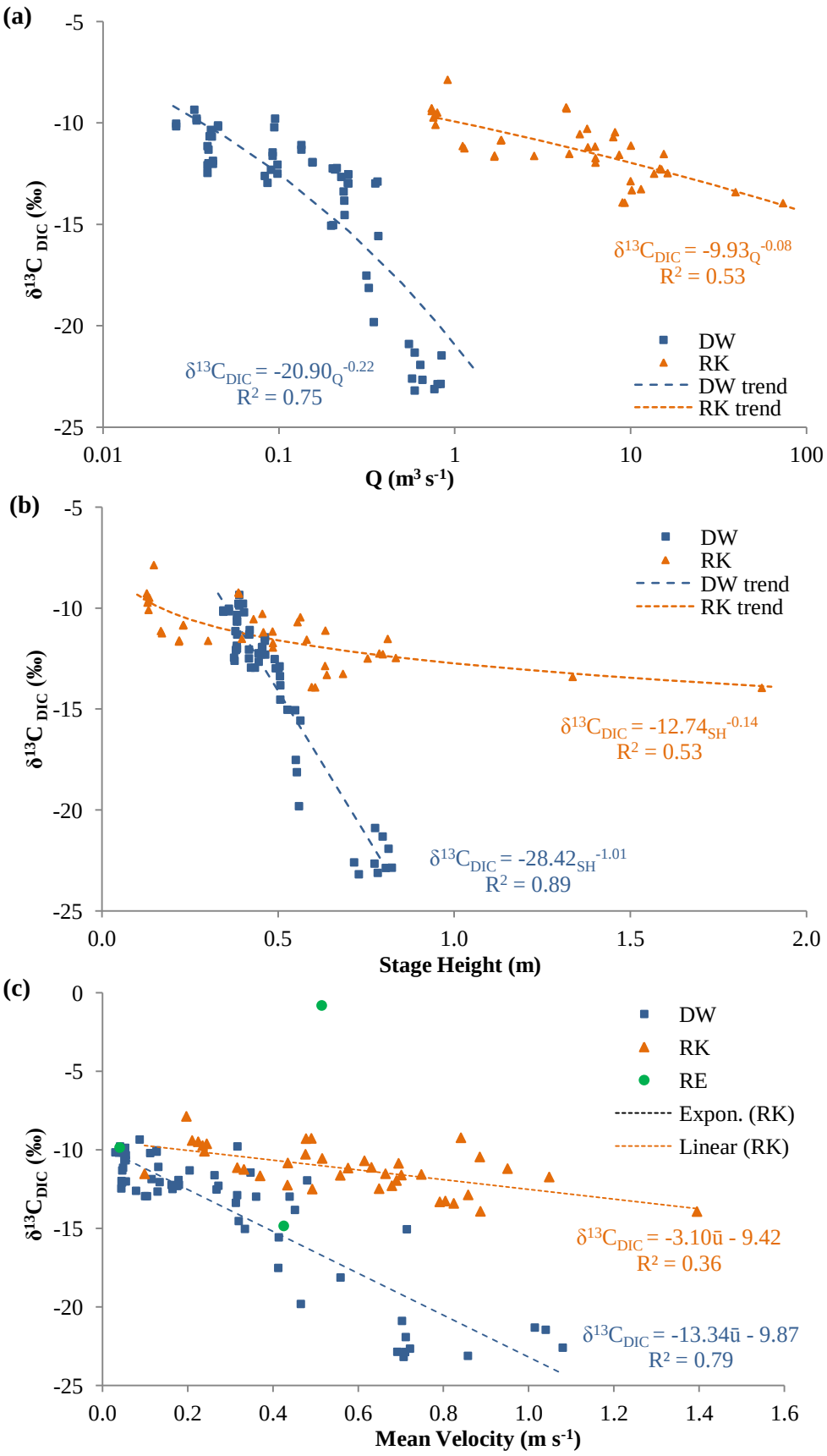

Figure 39: Relationship between $\delta^{13}C_{DIC}$ and measures of flow

$\delta^{13}C_{DIC}$ (‰) as a function of (a) discharge (with log scale), (b) stage height (relationship used for modelling, see 4.5.4.4) and (c) mean velocity. Strong, highly significant negative relationships are seen with $\delta^{13}C_{DIC}$ at DW and RK (see Table 10 for statistical significance values).

4.5.4.2 Relationships Between $\delta^{13}C_{DIC}$ and Water Chemistry Parameters

DW and RK $\delta^{13}C_{DIC}$ data correlate with pH, alkalinity (Table 10, Figure 40) and [DIC] (Figure 36). pH, alkalinity and [DIC] are auto-correlated and correlate with flow (Appendix G). As with [DIC]-$\delta^{13}C_{DIC}$ relationships (section 4.5.2.2), relationships between pH and alkalinity and $\delta^{13}C_{DIC}$ are: (i) positive with $\delta^{13}C_{DIC}$ becoming more ^{13}C-enriched with an increase in pH and alkalinity; (ii) curved to hyperbolic; (iii) RK and DW responses overlap; and, (iv) relationships are stronger and gradients slightly steeper at DW. Because data overlap well, the relationship of pooled DW and RK data has been included to generate an inter-site response. The limited data available for RE do not show relationships between $\delta^{13}C_{DIC}$ and water chemistry. $\delta^{13}C_{DIC}$ does not show a relationship with water temperature at any site.

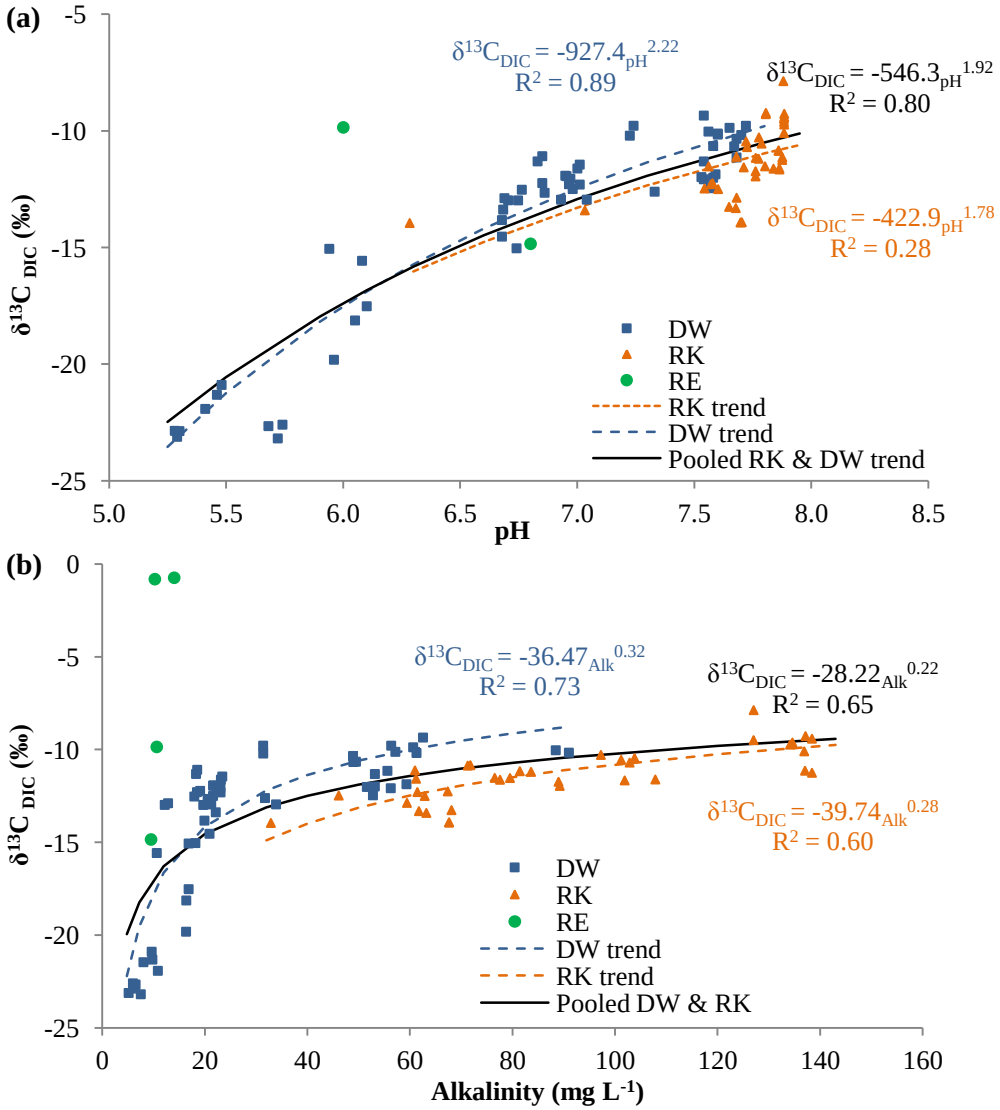

Figure 40: Relationship between $\delta^{13}C_{DIC}$ and influential DIC water chemistry parameters

$\delta^{13}C_{DIC}$ (‰) as a function of (a) pH (relationship used for modelling, see 4.5.4.4) and (b) alkalinity. Strong, highly significant, positive relationships are seen with water chemistry parameters at DW and RK (see Table 10 for statistical significance values), but not at RE.

4.5.4.3 Relationship Between CO_2 Efflux and Hydrochemical Parameters

Relationships exist between CO_2 efflux and pH and stage height (Figure 41). A strong (R^2 = 0.62), highly significant (p = <0.001), negative relationship exists between pH and CO_2 efflux at DW, whereby CO_2 efflux increases with decreasing pH. At RK the relationship is weaker (R^2 = 0.29), and no such relationship exists at RE (Figure 41a). A strong (R^2 = 0.64 DW, 0.49 RK), highly significant (p = <0.001 DW and RK), negative relationship exists between stage height and CO_2 efflux at both DW and RK, with CO_2 increasing with increasing stage height (Figure 41b). Data from the two sites overlaps, with the relationship stronger and gradient steeper at DW.

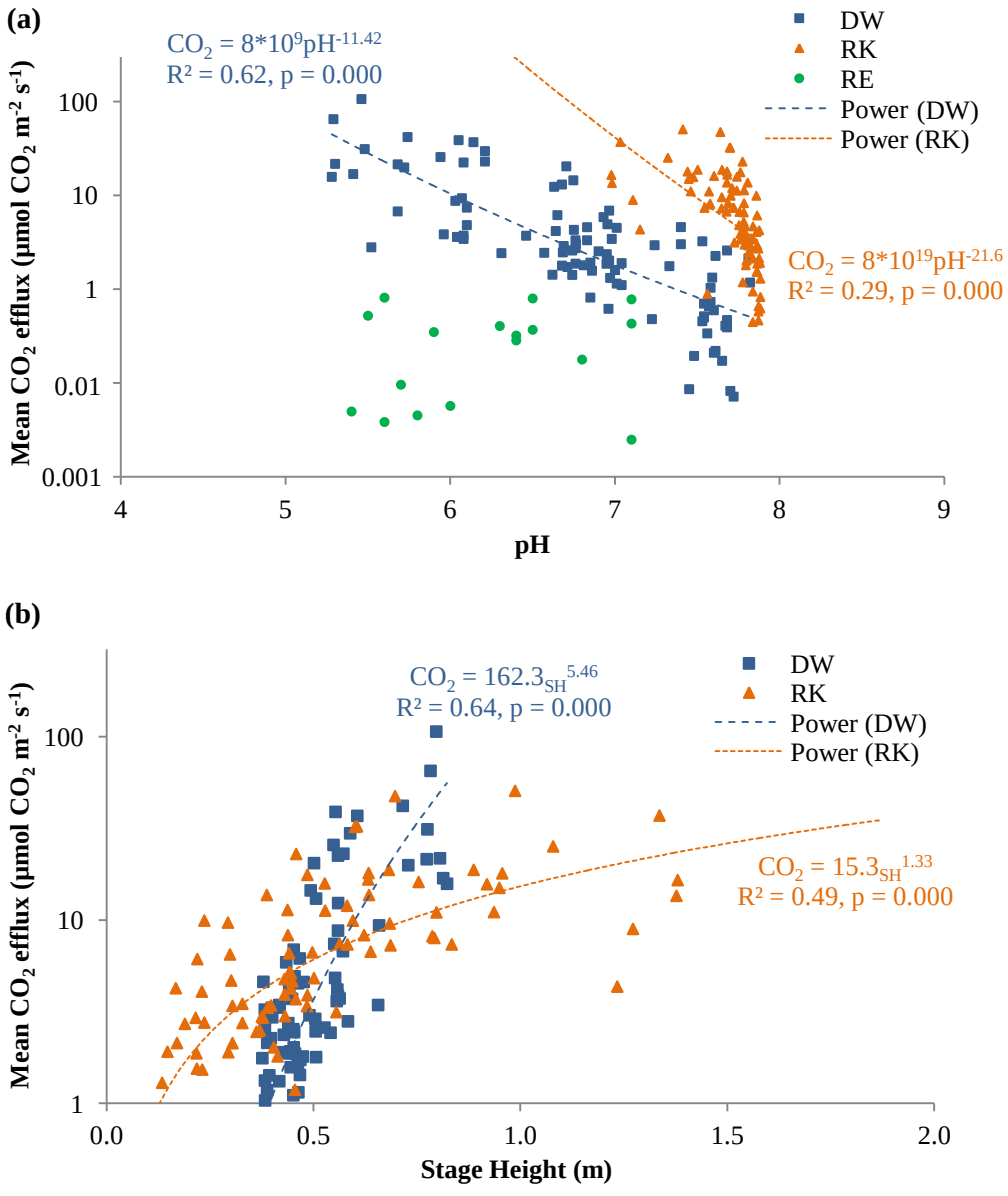

Figure 41: Relationship between CO_2 efflux and pH and stage height

(a) A strong, highly significant, negative relationship exists between pH and CO_2 efflux at DW (used for modelling, see 4.5.4.4). (b) A strong, highly significant, positive relationship exists between stage height and CO_2 efflux at DW. Efflux is displayed on a log scale.

4.5.4.4 Modelling of $\delta^{13}C_{DIC}$ and CO_2 Efflux at DW from pH and Stage Height

At DW, logged pH and stage height show the strongest relationships with $\delta^{13}C_{DIC}$ (Table 10), with the least scatter (Figure 39, Figure 40) and so these relationships have been selected to model $\delta^{13}C_{DIC}$. pH and stage height also have good relationships with CO_2 efflux (Table 10) and pH has been used to model CO_2 efflux. All models have the smallest 95% confidence intervals at high pH and low stage height, which occur under low flow conditions, and confidence intervals are largest under high flow conditions when low pH and high stage height occur (Figure 42). pH and stage height $\delta^{13}C_{DIC}$ models have very similar uncertainties: ~3.5 ‰ at highest/lowest measured pH/stage height, respectively, and ~8 ‰ at lowest/highest measured pH/stage height, respectively (Figure 42a, Figure 42b). Uncertainties on efflux are greater, up to 287 µmol CO_2 m^{-2} s^{-1} at the lowest sampled pH when flows and efflux are highest, but much reduced under low flow conditions when pH is high and efflux rate low (3.2 µmol CO_2 m^{-2} s^{-1} at the highest measured pH) (Figure 42c). For all relationships, data separate by visual water surface state, which is a proxy for turbulence, but this is particularly apparent for the pH-efflux relationship (Figure 42c).

When comparing measured $\delta^{13}C_{DIC}$ and CO_2 efflux values against modelled values (Figure 43), data for both parameters is scattered around the 1:1 line (the model), but the models show reasonable agreement with the measured data. $\delta^{13}C_{DIC}$ data show less scatter than the efflux data, with the majority of $\delta^{13}C_{DIC}$ data falling within +/- 15% of the 1:1 line (the model), indicating this model explains the data better. This is to be expected as the efflux-pH relationship has more uncertainty than the $\delta^{13}C_{DIC}$-pH and $\delta^{13}C_{DIC}$- stage height relationships.

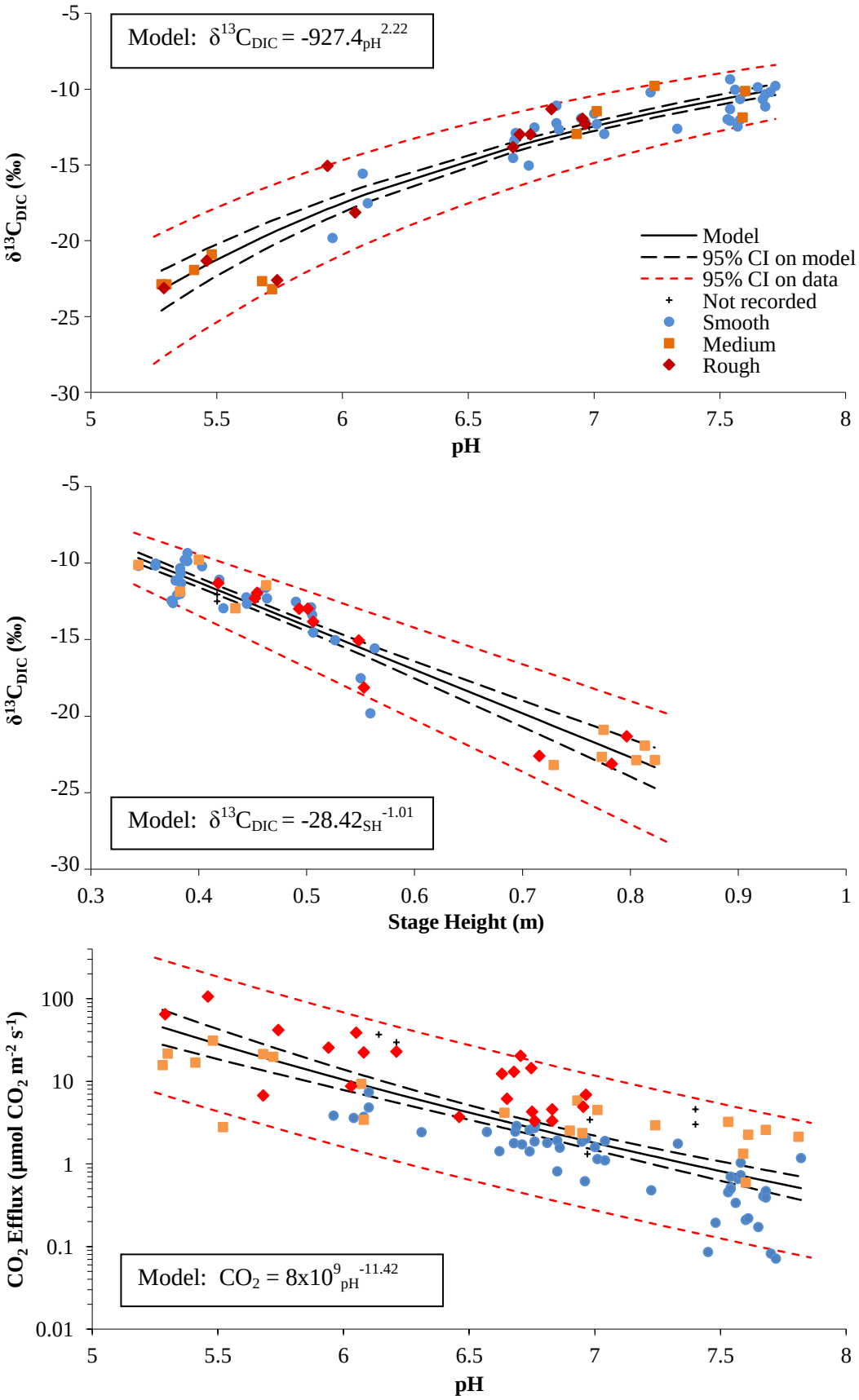

Figure 42: $\delta^{13}C_{DIC}$ and efflux model confidence intervals

95% confidence intervals for (a) $\delta^{13}C_{DIC}$–pH, (b) $\delta^{13}C_{DIC}$–stage height, and (c) Efflux–pH models and datasets, for DW. Efflux displayed on a log scale. The legend is the same for all three graphs.

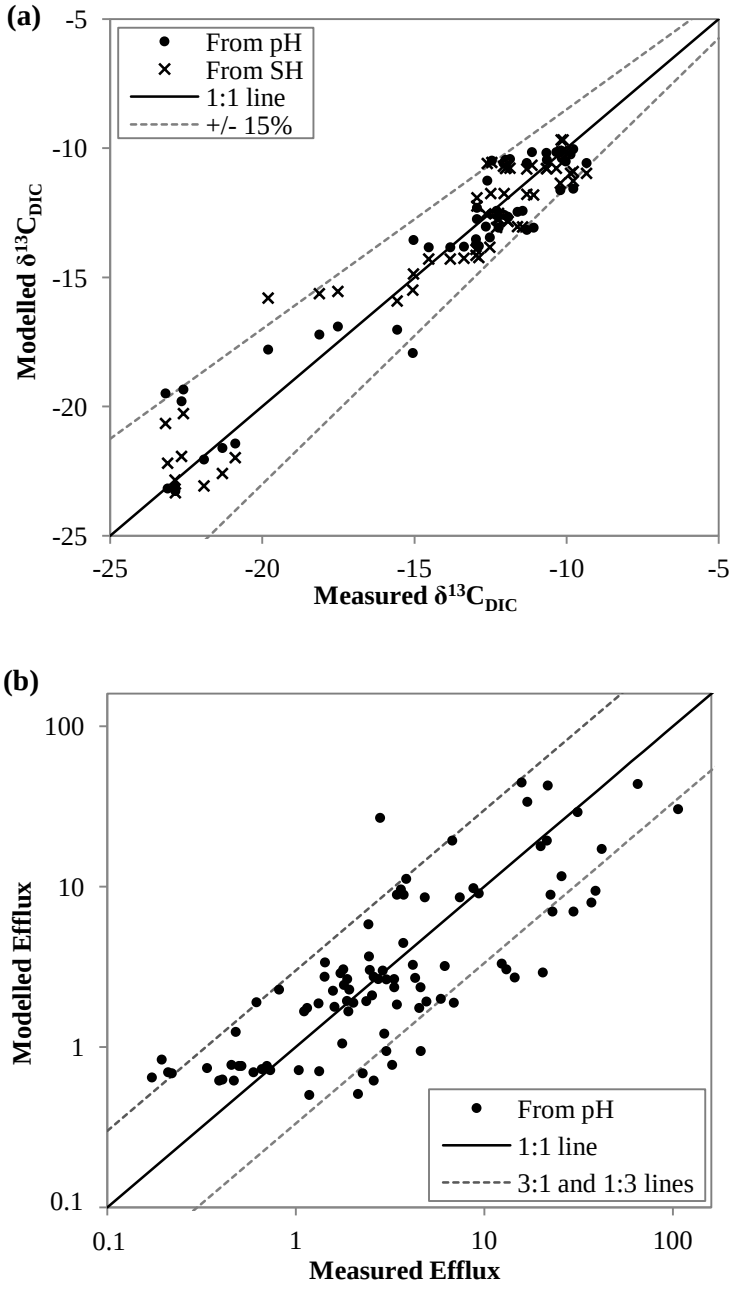

Figure 43: Comparison of measured and modelled $\delta^{13}C_{DIC}$ and efflux data

Comparison of measured and modelled (a) $\delta^{13}C_{DIC}$ (‰) and (b) CO_2 efflux rate (µmol CO_2 m^{-2} s^{-1}). The majority of $\delta^{13}C_{DIC}$ data fall within +/- 15% of the 1:1 line; the majority of efflux data fall within 3 times greater or smaller than the 1:1 line. SH = stage height. Efflux displayed on a log-log scale. Influx not included.

4.5.5 Reconstruction of $\delta^{13}C_{DIC}$ and Efflux over three Hydrological Years

Using the pH-$\delta^{13}C_{DIC}$ and $\delta^{13}C_{DIC}$-stage height models the DW pH and stage height time series can be used to reconstruct continuous $\delta^{13}C_{DIC}$ for the hydrological years 2011 –12, 2012-13 and 2013-14 (Figure 44 and Figure 45). Both models are considered to explore the robustness and weaknesses in these approaches. For example although pH is a more direct representation of the DIC pool, it may not be logged at all sites and so it is worth considering other commonly-logged parameters, such as stage height as possibilities for reconstruction.

The pH and stage height reconstructions are generally very similar with both showing maximum ^{13}C-depletion during high flow events (represented by peaks in stage height time series data), and ^{13}C-enrichment during low flow. Uncertainties (represented by 90% confidence intervals) are also very similar between reconstructions. However, at low flow reconstructed $\delta^{13}C_{DIC}$ is very similar between models, but at peak event flow, $\delta^{13}C_{DIC}$ can vary by up to 13 ‰ between models for brief periods of time, with neither model being consistently higher or lower than the other (Figure 46).

The models also differ is in their manifestation of diel variation. In the pH-$\delta^{13}C_{DIC}$ reconstruction there are multiple occasions where rapid, up to ~ 5 ‰ diel variation in $\delta^{13}C_{DIC}$ occurs (e.g. Jun-12, early Apr-13, mid Jun-13, end Apr-14, mid-late Sep-14; Figure 44). It occurs only during relatively long periods of low flow in late spring to early autumn, and not in winter low flow periods (e.g. Nov-11, Jan-13, early Mar-13, end Nov-13). In contrast, stage height reconstructions do not display any periods of diel variation in $\delta^{13}C_{DIC}$ (Figure 45), suggesting the predominant causes of diel variation in stream flow in temperate regions (evapotranspiration, snow-melt and loss of water from infiltration through the streambed; Nimik *et al*., 2011) are not prevalent here. pH may therefore be preferable to stage height as a DIC predictor, however stage height (which is routinely measured at high resolution) remains included as an alternative when pH is not available.

Using the pH-efflux model, efflux for the three HYs was also constructed from logged DW pH (Figure 47). Maxima in the efflux rate can be seen during high flow events (coinciding with depleted $\delta^{13}C_{DIC}$). During large flow events, these efflux maxima are modelled to be up to 292 µmol CO_2 m^{-2} s^{-1}, beyond what would be expected for rivers/streams globally (-0.2 to 135 µmol CO_2 m^{-2} s^{-1}, Long *et al*., 2015). Reconstructed efflux during smaller events or lower, more stable flow, is within the expected range. Uncertainties are largest at high flow (section 4.5.4.4) and larger than for $\delta^{13}C_{DIC}$ reconstructed data. As with pH-$\delta^{13}C_{DIC}$, diel variation (of up to ~ 3 µmol CO_2 m^{-2} s^{-1}) can also be seen in reconstructed CO_2 efflux during late-spring to early-autumn periods of low flow (e.g. Jun-12, early Apr-13, mid Jun-13, end Apr-14, mid-late Sep-14), and coincides directly with diel cycling of aquatic ^{13}C. It should be noted that both parameters were reconstructed from the same pH data, however other possible reasons for co-variation in these parameters will be discussed.

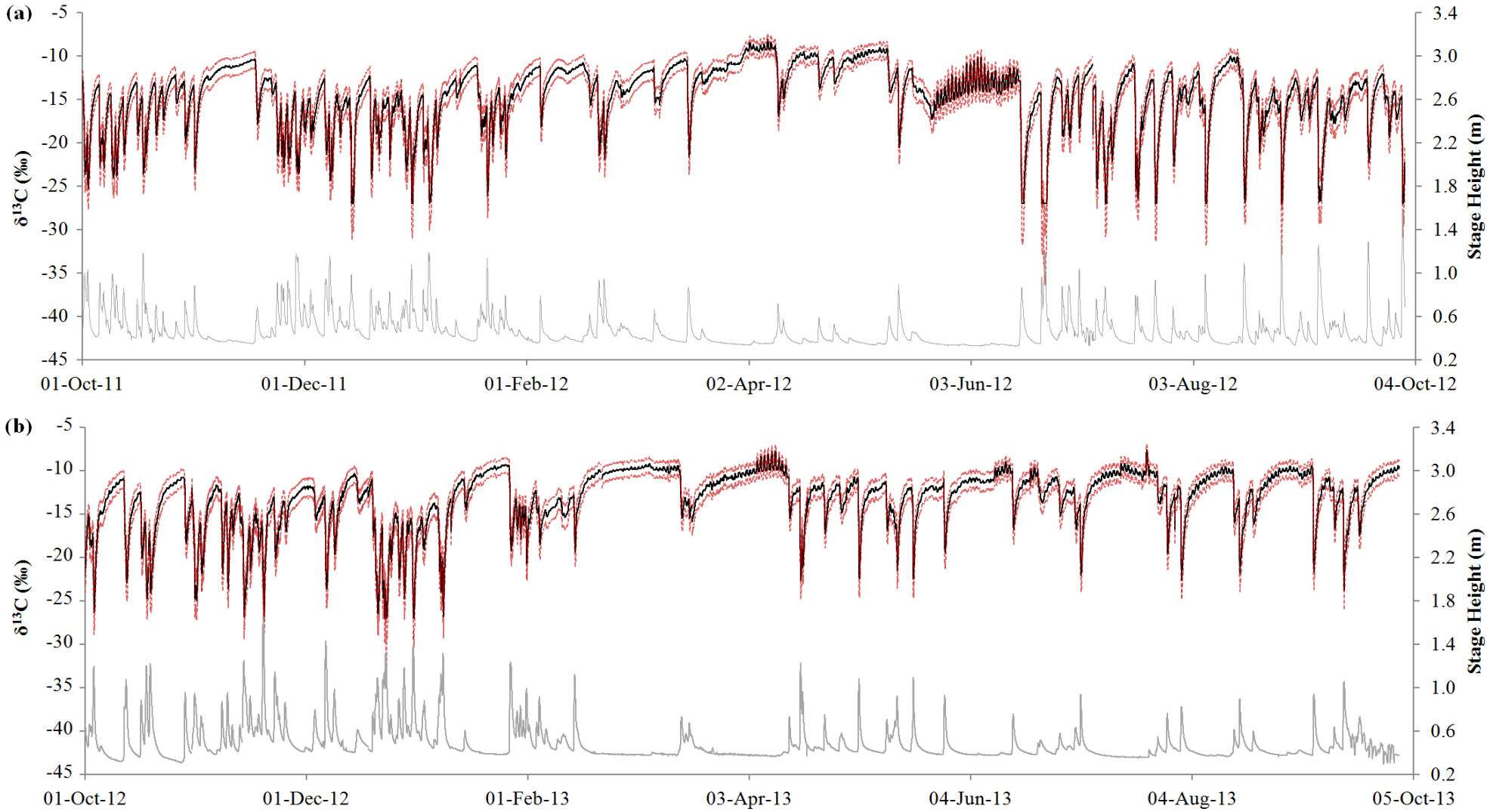
(a)
δ13C (‰)
-5
-10
-15
-20
-25
-30
-35
-40
-45
Stage Height (m)
3.4
3.0
2.6
2.2
1.8
1.4
1.0
0.6
0.2
01-Oct-11
01-Dec-11
01-Feb-12
02-Apr-12
03-Jun-12
03-Aug-12
04-Oct-12
(b)
δ13C (‰)
-5
-10
-15
-20
-25
-30
-35
-40
-45
Stage Height (m)
3.4
3.0
2.6
2.2
1.8
1.4
1.0
0.6
0.2
01-Oct-12
01-Dec-12
01-Feb-13
03-Apr-13
04-Jun-13
04-Aug-13
05-Oct-13

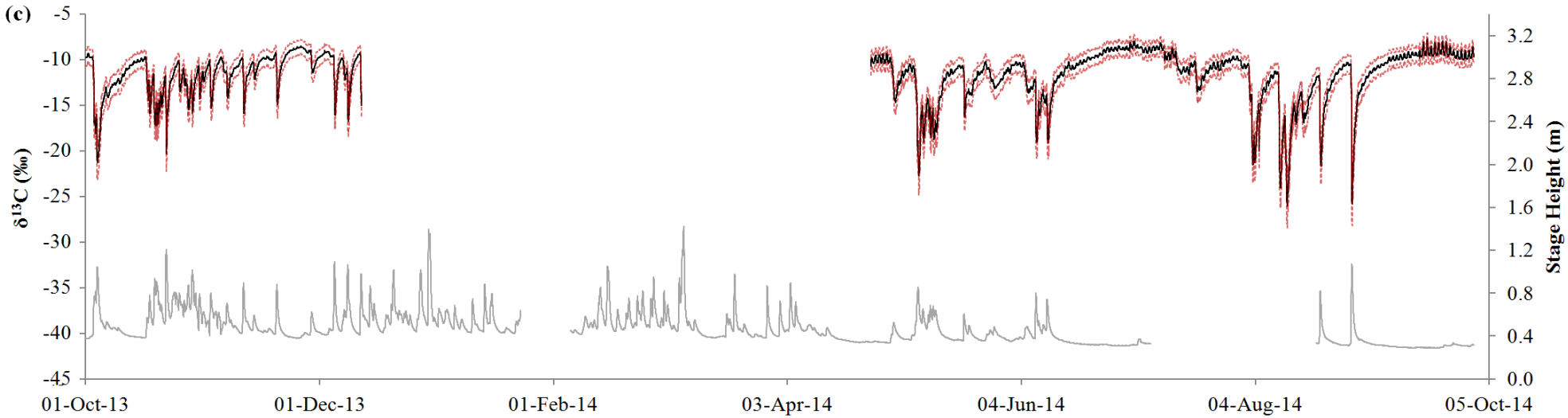

Figure 44: Reconstruction of $\delta^{13}C_{DIC}$ from the relationship with pH

For the three HYs covering the period of this study; (a) 2011-12, (b) 2012-13, (c) 2013-14. Solid black line = reconstructed $\delta^{13}C_{DIC}$, dotted red line = 90% confidence intervals on reconstructed data, solid grey line = stage height as hydrological time series. Reconstruction was not possible for Dec-13 to Apr-14 as no pH data was available.

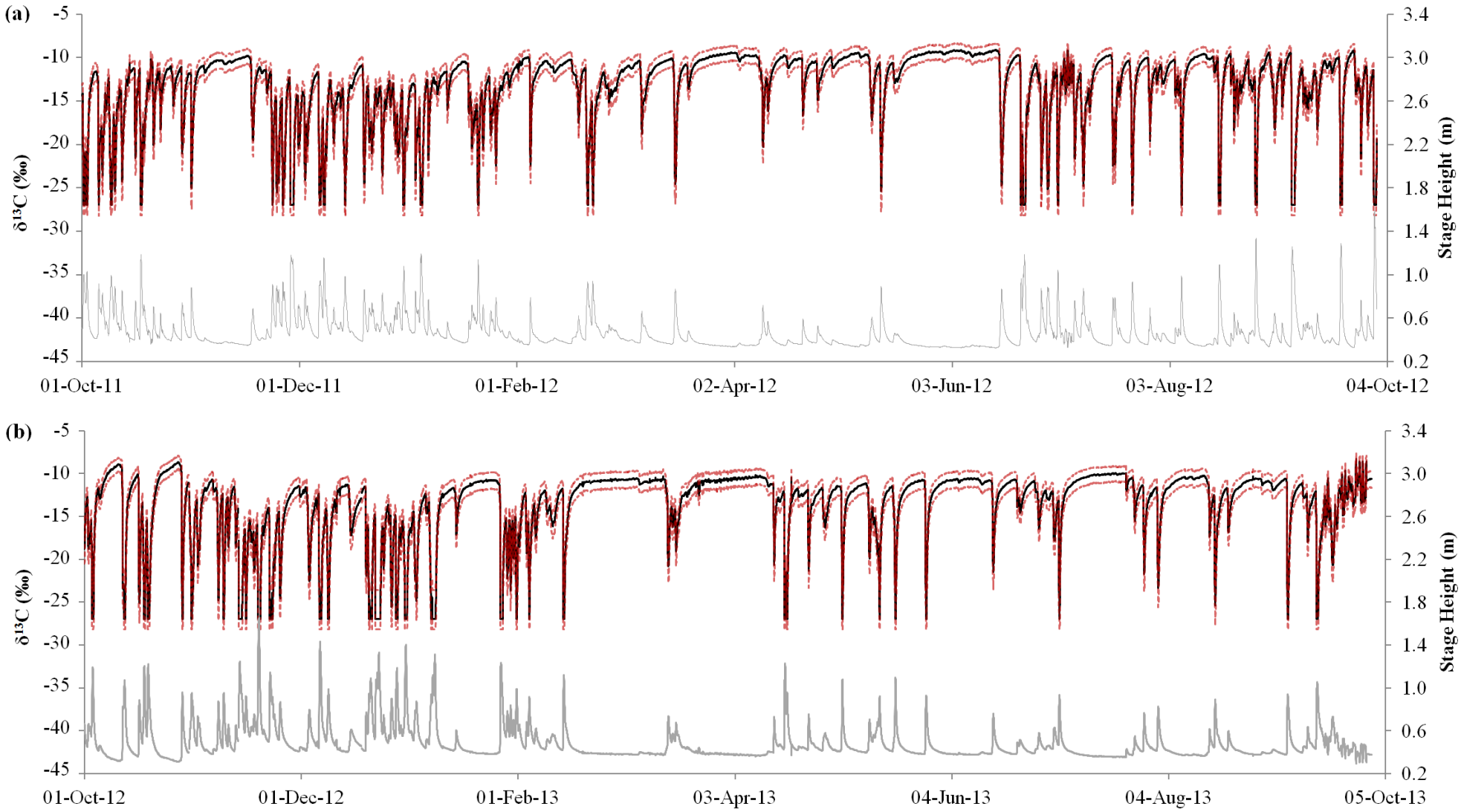
(a)
δ13C (‰)
-5
-10
-15
-20
-25
-30
-35
-40
-45
Stage Height (m)
3.4
3.0
2.6
2.2
1.8
1.4
1.0
0.6
0.2
01-Oct-11
01-Dec-11
01-Feb-12
02-Apr-12
03-Jun-12
03-Aug-12
04-Oct-12
(b)
δ13C (‰)
-5
-10
-15
-20
-25
-30
-35
-40
-45
Stage Height (m)
3.4
3.0
2.6
2.2
1.8
1.4
1.0
0.6
0.2
01-Oct-12
01-Dec-12
01-Feb-13
03-Apr-13
04-Jun-13
04-Aug-13
05-Oct-13

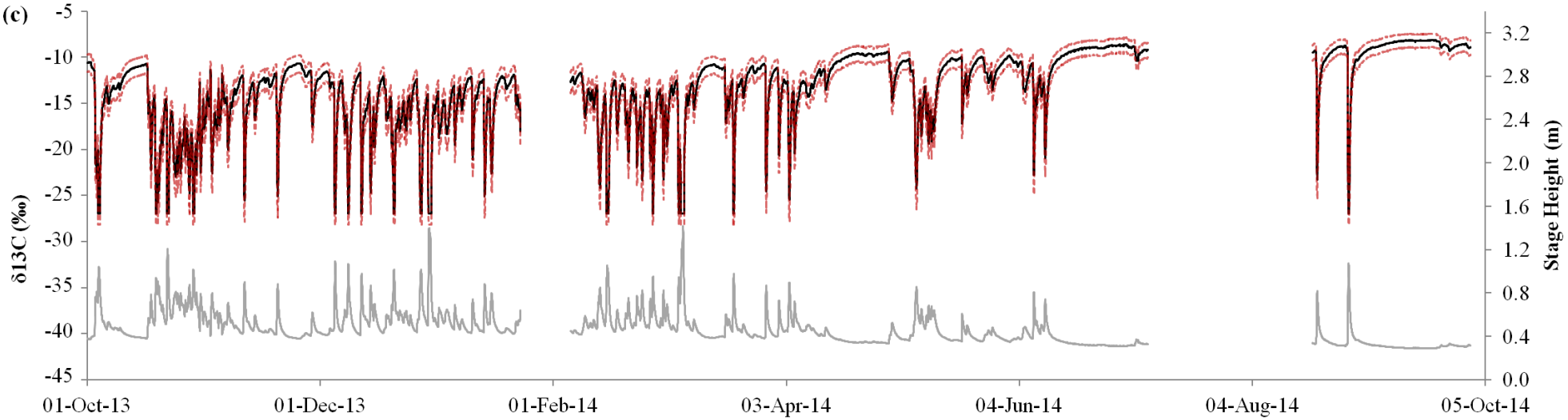

Figure 45: Reconstruction of $\delta^{13}C$ from the relationship with stage height

For the three HYs covering the period of this study; (a) 2011-12, (b) 2012-13, (c) 2013-14. Solid black line = reconstructed $\delta^{13}C_{DIC}$, dotted red line = 90% confidence intervals on reconstructed data, solid grey line = stage height as hydrological time series. Reconstruction not possible for end Jan-13 to early Feb-14, or July to Aug-14, as no stage height data was available.

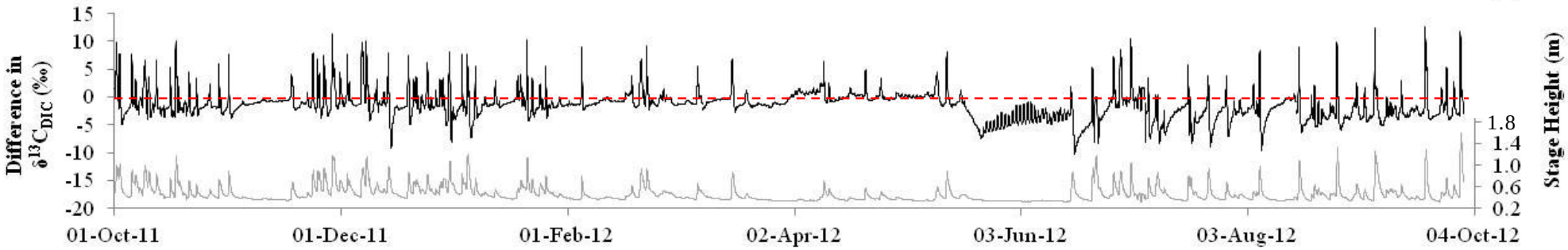

Figure 46: Difference between pH-reconstructed $\delta^{13}C_{DIC}$ and stage height reconstructed $\delta^{13}C_{DIC}$ for hydrological year 2011-12

Calculated as pH reconstruction minus stage height reconstruction. Black line = difference between reconstructions, red dashed line = zero/model agreement, grey line = stage height as hydrological time series.

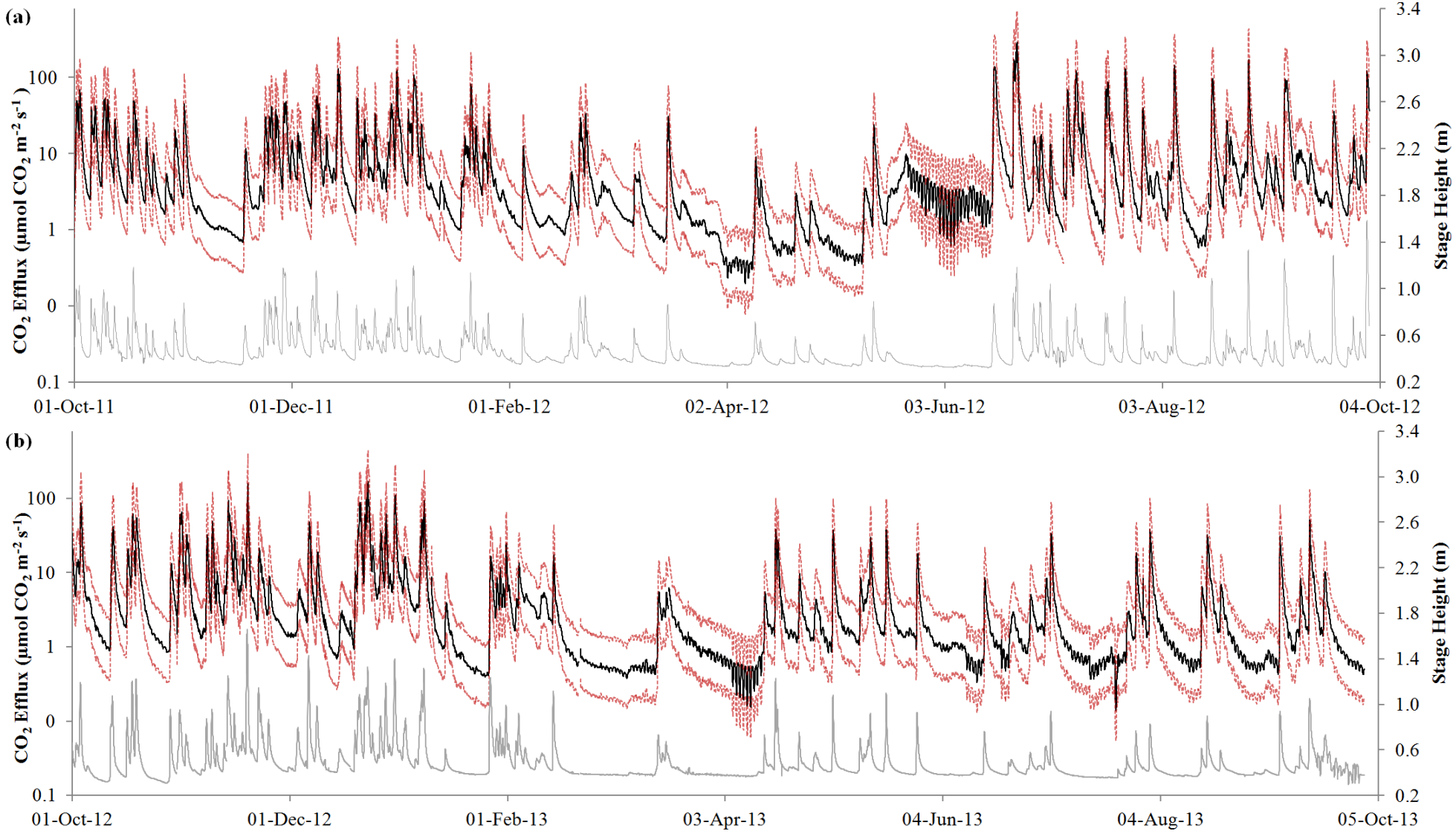
(a)
CO_2 Efflux (µmol CO_2 m^{-2} s^{-1})
100
10
1
0
0.1
Stage Height (m)
3.4
3.0
2.6
2.2
1.8
1.4
1.0
0.6
0.2
01-Oct-11
01-Dec-11
01-Feb-12
02-Apr-12
03-Jun-12
03-Aug-12
04-Oct-12
(b)
CO_2 Efflux (µmol CO_2 m^{-2} s^{-1})
100
10
1
0
0.1
Stage Height (m)
3.4
3.0
2.6
2.2
1.8
1.4
1.0
0.6
0.2
01-Oct-12
01-Dec-12
01-Feb-13
03-Apr-13
04-Jun-13
04-Aug-13
05-Oct-13

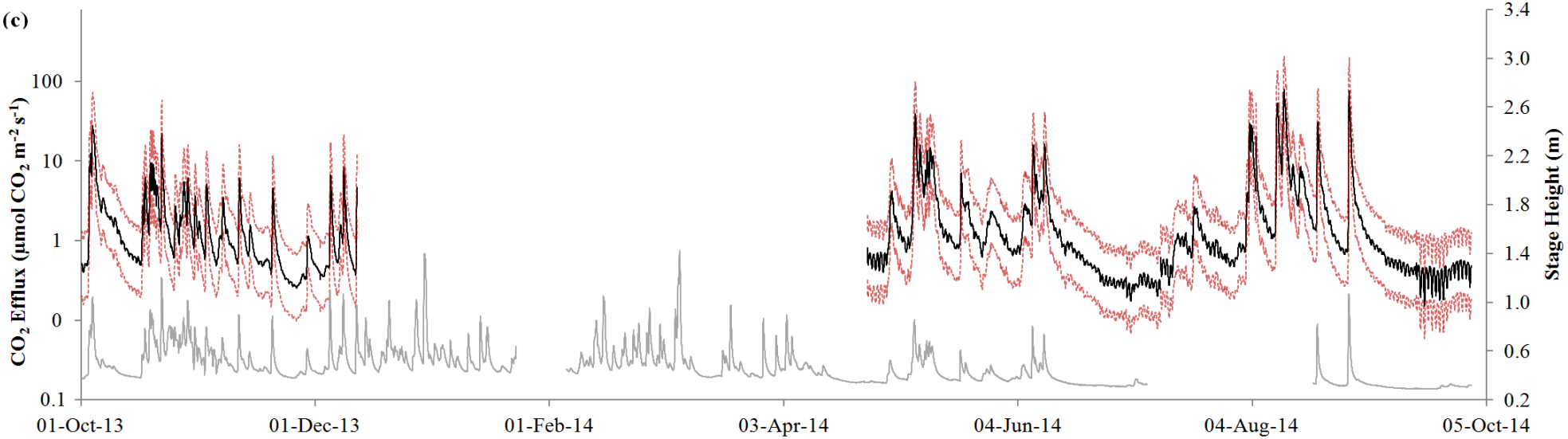

Figure 47: Reconstruction of CO_2 efflux from the relationship with pH

For the three HYs covering the period of this study; (a) 2011-12, (b) 2012-13, (c) 2013-14. Solid black line = reconstructed CO_2 efflux, dotted red line = 90% confidence intervals on reconstructed data, solid grey line = stage height as hydrological time series. Reconstruction was not possible for Dec-13 to Apr-14 as no pH data was available. Efflux is displayed on log scale.

Table 11: Ranges of reconstructed $\delta^{13}C_{DIC}$ for each hydrological year*

	$\delta^{13}C_{DIC}$ (‰)						CO_2 Efflux			
	From pH Reconstruction			From SH Reconstruction			From pH Reconstruction			
Hydrological Year	Min	Max	Range	Min	Max	Range	Min	Max	Range	Annual Total
2011-2012	-27	-8	19	-27	-9	18	0.2	292	292	11.9
2012-2013	-27	-8	19	-27	-8	19	0.1	169	169	6.7
2013-2014	*-26*	*-8*	*18*	*-27*	*-8*	*19*	*0.2*	*80*	*79*	*3.4**

*SH = stage height. Efflux in µmol CO_2 m^{-2} s^{-1}. Annual total CO_2 efflux in kg CO_2 m^{-2} y^{-1}. Values in italics indicate data was missing for part of the reconstruction. *Accounts for missing data by extrapolating data from 232 days to 365 days (method = (232 day total efflux/232)*365).

Ranges in reconstructed $\delta^{13}C_{DIC}$ are very similar between models and across HYs (Table 11). Minimum values are mostly identical across reconstructions and HYs at -27 ‰ (due to the model capping any generated values < -27 ‰), as are maximum values at -8 to -9 ‰ across all reconstructions and HYs. There are large differences in the ranges in reconstructed CO_2 efflux between HYs. The minimum reconstructed efflux rate is very similar between HYs, but the maximum rate varies by up to 212 µmol CO_2 m^{-2} s^{-1} (a 73% difference). Total annual efflux varies by 8.5 kg CO_2 m^{-2} y^{-1} (71%) between all HYs, and total efflux is highest in HY 2011-12 when the maximum efflux rate is highest.

Duration curves reveal further detail of inter-annual variation in modelled CO_2 efflux and $\delta^{13}C_{DIC}$ (Figure 48b and 17c). As both are linked to hydrology, a discharge duration curve is included for comparison (Figure 48a). All HYs show a high percentage occurrence of low discharge, low efflux and mid-range $\delta^{13}C_{DIC}$, compared to high discharge, high efflux and extremes (in context of this range) of $\delta^{13}C_{DIC}$, which occur only a small proportion of the time. At the lowest discharge and efflux and extremes of $\delta^{13}C_{DIC}$, percentage occurrence is very similar for all HYs, however, inter-annual differences are apparent at the low frequency high discharge, high efflux and mid-range $\delta^{13}C_{DIC}$.

HY 2012-13 has the largest maximum discharge and a slightly greater percentage occurrence of higher discharge than the other HYs. Conversely, HY 2013-14 has the lowest maximum discharge and the smallest frequency of the highest flows (Figure 48a). The greatest frequency of higher efflux occurs in HY 2011-12, which does not coincide with the year of maximum discharge (HY 2012-13) as might be expected (Figure 48b). However the year with the lowest frequency of high efflux (HY 2013-14), does coincide with the year of minimum discharge (HY 2013-14). The similarity in maximum and minimum $\delta^{13}C_{DIC}$ across HYs, noted from Table 11, can be seen in Figure 48c, and occurs because the range in $\delta^{13}C_{DIC}$ is constrained by end-members: ground water ~ -8 ‰, and soil water ~ -27 ‰. For each HY end-member composition is reached in only the very lowest or very highest flows (Figure 44 to Figure 47), and occurs for a small percentage of the time. However, in HY 2013-14, minimum $\delta^{13}C_{DIC}$ is not quite as ^{13}C-depleted as in the other HYs, and mid-range $\delta^{13}C_{DIC}$ is more ^{13}C-enriched a greater proportion of time (indicating a higher dominance of groundwater), while mid-range $\delta^{13}C_{DIC}$ is more ^{13}C-depleted for a greater proportion of time in HY 2011-12 (indicating a higher dominance of soil water).

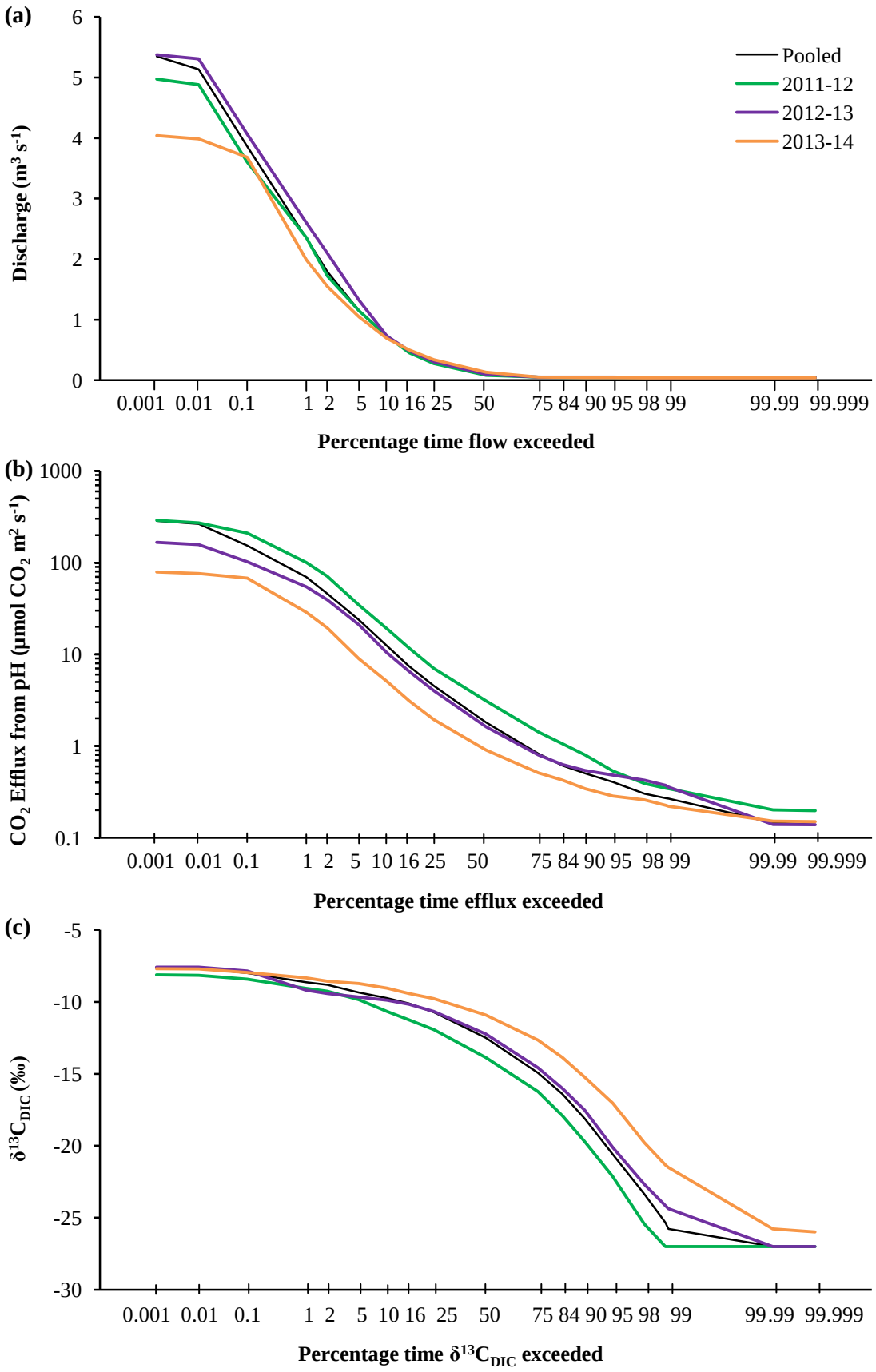

Figure 48: Discharge, CO_2 efflux and $\delta^{13}C_{DIC}$ duration curves for reconstructed data at DW

Each hydrological year is plotted to allow inter-year comparison of (a) discharge calculated from measured SH (see Chapter 2 section 2.2.3.5) (b) modelled CO_2 efflux, and (c) modelled $\delta^{13}C_{DIC}$ from pH (displayed on a log scale). It should be noted that some $\delta^{13}C_{DIC}$ and CO_2 efflux data is missing for HY 2013-14, but is accounted for because duration is calculated as a percentage. The legend is the same for all plots.

4.6 Discussion

4.6.1 Carbon Pool Magnitude and Range

There is a wide range in $\delta^{13}C_{DIC}$ and [DIC] across the study sites: $\delta^{13}C_{DIC}$ -23.2 to -0.7 ‰; [DIC] 0.04 to 2.03 mmol L^{-1} (Table 9, Figure 33). The $\delta^{13}C_{DIC}$ range is comparable to other temperate locations (e.g. Waldron et al, 2007; Polsenare et al., 2013), similar to that of tropical regions (e.g. Vihermaa et al., 2014; Khadka et al., 2014), but larger with a more ^{13}C-depleted minimum $\delta^{13}C_{DIC}$ than that of arctic locations (e.g. Giesler et al., 2013) (see Table 12 for values). Global [DIC] ranges broadly, however the [DIC] range here is within that of other sites globally, but towards the lower end (Table 12). The variation in $\delta^{13}C_{DIC}$ and [DIC] ranges across the sites of this study reflect variation in the sources, source contribution and biogeochemical processing of the DIC pool which will be discussed in the following sections.

4.6.2 Hydrological Control on Variation in Carbon Pool Composition

The DW and RK inorganic carbon pool has a hydrological response, both in concentration and isotopic composition (Figure 34a). When data from DW and RK are pooled, they largely overlie and the shape of the relationship between DIC concentration and $\delta^{13}C$ is hyperbolic (Figure 36), which has been observed in other fluvial systems and suggested to reflect the mixing of two end-members (Criss, 1999; Waldron et al., 2007; Khadka *et al*., 2014). However, the ranges are not exactly the same and so it is valuable to explore end-member composition as it may indicate differences in source inputs.

4.6.2.1 Low-Flow End-Members

At low flow (high [DIC]), [DIC] is of similar magnitude at the two sites, although remains higher at RK (at Q_{sp}^{-1} 370 m^3 km^2 s^{-1}: DW ~1.5 mmol L^{-1}, RK ~2.0 mmol L^{-1}; Figure 34a). Low flows are generally groundwater-dominated (Atekwana and Krishnamurthy, 1998; Waldron *et al*., 2007; Tobias and Böhlke, 2011; Polsenaere *et al*., 2013), and elevated [DIC] at RK at low flow may be due to the groundwater being more DIC-enriched at RK. Longer groundwater residence times lead to greater accumulation of weathering products and thus higher [DIC] (Jones and Mulholland, 1998; Polsenaere *et al*., 2013). The River Kelvin catchment is >20 times larger than that of DW, thus it seems plausible that a longer residence time has elevated [DIC] of RK groundwater.

Table 12: [DIC] and $\delta^{13}C_{DIC}$ of fluvial systems globally*

River System	Location	Climate	Catchment Type	Catchment Size (km^2)	DIC (mmol L^{-1})			$\delta^{13}C_{DIC}$ (‰)			Author
					min	max	average	min	max	average	
Main Trail	Peruvian Amazon	Tropical	Halpic Cambisols	5	0.06	0.12	0.10	-25.6	-23.6	-24.4	Vihermaa et al., 2014
New Colpita				7	0.15	0.52	0.33	-21.9	-18.8	-20.1	
La Torre				2000	0.20	0.30	0.24	-18.4	-15.2	-16.0	
Tambopata				14000	0.26	0.31	0.28	-13.1	-12.4	-12.9	
Various	Amazon	Tropical	Various	~6 x 10^6	-	-	-	-17.1	-7.9	-	Mayorga et al., 2005
Mitchel River	NE Australia	Tropical	Igneous & sedimentary bedrock, tropical rainforest & savanna plains	2500 km^2	0.19	0.76	-	-15.98	-9.91		Tweed et al., 2015
McLeod River				500 km^2	0.13	0.56	-	-17.45	-9.24		
Ichetucknee	*Florida*	*Sub-tropical*	*Limestone, aquifer fed*	*960*	*2.85*	*3.03*	*2.96*	*-11.5*	*-10.3*	*-11.0*	*De Montety et al., 2011*
Sante Fe	Florida	Sub-tropical	Silicate & carbonate, urban influence	3585	0.12	3.58	-	-22.0	-9.7	-	Khadka et al., 2014
Sugar Creek	*Indiana*	*Temperate*	*Carbonates & siliclastics, glacial sediments, corn agriculture*	*Headwater < 5*	*3.85*	*5.00*	-	*-8*	*-5*	-	*Tobias and Böhlke, 2011*
Sleepers	Vermont	Temperate	Metamorphic, calcareous units, glacial till overlying, hardwood forest	0.41	0.5	1.3	-	-15	-7	-	Doctor et al., 2008
Kalamazoo	Michigan	Temperate	Sandstone & glacial till, urban influence	~200	3.0	4.8	4.0	-11.4	-8.7	-9.9	Atekewana & Kryshnamurthy, 1998
Acadia Creek			Sandstone & glacial till, urban influence	tributary ~ < 30	4.6	5.6	5.0	-13.7	-10.9	-11.9	
Portage Creek			Sandstone & glacial till, urban influence	tributary ~ < 30	3.8	4.9	4.4	-11.7	-9.6	-10.5	
Spring Valley Creek			Sandstone & glacial till, urban influence	tributary ~ < 30	3.9	4.9	4.4	-12.4	-9.3	-11.0	
Allen Creek			Sandstone & glacial till	tributary ~ < 20	3.7	5.5	4.7	-12.5	-10.0	-10.9	
Spring Brook			Sandstone & glacial till	tributary ~ < 10	4.2	4.9	4.5	-11.9	-10.2	-10.8	
Big Hole	*Montana*	*Temperate*	*High altitude, low population, pristine*	*7200*	-	-	-	*-11.5*	*-10.0*	-	*Parker et al., 2005*
Big Hole	Montana	Temperate continental	High altitude, low population, pristine	7200	1.1	1.9	-	-11.5	-9.9	-	Parker et al., 2010
Clark Fork			High altitude, sewage, eutrophication	~ 2000	3.4	3.7	-	-12.4	-11.5	-	
Silver Bow Creek			High altitude, sewage, eutrophication	Headwater	2.0	2.5	-	-14.6	-10.3	-	
Silver Bow Creek	*Montana*	*Temperate*	*High altitude, sewage, eutrophication*	*270*	*1.8*	*2.4*	-	*-15*	*-10.5*	-	*Gammons et al., 2011*

Table 12 continued:

River System	Location	Climate	Catchment Type	Catchment Size (km^2)	DIC (mmol L^{-1})			$\delta^{13}C_{DIC}$ (‰)			Author
					min	max	average	min	max	average	
Gap Stream	South Korea	Temperate	Granite and metamorphosed sedimentary bedrock, carbonates in upper reaches. Forest, agriculture and urban landuse.	649	3.6	8.6	5.9	-15.2	-9.9	-12.1	Shin et al., 2015
Yudeung Stream				289	4.2	8.2	6.5	-14.6	-8.8	-11.6	
Daejeon Stream				49	3.6	8.4	6.1	-14.7	-10.7	-12.9	
Ottawa River	S. Canada	Temperate	Plutonic, metamorphic, carbonate and volcanic bedrock overlain by till and soil	149000	0.05	3.0	-	-17.4	-8.4	-	Telmer and Veizer, 1999
Rhône	France	Temperate	Limestone, urban influence	~200000	0.54	4.29	-	-13.0	-2.2	-	Aucour et al., 1999
Various	Arcachon Lagoon, France	Temperate	Quaternary sands, podzol soil, pine forest	4138	0.17	1.55	-	-24.6	-7.5	-	Polsenare et al., 2013
Renet	Arcachon Lagoon, France	Temperate	Non-carbonate, podzol soils, pine forest	<40	0.317	0.674	0.513	-21.2	-19.6	-20.3	Polsenaere & Abril, 2012
Milieu				<40	0.17	0.39	0.229	-24.6	-17.9	-19.7	
Leyre				~ 2500	0.255	0.612	0.403	-21.6	-12.5	-15.6	
St Lawrence River	N America	Temperate	Silicates & carbonates, urban influence	1.34×10^6	-	-	-	-4.7	+0.7	-	Yang et al., 1996
Various tributaries				various	-	-	-	-16.5	-6.7	-	
Vistula	Poland	Temperate	Siliclastics, limestones, glacial deposits, urban influence, heavy industry pollution	199813	-	-	-	-14.5	-9.0	-	Wachniew, 2006
Lagan	N.Ireland	Temperate	Sandstone, glacial till overlaying, urban & agricultural	609	0.36	2.94	-	-15.1	-10.2	-	Barth et al., 2003
Brocky Burn	Scotland	Temperate	Granite with schists, deep peaty podzols	1.3	0.01	0.31	-	-22.5	-5.5	-	Waldron et al., 2007
Water of Dye				41.7	0.02	0.47	-	-22.0	-5	-	
Water of Dye				90	0.05	0.34	-	-22.0	-3	-	
Chena	Alaska	Sub-Arctic	Discontinuous permafrost	5200	0.963	2.246	1.595	-	-	-	Cai et al., 2008
Various	N.Sweeden	Arctic	Mica schist, vegetation range forest/tundra	5 to 565	0.1	2.8	-	-15	-1	-	Giesler et al., 2013
A. Kuua	Greenland	Arctic	Metamorphic gneisses, continuous permafrost, proglacial rivers	proglacial	0.081	0.347	0.170	-	-	-	Ryu and Jacobson, 2012
Q. Kuussua				proglacial	0.147	0.342	0.209	-	-	-	

* Values for sites in italics are from a diel sampling only, where values for sites in normal font are from multiple spot samples over greater temporal ranges. A. Kuua = Akuliarusiarsuup Kuua, Q. Kuussua = Qinnguata Kuussua. Sites are ordered approximately by increasing latitude. [DIC] and $\delta^{13}C_{DIC}$ are presented as reported by the author.

However, this has not influenced the low-flow end-member $\delta^{13}C_{DIC,}$ estimated using the Keeling plot method to be -9 ‰ at both DW and RK (Figure 35). This is within the -21 to 0 ‰ range (Clark and Fritz, 1997; Chapter 1 section 1.6) of groundwaters, and similar to some temperate watersheds (-10.4 to -6.1 ‰, Waldron et al., 2007; -10 to -9 ‰ Tobias and Böhlke 2011) but considerably more ^{13}C-enriched than others (~ -17 ‰, Finlay, 2003). However this isotopic composition indicates low flow is groundwater rich. It is interesting that both systems have similar groundwater $\delta^{13}C_{DIC}$ despite their difference in scale; this suggests the two catchments share common lithology and that lithology influences groundwater $\delta^{13}C_{DIC}$ not water residence time. The similarity of $\delta^{13}C_{DIC}$ from DW and RK to other sites globally (4.6.1) suggests this observation may apply across scales.

4.6.2.2 High-Flow End-Members

As specific discharge increases [DIC] decreases (Figure 34a), reflecting the increased input of a lower [DIC] soil water - although the total DIC pool may not decrease due to the large volume of water (e.g. Akekwana and Kryshnamurthy, 1998; Waldron *et al*., 2007). Similarly, $\delta^{13}C_{DIC}$ depletion accompanies the reduction in [DIC] with increasing flow (Figure 34b). The change in $\delta^{13}C_{DIC}$ to values of ~ -23 ‰ and ~ -14 ‰ at the highest flows in DW and RK respectively (Figure 39), is consistent with the introduction of ^{13}C-depleted soil CO_2 (~ -23 ‰; Clark and Fritz, 1997; Khadka *et al*., 2014) to the river via flushing during rain/melt events, as noted in other studies (e.g. Waldron *et al.*, 2007; Polsenaere *et al.*, 2013, Khadka *et al*., 2014). However, unlike with groundwater, at high flow [DIC] and $\delta^{13}C_{DIC}$ diverge, with [DIC] an order of magnitude higher (at Q_{sp}^{-1} 1.0 m^3 km^2 s^{-1}: RK ~1.0 mmol L^{-1}, DW ~0.1 mmol L^{-1}; Figure 34a) and $\delta^{13}C_{DIC}$ more ^{13}C-enriched (~ -14 ‰ RK, ~ -23 ‰ DW) at RK than at DW, indicating contributions to the DIC pool differ between the sites at high flow.

The smaller decrease in [DIC] at high flows at RK than at DW is not a result of sampling excluding the highest flows at RK, as 94% and 34% of variation in stage height at RK and DW during the sampling period (Jun-2012 to May-2014) was captured by the sampling regimes. The two main differences between the DW and RK catchments are size and that RK has a 23% urban area (Singleton, 2013, unpublished data). The latter is likely the most important in shaping [DIC] at RK. [DIC] has been found to be consistently higher in rivers of highly-urbanised catchments than that of equivalent rural catchments, due to dissolution of concrete from urban structures, trade effluents and landfill leachates being introduced to a river through urban runoff (Baker *et al.*, 2008). Organic carbon from soot, coal, tyre abrasion, fuels (Glaser *et al.*, 2005) and sewage (Polsenaere *et al.*, 2010) are potential sources of carbon to a river in an urban environment, which, when/if respired, can contribute to the DIC pool. These inputs of urban IC and OC will be increased during events through increased runoff and activated storm overflow systems.

Lower high flow $\delta^{13}C_{DIC}$ at DW than at RK reflects closer hydrological linkages to the smaller more soil-dominated catchment, and suggests soil water almost entirely dominates the flow during event flow at DW, but not at RK where high flow sampled $\delta^{13}C_{DIC}$ is considerably more ^{13}C-enriched. The enrichment at RK indicates that there is a ^{13}C-enriched input of DIC to the pool at high flow. Concrete-derived carbonate in urban runoff (e.g. Baker *et al.*, 2008) has a ^{13}C-enriched $\delta^{13}C$ (-7 to +8 ‰; Chapter 1 section 1.6) and may be countering the ^{13}C-depletion by soil water in RK. However urban rivers do not exclusively have more ^{13}C-enriched $\delta^{13}C_{DIC}$ than rural rivers (Table 12). The range of sources of urban carbon inputs is broad (Baker *et al.*, 2008) and so $\delta^{13}C$ of inputs will vary greatly, and proportional inputs of urban and natural DIC will vary with hydrology.

The extended water residence time in the larger catchment of RK may also cause/add to the differentiation in high-flow $\delta^{13}C_{DIC}$ at RK and DW, by providing increased opportunity for air-water CO_2 isotopic equilibrium exchange and associated ^{13}C-enrichment of $\delta^{13}C_{DIC}$ (see 4.3.1.1), as has been postulated to be the cause of $\delta^{13}C_{DIC}$ enrichment in other large catchments (Yang *et al.*, 1996; Aucour *et al.*, 1999; Telmer and Veizer, 1999). It does appear that larger catchments have more-enriched $\delta^{13}C_{DIC}$ (Table 12), with the average and/or range of $\delta^{13}C_{DIC}$ in the multiple catchment studies of Atekwana and Kryshnamurthy (1998), Waldron *et al*. (2007), Parker *et al*. (2010), Polsenare and Abril (2012) and Vihermaa *et al*. (2014) scaling with catchment size. One exception stands out - a small catchment of <5 km^2 that has an enriched $\delta^{13}C_{DIC}$ range of -8 to -5 ‰ (Tobias and Böhlke, 2011; Table 12) - but this is explained by the prevalence of corn agriculture in the catchment (a C4 plant with ^{13}C-enriched $\delta^{13}C$; Chapter 1 section 1.7). Significant efflux or influx of CO_2 (beyond isotopic equilibrium exchange) over a longer soil-to-sample flow pathway in a larger catchment may also impact the DIC pool of RK, and is discussed in more detail in 4.6.3.2.

4.6.2.3 End-Member Mixing

If [DIC] and $\delta^{13}C_{DIC}$ of a river was simply a result of proportional mixing of the two end-members, data would all fall on a linear mixing line, e.g. Figure 49. In the relationship between [DIC] and $\delta^{13}C_{DIC}$ (Figure 36) the parabolic shape and scatter about the line indicate that either: (i) end-members are not constant in composition; or, (ii) that the DIC pool may have been altered by physical or biological processes (e.g. Waldron et al., 2007). End-members were not sampled, but the Keeling plot indicated groundwater $\delta^{13}C_{DIC}$ to be quite constant and the higher-flow end-members vary in composition between catchments. However, both will be subject to biological and physical processes, which have been mentioned but are considered in more detail below (4.6.3).

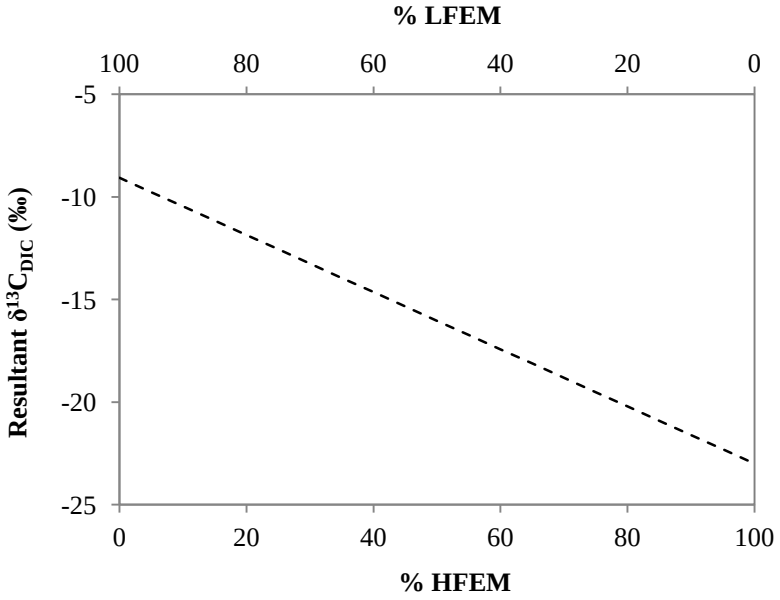

Figure 49: $\delta^{13}C_{DIC}$ two-end-member mixing line for DW and RK

The dotted black line shows the resultant $\delta^{13}C_{DIC}$ for a given % mixing of high flow end-member (HFEM) and low-flow end-members (LFEM) $\delta^{13}C_{DIC}$. HFEM and LFEM are the same for DW and RK: HFEM is soil CO_2 (-23 ‰, section 4.3.1.2) representing soil water, and LFEM is groundwater (-9 ‰, obtained from the Keeling plot, Figure 35).

4.6.3 Processes Amending Pool Composition

4.6.3.1 Biological Processes

Diel sampling was undertaken to assess for photosynthetic/respiration effects on the DIC pool. The diel patterns in $\delta^{13}C_{DIC}$ and [DIC] observed at DW (Figure 37) were measured under very stable low flow conditions, thus are unlikely to be a result of changing proportional mixing of groundwater and soil water, or changes in CO_2 efflux rates (which are hydraulically controlled at the site – Chapter 3). The pattern is instead consistent with biological mediation of the DIC pool (4.3.1.2), which is influencing pool magnitude as well as composition.

This response is rarely characterised due to the fieldwork commitment, logistics and resource requirement, however it is highly important to know whether the sampled DIC pool composition can be considered to be representative of time-integrated average conditions or mediated by biological processes (Gammons *et al*., 2011). For example, failure to incorporate diel cycles in a sampling strategy could lead to underestimation of downstream DIC flux (as sampling is commonly carried out in daylight hours when [DIC] is reduced by photosynthesis) or spurious spatial or temporal trends (if sampling time systematically changes over the sampling period) (Gammons *et al.*, 2011; Tobias and Böhlke, 2011). Careful consideration of sampling times is particularly important in systems where diel fluctuations are greater than seasonal variations (e.g. Yates *et al.*, 2007; Lynch *et al.*, 2010).

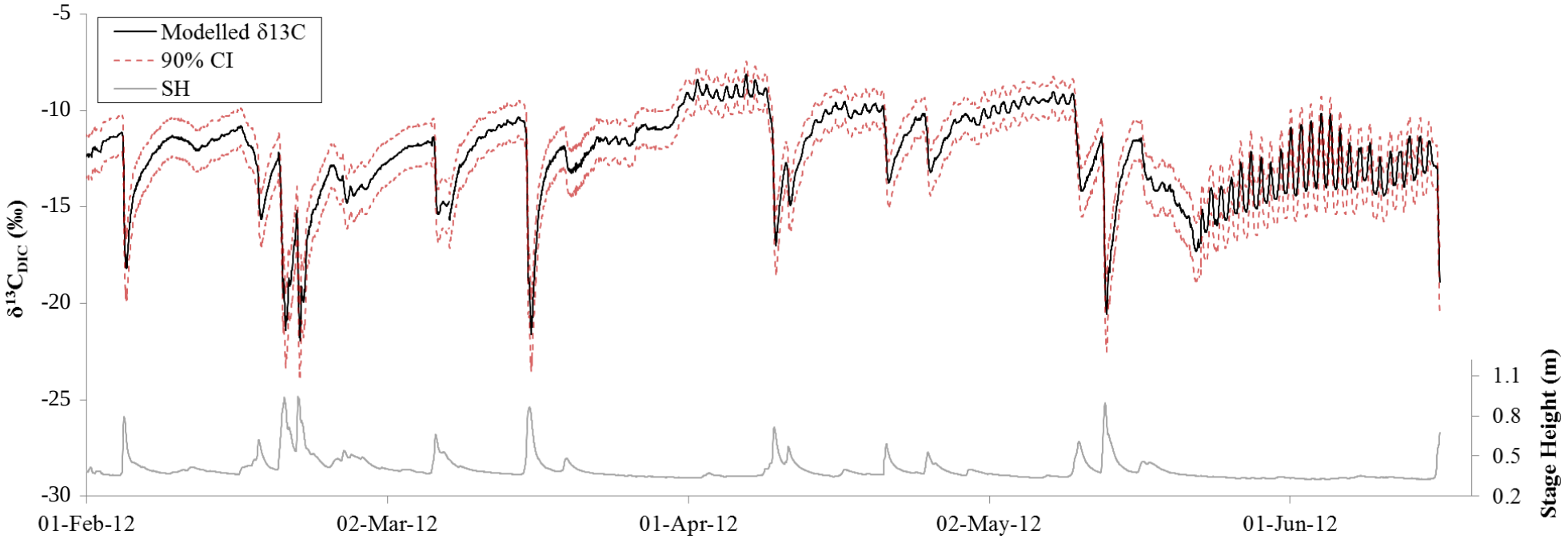

Figure 50: Enlarged view of diel patterns in reconstruction of $\delta^{13}C_{DIC}$ from the relationship with pH

Feb – June excerpt of HY 2011-12 (Figure 44). CI = confidence intervals. SH = stage height as hydrological time series.

As understanding of the importance of diel cycling grows, data is increasingly becoming available (e.g. Parker *et al*., 2005; Waldron *et al*., 2007; Parker *et al*., 2010; Gammons *et al*., 2011; Tobias and Böhlke, 2011; De Montety *et al*., 2011; Bass *et al*., 2013; Table 13). From this it is apparent the magnitude of diel variation in $\delta^{13}C_{DIC}$ and [DIC] at DW falls within, and approximately mid-way, the ranges of these other global catchments (Table 13). Fluvial systems with high primary productivity tend to experience the greatest ranges in $\delta^{13}C_{DIC}$ and [DIC] (e.g. Waldron *et al*., 2007 peaty catchment; Parker *et al*., 2010 (SBC) and Gammons *et al*., 2011 eutrophic streams; Bass *et al*., 2013, tropical floodplains), and it has been observed that magnitude of diel variation scales upwards with increasing net productivity (Parker *et al*., 2010) reflecting the increasing dominance of biological processes on the DIC pool, the more productive a catchment.

Table 13: Global ranges in diel $\delta^{13}C_{DIC}$ and [DIC]*

$\delta^{13}C_{DIC}$ (‰)			[DIC] (mmol L^{-1})			Author
min	**max**	**range**	**min**	**max**	**range**	
-12.5	**-10.3**	**2.2**	**0.5**	**1.1**	**0.7**	**DW - this study**
-8	-1	7	1.0	1.7	0.7	Bass *et al*., 2013
-11.5	-10.3	1.2	2.9	3.0	0.2	De Montety *et al*., 2011
-15	-10	5	1.8	2.4	0.6	Gammons *et al*., 2011
-11.5	-10.0	1.5	-	-	-	Parker *et al*., 2005
-15.0	-10.5	4.5	2	2.4	0.4	Parker *et al*., 2010 (SBC)
-13.0	-10.5	2.5	1.1	1.8	0.7	Parker *et al*., 2010 (BH)
-8	-5	3	3.9	5	1.1	Tobias and Böhlke, 2011
-13	-7	6	0.1	0.2	0.1	Waldron *et al*., 2007 (max)
-22	-20	2	0.03	0.04	0.01	Waldron *et al*., 2007 (min)
-12	-10	2	-	-	-	Wachinew, 2006

* For further site information see Table 12. SBC = Silver Bow Creek, BH = Big Hole River. Waldron *et al.* (2007) carried out multiple diel samplings, maximum and minimum diel ranges for the 1.3 km^2 catchment (the most similar size to DW catchment) only are presented here.

Because measured diel variation at DW is of moderate magnitude, it could be assumed that catchment productivity and the influence of biological processes on carbon pool composition and magnitude are also moderate. However, time series reconstruction of $\delta^{13}C_{DIC}$ from pH at DW (Figure 44) reveals that biological impact on the DIC pool varies over a year with catchment productivity and flow state. Diel cycling only occurs during late-spring to early Autumn, reflecting greater occurrence and magnitude of diel cycling when catchment productivity is high (e.g. Parker *et al*., 2010), and only under periods of low flow, reflecting greater activity of biofilms under slow flow conditions (e.g. Lau and Liu, 1993). When high catchment productivity and low flow occur in combination, diel variation can be prolonged and of high magnitude, e.g. June 2013: up to 5 ‰ daily variation in $\delta^{13}C_{DIC}$ over a 25 day period (see Figure 50). During spring-autumn event flow either any biological signal is masked by influx of soil water (e.g. Figure 39, Figure 44) or scouring

of biofilms prevents biological activity and/or establishment of a community (Lynch *et al.*, 2010). In the winter months shortened day length and low temperatures appear to prohibit sufficient biological activity whatever the flow state (e.g. Feb. and Mar., Figure 50). Another advantage of time series reconstructions is that they can reveal inter-year differences in the prevalence of diel cycling of the DIC pool, e.g. diel cycling occurred on 15%, 22% and 35% of days in 2011-12, 2012-13 and 2013-14 respectively.

The concomitant diel variation in reconstructed CO_2 efflux (up to 3 µmol CO_2 m^{-2} s^{-1}, Figure 47), although possibly an artefact of both parameters being reconstructed from the same dataset, could plausibly be due to daily variation in DIC pool size. As with $\delta^{13}C_{DIC}$, [DIC] is also subject to diel biological mediation (Figure 37; Table 12), and under stable low flow this will result in diel cycles in the availability of CO_2 for degassing, subsequently manifested in CO_2 efflux rates. Diel cycles in pCO_2 have been measured in rivers (e.g. Raymond *et al.*, 1997; Lynch *et al.*, 2010) and mangroves (e.g. Borges *et al.*, 2003) and postulated to induce diel cycles in air-water gas exchange (Lynch *et al.*, 2010), however there are no known published attempts to measure diel variation in CO_2 efflux.

4.6.3.2 CO_2 Efflux

CO_2 efflux can cause ^{13}C-enrichment of the DIC pool because the ^{12}C-containing molecules preferentially diffuse from the water to the atmosphere, causing the remaining DIC pool in the water to become progressively enriched with ^{13}C (Doctor *et al.*, 2008; Polsenaere and Abril, 2012). However, at DW and RK, when $\delta^{13}C_{DIC}$ is most ^{13}C-depleted, efflux rates are highest (Figure 38); this is because both parameters are heavily influenced by the hydrological conditions (Figure 34; Chapter 3, Figure 24 and Figure 27). Flow intensity was found to be primary control on efflux, with the highest efflux rates generally occurring at the highest flows (Chapter 3; Long et al., 2015). It appears that if there is fractionation by diffusive efflux, this is compensated for by the on-going input of ^{13}C-depleted DIC at high flows from flushing of the soils. However, efflux may still modify the $\delta^{13}C$ of the DIC pool.

$\delta^{13}C_{DIC}$ at high-efflux rates is more ^{13}C-enriched at RK than at DW (Figure 38), indicating that efflux at RK is from a source that has been enriched compared to DW. Similarly RE $\delta^{13}C_{DIC}$ is more ^{13}C-enriched still, greater than RK and DW, and this could indicate terrestrially-derived DIC is less dominant in RK and RE. The more ^{13}C-enriched $\delta^{13}C_{DIC}$ at high flow at RK, attributed earlier to urban run-off (4.6.2.2), and/or increased duration of air-water equilibrium exchange, could also/instead be due to CO_2 efflux. The catchment is large (335 km^2) and the sampling site is close to the end of the catchment, thus there is potential for a large amount of efflux to have occurred prior to water reaching the sampling site. DW, which has much more ^{13}C-depleted $\delta^{13}C_{DIC}$ at high flow, has a much smaller catchment (5.7 km^2) and so much less surface area and time for degassing of CO_2 upstream of the sampling point to enrich the DIC pool. As efflux has been found to cause only ~3 ‰ ^{13}C-enrichment (Doctor et al., 2008) it is unlikely to explain the ~10 ‰

difference between high-flow $\delta^{13}C_{DIC}$ at DW and RK, and it seems more likely that the high-flow ^{13}C-enrichment at RK is a result of a difference in HFEM source. However, degassing over the longer transit time may contribute, by removing almost all headwater soil CO_2 prior to the point of sampling, enabling the pool to become dominated by local $\delta^{13}C_{DIC}$ composition – the urban carbon inputs.

4.6.4 The River Etive

The data for RE is limited, but from the data that exist no relationships are apparent between $\delta^{13}C_{DIC}$ and [DIC] and efflux (Figure 38), flow (Figure 39c) or water chemistry parameters (Figure 40). RE therefore does not appear to have the same clear end-members as the other sites: data is broadly scattered on the Keeling plot (Figure 35), and does not fit on the end-member mixing curve of DW and RK (Figure 36). There is a much greater influence of snow-melt at RE. The catchment can have over 60 snow-lying days per year, compared with 0 - 20 days at DW and RK, and all sampling was carried out in the snow melt season. This may be an explanatory factor as snow-melt may introduce run-off that has had little soil contact (thus low [DIC] and/or limited $\delta^{13}C_{DIC}$ depletion). The DIC present may have a wide range as it likely reflects a mixture of entrained atmospheric CO_2, subsequently dissolved in the meltwater (^{13}C-enriched), and CO_2 from soil respiration (^{13}C-depleted), which can diffuse through snow (e.g. Sommerfeld *et al.*, 1996) and potentially dissolve in the meltwater. These inputs of IC may occur in varying quantities during the season of snow accumulation and depend on the snow-melt pathway, which can be highly variable (e.g. Soulsby *et al.*, 1997).

In another catchment where >50% of precipitation falls as snow, no relationship between [DIC] and $\delta^{13}C_{DIC}$ was also observed (Giesler et al., 2013). Snow-melt events have been observed to decrease [DIC] by dilution (Atekwana and Kryshnamurthy, 1998; Aucour *et al*., 1999; Doctor *et al*., 2008; Cai *et al*., 2008) and increase $\delta^{13}C_{DIC}$ in some instances (Doctor et al., 2008), but have no effect on $\delta^{13}C_{DIC}$ in other cases (Aucour et al., 1999; Atekwana and Kryshnamurthy, 1998). This would be consistent with temporally varying sources of snow-DIC entrainments. It therefore appears snow-melt may act as a third end-member at the site (additional to groundwater and soil water) but has varying influence and precise composition is difficult to constrain, resulting in noisy hydrological responses.

A further complication is that influx occurred on a much higher proportion of sampling occasions at RE than at DW and RK, thus atmospheric CO_2 provides a periodic fourth end-member. Unfortunately insufficient data exists at this site for a multiple-end-member mixing model to be carried out, but the data highlights that snow and ice dominated systems may behave very differently in terms of sources and mixing of DIC. The carbon pool dynamics of ice- and snow-melt dominated systems are explored further in Chapter 5.

4.6.5 Modelling and Reconstruction of $\delta^{13}C_{DIC}$ and CO_2 Efflux

All reconstructions across the three hydrological years (Figure 44, Figure 45, Figure 47) show a groundwater (low flow), ^{13}C-enriched $\delta^{13}C_{DIC}$, low efflux baseline, punctuated by relatively short duration $\delta^{13}C_{DIC}$ ^{13}C-depleted and high efflux events, which occur with event flows. This is consistent with other detailed observation of hydrologically-mediated DIC pool change: high efflux and low $\delta^{13}C_{DIC}$ during flood events (Aucour *et al.*, 1999; Khadka *et al.*, 2014); that carbon concentrations and associated parameters are highly linked to hydrology and runoff events (Polsenare *et al.*, 2013); that modelled $\delta^{13}C_{DIC}$ becomes significantly ^{13}C-depleted during high flows (Waldron *et al.*, 2007). This suggests that under low, stable flow conditions the CO_2 effluxed to the atmosphere is likely from a groundwater source, while during event flows CO_2 being returned to the atmosphere originates from a more terrestrial (soil) source. This can be seen in the relationship between modelled CO_2 efflux and $\delta^{13}C_{DIC}$ (Figure 51), and between directly measured CO_2 efflux and $\delta^{13}C_{DIC}$ (Figure 38).

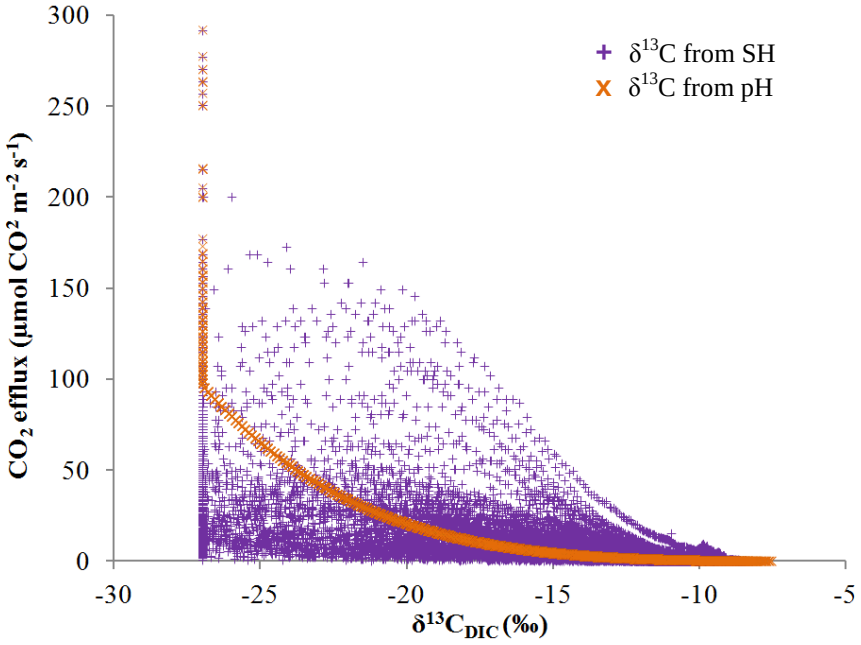

Figure 51: Relationship between modelled CO_2 efflux and modelled $\delta^{13}C_{DIC}$
Showing increasing $\delta^{13}C_{DIC}$ depletion with increasing CO_2 efflux. SH = stage height. The abrupt end to the data at $\delta^{13}C_{DIC}$ = -27 ‰ is due to model capping. The perfect correlation between CO_2 efflux and pH-$\delta^{13}C_{DIC}$ (orange data points) is due to both being reconstructed from the same pH data. The large amount of scatter in the SH-$\delta^{13}C_{DIC}$ (purple data points) is due to variation in the pH-stage height relationship caused by seasonality and extent of previous soil flushing.

Although variation in discharge and source of CO_2 was relatively small across the HYs (Table 11, Figure 48), there was large variation in total efflux (11.9, 6.7 and 3.4 kg CO_2 m^{-2} y^{-1} in 2011-12, 2012-13 and 2013-14 respectively; Table 11), suggesting efflux rate is sensitive to small changes in the hydrological regime. Inter-annual comparisons revealed that there was lowest total CO_2 efflux in the driest HY (HY 2013-14), and that this occurred over a lower frequency of less-large efflux events (Figure 48b), and the source was more groundwater dominated than in other HYs (Figure

48c). As such, it could be assumed that if the climate became drier, with less and/or smaller event flows, less CO_2 would be returned to the atmosphere via efflux, with the DIC and efflux originating from a more groundwater-dominated source. Conversely, if the climate became wetter, with more and/or larger event flows, more CO_2 would be returned to the atmosphere that originated from a terrestrial (soil) source.

It should be noted that all models, and the comparison of modelled vs. measured values, are limited at the high stage height or low pH end by the large uncertainties caused by a lack of measured data at the highest flows (Figure 39b, Figure 40a, Figure 41a, Figure 42). Event sampling data would improve the models, and alongside this it is important to find a way to make efflux measurements during the highest flows safely and without flooding the floating chamber/tubing. Additionally, these models may not apply (i) in the seasonal tropics where isotopic reversal can occur under heavy rainfall (Bass *et al.*, 2014a), and/or (ii) beyond the point of riverbank breach, when proportional water (and thus [DIC] and $\delta^{13}C_{DIC}$) source inputs can shift (e.g. Tweed *et al.*, 2015), and water surface area and flow velocity (parameters that highly impact CO_2 flux rates, e.g. Raymond *et al*., 2013 and Long *et al*., 2015), can alter vastly from channelised flow.

For a given stage height or pH, varying degrees of turbulence and water surface disturbance are possible, and it is known that flow intensity has a large influence on efflux (Long et al., 2015; Chapter 3). Uncertainty in the models appears to be generated because flow intensity has not been considered in the model. For all models, there is some separation by visual water surface state (a proxy for turbulence) (Figure 42), but this is more apparent for the pH-CO_2 efflux model where uncertainty/scatter above the model line occurs with rough and medium water surfaces, and uncertainty/scatter below the model line occurs with smooth water surfaces (Figure 42c). The pH-model will generate the same efflux for a given pH regardless of the turbulence, thus ideally models would include turbulence, particularly CO_2 efflux models. It is known that $R^*.pCO_2$ explains efflux much better than pH alone (Chapter 3), and so ideally efflux would be modelled using R^* and pCO_2 instead of pH. pH is available from many sensors and is routinely measured, and from it CO_2 availability can be calculated. Further, here, pH correlates with stage height (Appendix G) and so is a good indicator of catchment hydrology, and it has a strong relationship with efflux. Thus, here, pH is a good way to model efflux (and source of DIC) while indirectly incorporating turbulence. However future efflux models may be more accurate if including flow intensity, thus collection of continuous fluvial pCO_2 data using sensors (e.g. Johnson *et al.*, 2010) and routine measurement of flow velocity profiles (for calculation of R^*) alongside efflux measurements is recommended for upscaling.

As well as inter-annual variation, the reconstructions revealed diel cyclicity in $\delta^{13}C_{DIC}$ and CO_2 during periods of high productivity and low flow (discussed in 4.6.3.2). Thus these reconstructions have allowed insight into the dynamics of the carbon pool at DW over daily, to seasonal, to annual and potentially decadal scale. Direct CO_2 efflux measurement, and [DIC] and $\delta^{13}C_{DIC}$ sample

collection, at an intensity high enough to pick up diel variations over a decadal time period, would require enormous fieldwork commitment, logistics and resources and thus is likely impractical. Indeed, there are no known published attempts to reconstruct fluvial CO_2 efflux over long time periods. Thus despite the limitations of these reconstructions, they are invaluable in providing detailed insight into carbon pool dynamics over long periods of time and at 30 minute detail (the logged frequency). Such reconstructions could ultimately aid the community in improving global carbon budgets and predictions of the response of the fluvial carbon cycle to our changing climate.

4.7 Conclusions

Ranges and magnitudes of [DIC] and $\delta^{13}C_{DIC}$ at the three sites (DW, RK and RE) are comparable to other global locations, with RE most similar to Arctic locations. DIC pool concentration and source is predominantly hydrologically-controlled at the main sites (DW and RK), with the similar groundwater LFEMs indicating a common hydrogeological inheritance in DIC. Differences in the HFEMs reflect contrasting catchment land use and indicate soil water dominates the high flow DIC pool in rural systems, but in urban systems soil water can be absent or masked by urban runoff. Modification of the pool by biological (in-stream photosynthesis/respiration) and physical (CO_2 efflux) processes was insufficient to overcome hydrological responses. Limited data from a snow-melt dominated site (RE) indicate snow and ice dominated systems may behave very differently in terms of sources and mixing of DIC, and that multiple-end-member mixing models may need to be considered to understand the carbon pool dynamics of such systems.

Time series reconstructions of $\delta^{13}C_{DIC}$ and CO_2 efflux at DW reveal that terrestrial-aquatic-atmospheric carbon cycling is very rapid over event flows, degassing large amounts of terrestrially-sourced CO_2 to the atmosphere over a relatively short duration. In contrast, at low flow, CO_2 efflux is influenced more by the groundwater and of much smaller magnitude, thus there is more chance of the DIC pool transiting further down the system. Inter-year time series comparison indicates that under a drier climate with less and/or smaller magnitude event flows, fluvial systems will return less CO_2 to the atmosphere from a less terrestrial source than under a wetter climate. Additionally time series reconstructions reveal detail in carbon pool dynamics that manual sampling can easily omit, e.g. the duration, magnitude and seasonal pattern of diel variation, and they can enable incorporation of the role of short-term processes on decadal scale carbon fluxes (where hydrochemical data is available). There are many other examples of fluvial diel processes that are directly or indirectly linked to the daily sun cycle (Nimick et al., 2011), and it is imperative any diel cycle is considered in a sampling strategy to prevent non-representative findings (Gammons et al., 2011). This first known attempt to reconstruct CO_2 efflux at high resolution over a number of years identifies approaches that take us a step closer to improved global fluvial carbon budgets, and from this basis, more accurate projections of how/whether this component of the carbon cycle may act as a feedback to climate change.

5 Greenland Ice Sheet meltwaters are a pathway for the return of old carbon to the atmosphere and potentially a sink for CO_2

5.1 Abstract

Global ice melt and permafrost thaw are increasing due to climate change. The effects of melting ice and thawing permafrost on global carbon cycle stability depend on the carbon flux direction, magnitude, and reservoir (age) from which carbon is released, however these are little quantified. Impacts may include the release of pore-space CO_2 and dissolved organic carbon (DOC) upon ice melt, and with ice retreat the exposure and subsequent erosion and chemical weathering of old carbon-containing landscapes. Upon exposure and/or thaw, these soils and other high-latitude permafrost soils are subject to loss of old carbon through respiration and soil CO_2 efflux, and through export by drainage, where high DOC biolability may prime bacterial activity and feedback to climate change. Although it has been widely hypothesised that our changing climate may cause arctic regions to shift from a carbon sink to a source, the mechanisms and pathways through which carbon is released to the atmosphere are not thoroughly understood. Here new age and flux data linking the cryospheric carbon cycle, Arctic drainage systems and the atmosphere are reported for non-glaciated permafrost-landscape surface-drainage catchments and meltwaters from the west Greenland Ice Sheet (GrIS). Despite the GrIS exerting a globally significant role on climate, its mediation of the carbon cycle is unknown. It is found here that GrIS drainage waters quickly become under-saturated and can draw down atmospheric CO_2, and release old carbon to an otherwise modern carbon environment, and, while permafrost-landscape surface-thaw systems are cycling recently-fixed carbon and the permafrost does not appear to be degrading in this region, permafrost-landscape surface drainage is a net source of CO_2 to the atmosphere.

5.2 Introduction

To allow upscaling of fluvial CO_2 efflux to catchment/global scale, and/or make predictions of how systems will behave under a climate-induced changing hydrological cycle, a sufficiently generic model is needed and this requires measurement of multiple field sites of different catchment type and environmental sensitivities. Global coverage of published CO_2 data is incomplete; it has typically focussed on temperate regions and is particularly lacking in high latitude regions and the tropics (Raymond *et al.*, 2013). As such, I expanded my research to incorporate an Arctic location, to allow investigation of CO_2 efflux from the melt/thaw waters of ice and permafrost systems, which are not found under a temperate climate.

5.2.1 High Latitude Regions are Vulnerable to Climate Change

Global average temperatures are increasing, and the high latitudes are particularly vulnerable to climate change (IPCC, 2013; Vonk and Gustafsson, 2013; Vonk *et al.*, 2013). Climate models predict that climate change will be most intense at high latitudes (IPCC, 2007; Wang *et al.*, 2013), and with a 0.6^{o}C temperature increase per decade over the last 30 years, high latitudes are warming twice as fast as the global average (Schuur *et al.*, 2015). Under the best-case scenario of the IPCC report (2013), change in surface temperature 1986-2005 to 2081-2100 is predicted to be 2 – 4^{o}C, while under the worst case scenario temperatures may increase by more than 11^{o}C by 2100. Additionally, high latitude regions have great potential to feed back to climate change as they contain large amounts of stored carbon which is vulnerable to release under a warming climate (Vonk and Gustafsson, 2013; Vonk *et al.*, 2013; Wang *et al.*, 2013).

5.2.2 Carbon in the Cryosphere

Cryospheric systems are widespread in the high latitudes. Coming from "kryos", the Greek word for cold, the cryosphere incorporates all systems where water exists as ice, including icecaps, glaciers, sea ice, icebergs, snow and frozen ground (Harris and Murton, 2005). This chapter considers terrestrial cryospheric systems only – icecaps, glaciers (and any snow associated with them) and frozen ground (permafrost).

5.2.2.1 Permafrost

Permafrost, defined as subsurface Earth materials (organic and mineral soil, rock and ice) remaining below 0°C for two consecutive years (Shiklomanov and Nelson, 1999; Schuur *et al.*, 2008), occupies up to 24% of the exposed land area of the northern hemisphere (Romanovsky *et al.*, 2002; Schuur *et al.*, 2008). The permafrost soil surface thaws seasonally and is referred to as the active layer (Schuur *et al.*, 2008; Schaefer *et al.*, 2011; Vonk *et al.*, 2013). It can be <1 m to several 100 m thick depending predominantly on regional climate but is also influenced by a range of other factors including topography, hydrology, snow cover and subsurface material properties (Schuur *et al.*, 2008). Under the cold and frozen conditions, microbial activity, and thus the rate of decomposition, is considerably reduced or ceased (Schaefer *et al.*, 2011) and organic matter accumulates, sometimes to considerable depths and in some cases over 1000s of years (Vonk *et al.*, 2013). As a result, permafrost soils can contain large amounts of carbon that can be several 1000s of years old (Schuur *et al.*, 2008; Tarnocai *et al.*, 2009; Vonk and Gustafsson, 2013; Vonk *et al.*, 2013; Wang *et al.*, 2013; Schuur *et al.*, 2015). Permafrost soils are estimated to contain 2400 billion tonnes of carbon globally, with 1672 Pg of this in the northern hemisphere (Tarnocai *et al.*, 2009; Vonk *et al.*, 2013). Carbon stored in the northern hemisphere soils is approximately 50% of the total global below ground organic carbon pool (Tarnocai *et al.*, 2009), almost 4 times that of the

total global forest biomass (Vonk *et al.*, 2013) and over twice that currently stored in the atmosphere (Schuur *et al.*, 2015).

5.2.2.2 Ice

Ice (ice caps and glaciers) currently covers approximately 11% of the Earth's land surface (Hood *et al.*, 2015) and ice systems are now becoming recognised as unique ecosystems containing and cycling carbon (Hood *et al.*, 2009; Anesio and Laybourn-Parry, 2012; Bhatia *et al.*, 2013; Hood *et al.*, 2015). Glacier systems accumulate organic carbon via deposition from terrestrial and anthropogenic sources (Hood *et al.*, 2015). Carbon can be stored: (i) on the ice surface (supraglacial) e.g cryoconite holes (Hodson *et al.*, 2008; Anesio and Laybourn-Parry, 2012), and surpraglacial debris such as black carbon (Stubbins *et al.*, 2012); (ii) within the ice (englacial) e.g. old organic matter that was trapped during ice formation (Hodson *et al.*, 2008); or, (iii) under the ice (subglacial) e.g. old soils and organic matter produced during warmer ice-free eras which since been shielded by the ice (Hodson *et al.*, 2008; Anesio and Laybourn-Parry, 2012). There can also be in-situ primary production of modern carbon: ice surfaces host diverse microbial communities (e.g in cryoconite holes and red-snow) and during summer melt these become active and fix and respire carbon (Hodson *et al.*, 2008; Anesio and Laybourn-Parry, 2012; Cook *et al.*, 2015). These supraglacial bacteria have been found to be active at rates equivalent to other aquatic ecosystems in warmer climates (Anesio and Laybourn-Parry, 2012). Subglacial bacteria are also active in fixing and respiring carbon, but englacial bacteria tend to be dormant because there is little liquid water in the environment (Hodson *et al.*, 2008; Anesio and Laybourn-Parry, 2012).

The total amount of organic carbon stored in glaciers and ice sheets is now being estimated (~6 Pg C), however there is still much uncertainty in the precise amount of carbon stored in and released from ice bodies regionally/globally (Hood *et al.*, 2015).

5.2.3 Changing Melt/Thaw Seasons

The peripheries of permafrost zones, icecaps and glaciers exist on a borderline between frozen and thawed, and their extent is almost entirely governed by climate (Pavlov, 1994). Climate change is causing cryosphere summer melt seasons globally to become longer and more intense (Hanna *et al.*, 2008). As a result, global ice melt is increasing (IPCC, 2013), enhanced by feedback loops associated with temperature, water vapour, clouds and albedo and heat flux changes, and ultimately causing sea-level increase (Hansen *et al.*, 2005; Rignot *et al.*, 2011; Pithan and Mauritsen, 2014). Climate change-induced increased air and soil temperatures are causing permafrost soils to thaw for a greater period each year, over greater lateral extent and to greater depths, and ultimately the shrinking of the permafrost zones (Pavlov, 1994; Schuur *et al.*, 2008; Schaefer *et al.*, 2011; Vonk *et al.*, 2013; Wang *et al.*, 2013).

5.2.4 A Thawing Cryosphere Could Feedback to Climate Change

Thawing of the permafrost soils causes the flush of water and nutrients through the soil and draining of the soil; under these more favourable conditions, microbial activity and decomposition increase (Vonk and Gustafsson, 2013; Vonk *et al.*, 2013; Wang *et al.*, 2013) producing greenhouse gasses, and in turn accelerating climate warming which accelerates the permafrost degradation (Schaefer *et al.*, 2011; Vonk and Gustafsson, 2013; Vonk *et al.*, 2013). This has been termed the permafrost carbon feedback (PCF) (Schaefer *et al.*, 2011; Vonk *et al.*, 2013) (Figure 52). It is thus widely hypothesised that our changing climate may cause the Arctic region to shift from a carbon sink to a source (Vonk and Gustafsson, 2013; Vonk *et al.*, 2013; Wang *et al.*, 2013; Schuur *et al.*, 2015). Because of the size of the carbon pool and the intensity of climate forcing at high latitudes, release of carbon stored in permafrost is potentially the most significant climate feedback, yet one of the least understood (Tarnocai *et al.*, 2009).

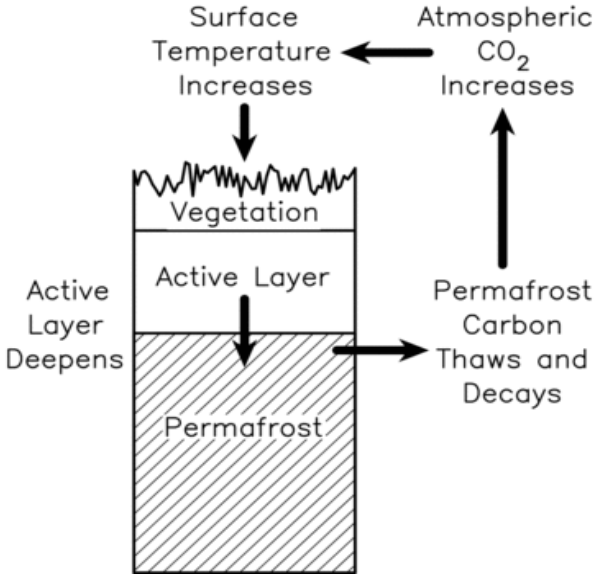

Figure 52: The basic dynamics of the permafrost carbon feedback

A schematic diagram, taken from Schaefer *et al.* (2011), showing an amplification of surface warming due to the release of carbon, currently frozen in permafrost, into the atmosphere.

Melting ice bodies also release carbon, mainly organic carbon in dissolved or particulate form (Vonk *et al.*, 2013; Wadham *et al.*, 2013; Hood *et al.*, 2015). DOC is the primary intermediary to global carbon cycling as it can be transported through cell membranes and is thus readily available for microbial metabolism to CO_2 or other greenhouse gasses (Battin *et al.*, 2008; Vonk *et al.*, 2013; Hood *et al.*, 2015). Additionally ice retreat exposes old landscapes; from these, carbon which was previously shielded from physical and chemical erosion can become available for transport and transformation (Sharp *et al.*, 1999), and may subsequently be returned to the atmosphere as CO_2.

Further glacier-derived DOC can be highly biologically available (biolabile) compared to terrestrial DOC (Hood *et al.*, 2009; Bhatia *et al.*, 2010; Singer *et al.*, 2012; Lawson *et al.*, 2014; Hood *et al.*, 2015), with up to 95% of DOC being readily metabolized in laboratory tests (Hood *et al.*, 2009; Singer *et al.*, 2012; Hood *et al.*, 2015), compared to 23% of DOC from a non-glaciated catchment in Montana (Hood *et al*., 2009). The high biolability is thought to be in-part due to a lack of pre-processing of the DOC prior to thaw (Hood *et al.*, 2009; Vonk *et al.*, 2013). As such glacial DOC entering aquatic ecosystems is likely to stimulate heterotrophic metabolism, including stimulating the metabolism of more stable DOC in the system to CO_2 (Bianchi, 2011; Vonk and Gustafsson, 2013; Hood *et al.*, 2015). Thus despite the small global magnitude of glacial DOC, it appears disproportionately relevant to carbon cycling (Hood *et al.*, 2015) and may ultimately feedback to climate change through increasing CO_2 efflux/amplifying the PCF (Hood *et al.*, 2009; Lawson *et al.*, 2014; Hood *et al.*, 2015). Highly biolabile carbon from glaciers and ice sheets can also enter the oceans, through runoff and iceberg calving, where it impacts upon marine ecosystems (Bianchi, 2011; Hood *et al.*, 2015). It is becoming clear that reactivity of the DOC is as important as magnitude for consideration in global carbon budgets (Vonk *et al.*, 2013).

5.2.5 Rationale for This Research

Climate-driven changes to glacier and ice sheet runoff are expected to be larger than climate impacts on other components of the hydrological cycle (Hood *et al.*, 2015), but despite the significance of this component of the hydrological cycle, there is scant knowledge of organic carbon export from ice sheets to the oceans (Bhatia *et al.*, 2013) and no directly measured data exists for CO_2 efflux from meltwaters to the atmosphere. Because of the size of the carbon pool and the intensity of climate forcing at high latitudes, carbon stored in permafrost is potentially Earth's most significant carbon-climate feedback, yet one of the least understood (Tarnocai *et al.*, 2009), and few direct measurements of CO_2 efflux from the thaw waters to the atmosphere are reported. Thus exploring linkages between the cryosphere carbon cycle, its fluvial drainage system and the atmosphere are crucial, and cryospheric systems need to be included in global carbon budgets.

This chapter aims to: (i) quantify, by direct measurement, and compare the magnitude of CO_2 effluxes from the melt/thaw waters of two cryospheric systems: the Greenland ice sheet and the local permafrost-landscape; (ii) determine the main controls on CO_2 efflux from these systems, by assessing relationships with other physicochemical parameters and spatiotemporal variation; (iii) investigate the source or sources of the carbon in both systems using stable isotope analysis, and assess whether physical and biological processes alter the source DIC pool using diel sampling; and, (iv) determine the age of the carbon in both systems using radiocarbon dating in order to determine whether old, biolabile, previously stored carbon is being returned to the atmosphere and feeding back to climate change.

By gaining this further understanding of carbon dynamics in the cryosphere, a system highly vulnerable to a changing climate, improved predictions of how this system might respond to climate change can be made, and global carbon-cycle budgets improved to more accurately include the high latitudes. Included in this chapter is an attempt to estimate the contribution of CO_2 efflux from an Arctic region to global CO_2 efflux.

5.2.5.1 Why Greenland?

Greenland is expected to warm at up to three times the global average by the end of the century (IPCC, 2007; Kamenos *et al.*, 2012) and so is highly vulnerable to ongoing climatic variations and change (Mernild and Hasholt, 2009). Warming of this region has been of considerable scientific interest as runnoff from the GrIS is the largest source of glacial runoff globally (Lawson *et al.*, 2014) and its magnitude is increasing and this has global implications for e.g. climate, sea level and ecosystems (Hanna *et al.*, 2008; Bhatia *et al.*, 2013; IPCC, 2013). If the ice sheet were to melt entirely there would be a 7m sea level rise (Bartholomew *et al.*, 2010). The Kangerlussuaq region was chosen for its relative accessibility (local airport and Kangerlussuaq International Science Support Centre), and because thawing permafrost-landscape and ice systems exist in close vicinity (logistically beneficial) while being hydrologically disconnected (allowing for straightforward comparisons).

5.3 Methods

5.3.1 Field Site Description

Kangerlussuaq is remote and the settlement has a population of 499 (Statbank Greenland, 2016), with an airport, a small tarmac road system and basic amenities in the settlement centre. Beyond the centre there are only two gravel roads, one leading NE that terminates close to the Ice Sheet, and one leading SW that terminates near the harbour. Access to and transport in the area is therefore restricted and slow, e.g. it takes two to three hours to get to the ice margin from the accommodation (at KISS) in Kangerlussuaq. Fieldwork was carried out in two contrasting systems: the proglacial Akuliarusiarsuup Kuua River (AR) and permafrost-landscape surface-thaw waters (PLST) (Figure 53).

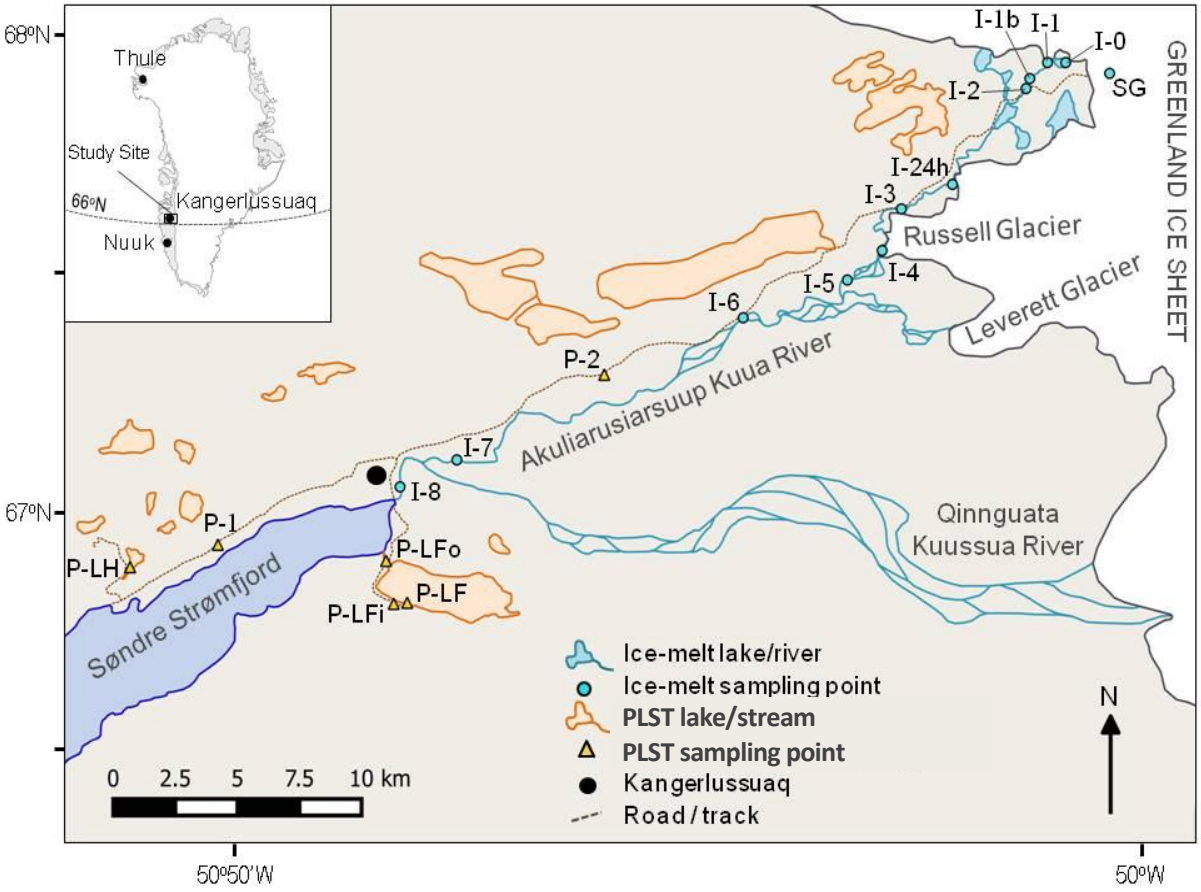

Figure 53: Kangerlussuaq region field site map

Showing sampling locations in the ice-melt and PLST (permafrost-landscape surface-thaw) systems. Also location of the ice margin, proglacial river system, landscape surface-thaw lakes and the fjord. All ice-melt locations begin with "I", all permafrost-landscape surface-thaw locations begin with "P", SG = supraglacial stream, 24h = diel sampling location, LF = Lake Ferguson, LFi and LFo = Lake Ferguson inlet springs and outlet stream respectively, LH = Lake Helen. Map features were traced from Google Earth images (taken between 2004 to 2014); diagrammatic river braiding represents the routes of the main channels at the time of the image.

The cold, semi-arid climate in this region limits the presence of humid luxuriant vegetation (Willemse, 2002). Much of the landscape vegetation is dominated by the deciduous shrub *Salix glauca* (willow family) and dwarf shrub vegetation *Betula nana* (birch family) and *Vaccinium uliginosum* (heather family) (Eisner *et al.*, 1995) which are C3 plants. On areas of glacial outwash plain, the vegetation is sparse and predominantly a xerophilos (adapted to dry conditions) grassland (Willemse, 2002). CAM photosynthesis dominates in desert ecosystems (Clark and Fritz, 1997) so it is possible these grasses are CAM plants, however, the natural vegetation of temperate and high latitude regions is almost exclusively C3 (Clark and Fritz, 1997) and 90% of the biomass of the xerophyte plants of the Asiatic cold desert are reported to be C3 species (Shuyskaya et al., 2012). Thus CAM species, if present in this region, are likely to be in low proportion and the vegetation is likely to be predominantly C3.

The predominant source of water to AR is subglacial drainage (Ryu and Jacobson, 2012). Supraglacial runoff contributions occur but are small in comparison (van As *et al.*, 2012). Other inputs of water to AR include lakes and precipitation (Ryu and Jacobson, 2012), but, due to the predominantly closed basin nature of these lakes (Aebly and Fritz, 2009), the continuous permafrost soils (Jørgensen and Andreasen, 2007), and the arid climate (Jørgensen and Andreasen, 2007; Russell, 2007) these are negligible compared to inputs from the GrIS (Ryu and Jacobson, 2012). The two systems are thus hydrologically disconnected allowing for comparisons to be made between the two systems as not complicated by their mixing. Chapter 2 contains an overview of each system and detail on climate and catchment characteristics; information of specific sampling points and regimes is provided here.

5.3.1.1 Akuliarusiarsuup Kuua River (AR)

This river has been termed the ice-melt system (prefix I on site names), and nine sampling sites span the full length of AR. Two additional sites were sampled, one in a supraglacial meltwater stream (SG, Figure 53) that drains into the headwaters of AR, and one after the confluence with the Qinnguata Kuussua River, in the Watson River, just before discharge into the fjord (I-8, Figure 53). Due to the equipment configuration and the large size of the channel, all measurement points (excluding SG) are located off-centre close to the banks. Measurement points are described below, see Figure 53 for locations. Channel widths were estimated (at the bank-full) in Google Earth using the ruler tool.

SG: 67°09’09”N, 50°01’55”W, 503 m.a.s.l., within a supraglacial meltwater stream, meandering channel 0.8 – 1.0 m wide, small ice chunks carried within the flow. Located 2.17 km upstream of the ice margin.

I-0: 67°09’20”N, 50°04’11”W, 436 m.a.s.l., approx 200 m downstream of the ice margin, within a braided channel with pebble/boulder bed. Located 0.25 km downstream of the ice margin.

I-1: 67°09’20”N, 50°05’11”W, 364 m.a.s.l., 40 m downstream from a large turbulent waterfall and 300 m downstream of a proglacial lake, within a braided channel with pebble/boulder bed, bordered by steep shrub-vegetated banks. Located 1.08 km downstream of the ice margin.

I-1b: 67°09’01”N, 50°06’07”W, 347 m.a.s.l., single 35 m wide channel with pebble/boulder bed, steep moraine and small shrub/grass-vegetated banks. Located 2.00 km downstream of the ice margin.

I-2: 67°08’48”N, 50°06’22”W, 332 m.a.s.l., single 55 m wide channel with pebble/boulder/soft sediment bed and flat moss/grass-vegetated banks. Located 2.45 km downstream of the ice margin.

I-24h: 67°06'50"N, 50°10'25"W, 293 m.a.s.l., single channel with pebble/boulder and exposed bedrock bed and banks. Grasses/mosses/shrubs on surrounding landscape. Channel runs close to the ice sheet but is separated from it by moraine deposit. Located 8.05 km downstream of the ice margin.

I-3: 67°06'19"N, 50°13'14"W, 194 m.a.s.l., single 35 m wide channel with sand/gravel bed, and a shallow gradient bank vegetated with shrubs. The opposite bank is moraine. Located 10.70 km downstream of the ice margin.

I-4: 67°05'29"N, 50°14'18"W, 162 m.a.s.l., single 60 m wide channel at the Russell Glacier snout with pebble/boulder bed. Bordered by glacier snout ice cliff on one side, and exposed gneiss bedrock and pebble/boulder bank on the other side. Surrounding hillsides dominated by shrub vegetation. Numerous ice blocks carried within the river. Located 13.90 km downstream of the ice margin.

I-5: 67°04'52"N, 50°16'17"W, 150 m.a.s.l., single 50 m wide channel with boulder/pebble bed and steep sandy/rocky banks with shrubs, grasses and flowering plants on the flatter tops. Located 15.80 km downstream of ice margin.

I-6: 67°04'11"N, 50°21'35"W, 126 m.a.s.l., in a 10 m wide channel within a braided channel with sand/gravel bed, and shallow gradient with grasses and large shrub vegetation. At the downstream edge of an area of sandur (glacial outwash plain). Located 21.90 km downstream of the ice margin.

I-7: 67°01'08"N, 50°37'45"W, 35 m.a.s.l., single 230 m wide channel with sand bars, and a sandy bed. The whole area is very sandy with wind-blown dunes and sparse grasses and flowering plants. Located 36.70 km downstream of the ice margin.

I-8: 67°00'35"N, 50°40'54"W, 8 m.a.s.l., single 160 m wide channel with sand bars and a sandy bed with some boulders. The whole area is very sandy with river banks comprised of sand, boulders and some exposed gneiss bedrock. Located 40.20 km downstream of the ice margin.

5.3.1.2 Permafrost-Landscape Surface-Thaw Waters (PLST)

Six sampling sites were chosen to include a variety of surface-thaw waters from the permafrost-landscape over a spatial range (prefix P on site names). Two small pools (P-1 and P-2, 50 and 130 m wide) one medium lake (Lake Helen, P-LH, 1200m in length) and one large lake (Lake Ferguson, P-LF, 5.5 km in length) were sampled, as well as inlet springs (P-LFi) and the outlet stream (P-LFo) of Lake Ferguson (Figure 53). Due to equipment configuration, all measurement points were located close to an edge of the pools and lakes. Measurement points are described below, see Figure 53 for locations.

P-LF: 66°58'15"N, 50°41'13"W, 72 m.a.s.l., south edge of Lake Ferguson, 5.5 km in length, with a surrounding landscape of gentle hills with exposed bedrock and shrub/moss vegetation. Ice covered the whole surface except the very edges on 03/06/2014, ice was broken and gathered at the outlet on 12/06/2014, ice was gone by 16/06/2014.

P-LFi: 66°58'10"N, 50°41'15"W, 85 m.a.s.l., within a spring system draining from the hillside into Lake Ferguson. 0.4 m wide channel, approximately 150 m from the lake bank, among shrub/moss vegetation. Spring flow was much reduced by 22/06/2014 and had dried up all together by 1/07/2014.

P-LFo: 66°59'04"N, 50°41'38"W, 60 m.a.s.l., outlet stream from Lake Ferguson flowing into Søndre Strømfjord. 1 m wide channel in gently sloping ground vegetated with shrubs grasses and mosses. Some grasses present within the channel.

P-LH: 66°58'56"N, 50°55'50"W, 112 m.a.s.l., western edge of Lake Helen, which is 1200 m in length with evidence of inlet and outlet channels albeit dry for the duration of the field campaign. Ice covered ~70% of the surface on 06/06/2014, ice was gone by 12/06/2016. The surrounding landscape is gentle rocky hills with dry grasses and some shrubs.

P-1: 66°59'23"N, 50°51'01"W, 92 m.a.s.l., pool within the permafrost-landscape, 130 m in length with no inlet or outlet streams. The surrounding landscape is gentle hills with some exposed bedrock and shrub/grass vegetation.

P-2: 67°02'54"N, 50°29'38"W, 96 m.a.s.l., pool within the permafrost-landscape, 55m wide with no inlet or outlet streams. The surrounding land is gentle hills with exposed bedrock and shrub/grass vegetation.

5.3.2 Sampling Regime

This fieldwork comprised a 5-week intensive field campaign in 2014, where sampling was carried out most days in order to collect as much data as possible. The sites above were chosen to cover a wide area of different types of freshwater system (within feasible access), and were sampled so that temporal ranges in the two melt/thaw water systems could also be considered.

5.3.2.1 AR

Transect sampling of the whole river reach - 8 – 10 of the 12 ice-melt river locations sampled consecutively within 36 hours - was carried out three times during the field campaign. The transects were sampled across the field campaign – 7th-8th June 2014, 19th-20th June 2014 and 1st-2nd July 2014 – and took two days to complete as lengthy travel time between sites (caused by the

length of the river, the gravel vehicle track and some sampling points being an hour's walk from the track) meant a maximum of 5 locations could be sampled in a day. For the two June transects, sampling order was from ice sheet to fjord, but for the July transect sampling order was reversed to allow any artefact of the time of day (e.g. diel flow regime/diel temperature cycle) to be identified. One mini-transect was carried out on 25th June where an upper (I-2), mid (I-24h) and lower (I-6) river site were sampled on the same day. In addition, two temporally separated diel sampling campaigns were carried out on 14th – 15th June and 3rd – 4th July (see 5.3.3.3).

5.3.2.2 PLST

The four lake sampling sites (LF, LH, P1 and P2) were sampled 3 – 4 times each over the course of the field campaign. Lake Ferguson inlet springs (P-LFi) were initially sampled on 5th June to gauge efflux magnitude for planning of further sampling (particularly $^{14}CO_2$ – see 5.3.3.2). Subsequently three paired samplings of Lake Ferguson inlet springs and outlet stream (P-LFo) were carried out on 11th, 16th and 23rd June. These were spread temporally, but after 23rd June the springs dried up so no further sampling was possible. An additional opportunistic sampling of the outlet stream only was carried out on 12th June 2014.

5.3.3 Field Methods

On each sampling occasion, CO_2 efflux, a flow velocity profile (for subsequent calculation of hydraulic parameters), and environmental parameters (air and water temperature, wind speed, humidity, light intensity, weather observations) were measured. Samples were collected for laboratory measurement of water chemistry parameters on return to the UK (alkalinity, [DIC], $\delta^{13}C_{DIC}$). Additionally a qualitative visual assessment of the water surface state was made at the time of each CO_2 flux measurement. Where possible a full set of these measurements were made but on occasion, flow conditions, time constrains and/or equipment malfunction meant a sub-set of measurements were taken. Full details of these methodologies can be found in Chapter 2. Additional methodologies specific to this chapter are described below.

5.3.3.1 [DOC]

Water samples for [DOC] analysis were collected at the time of CO_2 efflux measurement in 100 ml centrifuge tubes, pre-rinsed three times with stream/river/pool water. To reduce biological degradation of samples, bottles were filled and lids replaced below the water surface and samples stored in the dark, refrigerated, and filtered (see 5.3.4). Samples were returned to Glasgow University for analysis and this took place in August 2014.

5.3.3.2 Radiocarbon Sampling, $\delta^{13}C_{efflux}$ and $\delta^{13}C_{DOC}$

Paired samples of evading CO_2 and fluvial DOC were collected for radiocarbon (^{14}C) analysis. Samples were collected from AR during two diel sampling campaigns (14^{th} – 15^{th} June and 3^{rd} – 4^{th} July, 2014; see 5.3.3.3), and from Lake Ferguson inlet and outlet (P-LFi and P-LFo respectively) of PLST on three distinct dates throughout the field campaign (11^{th}, 16^{th} and 23^{rd} June, 2014). CO_2 influx occurred during the 3^{rd} – 4^{th} July diel sampling and 23^{rd} June lake outlet sampling and so CO_2 evasion samples could not be collected. $\delta^{13}C$ of effluxed CO_2 ($\delta^{13}C_{efflux}$) and $\delta^{13}C$ of DOC ($\delta^{13}C_{DOC}$) could also be obtained from these samples (see 5.3.5.2).

$^{14}CO_2$ Efflux and $\delta^{13}C_{efflux}$

Evaded CO_2, for $^{14}CO_2$ and $\delta^{13}C_{efflux}$ analysis, was accumulated in the head space of a floating chamber which had first been scrubbed of atmospheric CO_2 (1 hour) using a soda lime cartridge (Billett *et al.,* 2006; Vihermaa *et al.,* 2014). To yield sufficient material for analysis (5 mL) accumulation time ranged from 1.5 – 2.5 hours (due to low CO_2 efflux rates, see Fig. 1 of main article), depending on the sampling point and hydrological conditions. A cartridge containing a 13X zeolite molecular sieve was used to trap the CO_2 that accumulated in the headspace (Hardie *et al.*, 2005; Billett *et al.*, 2006; Vihermaa *et al.*, 2014). Molecular sieve cartridges (MSC) were returned to the Natural Environment Research Council (NERC) Radiocarbon Facility, East Kilbride, for processing.

$DO^{14}C$ and $\delta^{13}C_{DOC}$

Water samples, for $DO^{14}C$ and $\delta^{13}C_{DOC}$ analysis, were collected simultaneously with $^{14}CO_2$ evasion samples. DOC levels in AR were particularly low (Table 14) so to ensure enough material could be yielded from the water for $DO^{14}C$ analysis (5 mL) 3 litres of water were collected on each sampling occasion in 1 litre Nalgene plastic bottles, pre washed in 5 Molar nitric acid and rinsed five times with stream/river/pool water. To reduce biological degradation of samples, bottles were filled and lids replaced below the water surface and samples stored in the dark, refrigerated and filtered (see 5.3.4). Samples were returned to the NERC Radiocarbon Facility for analysis (see 5.3.5.2)

5.3.3.3 Diel Sampling

Diel sampling was carried out to assess for physical or biological processes that might influence efflux and/or modify the DIC pool. Two diel sampling campaigns were carried out on AR at site I-24h (Figure 53) on 14^{th} – 15^{th} June and 3^{rd} – 4^{th} July, 2014, these dates spread temporally to capture any changes over the melt season.

A full set of standard measurements (efflux, hydraulic, water chemistry and environmental; see 5.3.3 for list) was made 4 to 5 times over the 24-hour sampling period (maximum sampling

frequency due to time/other sampling constraints). The initial measurement time was repeated for the final measurement to ensure a complete sampling cycle, and measurements were made 5 to 10 hours apart. Between full measurement sets, sub-sampling was carried out (only [DIC]/$\delta^{13}C_{DIC}$ sample collection, and pH and air/water temperature measurement), as this took minimal time but provided valuable additional data for analysis of diel patterns in [DIC], $\delta^{13}C_{DIC}$ and pCO_2.

Three sets of paired samples of evading CO_2 and fluvial DOC were collected for radiocarbon (^{14}C) analysis during the diel sampling campaigns (see 5.3.3.2). Samples were collected a minimum of 5 and a maximum of 16 hours apart (but commonly 7.5 to 11 hours apart). Ideally these samples would have been collected 8 hours apart for even spacing over the 24-hour period, however, slow CO_2 accumulation times, equipment malfunction and time required for other necessary measurements/sampling deemed ^{14}C sampling times hard to control.

5.3.4 Storage and Transportation of Samples

Microbial activity, including photosynthesis and respiration, can alter the carbonate chemistry or water samples post collection (Atekwana and Krishnamurthy, 1998). Prior to storage and transportation water samples for DO^{14}C and [DOC] were filtered using pre-combusted 0.7um Whatman GF/F filter paper, to reduce biological degradation. For DO^{14}C samples this was 2 – 18 hours after collection for the permafrost-landscape surface-thaw samples, and 5 – 36 hours after collection for the ice-melt samples collected during diel sampling (the latter required only for samples collected early in the diel sampling period). For [DOC] samples this was within 36 hours of collection (usually 2 – 18 hours after collection, unless sampling over a 24-hour period). After filtration samples were stored in the dark and refrigerated for the duration of the field campaign.

It was not possible to filter [DIC]/$\delta^{13}C_{DIC}$ samples without exposing them to atmospheric CO_2, and because the sampling method involves acidification of the samples (Chapter 2) subsequent modification of the DIC pool by biological activity is unlikely (Wadlron *et al.*, 2014).

5.3.4.1 [DOC]

Samples were stored in the shade while in the field (2 to 18°C depending on location/time), then stored in the dark and refrigerated upon return from the field, after filtration, generally 2 to 12 hours after collection, but up to 36 hours after collection for samples collected during diel sampling campaigns. Upon completion of the field campaign, samples were transported to the UK by air in the 100 ml centrifuge collection containers, unrefrigerated, in the dark, and were returned to the University and refrigerated within 5 weeks.

5.3.4.2 [DIC] and $\delta^{13}C_{DIC}$

Samples were placed in the shade while in the field, then stored in the dark and refrigerated upon return from the field, generally 1 to 12 hours after collection, but up to 36 hours after collection for samples collected during the diel sampling campaign. Upon completion of the field campaign, samples were transported back to the UK unrefrigerated, in the dark, in their 12ml exetainers, cap down (so the liquid was in contact with the septa, to minimise air ingress/egress) within cardboard boxes. All samples were transported by air, half were transported in hand luggage and so were returned to the University and refrigerated within 3 days, half were transported by courier and were returned and refrigerated within 5 weeks.

5.3.4.3 $DO^{14}C$ and $^{14}CO_2$ (and $\delta^{13}C_{DOC}$ and $\delta^{13}C_{efflux}$)

$DO^{14}C$ samples (3L water) were stored in the dark and the shade while in the field and refrigerated and stored in the dark upon return from the field, after filtration – this was between 2 and 26 hours after collection. Samples were transported back to the UK by air in the 1 L nalgene collection bottles, unrefrigerated, in the dark, within a pelicase, and were returned to the University and refrigerated within 5 weeks. $^{14}CO_2$ samples (13X zeolite molecular sieve cartridges) were stored in a dark dry location for the duration of the field campaign, then transported back to the UK by air in hand luggage within 3 days.

5.3.5 Laboratory Methods

5.3.5.1 [DOC]

A known volume of filtrate was acidified to pH 3.9 upon return to the UK (within 12 weeks of sample collection) to convert any DIC to $CO_{2(g)}$, and placed in an ultrasonic bath for 15 mins to encourage CO_2 to leave the sample. Filtered, acidified samples were subsequently analysed for dissolved organic carbon concentration [DOC] using an Analytical Sciences Thermalox TOC 2020, with a correction made for the mass of acid that diluted the sample [DOC].

5.3.5.2 Radiocarbon

$^{14}CO_2$ and $\delta^{13}C_{efflux}$

Upon return to the NERC Radiocarbon Facility, CO_2 was released from the MSC by heating to 500°C and purified cryogenically while purging with high-purity nitrogen gas (Garnett and Murray, 2013). The CO_2 recovered was graphitized by iron/zinc reduction and ^{14}C measured by accelerator mass spectrometry at the Scottish Universities Environmental Research Centre (SUERC) AMS Laboratory (Billett *et al.*, 2006; Garnett and Murray, 2013; Vihermaa *et al.*, 2014). An un-graphitized sub sample was analysed for $\delta^{13}C_{efflux}$ on a dual-inlet isotope ratio mass spectrometer (VG Optima, UK) at the NERC Radiocarbon Facility (Garnett and Murray, 2013). Results were obtained within 18 weeks of sample collection.

DO^{14}C and $\delta^{13}C_{DOC}$

After filtration and storage during the field campaign, samples were subsequently returned to the NERC Radiocarbon Facility for analysis. A known volume of filtrate was condensed by rotary evaporation, freeze-dried, then concentrated hydrochloric acid added to hydrolyse and remove any inorganic carbon present. Following vacuum evacuation of the container, the evaporated/ dried/acidified sample was heated to 63^{o}C using a water bath, then DOC recovered as $CO_{2(g)}$ by heating with copper(II) oxide in a sealed quartz tube. The CO_2 recovered was graphitized by iron/zinc reduction and ^{14}C content determined by accelerator mass spectrometry at SUERC AMS Laboratory similar to method used in Evans *et al.* (2014). An un-graphitized sub sample was analysed for $\delta^{13}C_{DOC}$ concentration on a dual-inlet stable isotope mass spectrometer (Thermo Fisher Delta V) at the NERC Radiocarbon Facility. Results were obtained within 36 weeks of sample collection.

Notation

Following convention (Stuiver and Polach, 1977) ^{14}C results (DOC and CO_2) were normalized to δ^{13}C of -25 ‰ to account for mass dependent fractionation (Garnett and Murray, 2013; Vihermaa *et al.*, 2014). Results are expressed as %modern (relative to a baseline of 100% modern in 1950) and conventional radiocarbon age (in years BP, where 0 BP = 1950 AD), where conventional radiocarbon age (yr BP) = $-8033 \times \mathrm{LN}(\%\mathrm{modern}100^{-1})$ (Garnett and Murray, 2013; Vihermaa *et al.*, 2014). Both are expressed at ±1σ overall analytical confidence. At the time of this study, atmospheric Δ^{14}C value was ~103 % modern (calculated from Levin and Kromer, 2004 and Levin *et al*., 2013), and lower than that reported for 2008 (105 % modern, Hartley *et al*., 2013).

5.3.6 Data Analysis

5.3.6.1 CO_2 Efflux Upscaling

Field measurements were made in a river reach from the Greenland Ice Sheet (GrIS) margin to the head of Søndre Strømfjord, which includes both the Akuliarusiarsuup Kuua River and the Watson River. Their combined lengths were measured using the ruler tool Google Earth and totalled 41.1 km. Using the spatial pattern in CO_2 efflux (Figure 59), the transition point between overall efflux and only influx was calculated as the equidistant point (12.3 km), between the sampling points at 10.6 m where there was overall efflux and 13.6 km where there was only influx, and mean CO_2 efflux rate upstream and downstream of this transition point was calculated.

The bankfull width of the reach was measured every 500 m – 1 km using the ruler tool in Google Earth and average width upstream and downstream of the efflux-influx transition point calculated (0.135 km and 0.353 km respectively). Using these widths and the length measurements, river surface area was calculated upstream and downstream of the efflux-influx transition point.

The average melt period of the river reach was estimated to be on average 106.5 days, from Bartholomew *et al.* (2011); van As *et al.* (2012) and Hasholt *et al.* (2013) who reported the melt period for years between 2007 and 2010. Total CO_2 fluxes of the upper and lower reaches over 1 year were calculated by multiplying the average up- and down-stream CO_2 fluxes by the estimated up- and down-stream surface areas and average number of days in the melt season. Lewis and Smith (2009) report that there are 335 rivers draining the GrIS, which was used to estimate the total CO_2 flux for the whole of Greenland.

5.4 Results

Table 14 summarises the important carbon pools in each melt/thaw system, Table 15 provides the radiocarbon age of effluxed CO_2 and transported DOC in each system. Sections 5.4.1 to 5.4.7 detail the magnitude, controls and spatiotemporal variation of the CO_2 fluxes, the age and $\delta^{13}C$ of the carbon pools and upscaling of CO_2 efflux.

Table 14: Comparison of important carbon pools*

	Melt/Thaw Water System	
	Akuliarusiarsuup Kuua River (AR)	**Permafrost-Landscape Surface-Thaw (PLST)**
***n* efflux:*n* influx:*n* equilibrium**	12:25:2	19:3:0
CO_2 efflux (µmol CO_2 m^{-2} s^{-1})	-0.14 [-0.09] -2.19:4.31 *39*	0.27 [0.23] -3.15:1.28 *22*
[DIC] (mmol L^{-1})	0.07 [0.06] 0.01:0.17 *46*	0.71 [0.55] 0.11:1.91 *22*
δ^{13}_{DIC} (‰)	-3.1 [-2.9] -11.7:7.4 *43*	-4.2 [-3.4] -9.5:-0.04 *22*
pH	7.4 [7.3] 6.8:8.3 *43*	7.65 [7.75] 7.1: 8.25 *25*
[DOC] (mg L^{-1})	4.8 [4.8] 3.0:7.3 *45*	30.9 [24.7] 9.6:89.5 *22*
***p*CO_2 (ppm)**	115 [127] 4:181 *41*	596 [411] 220:2520 *22*
E*p*CO_2 (ppm)	-273 [-261] -384:-207 *41*	208 [23] -169:2132 *22*

*Mean [median] minimum:maximum *n*. *n* = number. CO_2 flux considered to be at equilibrium when efflux <0.01 or influx >-0.01.

Table 15: Comparison of radiocarbon age and associated $\delta^{13}C$*

	RADIOCARBON AGE					
	Melt/Thaw Water System					
	Akuliarusiarsuup Kuua River (AR)			**Permafrost-Landscape Surface-Thaw (PLST)**		
	Site	**Date,Time**	**(years BP ± 1σ ; $\delta^{13}C_{VPDB}$ ‰ ±1)**	**Site**	**Date,Time**	**(% Modern ± 1σ ; $\delta^{13}C_{VPDB}$ ‰ ±1)**
Effluxed CO_2	I-24h	14/06,16:45	966 ±36 ; -14.6	P-LFi	11/06,18:15	103.19 ±0.48 ; -14.5
	I-24h	15/06,00:15	886 ±38 ; -14.6	P-LFo	11/06,14:30	103.83 ±0.49 ; -12.3
	I-24h	15/06,11:00	809 ±38 ; -14.6	P-LFi	16/06,15:40	102.19 ±0.48 ; -15.0
		Mean:	**887 ; -14.6**	P-LFo	16/06,18:30	103.22 ±0.46 ; -12.7
		SD:	**79 ; 0.0**	P-LFi	23/06,12:50	102.75 ±0.48 ; -16.4
						Mean: 103.04 ; -14.2
						SD: 0.6 ; 1.7
DOC	I-24h	14/06,17:00	6258 ±38 ; -35.2	P-LFi	11/06,17:45	104.68 ±0.48 ; -28.0
	I-24h	15/06,00:40	6544 ±38 ; -26.5	P-LFo	11/06,15:00	101.80 ±0.47 ; -26.7
	I-24h	15/06,11:30	6048 ±37 ; -25.6	P-LFi	16/06,16:00	104.14 ±0.45 ; -27.7
	I-24h	03/07,13:30	5641 ±38 ; -25.4	P-LFo	16/06,18:40	102.95 ±0.45 ; -26.4
	I-24h	03/07,22:30	6678 ±39 ; -32.0	P-LFi	23/06,13:30	104.33 ±0.48 ; -28.0
	I-24h	04/07,07:30	5205 ±50 ; -31.4	P-LFo	23/06,15:45	101.81 ±0.47 ; -26.7
		Mean:	**6062 ; -29.4**			**Mean: 103.29 ; -27.3**
		SD:	**559 ; 4.1**			**SD: 1.3 ; 0.7**

*P-LFi = permafrost-landscape surface-thaw system, Lake Ferguson inlet spring; P-LFo = permafrost-landscape surface-thaw system, Lake Ferguson outlet stream; I-24h = ice sheet melt system, diel sampling site. See Figure 53 for locations.

5.4.1 Magnitudes of CO_2 Fluxes

CO_2 efflux rates ranged between -3.15 and 4.31 µmol CO_2 m^{-2} s^{-1} in the two systems. This range of efflux falls within previously reported values, but is very low compared to other systems globally (Appendix B – Long *et al*., 2015; Figure 71).

The two systems had comparable CO_2 efflux ranges, but the ice melt system had a negative mean CO_2 efflux (mean influx) and the permafrost-landscape surface-thaw system had a positive mean efflux: -0.14 and 0.27 µmol CO_2 m^{-2} s^{-1} respectively. Despite having a mean influx, the ice melt system had the highest maximum CO_2 efflux at 4.31 µmol CO_2 m^{-2} s^{-1} compared with 1.28 µmol CO_2 m^{-2} s^{-1} in the permafrost-landscape surface-thaw system. Both systems effluxed and influxed CO_2, however influx was measured on a greater proportion of sampling occasions in the GrIS melt system than in the PLST system which effluxed in the majority of measurements (Figure 54).

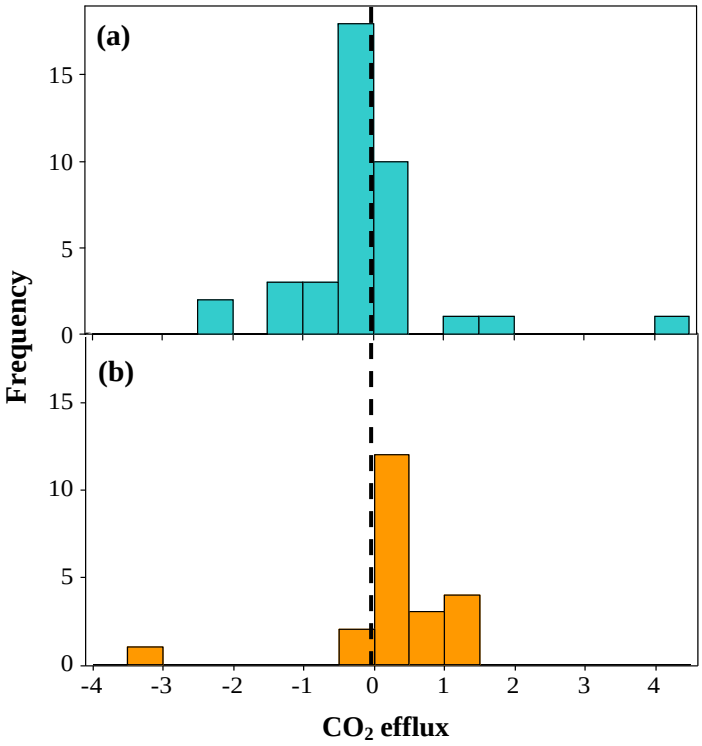

Figure 54: CO_2 efflux ranges in the ice-melt and permafrost-landscape surface-thaw systems

The ice-melt system (a) influxed in 64% of cases (n = 39) and the permafrost-landscape surface-thaw system (b) effluxed in 86% of cases (n = 22). Dashed line shows zero efflux point (equilibrium with the atmosphere).

5.4.2 Influence of Hydraulic Parameters

Unlike Drumtee water and River Kelvin (Chapter 3), and other reported temperate and tropical rivers (Long *et al.*, 2015) the rate of CO_2 efflux is not correlated with flow velocity (Figure 55) or other measures of turbulence and flow intensity (Appendix H).

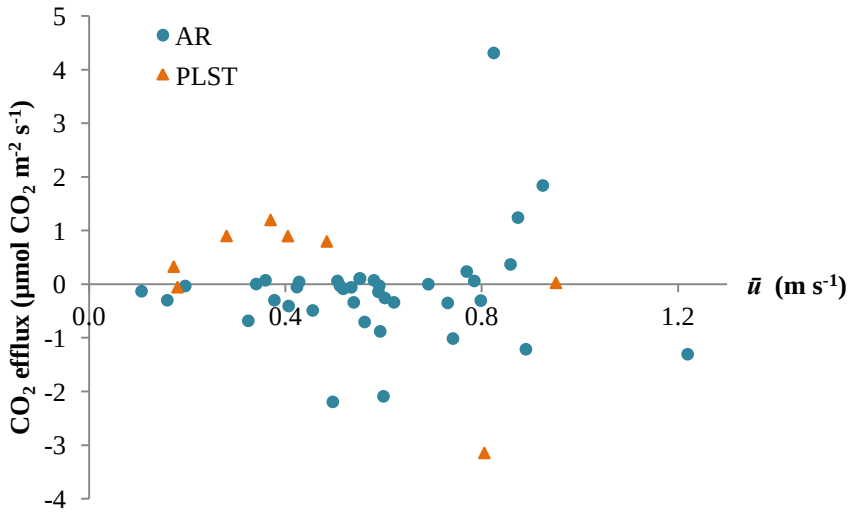

Figure 55: CO_2 efflux showing no relationship to flow intensity

Mean velocity ($\bar{u}$) is a proxy for flow intensity

5.4.3 Quantifying the Carbon Pools

The concentration ranges of ice meltwater carbon pools (AR) were much smaller than that for the permafrost-landscape surface-thaw water systems (PLST) (Table 14), and ratios (AR : PLST) between the median values are [DIC] 1 : 9.2; [DOC] 1 : 5.1; pCO_2 1 : 3.2.

5.4.3.1 pH, [DIC] and pCO_2

pH was relatively high in both systems (PLST 7.1 – 8.3; ice melt 6.8 – 8.3) compared to other global locations (Long *et al.*, 2015). [DIC] and pCO_2 in the ice melt system are very small (0.07 – 0.17 mmol and 4 – 180 ppm), with pCO_2 showing undersaturation of CO_2 with respect to the atmosphere on all sampling occasions (saturation is ~ 400 ppm; NOAA, 2016a), whereas [DIC] and pCO_2 in the PLST system (0.11 – 1.91 mmol and 220 – 2520 ppm) are comparable to systems with substantially higher efflux (Raymond *et al.*, 2013; Long *et al.*, 2015) and show oversaturation in 50% of cases.

pCO_2 incorporates the effects of pH and [DIC] and does not correlate with CO_2 efflux nor improve the relationship of hydraulic parameters and CO_2 efflux (Figure 56 and Figure 57), unlike observed elsewhere (Chapter 3; Long et al., 2015).

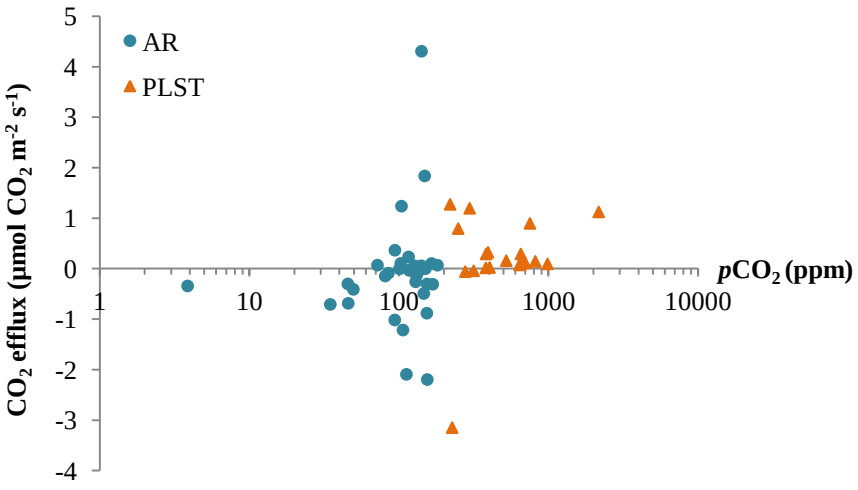

Figure 56: CO_2 efflux shows no relationship to pCO_2
pCO_2 is displayed on a logarithmic scale

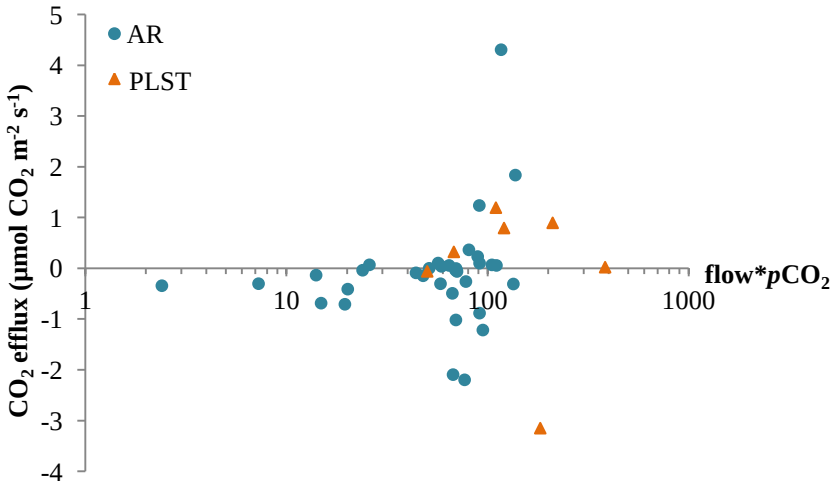

Figure 57: CO_2 efflux shows no relationship to flow*pCO_2
Flow*pCO_2 displayed on a logarithmic scale, flow in m s^{-1} and pCO_2 in ppm.

5.4.3.2 DOC

[DOC] was relatively high in PLST and very low in the ice meltwater (PLST, mean 30.9 mg L^{-1}, n = 22; ice meltwater, mean 4.8 mg L^{-1}, n = 41). These fall within previously reported ranges for other global sites (e.g. temperate peatland streams: 25 – 85 mg L^{-1}, Cummins and Farrell, 2003, 4 – 88 mg L^{-1}, Dinsmore *et al.*, 2013; temperate rivers: 0 – 135 mg L^{-1}, Worrall and Burt, 2010; tropical rainforest streams: 0.5 – 4 mg L^{-1}, Bass *et al.*, 2011; Arctic river: 5.5 – 165.8 mg L^{-1}, Spencer *et al.*, 2015; and lakes globally: 0.1 – 332 mg L^{-1}, Sobek *et al.*, 2007). There does not appear to be a relationship between CO_2 efflux and [DOC] in either melt/thaw system (Figure 58).

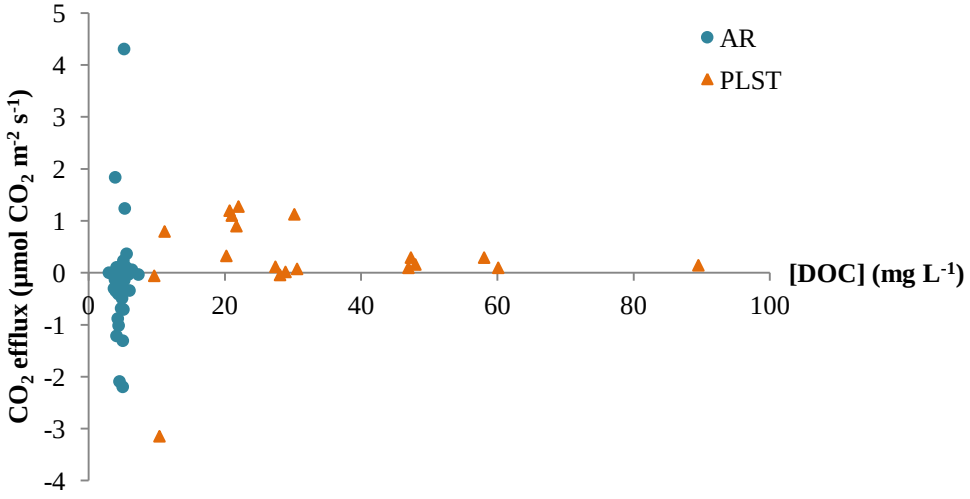

Figure 58: CO_2 efflux shows no relationship to [DOC]

5.4.4 Spatiotemporal Patterns of CO_2 Efflux

In the ice-melt system, CO_2 efflux varied spatially, decreasing with distance away from the ice margin (Figure 59), with no pattern over time. The highest CO_2 efflux rates were at the ice margin. This decreases rapidly to 2.45 km downstream where equilibrium with the atmosphere is reached, and beyond 10.7 km downstream the river only influxes. The supraglacial streams (-2.17 km, on top of the ice sheet) were consistently a sink for atmospheric CO_2 (-0.3 to -0.4 μmol CO_2 m^{-2} s^{-1}, n = 3, measured on three separate days).

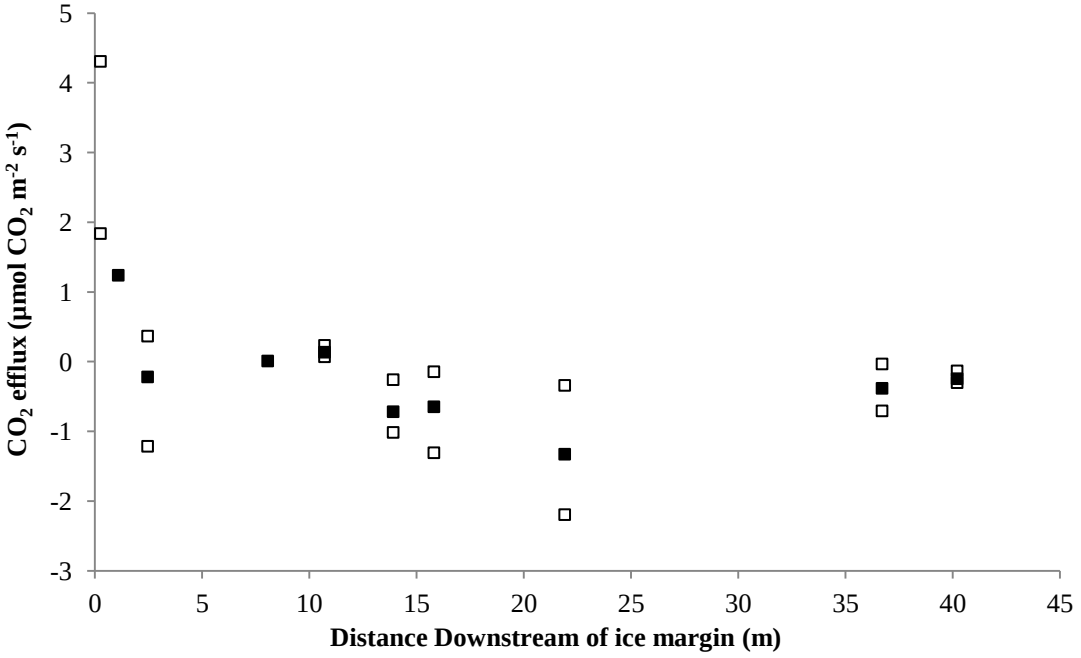

Figure 59: Spatial variation in CO_2 efflux from the ice-melt system

The ice margin is at 0 km. Solid squares indicate mean $\delta^{13}C_{DIC}$, and upper and lower squares indicate maximum and minimum $\delta^{13}C_{DIC}$, respectively. For locations where only one or two measurements were made, hollow squares are used and no average is displayed.

There was no temporal pattern of efflux during either of the diel monitoring periods in AR (Figure 60). Other water chemistry parameters ($\delta^{13}C_{DIC}$, [DIC], pH, alkalinity, temperature) were also monitored over the 24-hour periods; none showed diel patterns (Appendix I) except for $\delta^{13}C_{DIC}$ which is discussed in 5.4.6.1.

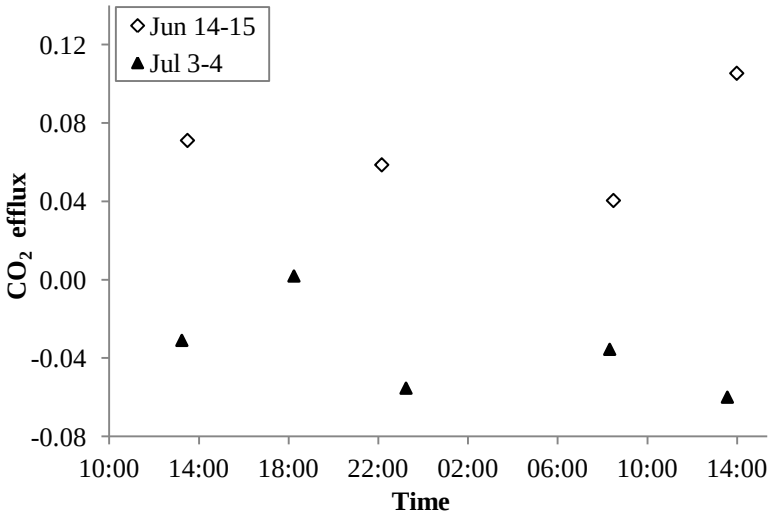

Figure 60: Temporal variation in CO_2 efflux over two 24-hour periods in the ice-melt system
CO_2 efflux in µmol CO_2 m^{-2} s^{-1}. From field observations peak flow was ~ 22:00. Diel sampling was not carried out in the permafrost-landscape surface-thaw system.

Efflux from PLST showed a temporal pattern: it was highest close to the start of the melt season and decreased over time (Figure 61). Lake Ferguson outlet stream began to influx towards the end of the study period.

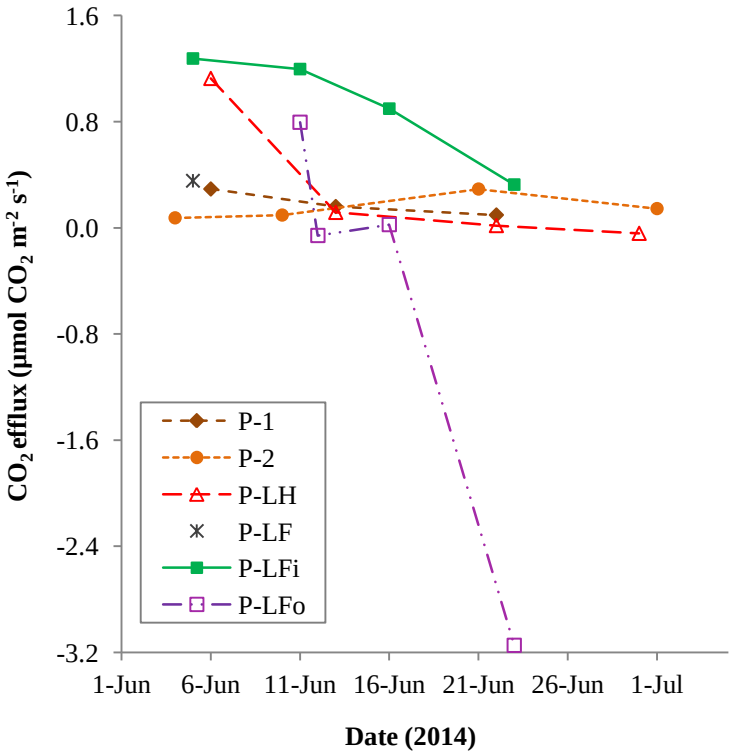

Figure 61: Temporal variation in CO_2 efflux from the permafrost-landscape surface-thaw system
All sites except P-2 show a decrease in CO_2 efflux over time. For site codes and locations see Figure 53.

5.4.5 Age of the Carbon Pool

5.4.5.1 Permafrost-Landscape

The permafrost-landscape surface-thaw water DOC and effluxed CO_2 had ages of 103.29 % and 103.04 modern, respectively (Table 15), indicating the carbon was fixed more recently than 1950 and is thus considered to be modern carbon.

5.4.5.2 Ice

The ice meltwater effluxed CO_2 and exported DOC had ages of 809 ±38 to 966 ±36 yrs BP and 5,205 ±50 to 6,678 ±39 yrs BP respectively (Table 15). The effluxed CO_2 is old, but the DOC exported was considerably (5 to 8 times) older, and older than DOC exported in SW Greenland (2,300 – 4,100 years BP, n = 5; Bhatia et al., 2013).

5.4.6 $\delta^{13}C$ of the Carbon Pool

5.4.6.1 $\delta^{13}C_{DIC}$

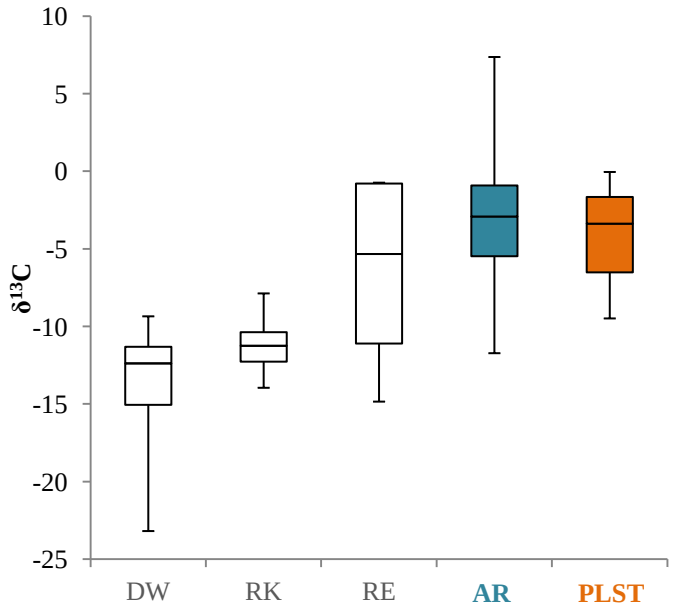

Figure 62: Ranges of $\delta^{13}C_{DIC}$
AR in turquoise and PLST in orange. The UK sites (Chapters 3 and 4) are included (colourless) for comparison.

$\delta^{13}C_{DIC}$ of ice meltwater is ^{13}C-enriched and often close to 0 ‰ with a median of -2.9 ‰ (Table 14; Figure 62). The $\delta^{13}C_{DIC}$ of PLST water is also ^{13}C-enriched, but generally less so than the ice meltwater, with the mean and median being -4.2 and -3.4 ‰ respectively. The range of $\delta^{13}C_{DIC}$ is greater in the ice meltwater (Table 14; Figure 62) with the maximum value being more ^{13}C-enriched at 7.4 ‰. When compared to the sites of Chapters 4 (DW, RK and RE) $\delta^{13}C_{DIC}$ of both the ice-melt and PLST systems is most similar to RE, although both sites have a slightly more ^{13}C-enriched range than RE (Figure 62).

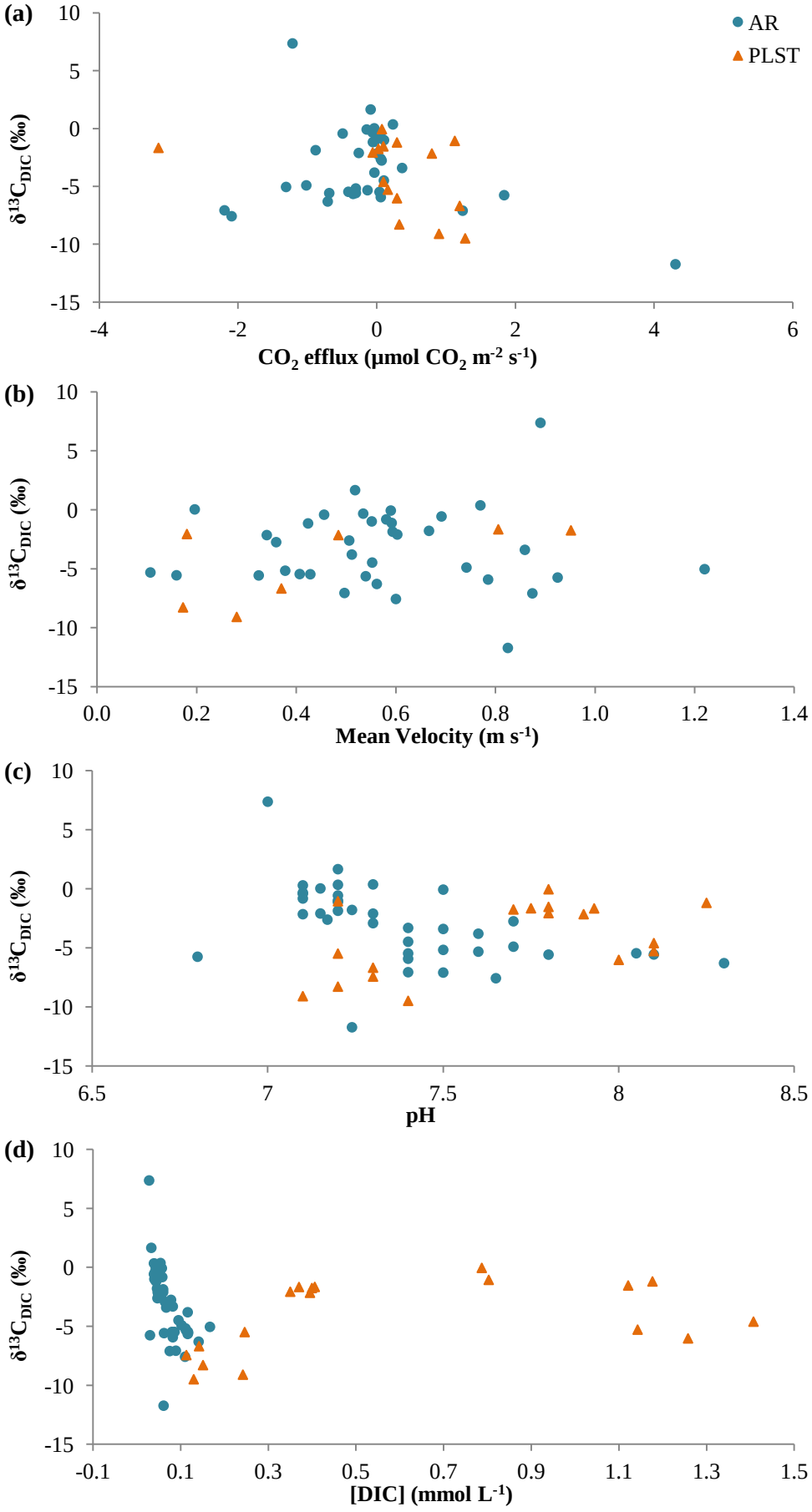

Figure 63: Relationship of $\delta^{13}C_{DIC}$ with CO_2 efflux, measures of flow and water chemistry

$\delta^{13}C_{DIC}$ shows no particular pattern with (a) CO_2 efflux (b) mean velocity, (c) pH and (d) [DIC] at AR or PLST. Legend is the same for all plots.

Unlike DW and RK, $\delta^{13}C_{DIC}$ at both AR and PLST does not show a relationship with CO_2 efflux, measures of flow (mean velocity) or water chemistry (pH and [DIC]) (Figure 63). The lack of relationship with [DIC] (Figure 63d) indicates that, unlike at DW and RK, end-members are not hydrologically controlled.

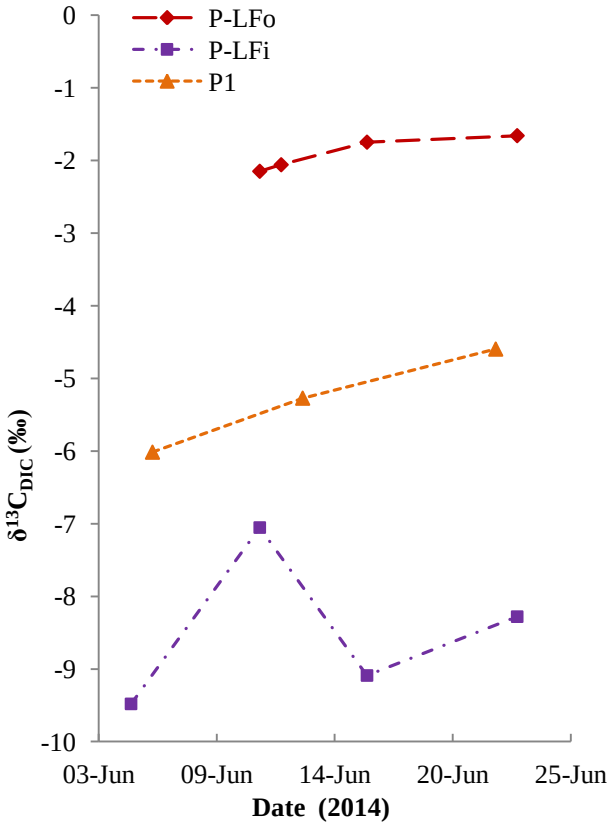

Figure 64: Temporal changes in $\delta^{13}C_{DIC}$ in the permafrost-landscape surface-thaw system
$\delta^{13}C_{DIC}$ becomes increasingly enriched over time in P-LFo (Lake Ferguson outlet stream) and P1 (pool within the permafrost landscape), but is more variable at P-LFi (Lake Ferguson inlet springs). For site locations see Figure 53.

In the permafrost-melt surface-thaw system there was variation between sites. The Lake Ferguson inlet springs were consistently less ^{13}C-enriched than the outlet (‰ ranges, mean: inlet -9.5 to -6.7, -8.2; outlet -5.5 to -1.7, -2.5), with the outlet becoming increasingly ^{13}C-enriched over time. The inlet springs are more variable, where P1 also shows increasing $\delta^{13}C_{DIC}$ enrichment over time (Figure 64). Unfortunately due to difficulties analysing samples with unknown and varying [DIC], there were not enough reliable results to determine a trend at LH or P2.

In the ice-melt system, there is a spatial pattern in $\delta^{13}C_{DIC}$ along the course of AR (Figure 65). $\delta^{13}C_{DIC}$ is most ^{13}C-depleted in the first ~2 km downstream of the ice margin, then increases to being most ^{13}C-enriched at 2.5 km downstream, followed by a steady decrease in $\delta^{13}C_{DIC}$ along the remainder of the course.

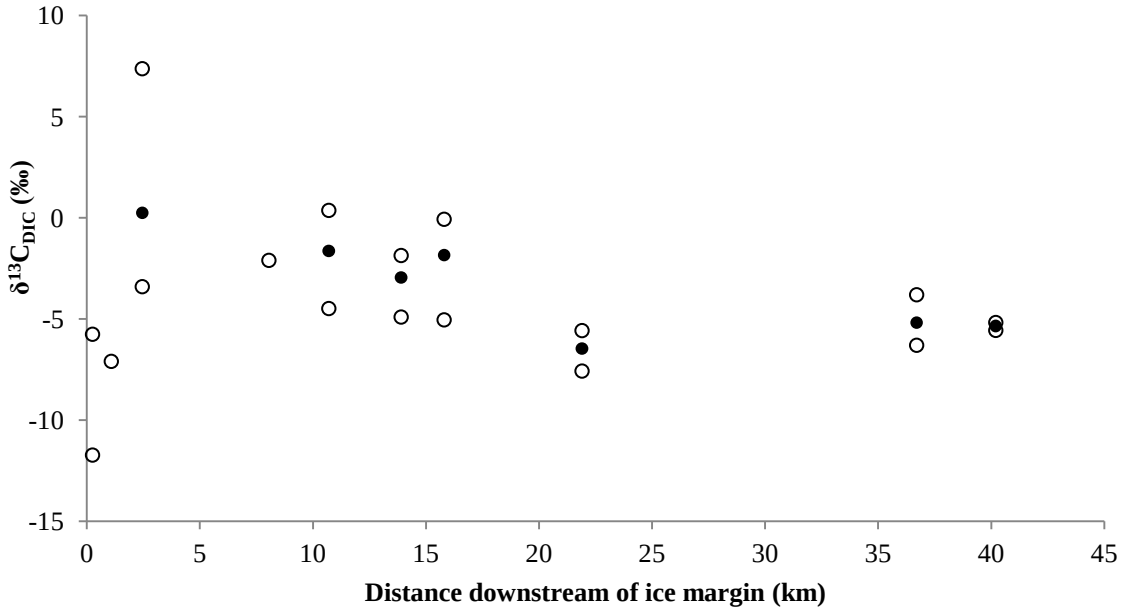

Figure 65: Spatial changes in $\delta^{13}C_{DIC}$ in the ice-melt system

The ice margin is at 0 km. Solid circles indicate mean $\delta^{13}C_{DIC}$, and upper and lower circles indicate maximum and minimum $\delta^{13}C_{DIC}$, respectively. For locations where only one or two measurements were made, hollow circles are used and no average is displayed.

When efflux spatial data (Figure 59) is overlaid onto $\delta^{13}C_{DIC}$ spatial data (Figure 65) the trend in the two datasets is very similar from 2.45 km downstream onwards (Figure 66). Upstream of 2.45 km this is not the case.

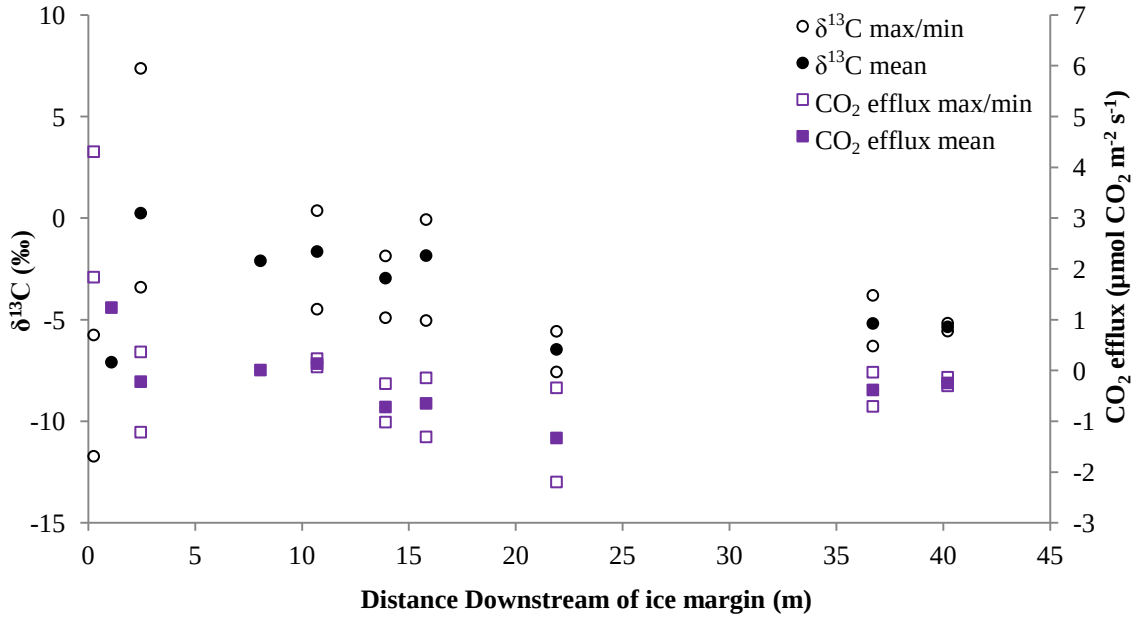

Figure 66: Spatial changes in $\delta^{13}C_{DIC}$ and CO_2 efflux in the ice-melt system

The ice margin is at 0 km. Solid shapes indicate mean values, hollow shapes indicate maximum and minimum values. For locations where only one or two measurements were made, hollow shapes are used and no average is displayed.

Temporal patterns may also exist in the $\delta^{13}C_{DIC}$ of the ice-melt system. For the 3rd – 4th July diel sampling data there seems to be a strong diel cycle whereby $\delta^{13}C_{DIC}$ is ^{13}C-depleted in the afternoon and more ^{13}C-enriched at night and into the early morning (Figure 67). If the grey-filled data point is discounted as possibly anomalous (as a diel pattern may be expected), there is a similar pattern for the 14th – 15th June diel sampling data, however it is less clear.

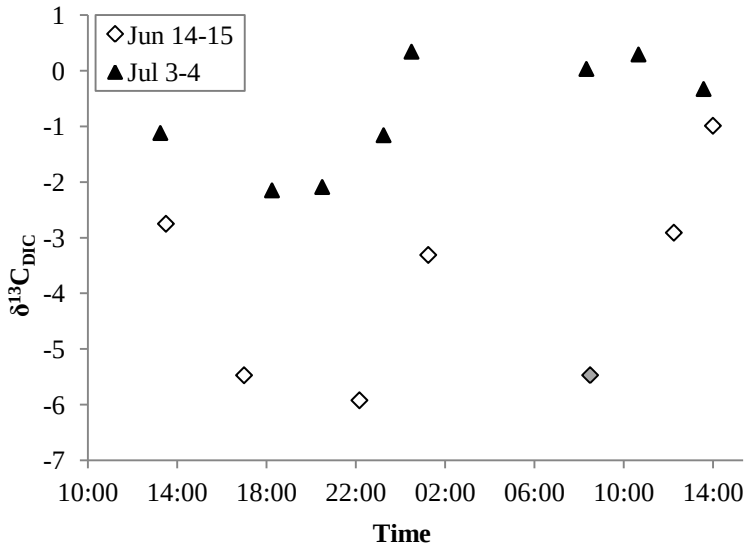

Figure 67: Temporal variation in $\delta^{13}C_{DIC}$ over two 24-hour periods in the ice-melt system
$\delta^{13}C_{DIC}$ in ‰. Grey-filled diamond indicates a possible anomaly. Diel sampling was not carried out in the permafrost-landscape surface-thaw system.

A Keeling plot (Keeling, 1961) reveals $\delta^{13}C_{DIC}$ of AR and PLST correlates with the inverse of [DIC] ($[DIC]^{-1}$) (Figure 68). Relationships at the sites are strong, linear and highly significant, with $p = <0.001$ at AR and 0.001 at PLST. However they differ in direction. At AR there is a positive relationship between inverse [DIC] and $\delta^{13}C_{DIC}$, indicating that $\delta^{13}C_{DIC}$ becomes increasingly ^{13}C-enriched with decreasing [DIC], while at PLST the relationship is negative indicating that $\delta^{13}C_{DIC}$ becomes increasingly ^{13}C-depleted with decreasing [DIC]. The intercept on the y-axis of the Keeling plot allows the $\delta^{13}C_{DIC}$ of an end-member to be estimated. The intercepts differ at the two sites being almost 7 ‰ different with -8.4 ‰ at AR, and -1.5 ‰ at PLST.

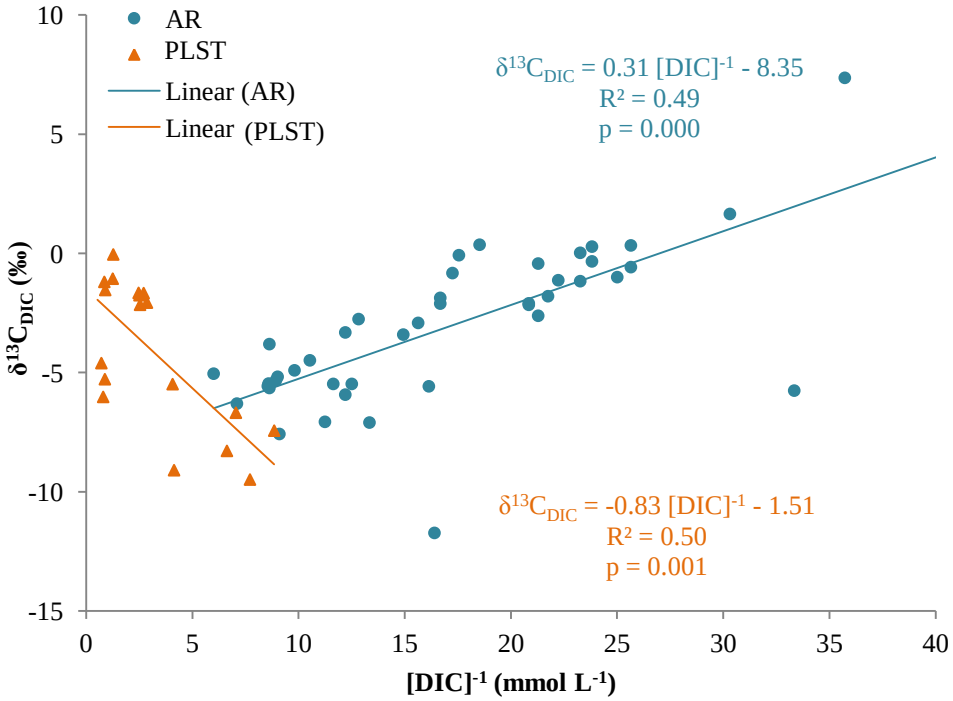

Figure 68: A keeling plot to consider end-member composition
Strong, significant linear relationships exist between $[DIC]^{-1}$ and $\delta^{13}C_{DIC}$ at AR and PLST.

5.4.6.2 $\delta^{13}C_{efflux}$

$\delta^{13}C_{efflux}$ of ice meltwater is consistent across a 24-hour period at -14.6 ‰ (SD = 0), whilst $\delta^{13}C_{efflux}$ from PLST varies temporally and spatially (range of 4.1‰, SD = 1.7) (Table 15, Figure 69). $\delta^{13}C_{efflux}$ of the Lake Ferguson inlet springs becomes less ^{13}C-enriched over a 12 day period (from -14.5 to -16.4 ‰) and is consistently less ^{13}C-enriched than the $\delta^{13}C_{efflux}$ of the outlet stream, which does not show much variation in composition over a 5 day period (-12.3 and -12.7 ‰). All $\delta^{13}C_{efflux}$ are less ^{13}C-enriched than all the $\delta^{13}C_{DIC}$, and these pools show a relationship, whereby $\delta^{13}C_{efflux}$ decreases with $\delta^{13}C_{DIC}$ (Figure 69).

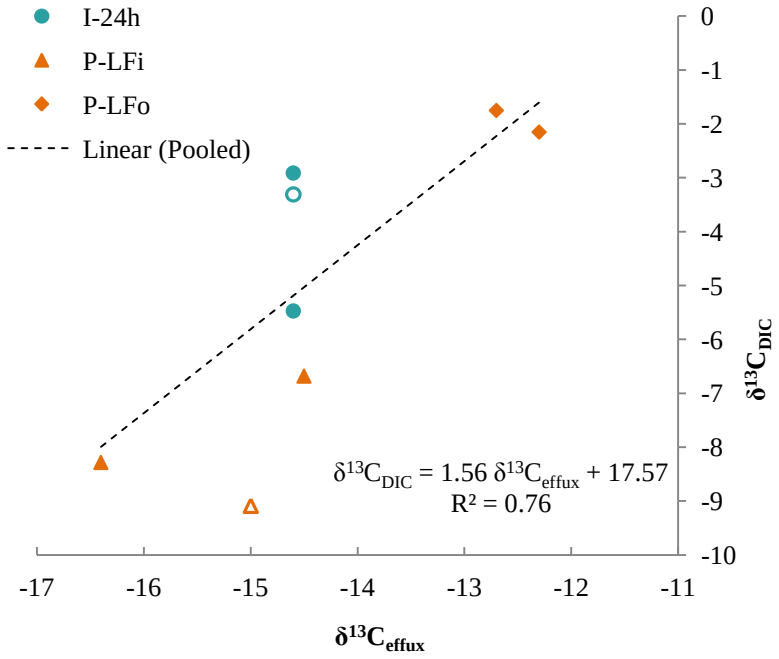

Figure 69: Relationship between $\delta^{13}C_{efflux}$ and $\delta^{13}C_{DIC}$

Paired $\delta^{13}C_{efflux}$ and $\delta^{13}C_{DIC}$ are plotted for the ice-melt and permafrost-landscape surface-thaw systems. The trendline excludes the two hollow data points that are less trusted due to timing of sample collection. For P-LFi hollow point the $\delta^{13}C_{efflux}$ and $\delta^{13}C_{DIC}$ samples were not closely paired, they were taken ~3h 45m apart, thus flow or water chemistry changes could have occurred between samples (all other $\delta^{13}C_{efflux}$ and $\delta^{13}C_{DIC}$ samples were taken within ~1h 40m of each other, usually less). For I-24h hollow point the sample was taken in the night, out with the time range (11:00-19:00) that all other samples were taken within, and so there is possibility of influence of diel variation. For site codes and locations see Figure 53.

5.4.6.3 $\delta^{13}C_{DOC}$

Average $\delta^{13}C_{DOC}$ of ice meltwater is more ^{13}C-depleted than that of PLST (-29.4 and -27.3 ‰ respectively) and all $\delta^{13}C_{DOC}$ values are much more ^{13}C-depleted than both the $\delta^{13}C_{DIC}$ and $\delta^{13}C_{efflux}$ (Figure 70). Maximum $\delta^{13}C_{DOC}$ of the ice meltwater and PLST are similar, ~ -26 ‰ and within 1.0 ‰; minimum $\delta^{13}C_{DOC}$ differs by 7.2 ‰ with the ice meltwater having a lower minimum value (-35.2 ‰) than PLST (-28.0 ‰). Ranges in the two systems are different. $\delta^{13}C_{DOC}$ of ice meltwater varies by 9.6 and 6.6 ‰ over the two 24-hour periods (from -35.2 to -25.6 ‰ and from -32.0 to -25.4 ‰). PLST $\delta^{13}C_{DOC}$ varies a little between the Lake Ferguson inlet and outlet, by up to 1.6 ‰, but is remarkably constant within each, varying by only 0.3 ‰ (-28.0 to -27.7 inlet; -26.7 to -26.4 outlet), despite sampling times varying between 11:00 and 19:00. There is no apparent correlation between $\delta^{13}C_{DOC}$ and $\delta^{13}C_{DIC}$ or $\delta^{13}C_{efflux}$ (Figure 70).

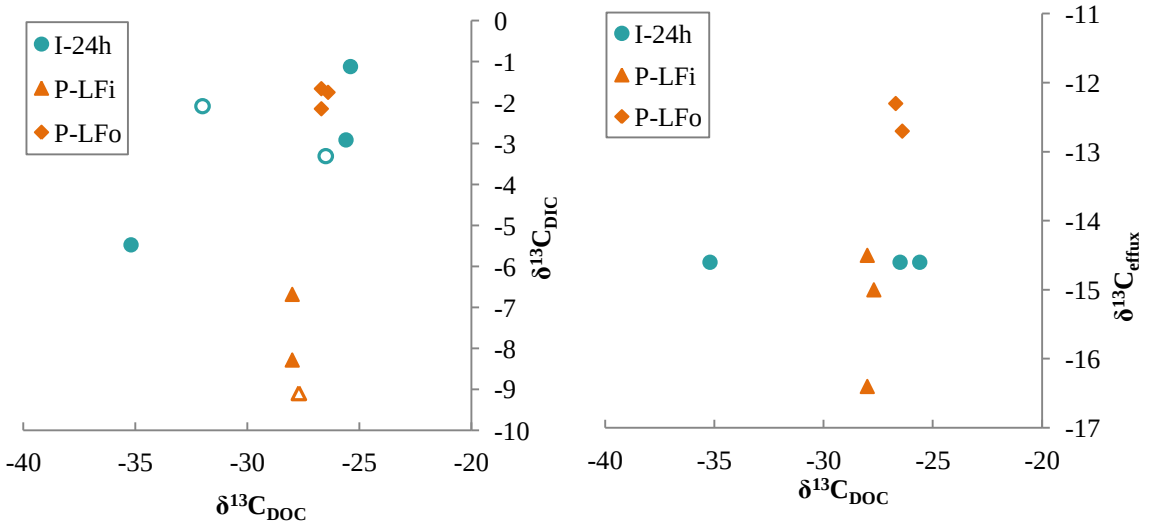

Figure 70: Relationship between $\delta^{13}C_{DOC}$ and $\delta^{13}C_{DIC}$ (left), and $\delta^{13}C_{DOC}$ and $\delta^{13}C_{efflux}$ (right)

There is no apparent relationship. Hollow points on left plot indicate samples that were collected out with the 11:00-19:00 time range (I-24h) and those that were not collected within the usual 1h 40m of each other (P-LFi). For site codes and locations see Figure 53.

5.4.7 CO_2 Efflux Upscaling

Mean CO_2 efflux upstream and downstream of the transition point was calculated as 0.713 µm CO_2 m^{-2} s^{-1} and -0.664 µm CO_2 m^{-2} s^{-1} respectively. Surface area of AR up and downstream of the transition point was calculated to be 1.66 km^2 and 10.2 km^2 respectively. Using these values and the average number of days in the melt season - 106.5 days (Bartholomew *et al.*, 2011; van As *et al.*, 2012; Hasholt *et al.*, 2013) - the fluxes of the upper and lower reaches were calculated to be 10897914 mol CO_2 yr^{-1}/479.6 t CO_2 yr^{-1} and -62108593 mol CO_2 yr^{-1}/-2733.4 t CO_2 yr^{-1} respectively, and thus overall this reach of river removes 2254 tonnes CO_2 per year from the atmosphere.

If all 335 rivers draining the GrIS (Lewis and Smith, 2009) behave as AR in terms of CO_2 efflux/influx balance and magnitude, and AR is of average surface area, then the GrIS fluvial drainage system could be absorbing 755017 t CO_2 yr^{-1} from the atmosphere (not including any supra-/en-/sub-glacial drainage systems). These broad assumptions have been made in the absence of published CO_2 efflux/influx and surface area data for the rivers draining the GrIS.

5.5 Discussion

5.5.1 Magnitude of CO_2 Efflux

The magnitude of CO_2 efflux from the ice-melt and permafrost-landscape surface-thaw systems was small compared to the main sites of Chapter 3 (DW and RK) and other systems globally (Figure 71) and both systems behaved as both sources and sinks of CO_2 at different times and locations (Table 14; Figure 54). Recording influx in fluvial systems is unusual with published incidences of influx rare in other systems globally (Figure 71; Long *et al*., 2015). PLST was an overall source of CO_2 to the atmosphere (effluxed in 86% of cases, n = 39; mean 0.27 µmol CO_2 m^{-2} s^{-1}), but ice meltwater was a net sink for atmospheric CO_2 (influxed in 64% of cases, n = 22; mean -0.14 µmol CO_2 m^{-2} s^{-1}) with the supraglacial streams of the ice-melt system a consistent sink (influxed in 100% of cases, n = 3) (see 5.4.4).

Although magnitudes of the fluxes are low, spatial coverage of ice and permafrost systems is large (see 5.2.2). Under a warming climate melting of ice and thawing of permafrost will increase (IPCC, 2013; Vonk *et al*., 2013) subsequently increasing the volume and surface area of their melt/thaw waters, and so the surface for CO_2 exchange with the atmosphere. That these systems periodically act as both sources and sinks for CO_2 needs consideration in global carbon cycle modelling.

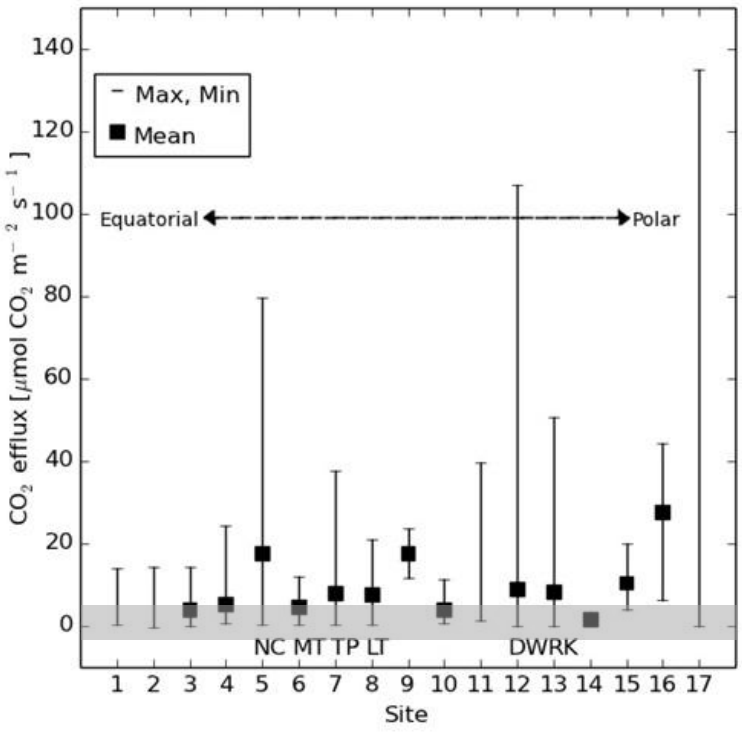

Figure 71: Global CO_2 efflux rates

This diagram provides efflux ranges obtained by direct measurement from flowing water (Long *et al*., 2015). The grey bar shows the range of CO_2 efflux measured across AR and PLST. Data sources and site references are in Table 1 of Long *et al.* (2015) (Appendix B). Sites are ordered by latitude. Specific site locations are listed in supporting information Figure S1of Long *et al*. (2015).

5.5.2 Controls on CO_2 Efflux

5.5.2.1 Hydraulics and the carbon pool

The lack of relationship between CO_2 efflux and flow velocity (or other hydraulic parameters) (Figure 55; Appendix H) indicates flow intensity is not a primary control on efflux in these arctic systems, as it is in the study sites of Chapter 3 (Drumtee water and River Kelvin) and previously reported temperate and tropical rivers (Long *et al.*, 2015). CO_2 efflux thus appears independent of hydraulic controls on gas release in AR and PLST.

With low [DIC] and high pH, it is likely these systems are supply and pH limited, through the already small DIC pool speciating to $CO_3^{2+}{}_{(aq)}$ and $HCO_3^{-}{}_{(aq)}$, which are not available for degassing, at high pH (Stumm & Morgan, 1996; Hoffmann & Schellnuber, 2010; Chapter 1). AR has particularly low [DIC] and PLST generally has higher pH (Table 14). pCO_2 incorporates the effects of pH and [DIC], however it does not appear a primary control on degassing (Figure 56) nor does it improve the relationship between flow and CO_2 efflux (Figure 57) as it did for the sites of Chapter 3 (Chapter, 3 Figure 27) and the other sites of Long *et al*. (2015) (Appendix B).

pCO_2 was undersaturated with respect to the atmosphere on all sampling occasion in the ice-melt system thus CO_2 influx might be expected on all occasions. However, efflux was measured directly in 30% of cases, and calculated pCO_2 saturation with respect to the atmosphere did not always concur with the direction of the measured CO_2 flux (Figure 72). Sensitivity analysis revealed equipment errors were not the cause of this (Figure 72), suggesting there are mechanisms acting to cause efflux when pCO_2 is under-saturated with respect to the atmosphere. Mechanisms could include physical pumping of CO_2 out of the water or entrainment, and subsequent release, of bubbles of atmospheric air into the water by surface waves/waterfalls. No similar published data exits to allow comparison or more thorough explanation. However, this phenomenon demonstrates that care is needed when including ice meltwaters in Arctic locations in global CO_2 efflux estimates based only on calculated pCO_2 over-/under-saturation values and the importance of direct measurements of CO_2 efflux.

Although PLST has larger carbon content than AR (Table 14), the carbon pools within both systems of this study are generally small compared to other systems globally (Cummins and Farrell, 2003; Worrall and Burt, 2010; Raymond *et al.*, 2013; Long *et al.*, 2015) (although they can be highly variable), and here, the slightly larger carbon content of PLST does not appear sufficient to overcome the limitations of pCO_2 on efflux.

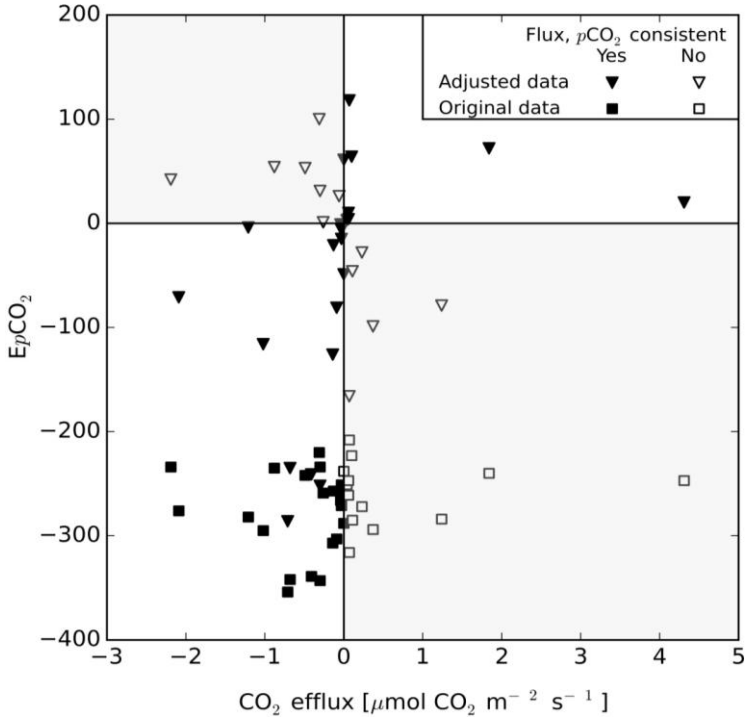

Figure 72: CO_2 efflux and EpCO_2 agreement in the ice-melt system.

This diagram shows the relationship between EpCO_2 (pCO_2 excess with respect to the atmosphere) and CO_2 efflux for all samples in the ice melt system. To explore if an efflux could still be measured whilst the river was still apparently under-saturated a sensitivity analysis was carried out on the data. Original data: EpCO_2 calculated from measured pH and DIC values. Negative EpCO_2 indicates under-saturation, positive EpCO_2 indicates oversaturation. Hollow data points and grey segments (top left and bottom right) indicate non-agreement between CO_2 efflux and EpCO_2. Adjusted data: EpCO_2 when pH adjusted by -0.4 (the maximum disagreement between handheld pH probes used in the field and a high accuracy Mettler Delta 320 lab-based pH meter; comparisons carried out using low conductivity waters (11.6, 20.1, and 39.5 µS cm^{-1})) and DIC adjusted by +0.027 (method accuracy reported by Waldron *et al*., 2014). The adjusted data represent the maximum enhancement of the free CO_2 pool if errors in pH and DIC exist for all values. The maximum reduction of the free CO_2 pool (+0.4 pH and -0.027 DIC) is not displayed as CO_2 and EpCO_2 agreement would be unaffected (EpCO_2 would only become more negative).

5.5.2.2 Spatiotemporal

In the ice-melt system, the supraglacial streams drawdown CO_2, yet the highest rates of efflux occur at the ice margin. This supports the interpretation that supraglacial melt is not the primary source of water in AR (Ryu and Jacobson, 2012; van As *et al.*, 2012), but instead basal drainage containing organic and inorganic carbon from the action of microbes in situ (Skidmore *et al.*, 2000; Anesio and Laybourn-Parry, 2012; Ryu and Jacobson, 2012). When this basal drainage emerges at the ice margin, an initial rapid degassing of CO_2, due to the sudden reduction in pressure and the lower CO_2 concentration of the atmosphere, would explain the high (relative to the rest of AR) efflux rates at the ice margin. Continued degassing of the river water during transit would reduce fluvial pCO_2, and likely explain the decrease in efflux rates to atmospheric equilibrium at ~2.5 km downstream, however another mechanism is needed to move beyond equilibrium to influx a further 8 km downstream (Figure 59). Biofilms were not observed on the bed or banks of AR, and as is common with glacial meltwaters (e.g. Milner and Petts, 1994), AR was highly turbid along the entire course. Thus in the limited light conditions it is unlikely biological processes, e.g. benthic

photosynthesis, are responsible for atmospheric CO_2 drawdown downstream of the degassing AR headwater. Rather, in glacial rivers, the comminuted bedrock undergoes chemical weathering (Ryu and Jacobson, 2012), sequestering CO_2 as it is transformed by hydrolysis to bicarbonate ions (Ryu and Jacobson, 2012; Wang *et al.*, 2014). The relatively high pH and low pCO_2 in the ice melt system could manifest from weathering reactions which consume H^+ to hydrolyse CO_2 (Ryu and Jacobson, 2012). Thus weathering and an increasing sediment load downstream could result in the transition from degassing to CO_2 influx.

The steady trend from efflux to influx also suggests there is no input of carbon-rich water along the course of AR, supporting that inputs of water from sources other than basal melt of the GrIS are negligible (Ryu and Jacobson, 2012; van As *et al.*, 2012), and that the ice-melt and permafrost-landscape surface-thaw systems are indeed hydrologically disconnected.

There did not seem to be a temporal pattern of CO_2 efflux in AR, either diel (Figure 60) or seasonal, but there was a seasonal pattern in PLST. The decrease in efflux from PLST over progression of the melt season (Figure 61) suggests that recharge from the soil CO_2, or from respiration of DOC, was insufficient to augment loss of trapped CO_2 built up under the ice over the frozen period (e.g. Kling *et al.*, 1992). This effect likely exacerbated by the draining and associated drying of the soils reducing hydrological connectivity as the melt season progressed. Influx occurred in Lake Helen (LH) and Lake Ferguson (LF) towards the end of the study period; this is another situation where an effluxing system moves from efflux beyond atmospheric equilibrium to influx. Influx did not occur in the inlet springs of LF or the small pools (P1 and P2), and so consumption of CO_2 could be occurring in LH and LF as a result of large lake processes and aquatic photosynthesis (e.g. Miller *et al.*, 1986).

5.5.3 Age and Source of the Carbon

5.5.3.1 ^{14}C age of carbon in the different pools

PLST CO_2 efflux and exported DOC $\Delta^{14}C$ values of 102.19 – 103.83 and 101.80 – 104.68 % modern respectively (Table 14) are consistent with significant derivation from recently-fixed carbon and similar to that of the contemporary atmosphere. Other studies have reported old organic carbon in the drainage of thawing permafrost. For example, exceptionally old DOC (>21000 years BP) is being mobilised in waters draining the Siberian Arctic Yedoma deposits by permafrost degradation (Vonk *et al.*, 2013), and major rivers of Alaska and Northern Canada (Sag, Mackenzie and Yukon) are transporting DOC that is 390 – 4900 years BP (Guo *et al.*, 2007). The young composition of the organic matter in the permafrost-landscape surface-thaw water of this study could be due to old DOC in the soils being respired directly to the atmosphere and never reaching the thaw waters. However, it is more likely that PLST waters drain a modern-carbon-containing landscape surface and not the permafrost below, where inputs of carbon are likely from contemporary vegetation and

autochthonous production within the thaw waters; this resulting in soil CO_2 dissolved by the thaw waters and the carbon-pool within PLST sharing a similar modern source. Additionally, arctic Siberia has higher annual precipitation than SW Greenland (NOAA, 2016b) and remained unglaciated during the last glacial maximum (Clark *et al.*, 2009; Carlson and Winsor, 2012; Vonk *et al.*, 2013) which allowed thick ancient accumulations of organic matter in the area (Vonk *et al.*, 2013). However SW Greenland has a semi-arid climate and the GrIS advanced beyond the current coastline during the last glacial maximum (Ten Brink and Weidick, 1974; Carlson and Winsor, 2012; Storms *et al.*, 2012), conditions far less conducive to old soil formation.

In contrast, CO_2 effluxed from the ice sheet melt system was old (809 ±38 to 966 ±36 yrs BP), and the DOC exported was considerably older (5,205 ±50 to 6,678 ±39 yrs BP) (Table 14) as well as older than has been previously observed elsewhere in SW Greenland (mid-late Holocene DOC, 2,300 – 4,100 years BP, Bhatia *et al.*, 2013). Old DOC in drainage waters could originate from organic matter trapped in or under the ice during formation and now released as DOC and CO_2, or subsequently converted to CO_2 and evaded (Cole *et al.*, 2007; Bhatia *et al.*, 2013). Sources of trapped organic matter could include: (i) formerly supraglacial carbon which became entrained by ice formation, this carbon originally from in situ-production by microbes on the ice surface and in red snow (Hodson *et al.*, 2008; Anesio and Laybourn-Parry, 2012) and/or cryoconite holes (Hodson *et al.*, 2008; Anesio and Laybourn-Parry, 2012) known to be present on the ice sheet in the Kangerlussuaq region (Langford *et al.*, 2010), or from direct deposition of black carbon from incomplete combustion of fossil and biofuels (Stubbins *et al.*, 2012; Spencer *et al.*, 2014); and, (ii) subglacial carbon from insitu production by microbes at the base of the ice (Anesio and Laybourn-Parry, 2012) and/or from over-ridden old soils shielded from errosion by the ice cover (Sharp *et al.*, 1999). Different ages of DOC may reflect different sources of melt and/or flow pathways, which vary between locations and as a result of seasonal/diel sub-glacial drainage evolution (Bhatia *et al.*, 2013).

Respiration of DOC is the most important intermediate in global carbon-cycling and is thus likely to fuel at least some of the CO_2 efflux (Battin *et al.*, 2008; Vonk *et al.*, 2013; Evans *et al.*, 2014; Spencer *et al.*, 2015). However, meltwater DOC is substantially older than the effluxed CO_2 indicating that it is not DOC alone that fuels the CO_2 efflux. To render the age younger, some effluxed CO_2 must come from modern atmospheric CO_2 through influx to the meltwater or entrainment by surface waves in super-critical flows (Thackston and Dawson, 2001; Gordon *et al.*, 2004), and, or, by annual release of trapped CO_2 or DIC during snow or glacial melt (of variable age from modern to ancient, depending on melt pathways). It was not possible to characterise the ^{14}C age of sintered glacier inorganic carbon due to challenges in isolating this, but $\delta^{13}C$ offers some insight as to the source of younger CO_2 efflux (see 5.5.3.2). In the permafrost-landscape surface-thaw system, atmospheric drawdown occurred in some lakes and streams (Figure 61), but is from the same age pool as DOC and so offset is minimal.

Glacier-derived DOC from Greenland, Antarctica, Alaska and Tibet (Lawson *et al.*, 2014; Hood *et al.*, 2015) has been found to be more biologically-available than terrestrial DOC and likely to stimulate heterotrophic metabolism and degradation of more stable DOC downstream (Hood *et al.*, 2009; Singer *et al.*, 2012; Spencer *et al.*, 2014). Such source degradation may therefore feedback to climate change by increasing CO_2 efflux. Conversely, glacial DOC could stimulate the autotrophic component of biofilms (Lovatt *et al.*, 2014), facilitating atmospheric CO_2 drawdown. It is of course possible that both processes occur contemporaneously, and, if so, the balance of these becomes important. The strength of these two processes are significant unknowns, but old ^{14}C in the efflux provides the first direct evidence that old carbon can enter aquatic ice-melt drainage systems and subsequently be returned to the atmosphere.

5.5.3.2 $\delta^{13}C$ to understand the source of carbon in the different pools

$\delta^{13}C$ of the DOC (average -29.4 ‰ AR, -27.3 ‰ PLST; Table 15) indicates that DOC in both the ice melt and permafrost-landscape surface-thaw systems is derived from C3 plant material which has a typical $\delta^{13}C$ of -24 to -34 ‰; (Faure, 1986). The more ^{13}C-depleted values from AR could indicate contributions from: (i) old organic matter formed in a past atmosphere not enriched by the burning of fossil fuels (Clark and Fritz, 1997); (ii) an anaerobic ^{13}C-depleted methane-based C cycle (e.g. Waldron *et al.*, 1998); (iii) bacterial breakdown products e.g. lipids (Niemann and Elvert, 2008); or, (iv) a mixture of the above. $\delta^{13}C_{DOC}$ of the ice-melt system is less consistent than PLST, which may reflect different sources of melt and/or flow pathways, as a result of diel or seasonal sub-glacial drainage variation/evolution (Bhatia *et al.*, 2013). The consistency in PLST $\delta^{13}C_{DOC}$ at Lake Ferguson inlet and outlet, likely reflects consistency of the source of DOC: thawing surface soil layer for the inlet springs and the lake for the outlet stream, by which point the effects of varied lake processes will be combined.

In contrast to $\delta^{13}C_{DOC}$, $\delta^{13}C_{DIC}$ was ^{13}C-enriched in both AR and PLST with $\delta^{13}C_{DIC}$ of AR often close to 0 ‰ (Table 14; Figure 59; Figure 68) and $\delta^{13}C_{DIC}$ of PLST sometimes close to 0 ‰ (Figure 68). The DIC pools are therefore not typical of C3-derived carbon, suggesting DOC released upon ice or soil thaw is not a large contributor to the pools, and AR is indeed hydrologically disconnected from the surrounding soils/lakes. With no carbonates in the area, $\delta^{13}C$ approaching 0 ‰ is typical of dissolved atmospheric CO_2 (Deuser and Degens, 1967; Waldron *et al.*, 2007). Thus, $\delta^{13}C_{DIC}$ supports IRGA measurements and radiocarbon findings from AR that atmospheric CO_2 drawdown occurs as the ice sheet melts and when the meltwater degasses the CO_2 it is a pool derived from both old and young carbon. The Keeling plot also confirms that the ice-melt system is experiencing influx and influx dominates the DIC pool at low [DIC] (Figure 68), as $\delta^{13}C_{DIC}$ becomes increasingly enriched towards 0 ‰ with decreasing [DIC] indicting increasing atmospheric drawdown with decreasing [DIC] concentrations. At greater [DIC], more ^{13}C-depleted $\delta^{13}C_{DIC}$ indicates influx is less dominant, and ^{13}C-depleted DOC has greater influence on the pool.

However the high [DIC] end-member is ^{13}C-enriched (-8.4 ‰) compared to the DOC (average $\delta^{13}C_{DOC}$ -29.4 ‰). It is possible that there is significant modification of $\delta^{13}C_{DOC}$ during conversion to DIC, but due to the magnitude of the modification (> 20 ‰) this seems unlikely. Thus the discrepancy between $\delta^{13}C_{DOC}$ and $\delta^{13}C_{DIC}$ suggests the high [DIC] end-member of the Keeling plot is actually a mixed pool with a contribution from DOC to the DIC pool, but that this is still small in comparison to CO_2 influx/atmospheric exchange. Melting ice surfaces are known to absorb CO_2 from the atmosphere (the supraglacial streams of this study and Wang *et al*., 2014), and much of the supraglacial melt in the Kangerlussuaq catchment passes through and under the ice (van As *et al.*, 2012) so it is very likely the resultant base flow which dominates the flow in AR (Ryu and Jacobson, 2012) contains a mix of DIC derived from DOC from within and under the ice, and atmospheric CO_2. A $\delta^{13}C_{DIC}$ of -8.4 ‰ indicates proportional mixing of 29% DIC converted from DOC and 71 % dissolved atmospheric CO_2 from influx.

Although less so than AR, $\delta^{13}C_{DIC}$ of PLST was also ^{13}C-enriched indicating atmospheric drawdown also occurred here but to a lesser extent, co-indicated by the percentage occurrence of efflux and influx in the two systems (Figure 54; 5.5.1). Contrary to AR, $\delta^{13}C_{DIC}$ becomes increasingly ^{13}C-depleted with decreasing [DIC] at PLST (Figure 68), as is the case for the soil-dominated systems of Chapter 4, and perhaps reflecting PLST's greater connection with the soils than AR. However, PLST does not experience event flow, as the sites of Chapter 4 do – all PLST sites are predominantly closed system (Aebly and Fritz, 2009) and inputs of water and flushing of the soils are through thawing for only a few weeks in the early melt. Thus, the mechanisms for this trend are likely different at PLST than DW and RK. The decrease in $\delta^{13}C_{DIC}$ with decreasing [DIC] may represent input of ^{13}C-depleted soil CO_2 during soil-thawing events, which may cause simultaneous [DIC] dilution of the pool, as has been reported in some cases with snow-melt (Doctor et al., 2008; Aucour et al., 1999; Atekwana and Kryshnamurthy, 1998). The PLST high [DIC] end-member at -1.5 ‰ is considerably ^{13}C-enriched (Figure 68). This is more ^{13}C-enriched than the ground waters of DW and RK (-8.64 DW, -9.07 RK, see Chapter 4), and although within the normal range for groundwater (-21 to 0 ‰ Clark and Fritz, 1997) seems unusual in the absence of carbonate rocks. Influx occurred in some of the permafrost-landscape surface-thaw systems which may be enriching the DIC pool, however, would be expected to be greatest at low [DIC], not high [DIC] as the keeling plot suggests. PLST sites effluxed on the majority of occasions (Figure 54), and efflux can also enrich the DIC pool (Finlay, 2003; Doctor et al., 2008; Polsenaere and Abril, 2012). However, the lack of relationship between CO_2 efflux and pCO_2 (which incorporates [DIC]; Figure 56) indicates that high [DIC] does not cause increased CO_2 efflux, and so in turn, enrichment of the DIC pool at high [DIC] is not a result of increased CO_2 efflux. Enrichment is therefore perhaps a result of long water-residence times in the mainly closed PLST systems (e.g. Anderson and Stedmon, 2007), allowing influx and efflux to slowly enrich the pool over multiple months/years, and, in the early to mid-melt season (the period sampled), warming water temperatures (as was measured) could cause further enrichment by diffusion fractionation (see

Appendix A) as warm water can hold less CO_2 than cold water (e.g. Wiebe and Gaddy, 1940). Evaporation of water in these warmer ice-free months could contemporaneously concentrate the DIC pool, leading to the increasing $\delta^{13}C_{DIC}$ trend with in increasing [DIC]. Then, when thawing occurs, this would input ^{13}C-depleted soil CO_2 and water to dilute the pool.

When compared to the sites of Chapter 4, range and median $\delta^{13}C_{DIC}$ at AR and PLST are most similar to those of RE (Figure 62), with AR, PLST and RE all having more ^{13}C-enriched DIC pools than DW and RK, and the ^{13}C-depletion at DW and RK reflect C3 soil-dominated systems. RE was a snowmelt-dominated system during the period of sampling (Chapter 4), and thus more similar in character to AR and PLST which are also melt/thaw-dominated systems. Despite being in different climatic zones, the three melt/thaw-dominated systems have remarkably similar $\delta^{13}C_{DIC}$, indicating there is reduced influence of soil CO_2 on the DIC pool in melt/thaw-dominated systems and processes related to melting/thawing may cause ^{13}C-enrichment of the DIC pool reported in some instances (e.g. Doctor *et al.*, 2008) but not others (e.g. Atekwana and Krishnamurthy, 1998; Aucour *et al.*, 1999). Unlike the main sites of Chapter 3 and 4 (DW and RK), but similarly to RE, there was no relationship between $\delta^{13}C_{DIC}$ and CO_2 efflux, measures of flow, or water chemistry, at either AR or PLST (Figure 63), further indicating the three melt/thaw-dominated sites have similar aquatic carbon cycling dynamics. Instead, AR and PLST showed spatiotemporal patterns in $\delta^{13}C_{DIC}$, and modification of the pool by physical processes.

$\delta^{13}C_{efflux}$ decreases contemporaneously with $\delta^{13}C_{DIC}$ (Figure 69) suggesting that the $\delta^{13}C_{DIC}$ influences the efflux composition. This is expected as DOC cannot directly degas, it has to first be converted to CO_2 (Battin et al., 2008; Vonk et al., 2013). Lighter CO_2 molecules will preferentially degas during efflux (See Appendix A; Doctor *et al.*, 2008) and consistent with this here is that $\delta^{13}C_{efflux}$ values are consistently more ^{13}C-depleted than $\delta^{13}C_{DIC}$ (Figure 69). This efflux ^{13}C-depletion may also arise from pH-inducted interspecies isotope fractionation whereby the hydration of $CO_{2(g)}$ to $HCO_3^-{}_{(aq)}$ causes 7 - 10‰ ^{13}C-enrichment (temperature dependant) (Finlay, 2003; Waldron *et al.*, 2007); increasing pH due to $CO_{2(aq)}$ loss from the system during degassing, would drive $CO_{2(g)}$ to $HCO_3^-{}_{(aq)}$ and cause enrichment of the DIC pool. Fractionation by efflux could explain the enrichment of $\delta^{13}C_{DIC}$ over time in the lake Ferguson outlet stream (from -2.2 to -1.7 ‰) and P1 (from -6.0 to -4.6 ‰) (Figure 64).

Although the rate of efflux decreased from PLST sites over time (Figure 61), continuing efflux over the melt period in the predominantly closed systems could cause a steady enrichment of the DIC pool, with diffusion fractionation of CO_2 in the warming waters possibly contributing to this. Similarly, the downstream pattern in $\delta^{13}C_{DIC}$ in AR could be a result of the spatial pattern of efflux in AR; $\delta^{13}C_{DIC}$ becomes increasingly enriched over the stretch that only effluxes, to a maximum (7.4 ‰) at 2.45 km (site I-2, Figure 53) where influx first occurs (Figure 66). Such a high degree of ^{13}C-enrichment indicates that a large amount of degassing took place prior to this location, or alternatively

a contribution from carbonate rock, but this is not known in the area (Ryu and Jacobson, 2012). Moving downstream from 2.45 km influx, which would introduce relatively ^{13}C-depleted CO_2 to the DIC pool (atmospheric CO_2 is typically -11 to -6 ‰ (Stuiver and Polach, 1977) and ~0 ‰ when dissolved in water (Waldron *et al*., 2007)), becomes increasingly prevalent (Figure 59 and Figure 66) coinciding with a steady reduction in $\delta^{13}C_{DIC}$ enrichment (Figure 65 and Figure 66).

The diel pattern in $\delta^{13}C_{DIC}$ in AR (afternoon depletion and night-time enrichment) (Figure 67) is opposite to what would be expected from biological mediation. In temperate locations $\delta^{13}C_{DIC}$ has been found to be enriched during daylight hours and more ^{13}C-depleted at night when photosynthesis ceases and respiration (which does not enrich the DIC pool) dominates (e.g. Waldron 2007, Parker et al., 2010; Chapter 3, Figure 37). At the time of diel sampling of AR, the region experienced 24-hour daylight which would weaken any photosynthetic diel cycle, and regardless, heavy suspended sediment load in AR renders fluvial photosynthetic life unlikely. The $\delta^{13}C_{DIC}$ diel signal in AR is therefore unlikely to be caused by biological mediation and more likely a result of diel melting patterns, which would vary with sun strength. Maximum sun strength was at 12:00, however a lag in peak melt at I-24h is likely due to a lag in heating of the air and ice and the residence time of the meltwater in the river. Informal observations of river depth over the diel monitoring periods suggested peak melt reached I-24 at ~22:00, approximately the time $\delta^{13}C_{DIC}$ enrichment begins. This suggests that more intense melting results in a more-enriched $\delta^{13}C_{DIC}$ and the more ^{13}C-depleted $\delta^{13}C_{DIC}$ values were from reduced melting. Increased volumes of ice melt would cause a flushing of DOC and DIC from the ice base, and perhaps higher efflux at the glacier margin during higher flows – although flow was found not to be not a control on CO_2 efflux in this system (Figure 55), it perhaps could be when all else is equal. Efflux enriches $\delta^{13}C_{DIC}$ and so could be causing the diel cycle. Another possibility is that suspended sediment load may vary with diel flow cycles causing diel variation in weathering reactions, which sequester atmospheric CO_2 during hydrolysis and cause ^{13}C fractionation (section 1.6.2.2; Ryu and Jacobson, 2012; Wang *et al.*, 2014). Alternatively, and perhaps most likely, as daily temperature fluctuations are likely to have a greater effect on surficial ice-melt than basal melt, and surface melt is known to draw down atmospheric CO_2 (Wang et al., 2014) that has $\delta^{13}C$ of ~ 0 ‰ when dissolved in water (Deuser et al., 1967), the enrichment towards 0 ‰ around the time of peak flow likely reflects an increased contribution of surface melt to river flow during increased air temperatures.

Reduction in $\delta^{13}C_{efflux}$ over time in the Lake Ferguson inlet springs (from -14.5 to -16.4 ‰ over a 12 day period) could result from increasing entrainment of soil organic matter over the melt period. Because C3 vegetation (~ -27 ‰, Faure, 1986) is dominant in the region (5.3.1) soil organic matter is likely ^{13}C-depleted (Clark and Fritz, 1997), which could manifest in $\delta^{13}C_{efflux}$ as breakdown of DOC can fuel efflux (Battin *et al.*, 2008). $\delta^{13}C_{efflux}$ of Lake Ferguson inlet springs was consistently more ^{13}C-depleted than the $\delta^{13}C_{efflux}$ of the outlet stream which is fairly constant over a 5 day period (-12.3 and -12.7 ‰) (Table 15). The relative ^{13}C-enrichment of the outlet stream may be a result of

lake processes such as aquatic photosynthesis (Miller *et al.*, 1986), as in-water photosynthesis causes ^{13}C-enrichment of the DIC pool (e.g. Atekwana and Krishnamurthy, 1998; Parker *et al.*, 2010; Khadka *et al.*, 2014) that fuels efflux (e.g. Doctor *et al.*, 2008; Tranvik *et al.*, 2009).

5.5.4 Upscaling to Greenland

If AR is representative of all rivers draining the GrIS (Lewis and Smith, 2009) (this broad assumption made due to an absence of published GrIS meltwater CO_2 flux and river surface area data, see section 5.4.7), meltwaters of the GrIS could be a net sink for CO_2, absorbing 755017 t CO_2 yr^{-1} (0.00076 Pg CO_2 yr^{-1}) from the atmosphere. Efflux rates are likely to be highest at the ice margin (Figure 59, section 5.5.2.2), however the first 250m of AR, immediately adjacent to the ice sheet, could not be measured/sampled due to safety and inaccessibility. As a result, the estimate of total CO_2 efflux in AR upstream of the tipping point (section 5.4.7) may be conservative and the magnitude of the sink an overestimate. AR may even be close to equilibrium with the atmosphere with respect to CO_2, but is unlikely to be a sizable source of CO_2. In addition, supraglacial streams are found here to be consistent sinks of CO_2 (5.4.4 and 5.5.1), and melting ice-surfaces have been found previously to drawdown atmospheric CO_2 due to consumption of H^+ by CO_2 hydrolysis (Wang *et al.*, 2014). Thus, although the estimated magnitude of the sink should be treated with caution, these results suggest that thawing ice sheets and glaciers and their pro-glacial melt systems are potentially an overall sink for CO_2, and as such, global carbon cycling modelling needs to account for these systems periodically acting as CO_2 sinks as well as sources.

5.6 Conclusions

Direct measurements of CO_2 evasion from the meltwaters of the GrIS and surface thaw-waters of the permafrost landscape in SW Greenland show ice-meltwaters to be a potential net sink for CO_2, and PLST a net source; this confirmed by isotopic tracers and carbon age. Flow intensity is not a primary control on CO_2 efflux, instead the systems are supply limited with a spatial influence on efflux from ice-melt, which decreased with distance from the ice margin, and a temporal influence on efflux from permafrost-landscape surface drainage, which decreased over the melt period.

Radiocarbon analysis revealed permafrost landscape systems in this region are cycling recently-fixed carbon and so do not appear to be degrading old carbon from the permafrost, as is observed elsewhere such as the Siberian Yedoma deposits (Vonk *et al.*, 2013). In contrast the melting GrIS is effluxing old CO_2 and discharging very old DOC. Despite the relatively small magnitude of glacial DOC, in this study and globally, it appears disproportionately important to regional carbon cycling due to its high bioavailability and the potential to feedback to climate change (Singer *et al.*, 2012; Hood *et al.*, 2015).

The paired radiocarbon ages from CO_2 efflux and DOC indicate the return of old C to the atmosphere from cryosphere-hydrosphere efflux and identify that this may be fuelled by carbon that was previously sequestered up to ~ 6,700 years BP (or prior to this if the ages reflect a mixing of different carbon sources). The isotopic tracing reveals this, and this is the first of the data of this kind to be applied to understanding cryospheric carbon cycling in the terrestrial-atmospheric loop.

It is known from ^{14}C measurements that human disturbance mobilises old carbon to rivers (Butman *et al.*, 2015), but we are now learning of older slower pathways where the driver of old carbon release is not direct disturbance, but climate mediation, either short-term meteorological responses (Vihermaa *et al.*, 2014) or as shown here, longer-term of drivers of change. These data add to a growing body of research differentiating source and magnitude of CO_2 fluxes on age (Van Der Laan *et al.*, 2010), and this study is the first to do this in an arctic location. Such data are crucial as polar regions are known to be critical components of global climate system and carbon cycle.

The magnitude and direction of CO_2 exchange, and the ages of released gasses and dissolved carbon, question understanding of the impact of the changing cryosphere on the carbon cycle. Although the fluxes are small, the extent and total annual melt volumes from ice sheets and glaciers are such that total flux may be of larger significance. [DOC] measured here (Table 14) are mostly an order of magnitude greater than previously reported discharge-weighted estimates (mean [DOC] proglacial rivers: 0.3 – 1.7 mg L^{-1}; Bhatia *et al.*, 2013) suggesting this latter estimate of DOC annual export from GrIS of 0.08 ±0.02 Tg is likely to be a significant under-estimate. Indeed, this is confirmed by a more recent estimate of DOC export in GrIS runoff of ~0.2 Tg yr^{-1} (Hood *et al.*, 2015).

Ice sheet melt and permafrost-landscape surface-thaw carbon dynamics must be understood to know the consequences of climate change-induced cryosphere loss on the carbon cycle: efflux may represent a new source of CO_2 to the atmosphere and conversely influx a sink, and exports may come from a reservoir previously isolated from the atmosphere, and may be larger than previously thought. This study highlights that the cryospheric-aquatic-atmospheric carbon cycle needs further consideration, and inclusion in global carbon budgets.

6 Discussion and Conclusions

6.1 Introduction

Although freshwater systems are now considered a significant component of the global carbon cycle (e.g. Hope *et al*., 2001; Cole *et al*., 2007; Waldron *et al*., 2007; Billett and Moore, 2008; Rasera *et al*., 2008; Tranvik *et al*., 2009; Alin *et al*., 2011; Aufdenkampe *et al*., 2011; Wallin *et al*., 2011; Polsenaere *et al*., 2013; Raymond *et al*., 2013; Long *et al*., 2015), with the importance of source and movement of carbon through a hydrological system now recognised (e.g. Waldron *et al*., 2007; Tobias and Böhlke, 2011; Khadka *et al.*, 2014), the specific controls on CO_2 efflux and its sources are not thoroughly understood (e.g. Zappa *et al.*, 2007; Alin *et al.*, 2011; Tobias and Böhlke, 2011; Raymond *et al*., 2013). Additionally, research has traditionally focused on temperate, soil-dominated catchments, thus there is a scarcity of data particularly for high-latitude, climate-change-sensitive regions (Raymond *et al.*, 2013; Table 1, Long et al., 2015; Table 12, Chapter 4). Due to limited detailed understanding of aquatic carbon cycling dynamics, and sparse global data coverage, global-scale upscaling attempts are few and subject to large uncertainties, yet accurate upscaling is crucial to predicting the response of aquatic environments (with their potential CO_2 feedback mechanisms) to climate change and anthropogenic impacts (Aufdenkampe *et al.*, 2011; Raymond *et al.*, 2013).

The overall objective of this research was to use new efflux, hydraulic and isotopic data to test critical hypotheses of fluvial carbon cycling dynamics and the return of carbon to the atmosphere via CO_2 efflux. The following section addresses how the three specific aims of the research (Chapter 1) were met (6.2). Subsequent sections will consider the key contributions this research has contributed to this area of science (6.3), and suggest directions for progression of this research (6.4)

6.2 Summary of Key Findings

6.2.1 Aim 1

"Improve current knowledge of the magnitude and primary controls on riverine CO_2 loss via efflux from a variety of fluvial systems with different catchment types, global locations and climate-change sensitivities, and assess whether: (i) controls on and magnitude of efflux are similar or different across this range of catchments; (ii) whether fluvial systems always behave as sources of CO_2 to the atmosphere; and, (iii) whether the magnitude and control mechanisms can be used to upscale CO_2 efflux on a regional or global scale."

Through direct and contemporaneous measurement of CO_2 efflux and hydraulic parameters, flow intensity, a generic term which is used for several measures of flow strength and turbulence (Long et al., 2015; Chapter 3), was found to be a primary control on efflux across three contrasting (size and land use) soil-influenced to soil-dominated UK catchments (Drumtee Water (DW), River

Kelvin (RK) and River Etive (RE)) (Chapter 3) and four contrasting (size, land use and streamflow regime) soil-dominated Amazonian catchments (Long *et al.*, 2015). pCO_2 was found to be a secondary control, indicating that controls on efflux can be consistent across rivers of different scales and across climatic zones. CO_2 efflux increased under increasing flow intensity and/or increasing pCO_2.

Of the hydraulic parameters measured, the shear Reynolds number (a measure of the fluid forces and energy that create turbulence) yielded the most significant relationship with CO_2 efflux across the three study sites (Chapter 3). However, shear Reynolds number is not routinely reported alongside efflux, but can be calculated from routine hydraulic measurements (Chapter 3; Moog and Jirka, 1999). Mean velocity, which is commonly measured and a bulk descriptor of flow hydraulics, can be used as a proxy for flow intensity where other hydraulic parameters have not been measured (Chapter 3; Long *et al.*, 2015). Using either shear Reynolds number or mean velocity, including pCO_2 in the analysis improved the flow intensity-efflux relationship by correcting for inter-site variability (Chapter 3; Long *et al.*, 2015). The regression models for the relationships were:

$$\log (CO_2) = -5.12 + 0.80 \log (R^* . pCO_2) \qquad (R^2 = 0.72;\ p = 0.000;\ N = 94)$$

$$\log (CO_2) = -2.58 + 1.22 \log (\bar{u}^* pCO_2) \qquad (R^2 = 0.74;\ p = 0.000;\ N = 96)$$

A visual classification method showed promise as a means of upscaling from visual imagery, potentially over large spatial and temporal scales, if subjectivity in interpreting water surface state can be reduced (Chapter 3, 6.4.3.2).

Fluvial systems are commonly assumed to be sources of CO_2 to the atmosphere (e.g. Cole *et al.*, 2007; Tranvik *et al.*, 2009; Aufdenkampe *et al.*, 2011) and although the sites in this research mainly behaved as such, there were some incidences of influx at two UK sites (RK and RE; Chapter 3), highlighting that predominantly effluxing systems can periodically shift to become sinks for atmospheric CO_2, and thus the importance of long-term monitoring. In these limited cases of influx, flow intensity appeared to be a control as it was for efflux, with influx increasing with increasing flow intensity. However, this interpretation of influx controls is preliminary due to small sample sizes and the absence of pCO_2 data.

High latitude cryospheric melt/thaw systems (Akuliarusiarsuup Kuua River (AR) and permafrost-landscape surface thaw-waters (PLST)) were not soil-dominated and were supply-limited, and thus behaved differently to the predominantly soil-dominated UK and Amazon systems (Chapter 5). CO_2 fluxes were of smaller magnitude than in the lower latitude sites, and influx was much more prevalent (46 % of measurements, compared to 2 % for the lower latitude sites combined). There

was no apparent hydraulic control on CO_2 efflux or influx, thus the flow intensity-efflux regression models did not apply, and spatio-temporal controls (over 41.1 km river reach, AR, and 4 week sampling period, PLST) were of greater importance to CO_2 fluxes. The permafrost-landscape surface-drainage was, over the full measurement period, a net source of CO_2 to the atmosphere, but CO_2 release decreased over time from the start of the melt season, as CO_2 built up under ice and in frozen soil over the winter (e.g. Kling *et al.*, 1992) was expended. While the ice-melt system initially effluxed CO_2 upon emergence from the Greenland ice sheet, it quickly became undersaturated and began to drawdown CO_2 as a result of weathering of the high suspended sediment load. Overall the ice-melt system was a net sink for CO_2.

6.2.2 Aim 2

"Improve current knowledge of the source of carbon in the dissolved inorganic carbon (DIC) pool of fluvial systems and determine whether there is an influence of internal processing of the DIC pool in the fluvial systems studied here. Subsequently assess whether this knowledge can be used to reconstruct DIC source and CO_2 efflux over time and the relationship between the two, to aid predictions of how fluvial carbon dynamics may respond to a climate-induced changing hydrological cycle."

Contemporaneous measurement of [DIC] and $\delta^{13}C_{DIC}$ revealed that DIC pool concentration and source have a strong hydrological response at more soil-dominated sites (DW and RK; Chapter 4). Groundwater dominates the pool at low flow, the remarkably similar composition at the two sites indicating a common hydrogeological inheritance in DIC. At high flow differences in the pools emerge relating to land use. In urban catchments (e.g. RK) there can be a smaller contribution of soil water to the pool and/or a dominance of inputs of carbonate-containing urban runoff. The fluvial carbon dynamics of snow- and ice-melt dominated systems (RE, AR and PLST) were distinctly different (Chapter 5), potentially having multiple end-members that were not hydrologically controlled, and there was less connectivity with the soils than DW and RK.

It is considered that catchment water residence time influences the fluvial carbon pool composition of all five systems of this research (Chapters 4 and 5). In temperate, soil-dominated catchments, greater air-water CO_2 equilibrium exchange and CO_2 efflux in a larger catchment (RK) contributed to reduced dominance of soil carbon (Chapter 4). In cryospheric melt/thaw systems, the cumulative effect of weathering-induced CO_2 drawdown along the length of the proglacial river (41.1 km) led to the source of DIC in the pool becoming increasingly atmosphere-derived downstream (spatial pool response) and the mainly closed basin nature of the permafrost-landscape surface-thaw systems enabled lengthy periods of influx/efflux/CO_2 equilibrium exchange which led to the pool becoming increasingly dominated by atmospheric CO_2 over time (temporal pool response) (Chapter 5).

Measured diel cycles at a temperate, soil-dominated site (DW) revealed that the fluvial carbon pool is modified by biological processes (in-stream or riparian photosynthesis/respiration), and reconstructions of $\delta^{13}C_{DIC}$ and CO_2 efflux implied that the influence of biological mediation is seasonally- and flow-controlled (Chapter 4). However, modification of the pool by biological processes was insufficient to overcome hydrological responses. Biological pool mediation in an arctic proglacial river (AR) was unlikely due to the high suspended sediment load and diel cycles were attributed to the impact of daily insolation on ice sheet surface melting, and subsequent variation in proportional mixing of surficial and basal ice meltwaters (Bartholomew *et al.*, 2011; Ryu and Jacobson, 2012; van As *et al.*, 2012) (Chapter 5). Melting patterns may be of consequence over larger temporal time-scales (e.g. seasonal ice acceleration, Bartholomew *et al.*, 2010; Bartholomew *et al.*, 2011). However, here, modification of the pool by melting variation was insufficient to overcome spatio-temporal pool responses.

Time series reconstructions (Chapter 4) revealed that in a soil-dominated temperate system (DW) terrestrial-aquatic-atmospheric carbon cycling is very rapid over event flows, degassing large amounts of terrestrially-sourced CO_2 to the atmosphere over relatively short durations. In contrast, during the relatively longer periods of base flow, CO_2 efflux is predominantly of groundwater origin and of much smaller magnitude, thus DIC in the pool is more likely to transit greater distances downstream. Inter-year comparison indicated that under a drier climate with less and/or smaller magnitude event flows, fluvial systems will return less CO_2 to the atmosphere and with a smaller terrestrial carbon content than under a wetter climate.

6.2.3 Aim 3

"Investigate the age of the carbon returned to the atmosphere in fluvial systems particularly vulnerable to climate change and assess whether carbon stores in these systems are being lost such that this loss may render these systems positive feedbacks to climate change."

Western Greenland permafrost-landscape thaw-systems are cycling recently fixed carbon and thus the permafrost appears not to be degrading as has been reported in other high latitude regions (e.g. Schaefer *et al.*, 2011; Vonk *et al.*, 2013). To avoid overestimations, global estimates of climate change-induced release of carbon from permafrost should consider that some permafrost regions may not yet have shifted to a source of CO_2 to the atmosphere. In contrast, the melting GrIS is discharging very old carbon (~ 6000 yrs BP) and returning old carbon (~890 Yrs BP) to the atmosphere. The magnitude of old DOC released to the meltwaters is relatively small, but due to its high bioavailability (e.g. Singer *et al.*, 2012; Hood *et al.*, 2015) could be disproportionately important to regional carbon cycling due to its rapid breakdown to CO_2 and tendency to stimulate heterotrophic bacteria downstream (Bianchi, 2011; Hood *et al.*, 2015). Simultaneous $\delta^{13}C$ analysis of the DOC indicated 29% the DIC pool in AR was converted from DOC.

6.3 Research Contributions

This research has compared fluvial carbon pool dynamics, including directly measured CO_2 efflux magnitudes, sources and controls, across a range of catchment types and climates. This range of sites is unusual as many previous studies have focused on a narrower range of sites and elements of fluvial carbon cycling and/or have calculated efflux or pool dynamics from proxy data.

This research is the first to use direct, contemporaneous measurements of hydraulic flow characteristics and CO_2 efflux to confirm that turbulence at high flows leads to higher efflux, and that flow intensity is a primary control on efflux where systems are not supply limited. Because climate change is projected to change regional hydrology, including seasonality (Gloor *et al.*, 2013; Charlton and Arnell, 2014), added understanding of the specific mechanisms by which turbulence leads to advection of gas within the water body and transfer to the atmosphere (e.g. Moog and Jirka, 1999; Jonsson *et al.*, 2008) is crucial to measuring the impact of climate change on this CO_2 feedback processes.

Having confirmed the significance of hydraulic controls over CO_2 efflux, a novel visual upscaling method has been proposed, which shows potential for improving both the coverage and accuracy of CO_2 efflux estimates from surface waters that are not supply limited. Earth surface aerial imagery is common and easy to collect over wide/remote areas compared to manual sampling, so could allow rapid upscaling of CO_2 efflux over large areas, which is currently very difficult to do due to unavailability of accurate river surface area data (Striegl *et al.*, 2012; Raymond *et al.*, 2013) and uncertainty in global flux magnitudes (Raymond *et al.*, 2013).

Published incidences of CO_2 influx into river systems are uncommon (Long *et al*., 2015), and the measured influxes in the arctic and, occasionally, temperate rivers in this research are novel. Previous studies have suggested that riverine atmospheric CO_2 drawdown results from silicate weathering (e.g. Krishnaswami and Singh, 2005; Gurumurthy *et al.*, 2012; Wang *et al.*, 2014), and while this seems to be the case in a highly-turbid river draining the GrIS (AR), this is the first research to present evidence for a hydraulic control on influx in soil-dominated temperate systems (RK and RE).

High latitude fluvial CO_2 fluxes have occasionally been estimated from equations using CO_2 concentration gradients and gas transfer velocities (Kling *et al.*, 1992; Striegl *et al.*, 2012) and global CO_2 flux estimates have been made from pCO_2 data (e.g. Raymond *et al.*, 2013), however, published, directly measured fluvial CO_2 flux data of either direction (efflux or influx) is rare in high latitude regions, thus this research has contributed to this data scarcity. Additionally, this is the first research to suggest that GrIS meltwaters are potentially a net sink for CO_2, and to attempt to calculate the contribution of all GrIS proglacial rivers to the global CO_2 efflux budget.

Included here is the first known reconstruction of CO_2 efflux at high resolution over a number of years (Chapter 4, section 4.5.5). Together with simultaneous reconstruction of fluvial carbon pool composition, such reconstructions enable incorporation of the role of short-term processes (e.g. diel and seasonal variation) on long-term carbon fluxes and could provide valuable insight into carbon pool dynamics and potential feedbacks to climate change over decadal scales (where suitable hydrochemical data is available). This leads us closer to improved global carbon budgets and more accurate predictions of the response of the fluvial carbon cycle to climate change.

Using radiocarbon as a tracer of the carbon cycle in a high latitude, climate-change-sensitive region (Chapter 5), has provided the first direct evidence that old biolabile carbon can enter aquatic ice-melt drainage systems and subsequently be returned to the atmosphere. This further expands our understanding that, in addition to known short-term drivers such as meteorological responses (e.g. Vihermaa *et al.*, 2014), human disturbance (e.g. Butman *et al.*, 2015) and burning of fossil fuels (e.g. Van der Laan, 2010), long-term drivers, such as climate (via melting ice sheets), may be modifying atmospheric carbon composition. Used in conjunction with stable isotopic tracing, this is the first data of this kind to be applied to understanding cryospheric carbon cycling in the terrestrial-atmospheric loop.

6.4 Potential Research Directions

6.4.1 Controls on CO_2 Efflux

Having confirmed the significance of hydraulic controls over CO_2 efflux, there is potential for improving both the accuracy of CO_2 efflux estimates from surface waters using the model (6.2.1; Chapter 3), which could subsequently support more accurate global upscaling. The $R^*_{.}pCO_2$ and $\bar{u}^*pCO_2$ models (6.2.1) were highly effective in describing variation in CO_2 efflux for three temperate UK systems and four tropical Amazonian systems, but could not be applied in two supply-limited cryospheric melt/thaw systems. This highlights the need for more thorough testing of the model across a wide range of catchment types, sizes, landuses, CO_2 saturation levels and locations to constrain where the model can and cannot be applied. For example, it is likely that the model will apply in other over-saturated systems such as peat-dominated catchments (e.g. Billett and Moore, 2008; Dinsmore and Billett, 2008), but not in other supply-limited systems such as tufa systems (e.g. Chen *et al.*, 2004; Pedley *et al.*, 2009) where pH speciation and/or availability of DIC can limit efflux, but flow velocity may still be high. By considering a range of catchment sizes for each catchment type, it may be possible to isolate the effects catchment size from those of land-use/anthropogenic influence/CO_2 saturation. Additionally, at the highest flows recorded in this research, the model describes CO_2 efflux rates less-well and so further data are required in high flow conditions to refine the model. However, high flows are difficult to sample due to safety and equipment configuration. Developments in equipment design, for example an automated and/or bank-mounted system that adjusts to the flow height maintaining a seal between the floating

chamber and the water surface, preventing water ingress, and not requiring human entry to the water, will facilitate collecting these data. Additionally, it is not known whether these models apply beyond the point of riverbank breach, thus data collection and model testing is required during flood events.

CO_2 influx may also be hydraulically controlled in non-cryospheric systems (Chapter 3), but data is scarce, so to test this hypothesis, CO_2 influx data is required from a variety of catchments. Collection of simultaneous pCO_2 data will allow testing of whether the $R^*{}_{\cdot}\, pCO_2$ and $\bar{u}^* pCO_2$ efflux models can be applied for influxes. Alongside this, the frequency and magnitude of influx in predominantly effluxing systems, and the events or conditions causing a system to shift to influx should be investigated. If the switch between influx and efflux is hydrologically controlled, changing climate could increase/decrease the prevalence of influx and thus should be considered in projections of CO_2 efflux.

6.4.2 Sources of DIC and CO_2 Efflux, and Local Upscaling

Understanding of carbon pool dynamics in temperate, predominantly soil-dominated, fluvial systems is growing, with pool composition recognised to be highly hydrologically responsive (e.g. Yang *et al.*, 1996; Atekwana and Krishnamurthy, 1998; Waldron *et al.*, 2007; Doctor *et al.*, 2008; Polsenaere *et al.*, 2013). However, data are lacking for a wider array of catchment types (e.g. urban, cryospheric, karst) which may have different carbon pool dynamics (e.g. source and hydrological response) than temperate soil-dominated fluvial systems (e.g. AR and PLST, Chapter 5). Collection of considerable [DIC] and $\delta^{13}C_{DIC}$ data (and corresponding CO_2 efflux) from a wide variety of catchments is required to enable the alternative or multiple end-members of non-soil-dominated systems to be more clearly defined. This is needed to enable detailed reconstructions of pool dynamics over time, and ultimately improve projections of how fluvial systems will respond to climate change. [DIC] and $\delta^{13}C_{DIC}$ measurements of surrounding soils and vegetation could aid end-member identification in any catchment. In snow- or ice-melt influenced/dominated catchments such as RE and AR, measurements of [DIC] and $\delta^{13}C_{DIC}$ from the snow/ice itself could establish the snow/ice end-member(s), and the use of the conservative tracer $\delta^{18}O$, which can trace freshwater inputs to aquatic environments (Bigg and Rohling, 2000), could support identification of this end-member (e.g. Smiley *et al.*, 2016). Further, complications may arise when investigating sources of DIC in catchments with mixed C4 and C3 vegetation as ^{13}C-enrichment due to internal processing (e.g. CO_2 efflux) could be difficult to decipher from inputs of soil CO_2 with a C4 $\delta^{13}C$ signature. Thus, additional [DIC] and $\delta^{13}C_{DIC}$ data collection is also required here.

Simultaneous reconstructions of fluvial carbon pool source and CO_2 efflux provided new insights into C cycling mechanisms at DW (see 6.2.2). Reconstructions of this type are needed across a wider variety of non-soil-dominated catchments beyond the temperate zone to provide insight into how alternate/multiple carbon pool end-members interact, and whether such systems are subject to

internal processing of the pool. It is not known whether these models would apply in the seasonal tropics where the hydrological response of the fluvial carbon pool can differ from that of DW (e.g. Bass *et al.*, 2014a; Tweed *et al.*, 2015), or if/when a river breaches its banks (e.g. Tweed *et al.*, 2015), thus data collection and model testing is required in strongly seasonal catchments and during flood events in all catchment types. Collection of substantial 24-hour data, to assess for diel cycling, could support investigations into internal pool processing. In fact, diel sampling should be carried out as routine practice in all systems across the array of water chemistry parameters affected by the daily sun cycle (e.g. Nimick *et al.*, 2011) to prevent the manifestation of non-representative results and spurious spatio-temporal trends (Gammons *et al.*, 2011; Tobias and Böhlke, 2011).

Although pH (used as the independent variable in predictive models and CO_2 efflux reconstructions here) is a reasonable indicator of CO_2 availability, $R^*.pCO_2$ explains variation in efflux much better than pH alone (Chapter 3). Thus future CO_2 efflux models and reconstructions should aim to use R^* and pCO_2 instead of pH. Sensors exist capable of direct and continuous measurement of pCO_2 from rivers (and other freshwaters) (e.g. Johnson *et al.*, 2010), and R^* is straightforward to calculate from flow velocity profiles (Chapter 3), thus collection of future CO_2 datasets should ideally be concomitant with the use of pCO_2 sensors and measurement of flow profiles. Additionally, the highest efflux occurs over a wide range of R^* (and associated flow velocities), suggesting additional controls, e.g. diel or seasonal responses and/or the impact of hydrological events, influence efflux and therefore should be incorporated empirically into the model.

A system has been developed capable of directly measuring [DIC] and $\delta^{13}C_{DIC}$ at sub-hourly resolution (ISCO-CADICA, Bass *et al.*, 2012). However this has not been deployed over time scales longer than a few weeks (e.g. 19 day continuous sampling of the Southern Ocean, Bass *et al.*, 2014), and has only occasionally been used in rivers, for a maximum of ~36 hours (Bass *et al.*, 2013; Bass *et al.*, 2014a; Tweed *et al.*, 2015). Use of ISO-CADICA over longer time-scales in fluvial systems could remove the need for reconstructing [DIC] and $\delta^{13}C_{DIC}$ from hydrochemical parameters (which have large uncertainty at high flows) in the future. Where ISO-CADICA is not available, models could be refined, and uncertainty reduced by inclusion of significant additional high-flow data (if safety and equipment restrictions can be overcome) and event sampling data. Additionally, to support the use of [DIC] and $\delta^{13}C_{DIC}$ as tracers of source of fluvial carbon, conservative tracers such as $\delta^{18}O$ and δD could be used to independently track the mixing of water sources in the river (e.g. Buhl *et al.*, 1991; Kebede *et al.*, 2005; Rock and Mayer, 2007; Hameed *et al.*, 2015; Smiley *et al.*, 2016).

Measurement of ^{14}C-age and $\delta^{13}C$ of efflux proved of considerable insight to the fluvial carbon pool dynamics of the cryospheric melt/thaw systems sampled in Greenland (Chapter 5). Applying this technique at the other three sites (DW, RK and RE) could provide new insight into their fluvial

carbon cycling and/or confirm findings of DIC pool source and controls from $\delta^{13}C_{DIC}$ data. For example, as preparation for radiocarbon sampling during the Greenland field campaign, one CO_2 efflux sample was collected at RK on 15-May-2014 and subsequently tested for ^{14}C age and $\delta^{13}C_{efflux}$, which were 1682 +/-37 yrs BP and -19.9 ‰ respectively (all methods were identical to Chapter 5). The old age of the effluxed carbon could confirm the influence of carbonates in concrete that are contained within urban runoff on the DIC pool (suspected from $\delta^{13}C_{DIC}$ results), as marine carbonates are millions of years in age and thus radiocarbon dead and so would increase the ^{14}C-age of the pool (e.g. Vihermaa *et al.*, 2014). Further, the application of ^{14}C age tracing across a range of urban catchments could enable refinement of the "urban stream syndrome"; a term which describes urban effects on stream ecosystem processes, and symptoms of which include flashier hydrology, elevated concentrations of nutrients and contaminants, altered channel morphology and reduced biotic richness (Walsh *et al.*, 2005). The $\delta^{13}C_{efflux}$ being more ^{13}C-depleted than the minimum $\delta^{13}C_{DIC}$ measured at the site could confirm that efflux at the site is ^{13}C-depleted and thus enriching the DIC pool (e.g. Doctor *et al.*, 2008). Of course, it is difficult to make any firm conclusions from one sample, however these results highlight that further research could enhance understanding of carbon pool dynamics of fluvial systems, particularly in urban systems where no other published data exist. As an example, collection of efflux could be synchronously carried out along the length of the River Kelvin (and subsequently analysed for ^{14}C-age and $\delta^{13}C_{efflux}$) to investigate if the old CO_2 signature is derived from the rural or urban landscape. Carrying this investigation out across a wide array of catchment types has the potential to significantly improve our knowledge of carbon cycling dynamics globally.

Although it is known that CO_2 degassing can be regulated by riparian and hyporheic CO_2 inputs (Abril *et al.*, 2000; Billett *et al.*, 2004; Polsenaere and Abril, 2012; Peter *et al.*, 2014), knowledge is lacking of CO_2 recharge from the interaction of the water column with the riparian, benthic and hyporheic zones, and how this influences the capacity of a fluvial system to degas. Riparian, benthic and hyporheic influences on the fluvial carbon pool needs consideration and should be included in any models that estimate CO_2 degassing at catchment scale (Abril *et al.*, 2014).

6.4.3 Large-Scale Upscaling

6.4.3.1 River Surface Area

Upscaling of CO_2 efflux over large areas is currently very difficult due to unavailability of accurate river surface area data (Striegl *et al.*, 2012; Raymond *et al.*, 2013). More accurate estimate of river surface area are beginning to be made (e.g. Striegl *et al.*, 2012; Denfeld *et al.*, 2013), but global coverage remains poor, and is particularly sparse at high latitudes (Raymond *et al.*, 2013, Khadka *et al.*, 2014). As river surface area is as important to regional CO_2 efflux estimates as the rate of efflux per unit area (Aufdenkampe *et al.*, 2011; Denfeld *et al.*, 2013), any attempts to upscale CO_2 efflux at large spatial scale requires this data scarcity be addressed.

6.4.3.2 Visual Water Surface Classification

Further testing of the proposed visual approach to upscaling CO_2 (e.g. Figure 73) is required to reduce the potential for subjectivity and variation in water surface state estimates between observers, and to constrain where the method can and cannot be applied.

Figure 73: Example of visual water surface classification

On the left is an example of varied water surfaces at RK. On the right is an example of classifying the water surface types: blue = smooth, yellow = medium, orange = rough. For water surface state classification method see Chapter 2.

The testing involves three phases: (1) clarification of visual classification, for example a Beaufort Scale equivalent for river surface appearance; (2) local scale comparisons between nearby reaches with different surface state; (3) inter-catchment comparisons over a range of catchment sizes, land uses and global locations. The Beaufort Scale (available at: www.spc.noaa.gov/faq/tornado/beaufort .html) is used in the open ocean and directly relates sea-surface state to wind speed. River and stream surfaces are far less impacted by wind than the ocean or large lakes due to short fetch distances (Gordon et al., 2004; Alin et al., 2011). Bed roughness and slope, both of which control the inter-dependent quantities of flow depth and velocity, are more significant controls over river surface disturbance, and are reflected in the Froude number (Gordon *et al*., 2004). A river-equivalent scale could therefore be calibrated using *Fr* measurements (which were found to have a strong relationship with CO_2 efflux, Chapter 3, section 3.4) and thus visual classification provide estimates of *Fr*, and subsequently efflux, where direct measurement is not possible. If this visual classification method can be sufficiently refined, this approach could be used to estimate *Fr* from the water surface state measured from aerial imagery (e.g. Gordon, 2005), thus allowing for rapid upscaling of CO_2 efflux over large areas. Additionally, estimates of CO_2 efflux from low-order and/or inaccessible streams could be more accurately incorporated into catchment scale or global estimates of riverine CO_2 efflux.

6.4.3.3 The Arctic

This research has demonstrated the need to include melting/thawing cryospheric systems in global carbon budgets, particularly as a warming climate is predicted to increase melting of ice and thawing of permafrost and thus the volume and surface area of their melt/thaw waters (IPCC, 2013; Vonk *et al*., 2013). Although it has been demonstrated here that the systems can periodically act as sources and sinks for CO_2 (Chapter 5), there is very little other directly measured CO_2 efflux data available for the Arctic, thus the magnitude, direction and distribution of efflux/influx over the region as a whole is unknown. As such, the preliminary upscaling of GrIS meltwater CO_2 efflux here (Chapter 5) is subject to large assumptions. For more precise CO_2 efflux budgets to be calculated for the Arctic, significant collection of directly measured CO_2 efflux data from a range of rivers across the region, and covering a broad temporal range is required to address these unknowns. Ideally data collection should span the entire melt season so any effects of seasonality on efflux can be accounted for.

There is also very limited information on source of DIC in the fluvial pool. Although a few studies report $\delta^{13}C_{DOC}$ of arctic fluvial systems (e.g. Hood *et al.*, 2009; Bhatia *et al.*, 2013; Vonk *et al.*, 2013), fewer report $\delta^{13}C_{DIC}$ (e.g. Giesler *et al.*, 2013), a small number report age of DOC (e.g. Hood *et al.*, 2009; Bhatia *et al.*, 2013; Vonk *et al.*, 2013; Mann *et al.*, 2015; Spencer *et al.*, 2015) and no other studies report the age of efflux (reported here in Chapter 5). If these data were to be collected across a broad range of arctic melt/thaw waters, both spatially and temporally, they would provide further detail of carbon pool dynamics and the sources of the effluxing CO_2 in cryospheric systems, for more accurate inclusion into global carbon budgets, upscaling attempts and projections of response to climate change. These data are also important to any studies using ^{14}C as a tracer of residence time or source of atmospheric CO_2 (e.g. Levin *et al.*, 2008; Van Der Laan *et al.*, 2010; Levin *et al.*, 2013), and it is important such studies consider that melting ice sheets may be modifying atmospheric carbon composition, alongside other processes such as burning of fossil fuels.

The role of glacier-derived DOC in a fluvial system needs further consideration. Although it is agreed that this DOC is more biologically-available than terrestrial DOC (e.g. Lawson *et al.*, 2014; Hood *et al.*, 2015), it is not clear whether the net effect is a feed back to climate change through stimulation of heterotrophic degradation of more stable DOC downstream (e.g. Singer *et al.*, 2012; Hood *et al.*, 2015), or facilitation of atmospheric CO_2 drawdown through stimulation of the autotrophic component of biofilms (Lovatt *et al.*, 2014). The balance of these processes is a significant unknown, but requires clarification as it could affect the direction in which melting glaciers/ice sheets impact upon climate change.

In summary, new data presented in this research has led to a greater understanding of the controls and origins of CO_2 efflux, across an array of catchment types, sizes, land uses and global locations, and has made significant contributions of novel data to a number of areas of fluvial carbon cycling research where there are scarcities. However, as with all scientific research, a number of exciting new questions have been raised that challenge our conceptualisation of the processes and our technical ability to collect the required data. Meeting these challenges in the Anthropocene (e.g. Vitousek *et al.*, 1997; Meybeck, 2003; Zalasiewicz *et al.*, 2011), an era where the continental aquatic systems can no longer be considered as being controlled by only Earth system processes (Meybeck, 2003), is vital to offer further understanding of a world that is changing at an unprecedented rate.

Appendices

Appendix A – Stable Isotopes: Extra Information

Isotopes, a concept first proposed by Frederick Soddy in 1914 at the University of Glasgow, are atoms with identical numbers of protons and electrons but a different number of neutrons (Michener and Lajtha, 2008) Criss, 1999). Due to these varying numbers of neutrons, isotopes are "versions" of an element with identical chemical properties but different atomic masses (Clark and Fritz, 1997). Most elements are known to have at least two stable isotopes, with the lighter of the two usually the most abundant, and by a large margin (Clark and Fritz, 1997). Stable isotopes do not undergo radioactive decay.

The naturally occurring isotopes of elements abundant in the environment are known as environmental isotopes; these are C, H, N, O and S. As the principle elements of hydrological, biological and geological systems their stable isotopes serve as tracers of water carbon and nutrient cycling (Clark and Fritz, 1997). All the environmental isotopes have low atomic mass thus the relative mass differences between isotopes is large, imparting measurable fractions during physical and chemical reactions (Clark and Fritz, 1997; Michener and Lajtha, 2008). Most relevant to this study are the two stable isotopes of carbon, ^{12}C and ^{13}C. ^{12}C, the lighter isotope, is vastly more abundant (98.89%) than the heavier ^{13}C (1.11%) (Clark and Fritz, 1997) and the relative mass difference between ^{12}C and ^{13}C is 8.3% (Michener and Lajtha, 2008).

Fractionation

Isotopic fractionation is the partitioning of isotopes between two substances or two phases of the same substance, and causes the isotope ratios in different materials and samples to vary (Criss, 1999 (Hoefs, 1997). The isotopic configuration of a molecule affects its mass and thus its reaction rate (Clark and Fritz, 1997); molecules bearing the lighter isotope will generally react more readily than those bearing the heavy isotope as light isotope intra- and inter-molecular bonds are weaker (Hoefs, 1997). Thus ultimately is it isotopic mass differences that lead to fractionation (Urey, 1947) causing a disproportionate concentration of one isotope over another on one side of the reaction (Clark and Fritz, 1997). Isotope fractionation is dependent on the temperature of the reaction (Clark and Fritz, 1997). The main mechanisms that lead to isotopic fractionation are equilibrium fractionation and kinetic processes (Michener and Lajtha 2008; Hoefs, 1997):

Equilibrium fractionation

Equilibrium fractionation occurs when a reaction is in equilibrium, and leads to differing isotope distribution between chemical substances or phases or individual molecule due to stronger intramolecular bonds formed by heavier isotopes (O'Neil, 1986; Clark and Fritz, 1997; Criss 1999); stronger bonds require more energy to break, thus heavier isotopes react more slowly and

tend to accumulate in the densest phase where bonds are generally the strongest (Michener and Lajtha 2008; Hoefs, 1997; Clark and Fritz, 2007). Equilibrium fractionations tend to be small (Criss, 1999), but will be largest in elements which have low atomic weight, and so can be significant for the environmental isotopes, including carbon.

Kinetic isotope effects

Kinetic isotope effects occur in fast, incomplete or unidirectional reactions, e.g. reactions in an open system or where the reverse reaction is inhibited (O'Neil, 1986; Michener and Lajtha, 2008; Criss, 1999). Kinetic fractionations are often relatively large, usually much larger than equilibrium fractionations, and again, isotope velocity and bond strength are again important with the weaker light isotope bonds resulting in the light isotope accumulating in the product (Michener and Lajtha, 2008). The key processes that cause a kinetic isotope effect are evaporation (O'Neil, 1986; Hoefs, 1997; Clark and Fritz, 1997; Criss 1999), diffusion (O'Neil, 1986, Hoefs, 1997, Criss, 1999), dissociation (Criss, 1999), and metabolism (Clark and Fritz, 1997; Criss, 1999).

a) Evaporation: fractionation is due to differences in vapour pressure of isotopic compounds. The lighter molecular species have greater translational velocities and so tend to preferentially form vapour, this leading to isotopic fractionation between the vapour and the liquid phase, with the vapour enriched in the light isotope and the residual liquid becoming progressively enriched in the heavy isotope (O'Neil, 1986; Hoefs, 1997; Clark and Fritz, 1997; Criss 1999). The extent of fractionation is dependent on temperature (Hoefs, 1997; Clark and Fritz, 1997).

b) Diffusion: fractionation occurs as molecules diffuse across a concentration gradient, due to the mass-caused difference in diffusive velocities between isotopes (Clark and Fritz, 1997; Criss, 1999). In general, light isotopes are more mobile and move faster and can thus preferentially diffuse out of a system, leaving the heavy isotopes to become progressively more enriched in the residue (O'Neil, 1986, Hoefs, 1997, Criss, 1999).

c) Dissociation: fractionation occurring in reactions where the reaction rate-determining step involves the breaking of a chemical bond (dissociation). Because the vibrational frequency of intermolecular bonds involving the lighter isotopes tends to be higher, bonds are substantially easier to break than those involving the heavy isotope, thus the light isotope is preferentially incorporated in the product of an incomplete reaction, and the unreacted residue enriched in the heavy isotope (Criss, 1999).

d) Metabolic Effects. Biological metabolic processes often show isotopic preferences and are essentially irreversible reactions. Enzymatic reaction pathways can be complex, are usually redox, and can involve very large isotopic fractionation effects. Metabolic effects can simultaneously incorporate the effects of several kinetic effects, as well as equilibrium effects. Important examples are bacteria mediated reactions and photosynthesis (Clark and Fritz, 1997; Criss, 1999).

Photosynthetic Pathways

C3: operates in ~85% of plant species and dominates in most terrestrial ecosystems. Causes a ^{13}C depletion ~ 22‰ from atmospheric values by C3 plants, and most have $\delta^{13}C$ values that range from -23 to -34 ‰ with an average of about -27 ‰ (Faure 1986; Vogel, 1993). The natural vegetation of temperate and high latitude regions is almost exclusively C3, which also dominates in tropical forests and most major crops (Clark and Fritz, 1997).

C4: occurs in < 5% of plants. It is a more recently evolved photosynthetic pathway and is more efficient. $\delta^{13}C$ ranges from -10 to -16 ‰, with a mean of ~ -12.5 ‰ (Vogel 1993). C4 dominates in hot open ecosystems such as tropical and temperate grasslands and is common agricultural plants (Clark and Fritz, 1997).

CAM: occurs in ~10% of plants, dominating in desert ecosystems in species such as cacti. CAM plants have the ability to alter between C3 during the day to C4 at night. Their isotopic composition thus spans the range of both C3 and C4 plants but is usually intermediate (Clark and Fritz, 1997).

Extra Information on Measurement and Notation of $\delta^{13}C_{DIC}$

Isotopic composition is reported as the relative difference between an internationally accepted standard and a sample (detailed guidelines available in Coplen et al., 2011). Materials are established as internationally recognised isotope standards to allow standardisation between laboratories, however laboratories may use calibrated internal working standards for measurement (Clark and Fritz, 1997; Michener and Lajtha, 2008). The international standard for carbon was Pee Dee Belemnite, introduced by Craig (1957) and sourced from the internal calcite structure of a fossil *Belemnitella americana* from the cretaceous Pee Dee Formation in South Carolina. The original PDB is no longer available, thus the United Nations International Atomic Energy Agency (IAEA) in Vienna has defined a hypothetical VPDB as the reference against which all $\delta^{13}C$ measurements are reported and it's R-value is set as 0.011237 (Clark and Fritz, 1997).

A positive δ-value, e.g. $\delta^{13}C$ = +10 ‰, signifies that a sample has more (10 permil more) of the heavy isotope (^{13}C) than the standard, thus it ^{13}C 'enriched'; conversely, a negative δ-value (e.g. $\delta^{13}C$ = -10 ‰) indicates the sample has less (10 permil less) of the heavy isotope than the standard, and it is ^{13}C 'depleted' (Clark and Fritz, 1997; Michener and Lajtha, 2008).

Appendix B – Publication by Long *et al*. (2015)

Details of the publication by Long *et al*. (2015):

AGU Publications

Journal of Geophysical Research: Biogeosciences

"Hydraulics are a first-order control on CO_2 Efflux from Fluvial Systems"

Hazel Long[1], Leena Vihermaa[1], Susan Waldron[1], Trevor Hoey[1], Simon Quemin[1,2,3,4], and Jason Newton[5]

[1] School of Geographical and Earth Sciences, University of Glasgow, Glasgow, UK
[2] ENSTA ParisTech, Palaiseau, France
[3] Now at Centre of Geopolitics of Energy and Raw Materials, Paris-Dauphine University, Paris, France
[4] Now at Climate Economics Chair, Paris, France
[5] Scottish Universities Environmental Research Centre, East Kilbride, UK

Volume 120, pages 1912-1922, doi: 10.1002/2015JG002955.

Published Online 8 October 2015

The publication covers pages 162 – 172 of this thesis.

Appendix C – Supporting Information for Long *et al*. (2015)

Biogeosciences

Supporting Information for

Hydraulics are a first order control on CO_2 efflux from fluvial systems

Hazel Long[1], Leena Vihermaa[1], Susan Waldron[1], Trevor Hoey[1], Simon Quemin[1,2,3], Jason Newton[4]

[1] *School of Geographical and Earth Sciences, University of Glasgow, Glasgow, G12 8QQ, UK*

[2]*ENSTA ParisTech, 828 Boulevard des Maréchaux, 91120 Palaiseau, France*

[3]*Now at: Paris-Dauphine University, Place du Maréchal de Lattre de Tassigny, 75775 Paris Cedex 16 and the Climate Economics Chair, Palais de la Bourse, 75002 Paris*

[4]*Scottish Universities Environmental Research Centre, Scottish Enterprise Technology Park, East Kilbride, G75 0QF, UK*

Contents of this file

Introduction

i) The figures below provide additional information for:

ii) The location of sites used in global a comparison of directly measured CO_2 efflux rates from flowing waters (Fig.1 and Table 1 of main article).

iii) The set-up of the equipment used to measure CO_2 efflux. CO_2 efflux was quantified from the rate of CO_2 accumulation in a floating chamber of known volume (0.0029 m^3). Identical method and equipment set-up was used throughout the period of study (June 2012 to December 2013).

iv) The relationship between pH and discharge used to calculate pH for one of the six study sites; the River Kelvin where pH measurements were lacking due to instrument malfunction. This was created using discharge and pH data supplied by the Scottish Environment Protection Agency (SEPA) from their Killermont gauging station (station reference number NS 55828 70516) located 9 km upstream of the sampling location of this study. Data from 10 discrete sampling

dates during the period of study (June 2012 to December 2013) were used. The use of Killermont data to predict pH at our sampling site was justified by results from Kelvin River spatial sampling that showed close agreement both in pH and conductivity between these sampling points.

v) Estimating the uncertainty in pCO_2 resulting from the quantification of the DIC pool ([DIC]) and the measurement of pH.

vi) The distribution of the residuals from the multiple regression model (Eq. 3 main article) and the relationship between the linear regression and linear mixed effect model predictions and measured CO_2 efflux (Eq. 3 and 4 main article). This analysis was carried out using R statistical package version 3.1.0.

vii) The relationship between CO_2 efflux and the product of flow velocity and pCO_2. By including the influence of pCO_2, NC falls in line with the other five study sites whether or not the axes are not log transformed

viii) The visual classification of water surface state.

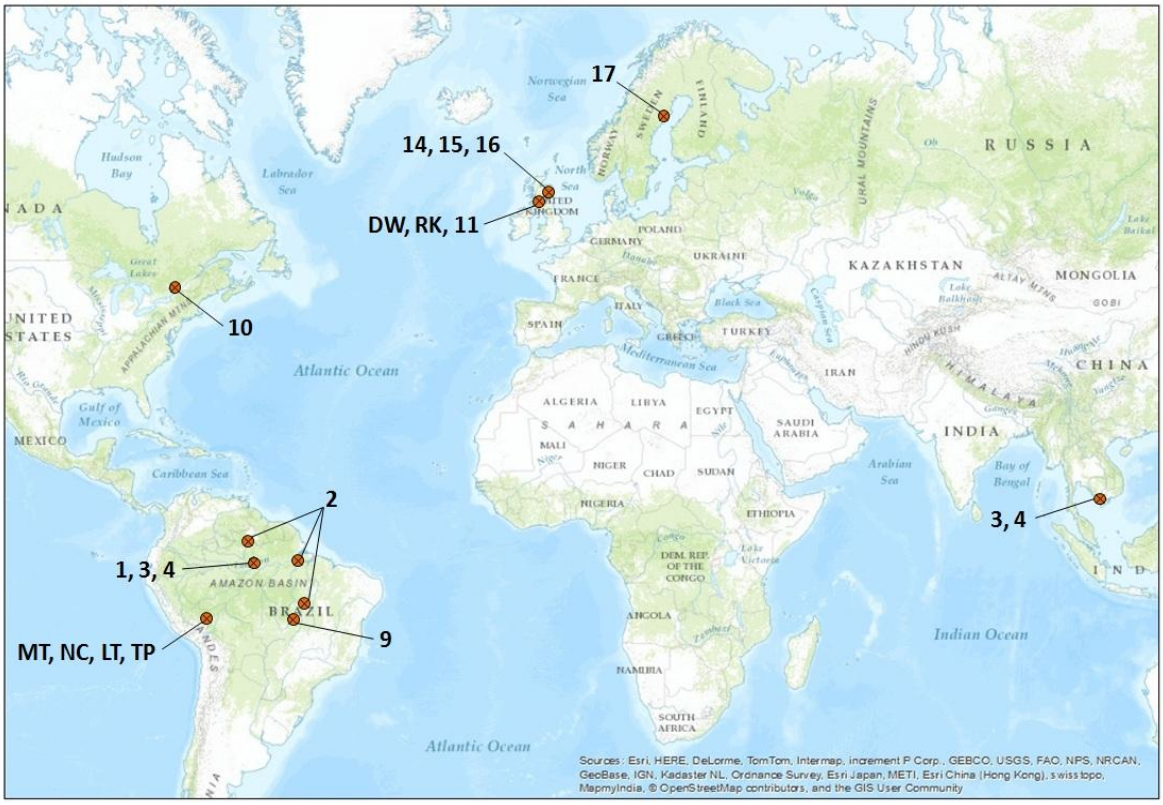

Figure S1: Locations of sites coded in Fig. 1 and Table 1. Site labels were added to a World Topo Map which was created using ArcGIS® software by Esri. ArcGIS® and ArcMap™ are the intellectual property of Esri and are used herein under license. Copyright © Esri. All rights reserved. For more information about Esri® software, please visit www.esri.com.

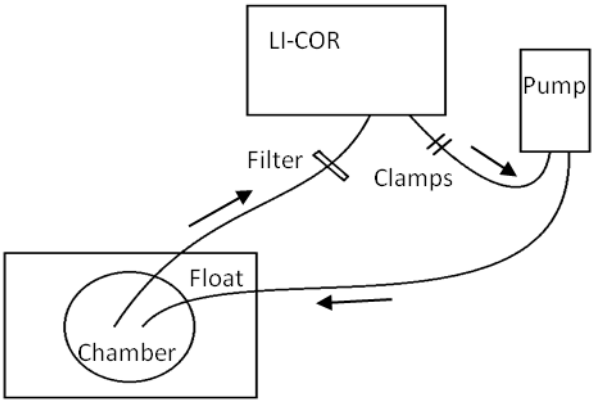

Figure S2. Schematic diagram (not to scale) of the closed-loop floating chamber system. Pump (Schego Optimal) is to ensure internal air circulation. Arrows show direction of air flow. Filter is in place to protect LI-COR from water/particles that may enter the tubing. Clamps are to maintain the circulating airflow at speed 0.3 – 1.0 L min^{-1}.

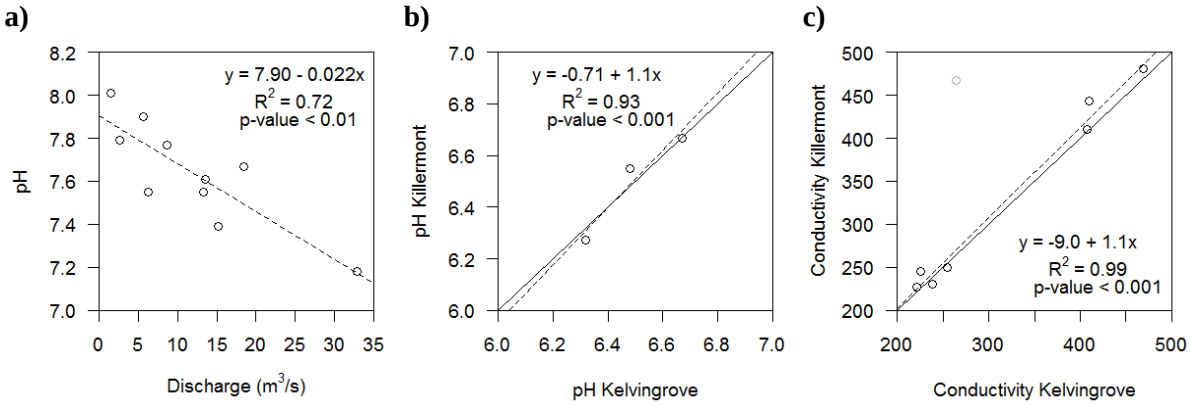

Figure S3. a) The relationship between discharge and pH (n=10) observed at the SEPA Killermont monitoring station, used to calculate pH for the River Kelvin. b-c) Kelvin spatial sampling data (Hemanth Pasumarthi unpublished data) showing good agreement in pH (n=3) and conducticity (n=7, µS/cm) between the SEPA sampling point at Killermont and our sampling point in Kelvingrove park. Dotted line is the best fit regression line and solid line the 1:1 line. In conductivity data one outlying value (marked in grey) was observed in January 2014 and the regression was fitted excluding this value.

Estimating Uncertainty in pCO_2:

The two measurement components that influence pCO_2 calculation the most are the quantification of the DIC pool, and the measurement of pH that is used in calculating the proportion of the pool that is free CO_2 [e.g. *Abril et al.*, 2015]. As the systems were both calibrated with standards purchased externally, or made gravimetrically and used across multiple other systems, accuracy is assumed to be acceptable and not inducing error that needs to be considered here.

Here pH is precise to ± 0.1 pH units (the manufacturers specification for the Troll 9000 and 9500) and DIC to ± 0.027 mmol L^{-1} (the mean worst case scenario generated using statistically rigorous inverse confidence interval calibrations and so conservative; the error quantification approach is reported extensively in *Waldron et al.*, 2014). For River Kelvin pH calculations, the % residuals indicated uncertainty of 1.3% (Fig. S3).

We propagated these uncertainties in our pCO_2 calculations. Table S1 summaries for each site the percentage uncertainty in pCO_2 that arises for these individual components as well as the total error arising from both sources. There are two values associated with uncertainty from pH as DIC equilibrium renders this asymmetrical dependent on the sample field pH. The total uncertainty for each pCO_2 estimate is shown in figure S4.

Our error propagation suggests there is on average 14.4 – 32.8% total uncertainty in our pCO_2 values (Table S1 and Fig. S4). This may have been greater if we had calculated [DIC] from total alkalinity (TA) than from sample acidification and headspace analysis [Raymond et al., 1997; Waldron et al 2014; Aberg and Wallin, 2014]. Indeed pH/[DIC] calculation of pCO_2 has been used as a method of correcting errors arising from alkalinity titrations [Hunt et al., 2011].

Table S16: Uncertainty in pCO_2 values that arises with the measurement capacity precision.

	% uncertainty in pCO_2							
	DIC		pH +0.1		pH -0.1		Mean total %	
Site	mean	range	mean	range	mean	range	plus	minus
New Colpita	6.9	3.5 to 16.0	12.4	8.7 to 16.0	-12.6	-8.2 to -17.7	14.4	14.6
Main Trail	32.7	18.0 to 52.6	1.2	-0.2 to 1.7	-1.1	-0.4 to -2.2	32.8	32.8
La Torre	12.4	5.9 to 35.9	14.7	2.3 to 19.2	-16.4	-1.9 to 23.2	20.2	21.7
Tambopata	11.0	6.8 to 19.3	17.1	12.0 to 19.4	-19.7	-12.1 to -23.6	20.5	22.7
Drumtee Water	12.8	1.9 to 40.8	15.3	2.3 to 20.3	-17.7	-1.9 to -25.1	22.4	24.7
Kelvin River	2.2	1.2 to 5.6	20.4	18.3 to 20.9	-25.3	-21.8 to -26.2	20.6	25.5

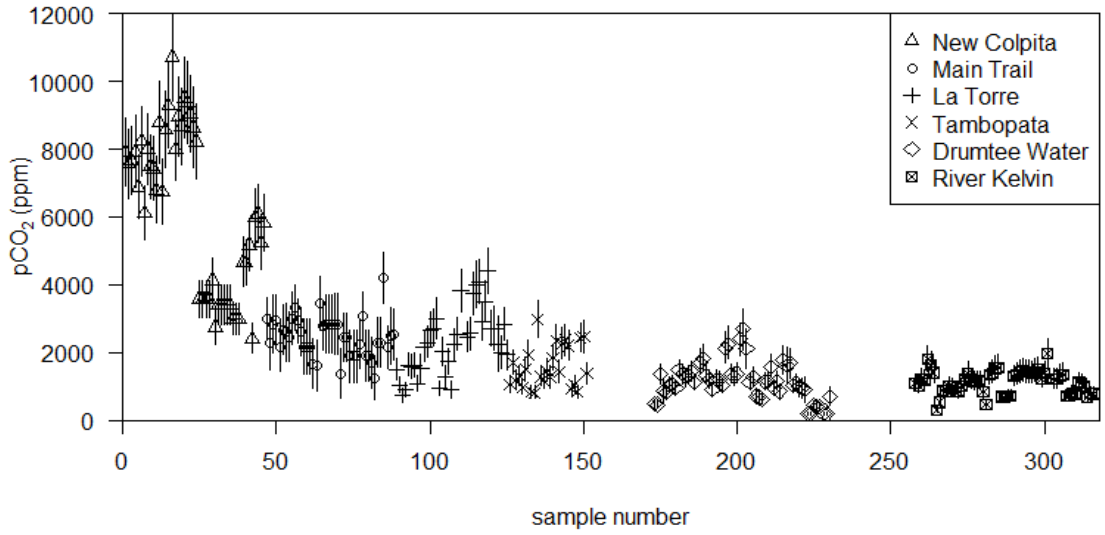

Figure S4: pCO_2 data for all UK (DW, RK) and Amazonian sites (NC, MT, LT, TP). The error bars show the total uncertainties in the pCO_2 estimates arising from the pH and DIC measurements. One-way ANOVA shows NC is statistically different in pCO_2 from the other sites at p = <0.001.

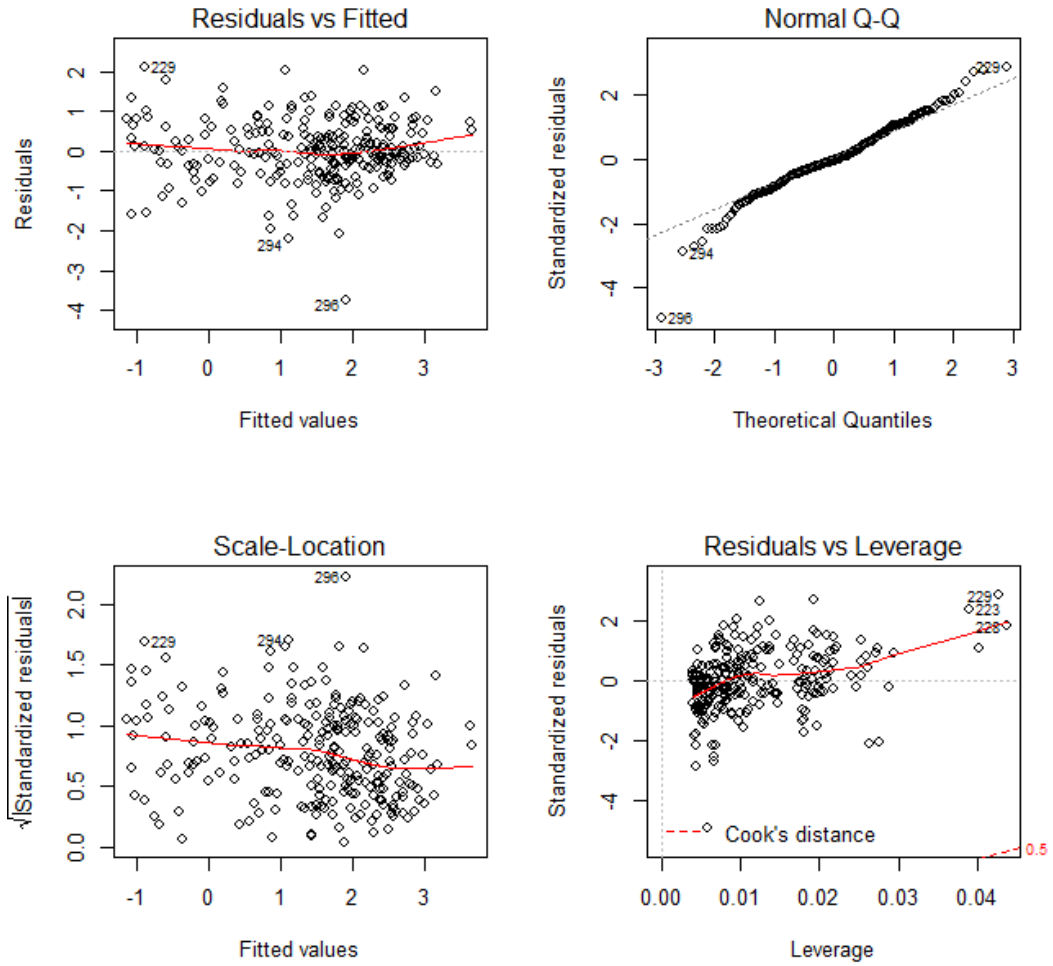

Figure S5. Residuals from multiple regression model (Eq. 3). These are close to normally distributed and are random with respect to the fitted values. Analysis carried out using R statistical package version 3.1.0.

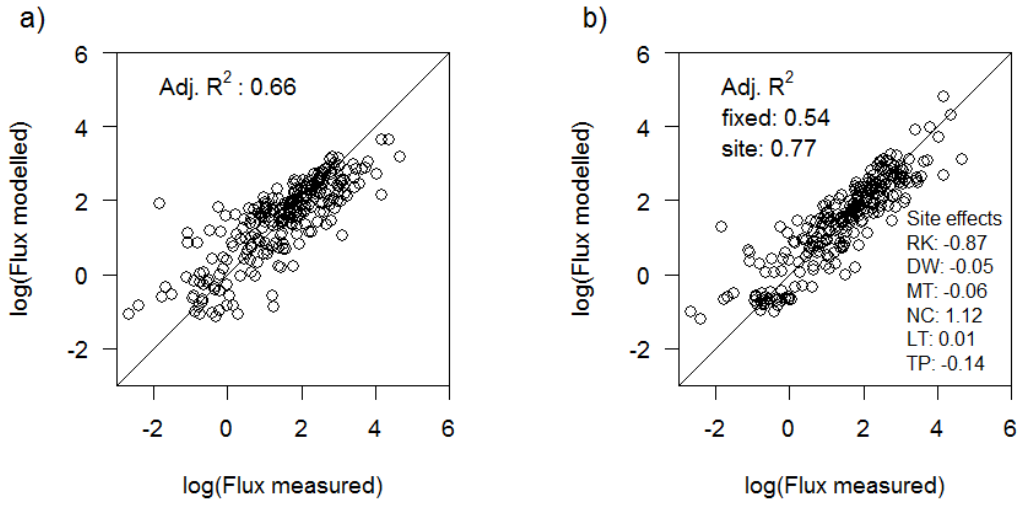

Figure S6. Results from the regression models. a) Linear regression (Eq. 3) predictions plotted against measured CO_2 efflux; concordance correlation coefficient (ccc) for the relationship was 0.80. b) Linear mixed effect model (Eq. 4) predictions plotted against measured CO_2 efflux, ccc = 0.88. R^2 was calculated using the furnival function for the fixed effects of flow and pCO_2 only and including the site specific random effects on the intercept listed on the bottom right. Analysis carried out using R statistical package version 3.1.0.

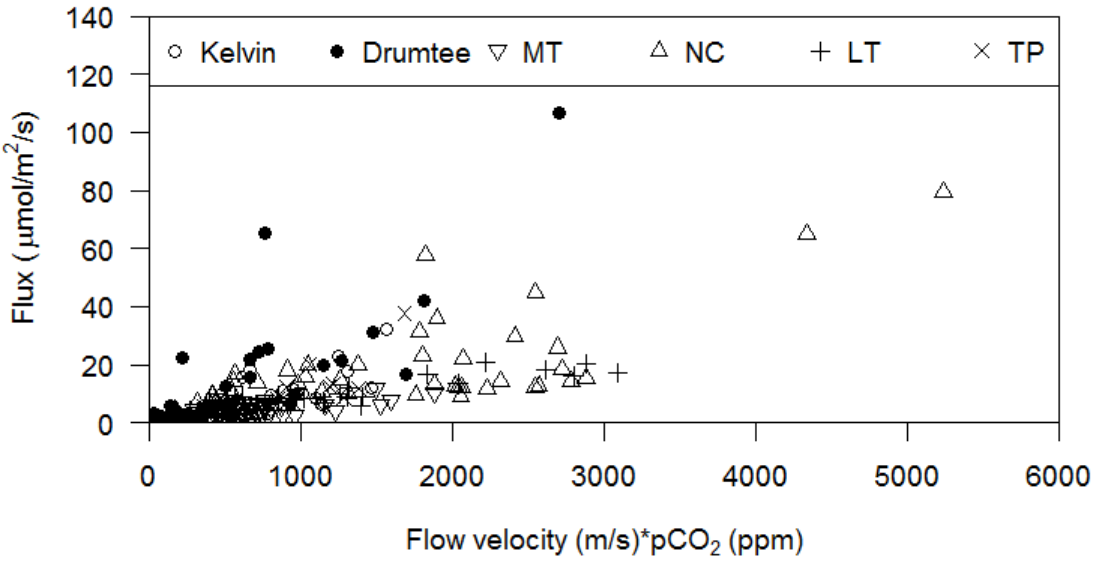

Figure S7: Data from all UK (RK, DW) and Amazonian sites (MT, NC, LT, TP) demonstrating a relationship between CO_2 efflux and the product of flow velocity and pCO_2. By including the influence of pCO_2, NC falls in line with the rest of the study sites whether the axes are not log transformed (as here) or are log transformed (see Fig. 4 main article).

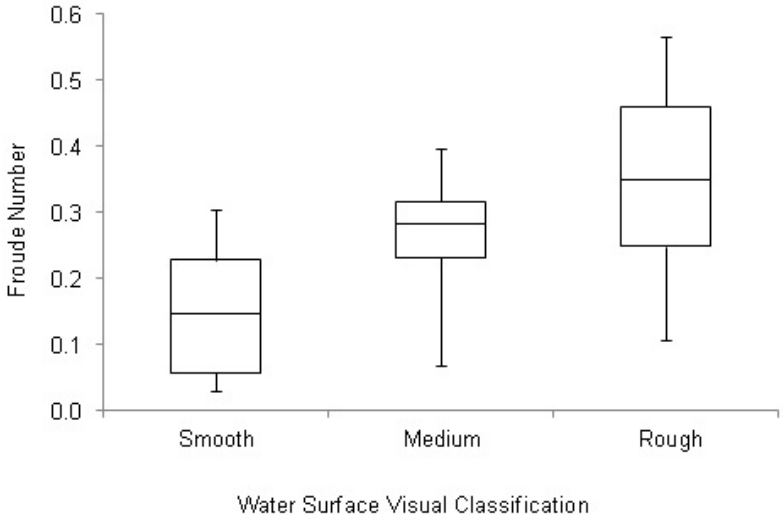

Figure S8. Water surfaces classified as 'smooth' separate by Froude number from those classified as 'medium' and 'rough'. Boxes represent interquartile range with the horizontal line as the median, upper and lower whiskers represent maximum and minimum values respectively. One-way ANOVA, with smooth, medium and rough categories, confirmed that the differences between classes are significant ($F = 48.8$; $p<0.001$). Means of each of the three pairs of classes (smooth-medium; smooth-rough; medium-rough) are also significantly different (t-tests; $p<0.001$ in all cases).

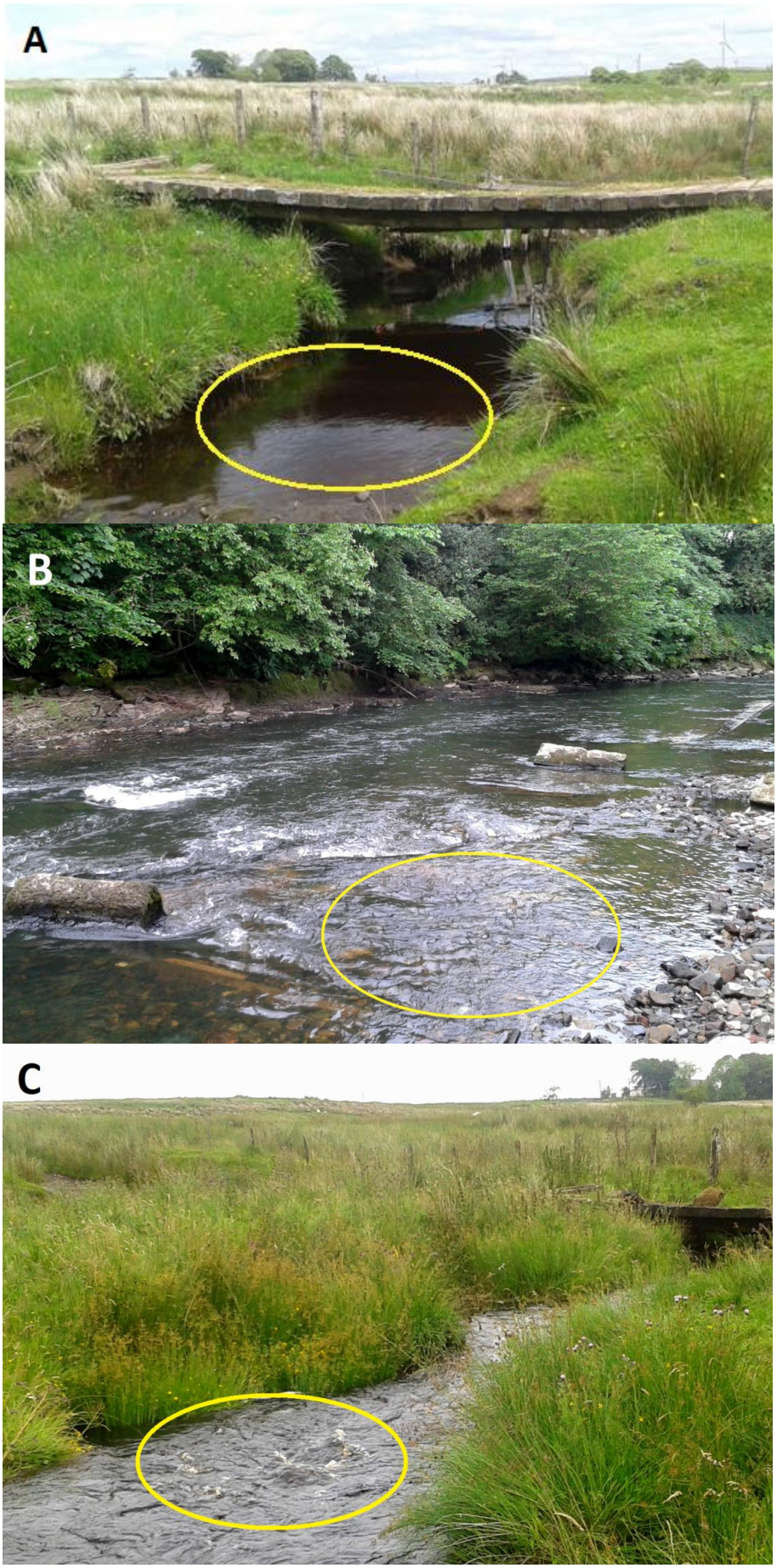

Figure S9. Photographic examples of water surface state classifications – Water surface highlighted with yellow oval. A) Smooth = a flat water surface; B) Medium = ripples, with no white water; C) Rough = ripples with white water.

REFERENCES:

Åberg, J., and M. B. Wallin (2014), Evaluating a fast headspace method for measuring DIC and subsequent calculation of pCO_2 in freshwater systems, Inland Waters, 4, 157–166, doi: 10.5268/IW-4.2.694

Abril, G., J-M. Martinez, L. F. Artigas, P. Moreira-Turcq, M. F. Benedetti, L. Vidal, T. Meziane, J-H. Kim, M. C. Bernardes, N. Savoye, J. Deborde, E. L. Souza, P. Albéric, M. F. Landim de Souza, and F. Roland (2014), Amazon River carbon dioxide outgassing fuelled by wetlands, Nature, 505, 395-398, doi:10.1038/nature12797.Abril, G., S. Bouillon, F. Darchambeau, C. R. Teodoru, T. R. Marwick, F. Tamooh, F. Ochieng Omengo, N. Geeraert, L. Deirmendjian, P. Polsenaere, and A. V. Borges (2015), Technical Note: Large overestimation of pCO_2 calculated from pH and alkalinity in acidic, organic-rich freshwaters, Biogeosciences, 12, 67-78, doi:10.5194/bg-12-67-2015.

Hunt, C. W., J. E. Salisbury, and D. Vandemark (2011), Contribution of non-carbonate anions to total alkalinity and overestimation of pCO_2 in New England and Brunswick rivers, Biogeosciences, 8, 3069-3076, doi: 10.5194/bg-8-3069-2011.

Raymond, P. A., N.F. Caraco, and J. J. Cole (1997), Carbon dioxide concentration and atmospheric flux in the Hudson River, Estuaries, 20, 381–390, doi: 10.2307/1352351.

Waldron, S., E. M. Scott, L. E. Vihermaa, and J. Newton (2014), Quantifying precision and accuracy of measurements of dissolved inorganic carbon stable isotopic composition using continuous-flow isotope-ratio mass spectrometry, Rapid Communications Mass Spectrometry, 28, 1117-1126, doi: 10.1002/rcm.6873.

Appendix D – Hydrographs for DW and RK with Timing of Sampling Occasions

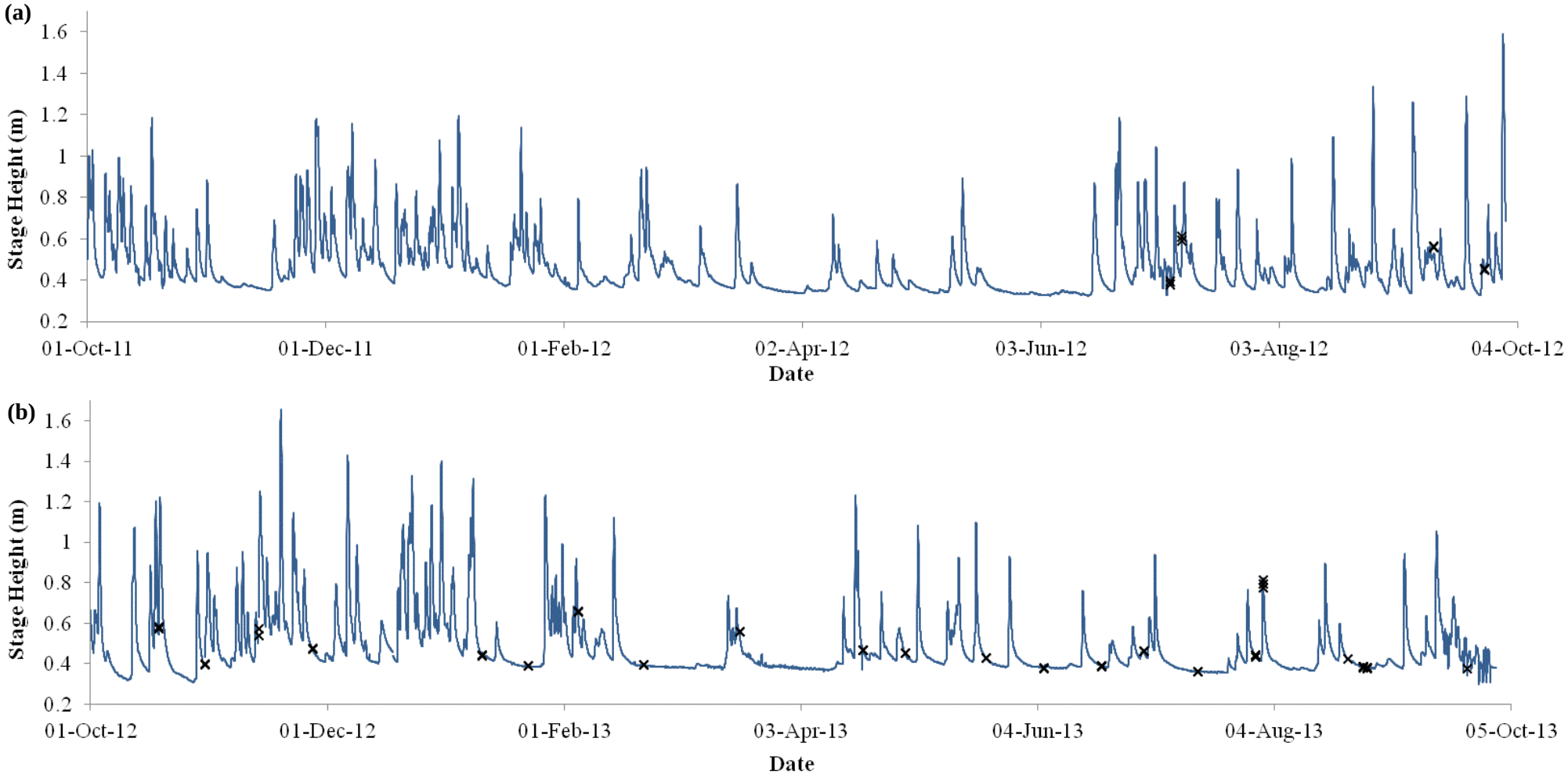

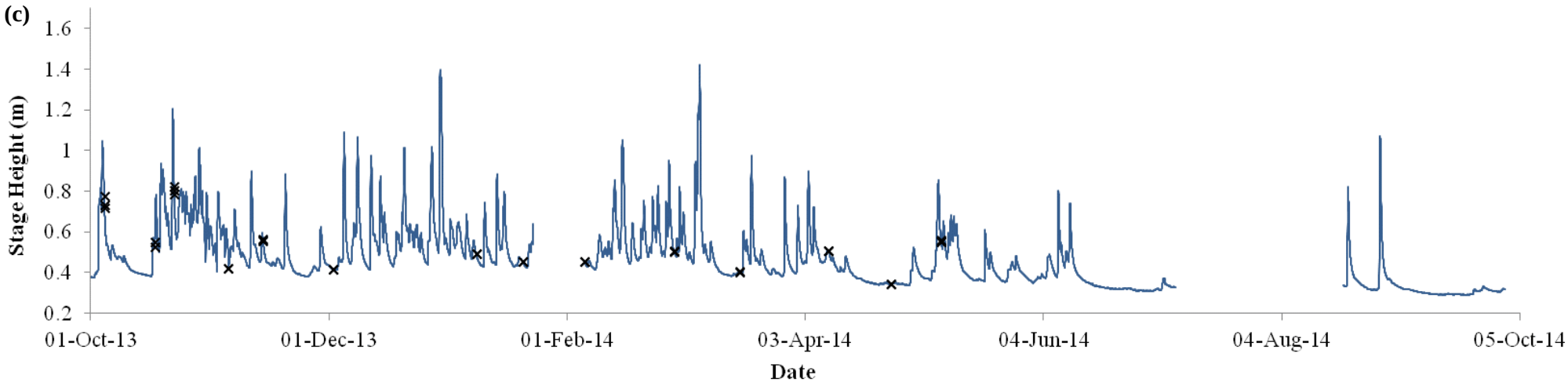

Figure D1: Hydrographs for DW with timing of sampling occasions

Hydrographs are for the three hydrological years covering the period of this study: (a) HY 2011-12, (b) HY 2012-13, (c) HY 2013-14. Blue line = stage height as hydrological time series, black X = timing and stage height of full- or part-sampling occasion.

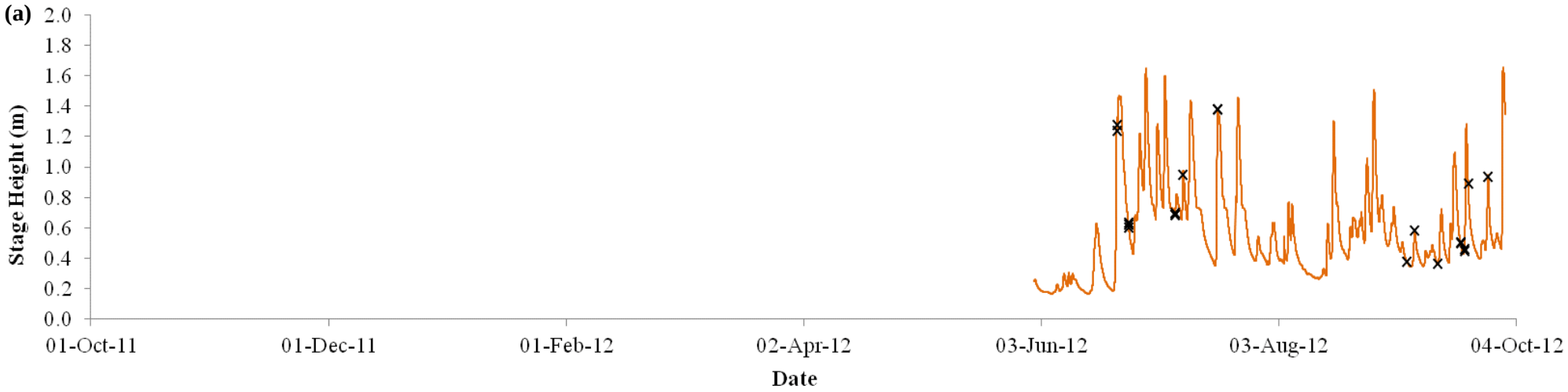
(a)
Stage Height (m)
2.0
1.8
1.6
1.4
1.2
1.0
0.8
0.6
0.4
0.2
0.0
01-Oct-11
01-Dec-11
01-Feb-12
02-Apr-12
03-Jun-12
03-Aug-12
04-Oct-12
Date

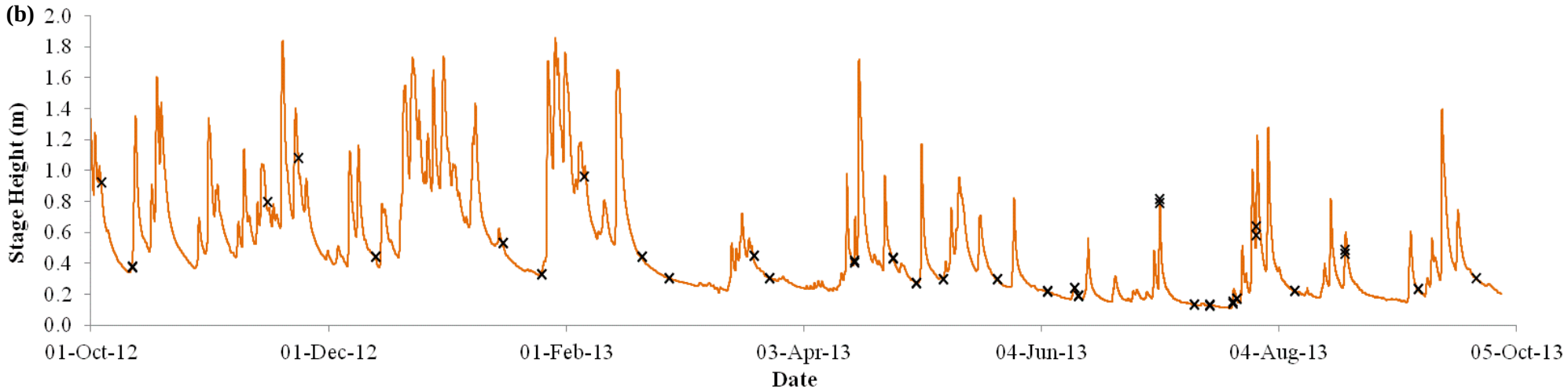
(b)
Stage Height (m)
2.0
1.8
1.6
1.4
1.2
1.0
0.8
0.6
0.4
0.2
0.0
01-Oct-12
01-Dec-12
01-Feb-13
03-Apr-13
04-Jun-13
04-Aug-13
05-Oct-13
Date

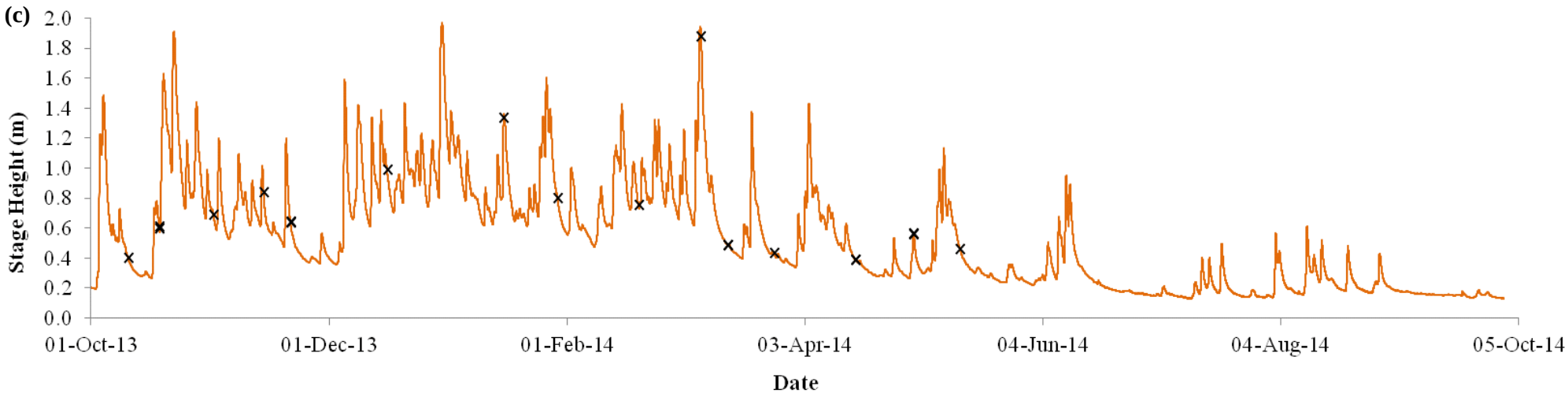

Figure D2: Hydrographs for RK with timing of sampling occasions

Hydrographs are for the three hydrological years covering the period of this study: (a) HY 2011-12, (b) HY 2012-13, (c) HY 2013-14. Blue line = stage height as hydrological time series, black X = timing and stage height of full- or part-sampling occasion.

Appendix E – Relationship between CO_2 Efflux and τ and u^* at DW, RK and RE

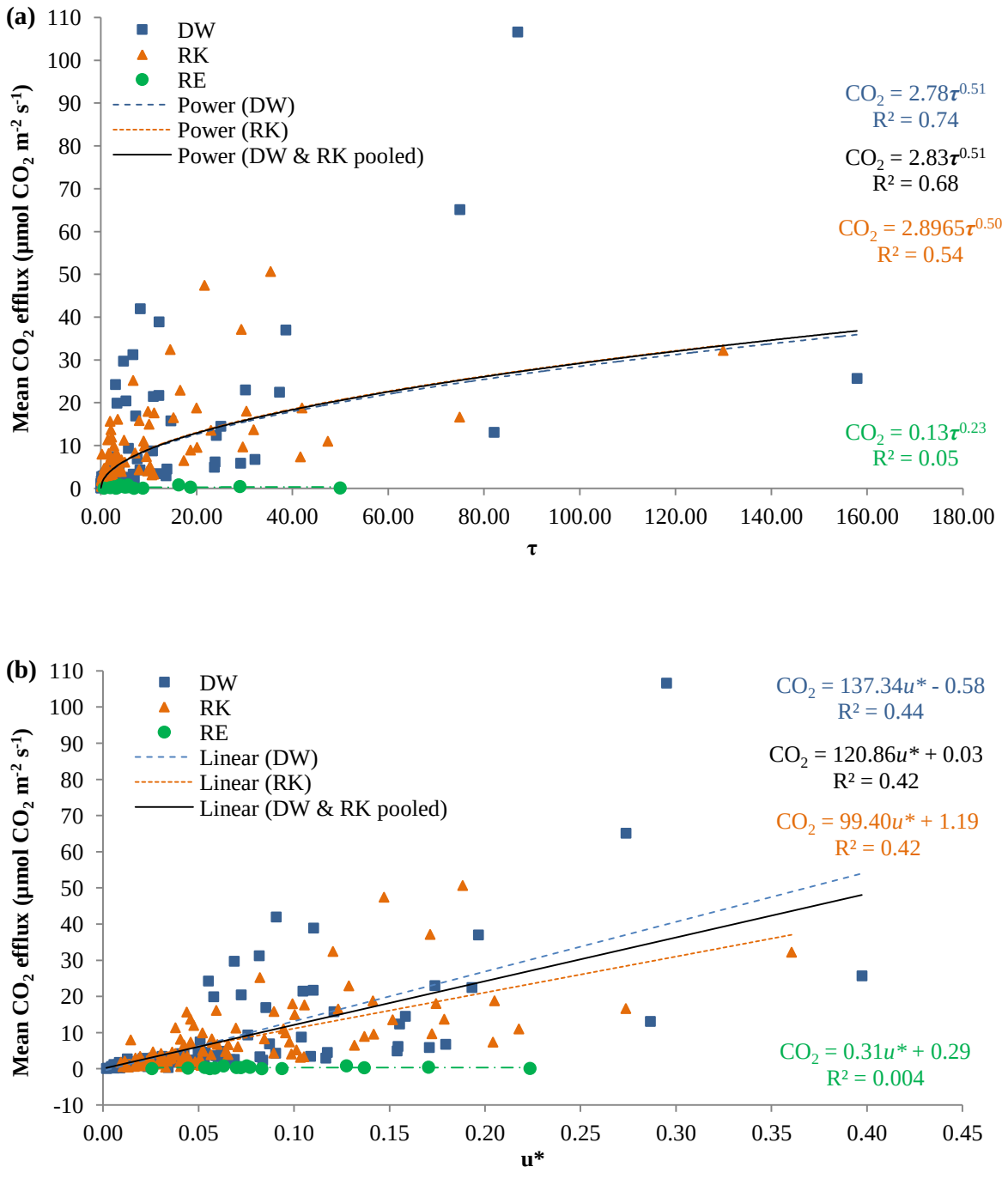

Figure E1: Relationship between CO_2 efflux and hydraulic parameters τ and u^* at DW, RK and RE

CO_2 efflux against (a) shear stress (τ), and (b) shear velocity (u^*). Strong, positive relationships are seen with CO_2 efflux at DW and RK. Influx values have not been plotted here, as gas transfer processes act in the opposite direction and trendlines used here cannot incorporate negative values.

Appendix F – Flow Parameters are Auto-correlated

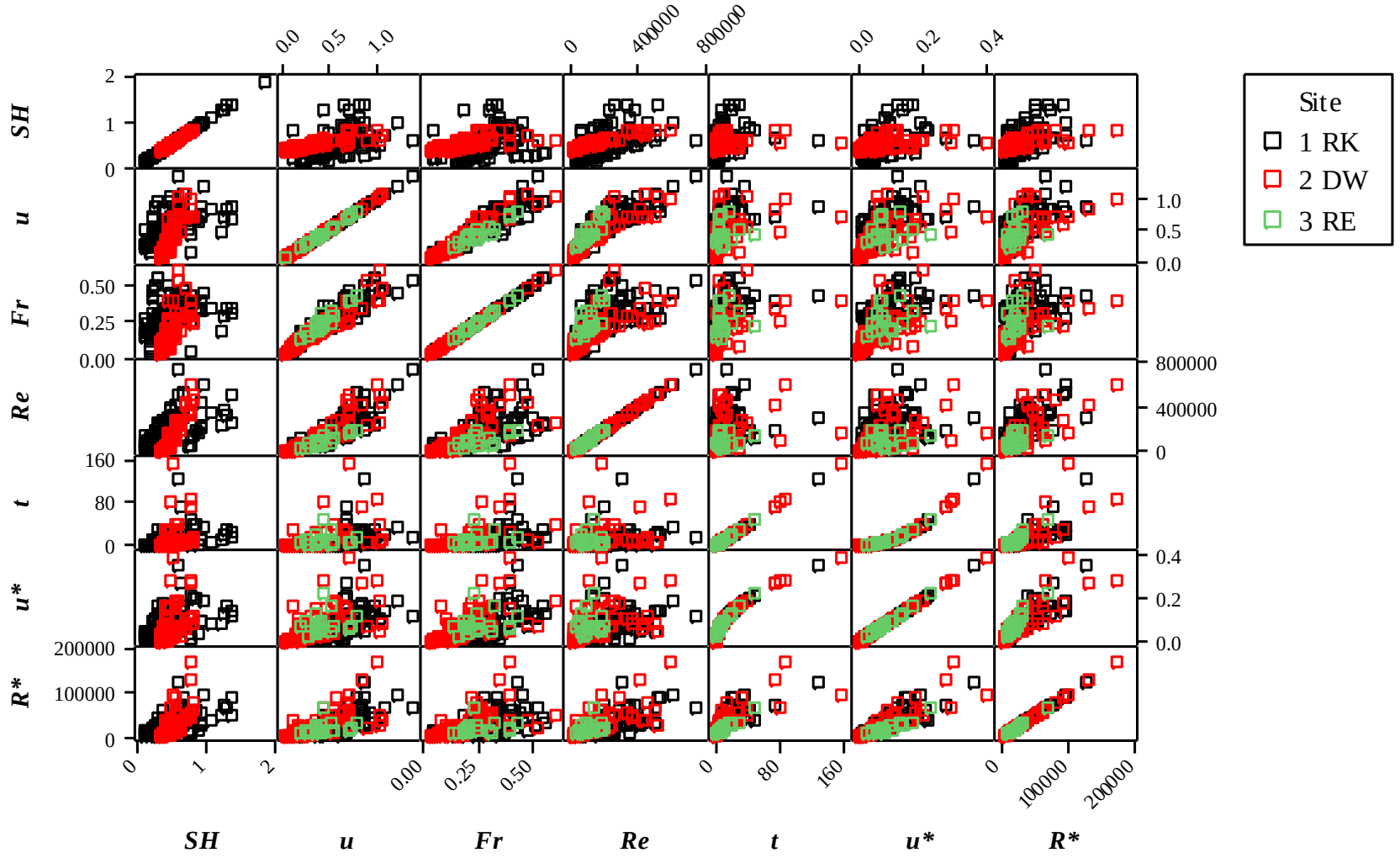

Figure F1: Flow parameters are auto-correlated

Appendix G – Water Chemistry Parameters are Auto-correlated and Correlate with Flow

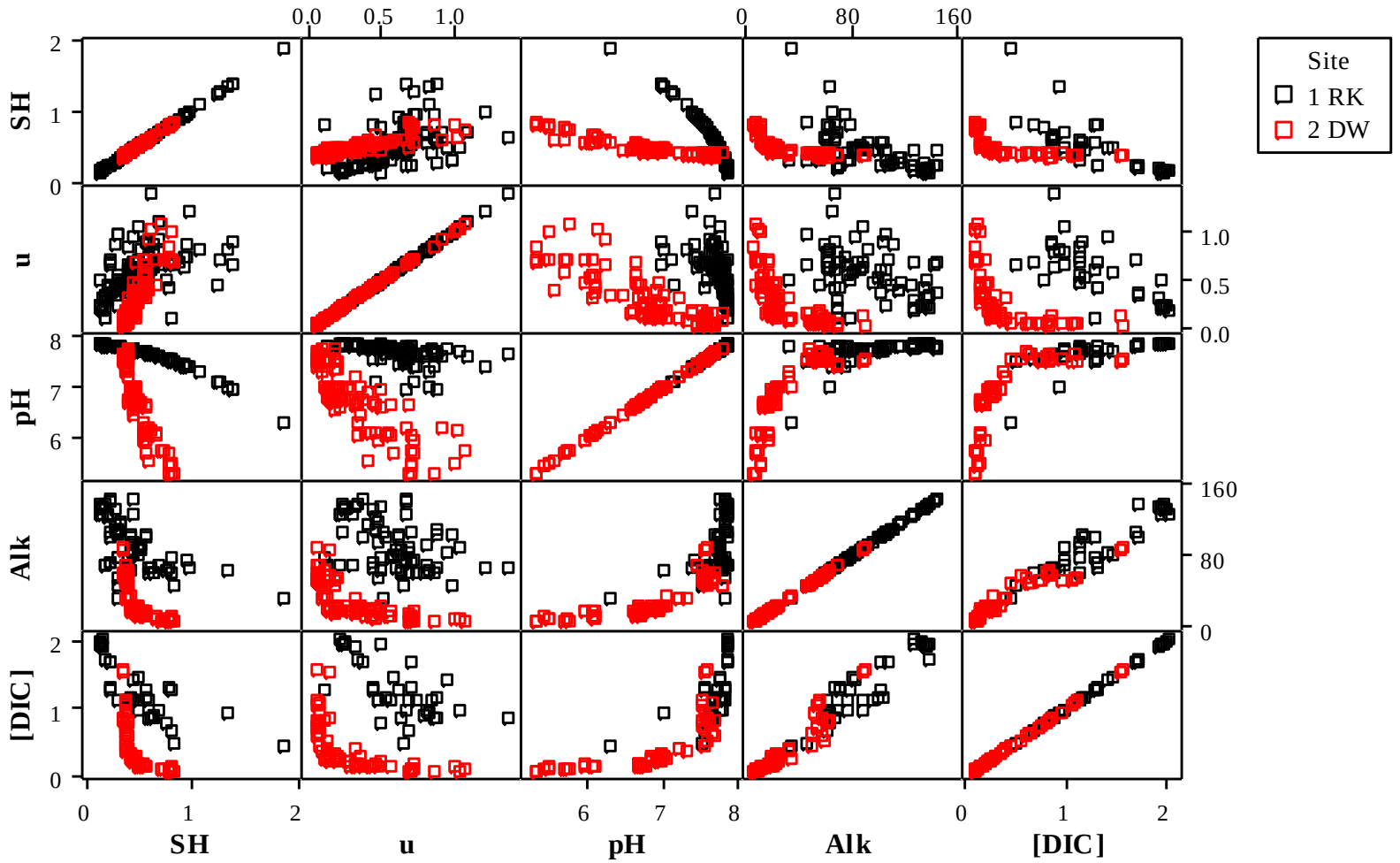

Figure G1: Water chemistry parameters are auto-correlated and correlate with measures of flow

Appendix H – Relationship Between CO_2 Efflux and Hydraulic Parameters at AR and PLST

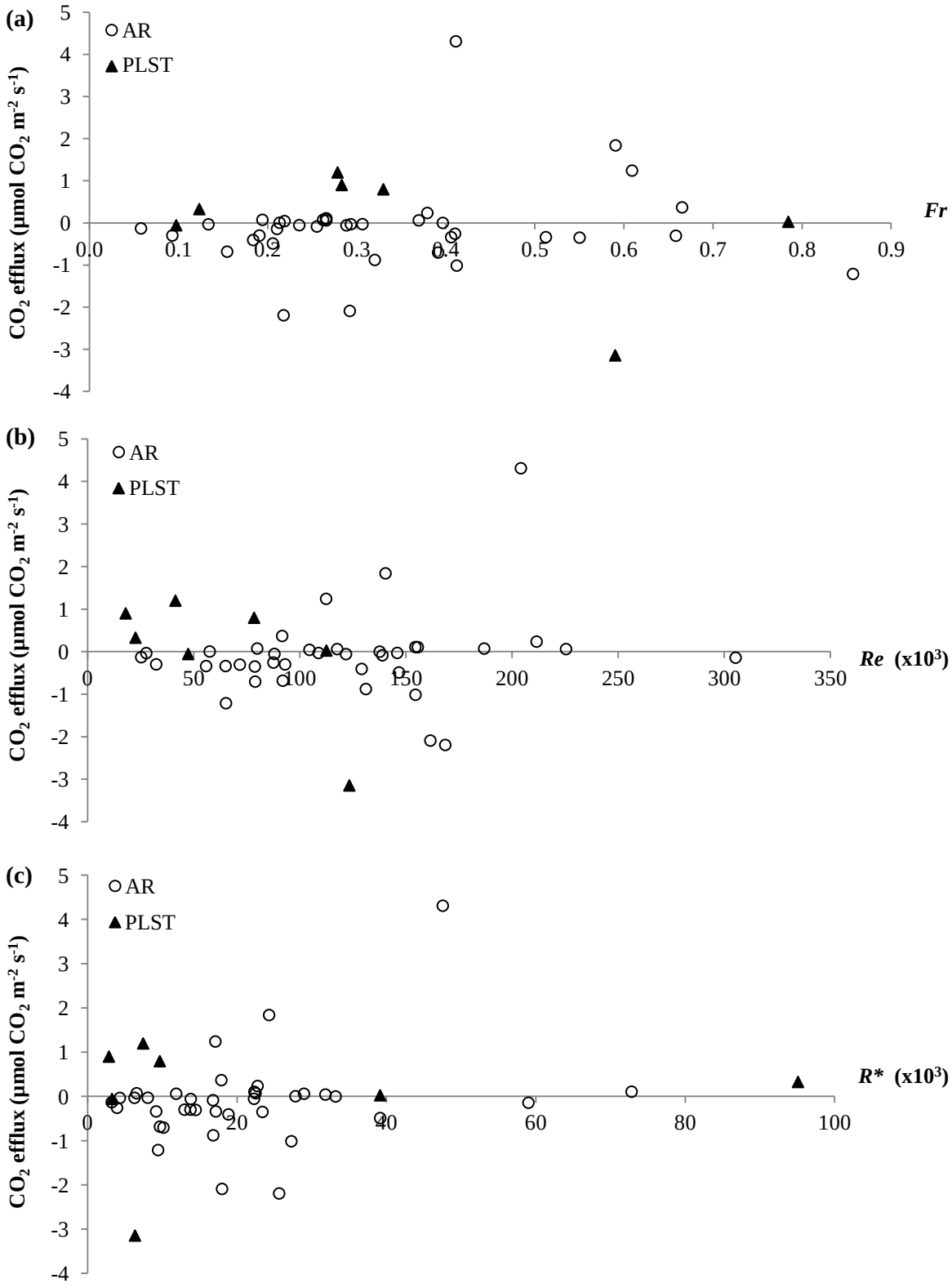

Figure H1: Relationship between CO_2 efflux and hydraulic parameters at AR and PLST

No relationship is apparent between CO_2 efflux and (a) *Fr*, (b) *Re* or (c) *R** at either AR or PLST

Appendix I – Diel Variation in pH, Alkalinity and [DIC] in AR

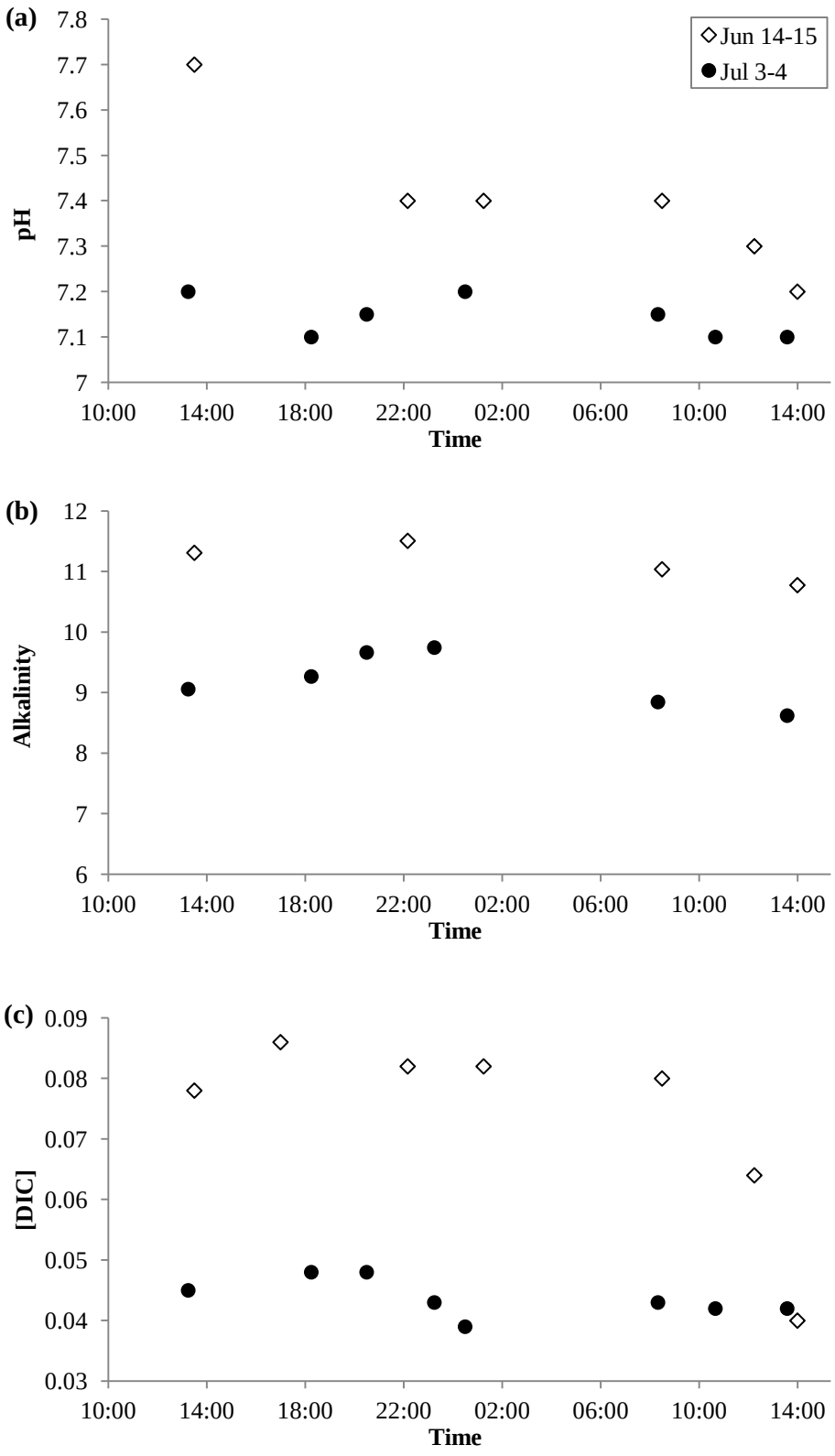

Figure I1: Temporal variation in water chemistry over two 24-hour periods in AR

No diel variation is apparent in (a) pH, (b) alkalinity, or (c) [DIC] in AR. Legend is the same for all plots. From field observations peak flow was ~ 22:00. During sampling there was 24-hour daylight.

Appendix J – Butman and Raymond (2011); Relationship Between kCO_2 and Slope*Velocity

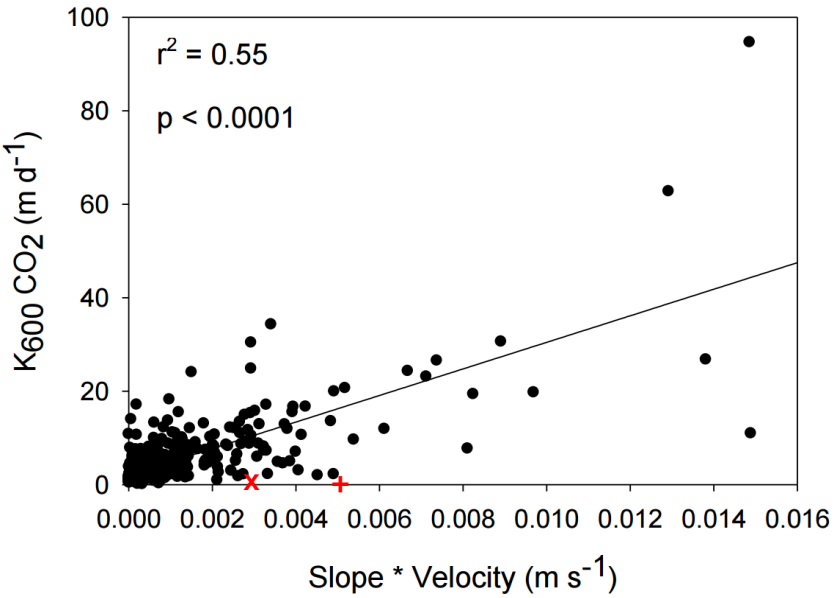

Figure J1: The relationship between the gas transfer velocity ($K_{600}CO_2$) and the product of slope and velocity (Slope*Velocity)

From Butman and Raymond (2011) supplementary information. K_{600} measurements made by direct gas tracer releases, n = 563. There is a significant increase in the gas transfer velocity with slope*velocity. Approximate data for DW (**x**) and RE (+) have been overlain on Butman and Raymond (2011) data, and fall just below the main dataset. Data is not available for RK.

At DW and RE, slope*velocity is approximately 0.003 and 0.005 m s^{-1}, respectively, calculated by dividing the sampling reach elevation change by the reach distance (both estimated using Google Earth elevations and the ruler tool), and multiplying by the mean velocity at the site (Table 4). Slope data was not available for RK.

Mean kCO_2 was calculated as 0.009 and 0.0007 m day^{-1}, respectively, using the equation:

$$CO_2 \text{ flux} = k \times (pCO_{2w} - pCO_{2a})$$

where pCO_{2w} is the partial pressure of CO_2 in the water, pCO_{2a} is the partial pressure of CO_2 in the atmosphere and k is the gas transfer velocity (m d^{-1}) (e.g. Raymond et al. 2000, Alin et al., 2011, Bass *et al.*, 2013). Mean pCO_{2w} for each site was used (see Table 3) and pCO_{2a} was assumed to be 400ppm (NOAA, 2016a).

DW and RE data fall just below that of Butman and Raymond (2011).

References

Abril, G., Bouillon, S., Darchambeau, F., Teodoru, C. R., Marwick, T. R., Tamooh, F., Ochieng Omengo, F., Geeraert, N., Deirmendjian, L., Polsenaere, P. & Borges, A. V. 2015. Technical Note: Large overestimation of pCO_2 calculated from pH and alkalinity in acidic, organic-rich freshwaters. *Biogeosciences,* 12**,** 67-78.

Abril, G., Etcheber, H., Borges, A. V. & Frankignoulle, M. 2000. Excess atmospheric carbon dioxide transported by rivers into the Scheldt estuary. *Comptes Rendus de l'Académie des Sciences - Series IIA - Earth and Planetary Science,* 330**,** 761-768.

Abril, G., Martinez, J.-M., Artigas, L. F., Moreira-Turcq, P., Benedetti, M. F., Vidal, L., Meziane, T., Kim, J.-H., Bernardes, M. C. & Savoye, N. 2014. Amazon River carbon dioxide outgassing fuelled by wetlands. *Nature,* 505**,** 395-398.

Aebly, F. A. & Fritz, S. C. 2009. Palaeohydrology of Kangerlussuaq (Søndre Strømfjord), West Greenland during the last ~8000 years. *The Holocene,* 19**,** 91-104.

Alin, S. R., De Fátima Fl Rasera, M., Salimon, C. I., Richey, J. E., Holtgrieve, G. W., Krusche, A. V. & Snidvongs, A. 2011. Physical controls on carbon dioxide transfer velocity and flux in low-gradient river systems and implications for regional carbon budgets. *Journal of Geophysical Research: Biogeosciences,* 116.

Allen, P. A. 2009. *Earth Surface Processes, 2nd edition,* Chichester, John Wiley & Sons.

Anderson, J. G. C. 1937. The Etive Granite Complex. *Quarterly Journal of the Geological Society,* 93**,** 487-488,NP,490-498,NP,500-532,NP,533.

Anderson, N. J., Harriman, R., Ryves, D. B. & Patrick, S. T. 2001. Dominant Factors Controlling Variability in the Ionic Composition of West Greenland Lakes. *Arctic, Antarctic, and Alpine Research,* 33**,** 418-425.

Anderson, N. J. & Stedmon, C. A. 2007. The effect of evapoconcentration on dissolved organic carbon concentration and quality in lakes of SW Greenland. *Freshwater Biology,* 52**,** 280-289.

Anesio, A. M. & Laybourn-Parry, J. 2012. Glaciers and ice sheets as a biome. *Trends in Ecology & Evolution,* 27**,** 219-225.

Atekwana, E. A. & Krishnamurthy, R. V. 1998. Seasonal variations of dissolved inorganic carbon and δ13C of surface waters: application of a modified gas evolution technique. *Journal of Hydrology,* 205**,** 265-278.

Aucour, A.-M., Sheppard, S. M. F., Guyomar, O. & Wattelet, J. 1999. Use of 13C to trace origin and cycling of inorganic carbon in the Rhône river system. *Chemical Geology,* 159**,** 87-105.

Aufdenkampe, A. K., Mayorga, E., Raymond, P. A., Melack, J. M., Doney, S. C., Alin, S. R., Aalto, R. E. & Yoo, K. 2011. Riverine coupling of biogeochemical cycles between land, oceans, and atmosphere. *Frontiers in Ecology and the Environment,* 9**,** 53-60.

Baldocchi, D. 2014. Measuring fluxes of trace gases and energy between ecosystems and the atmosphere – the state and future of the eddy covariance method. *Global Change Biology,* 20**,** 3600-3609.

Banerjee, S. 2007. The air-water interface: Turbulence and scalar exchange. *Transport at the Air-Sea Interface.* Springer.

Barth, J. a. C., Cronin, A. A., Dunlop, J. & Kalin, R. M. 2003. Influence of carbonates on the riverine carbon cycle in an anthropogenically dominated catchment basin: evidence from major elements and stable carbon isotopes in the Lagan River (N. Ireland). *Chemical Geology,* 200**,** 203-216.

Bartholomew, I., Nienow, P., Mair, D., Hubbard, A., King, M. A. & Sole, A. 2010. Seasonal evolution of subglacial drainage and acceleration in a Greenland outlet glacier. *Nature Geoscience,* 3**,** 408-411.

Bartholomew, I., Nienow, P., Sole, A., Mair, D., Cowton, T., Palmer, S. & Wadham, J. 2011. Supraglacial forcing of subglacial drainage in the ablation zone of the Greenland ice sheet. *Geophysical Research Letters,* 38.

Bass, A., O'grady, D., Berkin, C., Leblanc, M., Tweed, S., Nelson, P. & Bird, M. 2013. High diurnal variation in dissolved inorganic C, $\delta^{13}C$ values and surface efflux of CO_2 in a seasonal tropical floodplain. *Environmental chemistry letters,* 11**,** 399-405.

Bass, A. M., Bird, M. I., Liddell, M. J. & Nelson, P. N. 2011. Fluvial dynamics of dissolved and particulate organic carbon during periodic discharge events in a steep tropical rainforest catchment. *Limnology and Oceanography,* 56**,** 2282-2292.

Bass, A. M., Bird, M. I., Morrison, M. J. & Gordon, J. 2012a. CADICA: Continuous Automated Dissolved Inorganic Carbon Analyzer with application to aquatic carbon cycle science. *Limnology and Oceanography: Methods,* 10**,** 10-19.

Bass, A. M., Bird, M. I., Munksgaard, N. C. & Wurster, C. M. 2012b. ISO-CADICA: Isotopic – continuous, automated dissolved inorganic carbon analyser. *Rapid Communications in Mass Spectrometry,* 26**,** 639-644.

Bass, A. M., Munksgaard, N., Leblanc, M., Tweed, S. & Bird, M. 2014a. Contrasting carbon export dynamics of human impacted and pristine tropical catchments in response to a short‐lived discharge event. *Hydrological Processes,* 28**,** 1835-1843.

Bass, A. M., Munksgaard, N. C., O'grady, D., Williams, M. J., Bostock, H. C., Rintoul, S. R. & Bird, M. I. 2014b. Continuous shipboard measurements of oceanic $\delta^{18}O$, δD and $\delta^{13}C$ DIC along a transect from New Zealand to Antarctica using cavity ring-down isotope spectrometry. *Journal of Marine Systems,* 137**,** 21-27.

Battin, T. J., Kaplan, L. A., Findlay, S., Hopkinson, C. S., Marti, E., Packman, A. I., Newbold, J. D. & Sabater, F. 2008. Biophysical controls on organic carbon fluxes in fluvial networks. *Nature Geoscience,* 1**,** 95-100.

Beaulieu, J. J., Shuster, W. D. & Rebholz, J. A. 2012. Controls on gas transfer velocities in a large river. *Journal of Geophysical Research: Biogeosciences,* 117.

Bergeron, N. E. & Abrahams, A. D. 1992. Estimating shear velocity and roughness length from velocity profiles. *Water Resources Research,* 28**,** 2155-2158.

Best, J. 1992. On the entrainment of sediment and initiation of bed defects: insights from recent developments within turbulent boundary layer research. *Sedimentology,* 39**,** 797-811.

Bhatia, M. P., Das, S. B., Longnecker, K., Charette, M. A. & Kujawinski, E. B. 2010. Molecular characterization of dissolved organic matter associated with the Greenland ice sheet. *Geochimica et Cosmochimica Acta,* 74**,** 3768-3784.

Bhatia, M. P., Das, S. B., Xu, L., Charette, M. A., Wadham, J. L. & Kujawinski, E. B. 2013. Organic carbon export from the Greenland ice sheet. *Geochimica et Cosmochimica Acta,* 109**,** 329-344.

Bianchi, T. S. 2011. The role of terrestrially derived organic carbon in the coastal ocean: A changing paradigm and the priming effect. *Proceedings of the National Academy of Sciences,* 108**,** 19473-19481.

Bigg, G. R. & Rohling, E. J. 2000. An oxygen isotope data set for marine waters. *Journal of Geophysical Research: Oceans,* 105**,** 8527-8535.

Billett, M., Garnett, M. & Hardie, S. 2006. A Direct Method to Measure $^{14}CO_2$ Lost by Evasion from Surface Waters. *Radiocarbon,* 48**,** 61.

Billett, M. & Moore, T. 2008. Supersaturation and evasion of CO_2 and CH_4 in surface waters at Mer Bleue peatland, Canada. *Hydrological Processes,* 22**,** 2044-2054.

Billett, M. F., Palmer, S. M., Hope, D., Deacon, C., Storeton-West, R., Hargreaves, K. J., Flechard, C. & Fowler, D. 2004. Linking land-atmosphere-stream carbon fluxes in a lowland peatland system. *Global Biogeochemical Cycles,* 18.

Biron, P. M., Lane, S. N., Roy, A. G., Bradbrook, K. F. & Richards, K. S. 1998. Sensitivity of bed shear stress estimated from vertical velocity profiles: The problem of sampling resolution. *Earth Surface Processes and Landforms,* 23**,** 133-139.

Bishop, K., Buffam, I., Erlandsson, M., Fölster, J., Laudon, H., Seibert, J. & Temnerud, J. 2008. Aqua Incognita: the unknown headwaters. *Hydrological Processes,* 22**,** 1239-1242.

Bock, E. J., Hara, T., Frew, N. M. & Mcgillis, W. R. 1999. Relationship between air‐sea gas transfer and short wind waves. *Journal of Geophysical Research: Oceans,* 104**,** 25821-25831.

Bomminayuni, S. & Stoesser, T. 2011. Turbulence statistics in an open-channel flow over a rough bed. *Journal of Hydraulic Engineering,* 137**,** 1347-1358.

Borges, A., Djenidi, S., Lacroix, G., Théate, J., Delille, B. & Frankignoulle, M. 2003. Atmospheric CO_2 flux from mangrove surrounding waters. *Geophysical Research Letters,* 30.

Brezonik, P. & Arnold, W. 2011. *Water chemistry: an introduction to the chemistry of natural and engineered aquatic systems,* Oxford University Press.

Broecker, H. C. & Siems, W. 1984. The role of bubbles for gas transfer from water to air at higher windspeeds. Experiments in the wind-wave facility in Hamburg. *Gas transfer at water surfaces.* Springer.

Broecker, W. S. & Peng, T. H. 1974. Gas exchange rates between air and sea1. *Tellus,* 26**,** 21-35.

Brown, G. H. 2002. Glacier meltwater hydrochemistry. *Applied Geochemistry,* 17**,** 855-883.

Buhl, D., Neuser, R. D., Richter, D. K., Riedel, D., Roberts, B., Strauss, H. & Veizer, J. 1991. Nature and nurture: Environmental isotope story of the River Rhine. *Naturwissenschaften,* 78**,** 337-346.

Butman, D. & Raymond, P. A. 2011. Significant efflux of carbon dioxide from streams and rivers in the United States. *Nature Geoscience,* 4**,** 839-842.

Butman, D. E., Wilson, H. F., Barnes, R. T., Xenopoulos, M. A. & Raymond, P. A. 2015. Increased mobilization of aged carbon to rivers by human disturbance. *Nature Geoscience,* 8**,** 112-116.

Cai, Y., Guo, L. & Douglas, T. A. 2008. Temporal variations in organic carbon species and fluxes from the Chena River, Alaska. *Limnology and Oceanography,* 53**,** 1408.

Carlson, A. E. & Winsor, K. 2012. Northern Hemisphere ice-sheet responses to past climate warming. *Nature Geoscience,* 5**,** 607-613.

Cerling, T. E., Solomon, D. K., Quade, J. & Bowman, J. R. 1991. On the isotopic composition of carbon in soil carbon dioxide. *Geochimica et Cosmochimica Acta,* 55**,** 3403-3405.

Charlton, M. B. & Arnell, N. W. 2014. Assessing the impacts of climate change on river flows in England using the UKCP09 climate change projections. *Journal of Hydrology,* 519**,** 1723-1738.

Chen, J., Zhang, D. D., Wang, S., Xiao, T. & Huang, R. 2004. Factors controlling tufa deposition in natural waters at waterfall sites. *Sedimentary Geology,* 166**,** 353-366.

Clark, I. D. & Fritz, P. 1997. *Environmental isotopes in hydrogeology*, CRC press.

Clark, P. U., Dyke, A. S., Shakun, J. D., Carlson, A. E., Clark, J., Wohlfarth, B., Mitrovica, J. X., Hostetler, S. W. & Mccabe, A. M. 2009. The last glacial maximum. *science,* 325**,** 710-714.

Cole, J. J., Prairie, Y. T., Caraco, N. F., Mcdowell, W. H., Tranvik, L. J., Striegl, R. G., Duarte, C. M., Kortelainen, P., Downing, J. A., Middelburg, J. J. & Melack, J. 2007. Plumbing the Global Carbon Cycle: Integrating Inland Waters into the Terrestrial Carbon Budget. *Ecosystems,* 10**,** 172-185.

Cook, J., Edwards, A. & Hubbard, A. 2015. Biocryomorphology: Integrating Microbial Processes with Ice Surface Hydrology, Topography, and Roughness. *Frontiers in Earth Science,* 3**,** 78.

Cox, C. & Munk, W. 1954. Measurement of the roughness of the sea surface from photographs of the sun's glitter. *JOSA,* 44**,** 838-850.

Cramer, W., Kicklighter, D., Bondeau, A., Iii, B. M., Churkina, G., Nemry, B., Ruimy, A., Schloss, A., Intercomparison, T. & Model, P. O. T. P. N. 1999. Comparing global models of terrestrial net primary productivity (NPP): overview and key results. *Global change biology,* 5**,** 1-15.

Criss, R. E. 1999. *Principles of stable isotope distribution*, Oxford University Press.

Cudden, J. R. & Hoey, T. B. 2003. The causes of bedload pulses in a gravel channel: The implications of bedload grain‐size distributions. *Earth Surface Processes and Landforms,* 28**,** 1411-1428.

Cummins, T. & Farrell, E. P. 2003. Biogeochemical impacts of clearfelling and reforestation on blanket-peatland streams: II. major ions and dissolved organic carbon. *Forest Ecology and Management,* 180**,** 557-570.

D'asaro, E. A., Thomson, J., Shcherbina, A. Y., Harcourt, R. R., Cronin, M. F., Hemer, M. A. & Fox-Kemper, B. 2014. Quantifying upper ocean turbulence driven by surface waves. *Geophysical Research Letters,* 41**,** 102-107.

De Montety, V., Martin, J., Cohen, M., Foster, C. & Kurz, M. 2011. Influence of diel biogeochemical cycles on carbonate equilibrium in a karst river. *Chemical Geology,* 283**,** 31-43.

Denfeld, B. A., Frey, K. E., Sobczak, W. V., Mann, P. J. & Holmes, R. M. 2013. Summer CO_2 evasion from streams and rivers in the Kolyma River basin, north-east Siberia. *Polar Research,* 32.

Deuser, W. G. & Degens, E. T. 1967. Carbon Isotope Fractionation in the System CO_2(gas)-CO_2(aqueous)-HCO_3^-(aqueous). *Nature,* 215**,** 1033-1035.

Dinsmore, K. J. & Billett, M. F. 2008. Continuous measurement and modeling of CO_2 losses from a peatland stream during stormflow events. *Water Resources Research,* 44.

Dinsmore, K. J., Billett, M. F. & Dyson, K. E. 2013. Temperature and precipitation drive temporal variability in aquatic carbon and GHG concentrations and fluxes in a peatland catchment. *Global Change Biology,* 19**,** 2133-2148.

Doctor, D. H., Kendall, C., Sebestyen, S. D., Shanley, J. B., Ohte, N. & Boyer, E. W. 2008. Carbon isotope fractionation of dissolved inorganic carbon (DIC) due to outgassing of carbon dioxide from a headwater stream. *Hydrological Processes,* 22**,** 2410-2423.

Eisner, W. R., Törnqvist, T. E., Koster, E. A., Bennike, O. & Van Leeuwen, J. F. N. 1995. Paleoecological Studies of a Holocene Lacustrine Record from the Kangerlussuaq (Søndre Strømfjord) Region of West Greenland. *Quaternary Research,* 43**,** 55-66.

Elayouty, A., Scott, M., Miller, C., Waldron, S. & Franco-Villoria, M. 2016. Challenges in modeling detailed and complex environmental data sets: a case study modeling the excess partial pressure of fluvial CO_2. *Environmental and Ecological Statistics,* 23**,** 65-87.

Eugster, W., Kling, G., Jonas, T., Mcfadden, J. P., Wüest, A., Macintyre, S. & Chapin, F. S. 2003. CO_2 exchange between air and water in an Arctic Alaskan and midlatitude Swiss lake: Importance of convective mixing. *Journal of Geophysical Research: Atmospheres,* 108.

Evans, C. D., Page, S. E., Jones, T., Moore, S., Gauci, V., Laiho, R., Hruška, J., Allott, T. E. H., Billett, M. F., Tipping, E., Freeman, C. & Garnett, M. H. 2014. Contrasting vulnerability of drained tropical and high-latitude peatlands to fluvial loss of stored carbon. *Global Biogeochemical Cycles,* 28**,** 1215-1234.

Faure, G. 1986. Principles of Isotope Geology Wiley. *New York.*

Finlay, J. C. 2003. Controls of Streamwater Dissolved Inorganic Carbon Dynamics in a Forested Watershed. *Biogeochemistry,* 62**,** 231-252.

Fortescue, G. & Pearson, J. 1967. On gas absorption into a turbulent liquid. *Chemical Engineering Science,* 22**,** 1163-1176.

Frankignoulle, M. 1988. Field measurements of air-sea CO_2 exchange. *Limnology and Oceanography,* 33**,** 313-322.

Gammons, C. H., Babcock, J. N., Parker, S. R. & Poulson, S. R. 2011. Diel cycling and stable isotopes of dissolved oxygen, dissolved inorganic carbon, and nitrogenous species in a stream receiving treated municipal sewage. *Chemical Geology,* 283**,** 44-55.

Garnett, M. & Murray, C. 2013. Processing of CO_2 samples collected using zeolite molecular sieve for ^{14}C analysis at the NERC Radiocarbon Facility (East Kilbride, UK). *Radiocarbon,* 55**,** 410-415.

Giesler, R., Mörth, C.-M., Karlsson, J., Lundin, E. J., Lyon, S. W. & Humborg, C. 2013. Spatiotemporal variations of pCO_2 and $\delta^{13}C$-DIC in subarctic streams in northern Sweden. *Global Biogeochemical Cycles,* 27**,** 176-186.

Glaser, B., Dreyer, A., Bock, M., Fiedler, S., Mehring, M. & Heitmann, T. 2005. Source apportionment of organic pollutants of a highway-traffic-influenced urban area in Bayreuth (Germany) using biomarker and stable carbon isotope signatures. *Environmental science & technology,* 39**,** 3911-3917.

Gloor, M., Brienen, R. J., Galbraith, D., Feldpausch, T., Schöngart, J., Guyot, J. L., Espinoza, J., Lloyd, J. & Phillips, O. 2013. Intensification of the Amazon hydrological cycle over the last two decades. *Geophysical Research Letters,* 40**,** 1729-1733.

Gordon, H. R. 2005. Normalized water-leaving radiance: revisiting the influence of surface roughness. *Applied Optics,* 44**,** 241-248.

Gordon, N. D., Finlayson, B. L. & Mcmahon, T. A. 2004. *Stream hydrology: an introduction for ecologists,* John Wiley and Sons.

Guo, L., Ping, C. L. & Macdonald, R. W. 2007. Mobilization pathways of organic carbon from permafrost to arctic rivers in a changing climate. *Geophysical Research Letters,* 34.

Gurumurthy, G., Balakrishna, K., Riotte, J., Braun, J.-J., Audry, S., Shankar, H. U. & Manjunatha, B. 2012. Controls on intense silicate weathering in a tropical river, southwestern India. *Chemical Geology,* 300**,** 61-69.

Hameed, A. S., Resmi, T., Suraj, S., Warrier, C. U., Sudheesh, M. & Deshpande, R. 2015. Isotopic characterization and mass balance reveals groundwater recharge pattern in Chaliyar river basin, Kerala, India. *Journal of Hydrology: Regional Studies,* 4**,** 48-58.

Hanna, E., Huybrechts, P., Steffen, K., Cappelen, J., Huff, R., Shuman, C., Irvine-Fynn, T., Wise, S. & Griffiths, M. 2008. Increased runoff from melt from the Greenland Ice Sheet: a response to global warming. *Journal of Climate,* 21**,** 331-341.

Hansen, J., Nazarenko, L., Ruedy, R., Sato, M., Willis, J., Del Genio, A., Koch, D., Lacis, A., Lo, K. & Menon, S. 2005. Earth's energy imbalance: Confirmation and implications. *science,* 308**,** 1431-1435.

Hardie, S., Garnett, M., Fallick, A., Rowland, A. & Ostle, N. 2005. Carbon Dioxide Capture Using a Zeolite Molecular Sieve Sampling System for Isotopic Studies (^{13}C and ^{14}C) of Respiration. *Radiocarbon,* 47**,** 441.

Harris, C. & Murton, J. B. 2005. Interactions between glaciers and permafrost: an introduction. *Geological Society, London, Special Publications,* 242**,** 1-9.

Hartley, I. P., Garnett, M. H., Sommerkorn, M., Hopkins, D. W. & Wookey, P. A. 2013. The age of CO_2 released from soils in contrasting ecosystems during the arctic winter. *Soil Biology and Biochemistry,* 63**,** 1-4.

Hasholt, B., Bech Mikkelsen, A., Holtegaard Nielsen, M. & Andreas Dahl Larsen, M. 2013. Observations of Runoff and Sediment and Dissolved Loads from the Greenland Ice Sheet at Kangerlussuaq, West Greenland, 2007 to 2010. *Zeitschrift für Geomorphologie, Supplementary Issues,* 57**,** 3-27.

Heggen, R. J. 1983. Thermal Dependent Physical Properties of Water. *Journal of Hydraulic Engineering,* 109**,** 298-302.

Herczeg, A. L. & Hesslein, R. H. 1984. Determination of hydrogen ion concentration in softwater lakes using carbon dioxide equilibria. *Geochimica et Cosmochimica Acta,* 48**,** 837-845.

Hodson, A., Anesio, A. M., Tranter, M., Fountain, A., Osborn, M., Priscu, J., Laybourn-Parry, J. & Sattler, B. 2008. Glacial Ecosystems. *Ecological Monographs,* 78**,** 41-67.

Hoefs, J. 1997. *Stable isotope geochemistry*, Springer.

Hofmann, M. & Schellnhuber, H. J. 2010. Ocean acidification: a millennial challenge. *Energy & Environmental Science,* 3**,** 1883-1896.

Hood, E., Battin, T. J., Fellman, J., O'neel, S. & Spencer, R. G. M. 2015. Storage and release of organic carbon from glaciers and ice sheets. *Nature Geoscience,* 8**,** 91-96.

Hood, E., Fellman, J., Spencer, R. G. M., Hernes, P. J., Edwards, R., D/'Amore, D. & Scott, D. 2009. Glaciers as a source of ancient and labile organic matter to the marine environment. *Nature,* 462**,** 1044-1047.

Hope, D., Palmer, S. M., Billett, M. F. & Dawson, J. J. 2001. Carbon dioxide and methane evasion from a temperate peatland stream. *Limnology and Oceanography,* 46**,** 847-857.

Ingvarsson, M. 2008. Quantifying CO_2 Evasion From a Headwater Stream: A Multidimensional Study. *Master Swedish University for Agricultural Sciences, Uppsala*.

IPCC, 2007. Solomon, S., Qin, D., Manning, M., Chen, Z., Marquis, M., Averyt, K., Tignor, M. & Miller, H. 2007. Summary for Policymakers, Climate Change 2007: The Physical Science Basis. Contribution of Working Group I to the Fourth Assessment Report of the Intergovernmental Panel on Climate Change. Cambridge University Press, New York.

IPCC, 2013. Stocker, T., Qin, D., Plattner, G., Tignor, M., Allen, S., Boschung, J., Nauels, A., Xia, Y., Bex, V. & Midgley, P. 2013. Summary for policymakers. Climate change 2013: the physical science basis. Contribution of Working Group I to the fifth assessment report of the Intergovernmental Panel on Climate Change. *IPCC,* 9**,** 2013.

Johnson, M. S., Billett, M. F., Dinsmore, K. J., Wallin, M., Dyson, K. E. & Jassal, R. S. 2010. Direct and continuous measurement of dissolved carbon dioxide in freshwater aquatic systems—method and applications. *Ecohydrology,* 3**,** 68-78.

Jonsson, A., Åberg, J., Lindroth, A. & Jansson, M. 2008. Gas transfer rate and CO_2 flux between an unproductive lake and the atmosphere in northern Sweden. *Journal of Geophysical Research: Biogeosciences,* 113.

Jørgensen, A. S. & Andreasen, F. 2007. Mapping of permafrost surface using ground-penetrating radar at Kangerlussuaq Airport, western Greenland. *Cold Regions Science and Technology,* 48**,** 64-72.

Kamenos, N. A., Hoey, T. B., Nienow, P., Fallick, A. E. & Claverie, T. 2012. Reconstructing Greenland ice sheet runoff using coralline algae. *Geology,* 40**,** 1095-1098.

Kebede, S., Travi, Y., Alemayehu, T. & Ayenew, T. 2005. Groundwater recharge, circulation and geochemical evolution in the source region of the Blue Nile River, Ethiopia. *Applied Geochemistry,* 20**,** 1658-1676.

Keeling, C. D. 1961. The concentration and isotopic abundances of carbon dioxide in rural and marine air. *Geochimica et Cosmochimica Acta,* 24**,** 277-298.

Khadka, M. B., Martin, J. B. & Jin, J. 2014. Transport of dissolved carbon and CO_2 degassing from a river system in a mixed silicate and carbonate catchment. *Journal of Hydrology,* 513**,** 391-402.

Kling, G. W., Kipphut, G. W. & Miller, M. C. 1992. The flux of CO_2 and CH_4 from lakes and rivers in arctic Alaska. *Hydrobiologia,* 240**,** 23-36.

Knighton, D. 1998. Fluvial forms and processes: London. *Edward Arnold*.

Komori, S., Nagaosa, R., Murakami, Y., Chiba, S., Ishii, K. & Kuwahara, K. 1993. Direct numerical simulation of three‐dimensional open‐channel flow with zero‐shear gas–liquid interface. *Physics of Fluids A: Fluid Dynamics (1989-1993),* 5**,** 115-125.

Kremer, J. N., Nixon, S. W., Buckley, B. & Roques, P. 2003. Technical note: Conditions for using the floating chamber method to estimate air-water gas exchange. *Estuaries and Coasts,* 26**,** 985-990.

Krishnaswami, S. & Singh, S. K. 2005. Chemical weathering in the river basins of the Himalaya, India. *Current Science,* 89**,** 841-849.

Lamont, J. C. & Scott, D. 1970. An eddy cell model of mass transfer into the surface of a turbulent liquid. *AIChE Journal,* 16**,** 513-519.

Langergraber, G., Fleischmann, N. & Hofstaedter, F. 2003. A multivariate calibration procedure for UV/VIS spectrometric quantification of organic matter and nitrate in wastewater. *Water science and technology,* 47**,** 63-71.

Lau, Y. L. & Liu, D. 1993. Effect of flow rate on biofilm accumulation in open channels. *Water Research,* 27**,** 355-360.

Lauerwald, R., Hartmann, J., Moosdorf, N., Kempe, S. & Raymond, P. A. 2013. What controls the spatial patterns of the riverine carbonate system? A case study for North America. *Chemical geology,* 337**,** 114-127.

Lawson, E. C., Wadham, J. L., Tranter, M., Stibal, M., Lis, G. P., Butler, C. E. H., Laybourn-Parry, J., Nienow, P., Chandler, D. & Dewsbury, P. 2014. Greenland Ice Sheet exports labile organic carbon to the Arctic oceans. *Biogeosciences,* 11**,** 4015-4028.

Leith, F. I., Garnett, M. H., Dinsmore, K. J., Billett, M. F. & Heal, K. V. 2014. Source and age of dissolved and gaseous carbon in a peatland-riparian-stream continuum: a dual isotope (C-14 and delta C-13) analysis. *Biogeochemistry,* 119**,** 415-433.

Leopold, L. B. & Maddock Jr, T. 1953. The hydraulic geometry of stream channels and some physiographic implications. *Professional Paper*. No. 252.

Levin, I., Hammer, S., Kromer, B. & Meinhardt, F. 2008. Radiocarbon observations in atmospheric CO_2: determining fossil fuel CO_2 over Europe using Jungfraujoch observations as background. *Science of the Total Environment,* 391**,** 211-6.

Levin, I. & Kromer, B. 2004. The tropospheric $^{14}CO_2$ level in mid latitudes of the northern hemisphere (1959-2003). *Radiocarbon,* 46**,** 1261-1271.

Levin, I., Kromer, B. & Hammer, S. 2013. Atmospheric $\Delta\ ^{14}CO_2$ trend in Western European background air from 2000 to 2012. *Tellus B,* 65.

Lewis, S. M. & Smith, L. C. 2009. Hydrologic drainage of the Greenland Ice Sheet. *Hydrological Processes,* 23**,** 2004-2011.

Lin, G. & Ehleringer, J. R. 1997. Carbon isotopic fractionation does not occur during dark respiration in C3 and C4 plants. *Plant Physiology,* 114**,** 391-394.

Lin, X., Zhang, Z., Wang, S., Hu, Y., Xu, G., Luo, C., Chang, X., Duan, J., Lin, Q. & Xu, B. 2011. Response of ecosystem respiration to warming and grazing during the growing seasons in the alpine meadow on the Tibetan plateau. *Agricultural and Forest Meteorology,* 151**,** 792-802.

Liss, P. S. 1973. Processes of gas exchange across an air-water interface. *Deep Sea Research and Oceanographic Abstracts,* 20**,** 221-238.

Liss, P. S. & Merlivat, L. 1986. Air-sea gas exchange rates: Introduction and synthesis. *The role of air-sea exchange in geochemical cycling.* Springer.

Long, H., Vihermaa, L., Waldron, S., Hoey, T., Quemin, S. & Newton, J. 2015. Hydraulics are a first-order control on CO_2 efflux from fluvial systems. *Journal of Geophysical Research: Biogeosciences,* 120**,** 1912-1922.

Lorke, A., Bodmer, P., Noss, C., Alshboul, Z., Koschorreck, M., Somlai-Haase, C., Bastviken, D., Flury, S., Mcginnis, D. F. & Maeck, A. 2015. Technical note: drifting versus anchored flux chambers for measuring greenhouse gas emissions from running waters.

Lovatt, C., Kominoski, J. S., Sakamaki, T., Macleod, B. & Richardson, J. S. 2014. Leaf-litter leachate and light interactively enhance accrual of stream biofilms. *Fundamental and Applied Limnology,* 184**,** 297-306.

Lu, X., Fan, J., Yan, Y. & Wang, X. 2013. Responses of soil CO_2 fluxes to short-term experimental warming in alpine steppe ecosystem, Northern Tibet. *PloS one,* 8, e59054.

Lutgens, F. & Tarbuck, E. 2001. *The Atmosphere: An Introduction to Meteorology.* , Prentice Hall, New York.

Lynch, J. K., Beatty, C. M., Seidel, M. P., Jungst, L. J. & Degrandpre, M. D. 2010. Controls of riverine CO_2 over an annual cycle determined using direct, high temporal resolution pCO_2 measurements. *Journal of Geophysical Research: Biogeosciences,* 115.

Maberly, S. C., Barker, P. A., Stott, A. W. & De Ville, M. M. 2013. Catchment productivity controls CO_2 emissions from lakes. *Nature Climate Change,* 3**,** 391-394.

Manahan, S. E. 1993. *Fundamentals of environmental chemistry,* Chelsea, MI, USA, Lewis Publishers.

Mann, P. J., Eglinton, T. I., Mcintyre, C. P., Zimov, N., Davydova, A., Vonk, J. E., Holmes, R. M. & Spencer, R. G. 2015. Utilization of ancient permafrost carbon in headwaters of Arctic fluvial networks. *Nature communications,* 6.

Mayorga, E., Aufdenkampe, A. K., Masiello, C. A., Krusche, A. V., Hedges, J. I., Quay, P. D., Richey, J. E. & Brown, T. A. 2005. Young organic matter as a source of carbon dioxide outgassing from Amazonian rivers. *Nature,* 436**,** 538-541.

Melack, J. 2011. Biogeochemistry: Riverine carbon dioxide release. *Nature Geoscience,* 4**,** 821-822.

Mernild, S. H. & Hasholt, B. 2009. Observed runoff, jökulhlaups and suspended sediment load from the Greenland ice sheet at Kangerlussuaq, West Greenland, 2007 and 2008. *Journal of Glaciology,* 55**,** 855-858.

Meybeck, M. 1993. Riverine transport of atmospheric carbon: sources, global typology and budget. *Water, Air, and Soil Pollution,* 70**,** 443-463.

Meybeck, M. 2003. Global analysis of river systems: from Earth system controls to Anthropocene syndromes. *Philosophical Transactions of the Royal Society of London B: Biological Sciences,* 358**,** 1935-1955.

Michaelis, J., Usdowski, E. & Menschel, G. 1985. Partitioning of ^{13}C and ^{12}C on the degassing of CO_2 and the precipitation of calcite-Rayleigh-type fractionation and a kinetic model. *American Journal of Science;(United States),* 285.

Michener, R. & Lajtha, K. 2008. *Stable isotopes in ecology and environmental science,* John Wiley & Sons.

Miller, M., Hater, G., Spatt, P., Westlake, P. & Yeakel, D. 1986. Primary production and its control in Toolik Lake, Alaska. *Archiv für Hydrobiologie. Supplementband. Monographische Beiträge,* 74**,** 97-131.

Milner, A. M. & Petts, G. E. 1994. Glacial rivers: physical habitat and ecology. *Freshwater Biology,* 32**,** 295-307.

Moog, D. B. & Jirka, G. H. 1998. Analysis of reaeration equations using mean multiplicative error. *Journal of Environmental Engineering,* 124**,** 104-110.

Moog, D. B. & Jirka, G. H. 1999. Air-Water Gas Transfer in Uniform Channel Flow. *Journal of Hydraulic Engineering,* 125**,** 3-10.

Neff, J. C. & Asner, G. P. 2001. Dissolved organic carbon in terrestrial ecosystems: synthesis and a model. *Ecosystems,* 4**,** 29-48.

Neu, V., Neill, C. & Krusche, A. V. 2011. Gaseous and fluvial carbon export from an Amazon forest watershed. *Biogeochemistry,* 105**,** 133-147.

Nezu, I., Nakagawa, H. & Jirka, G. H. 1994. Turbulence in open-channel flows. *Journal of Hydraulic Engineering,* 120**,** 1235-1237.

Niemann, H. & Elvert, M. 2008. Diagnostic lipid biomarker and stable carbon isotope signatures of microbial communities mediating the anaerobic oxidation of methane with sulphate. *Organic Geochemistry,* 39**,** 1668-1677.

Nieminen, M. 2003. Effects of clear-cutting and site preparation on water quality from a drained Scots pine mire in southern Finland. *Boreal environment research,* 8**,** 53-59.

Nimick, D. A., Gammons, C. H. & Parker, S. R. 2011. Diel biogeochemical processes and their effect on the aqueous chemistry of streams: A review. *Chemical Geology,* 283**,** 3-17.

NOAA (2016a) Earth Systems Research Laboratory Global monitoring division; Global Greenhouse Gas Reference Network. Available at: http://www.esrl.noaa.gov/gmd/ccgg/, accessed June 2016.

NOAA (2016b) National Centres for Environmental Information. Available at: http://www.ncdc.noaa.gov/, accessed August 2016.

O'connor, D. J. & Dobbins, W. E. 1958. Mechanism of reaeration in natural streams. *Transactions of the American Society of Civil Engineers,* 123**,** 641-666.

Oberbauer, S. F., Tweedie, C. E., Welker, J. M., Fahnestock, J. T., Henry, G. H., Webber, P. J., Hollister, R. D., Walker, M. D., Kuchy, A. & Elmore, E. 2007. Tundra CO_2 fluxes in response to experimental warming across latitudinal and moisture gradients. *Ecological Monographs,* 77**,** 221-238.

Palumbo, J. E. & Brown, L. C. 2013. Assessing the performance of reaeration prediction equations. *Journal of Environmental Engineering,* 140**,** 04013013.

Parker, S. R., Gammons, C. H., Poulson, S. R., Degrandpre, M. D., Weyer, C. L., Smith, M. G., Babcock, J. N. & Oba, Y. 2010. Diel behavior of stable isotopes of dissolved oxygen and dissolved inorganic carbon in rivers over a range of trophic conditions, and in a mesocosm experiment. *Chemical Geology,* 269**,** 22-32.

Parker, S. R., Poulson, S. R., Gammons, C. H. & Degrandpre, M. D. 2005. Biogeochemical controls on diel cycling of stable isotopes of dissolved O_2 and dissolved inorganic carbon in the Big Hole River, Montana. *Environmental science & technology,* 39**,** 7134-7140.

Pavlov, A. 1994. Current changes of climate and permafrost in the arctic and sub‐arctic of Russia. *Permafrost and Periglacial processes,* 5**,** 101-110.

Pedersen, O., Colmer, T. D. & Sand-Jensen, K. 2013. Underwater photosynthesis of submerged plants – recent advances and methods. *Frontiers in Plant Science,* 4.

Pedley, M., Rogerson, M. & Middleton, R. 2009. Freshwater calcite precipitates from in vitro mesocosm flume experiments: a case for biomediation of tufas. *Sedimentology,* 56**,** 511-527.

Peter, H., Singer, G. A., Preiler, C., Chifflard, P., Steniczka, G. & Battin, T. J. 2014. Scales and drivers of temporal pCO_2 dynamics in an Alpine stream. *Journal of Geophysical Research: Biogeosciences,* 119**,** 1078-1091.

Pithan, F. & Mauritsen, T. 2014. Arctic amplification dominated by temperature feedbacks in contemporary climate models. *Nature Geoscience,* 7**,** 181-184.

Polsenaere, P. & Abril, G. 2012. Modelling CO_2 degassing from small acidic rivers using water pCO_2, DIC and delta C-13-DIC data. *Geochimica Et Cosmochimica Acta,* 91**,** 220-239.

Polsenaere, P., Savoye, N., Etcheber, H., Canton, M., Poirier, D., Bouillon, S. & Abril, G. 2013. Export and degassing of terrestrial carbon through watercourses draining a temperate podzolized catchment. *Aquatic sciences,* 75**,** 299-319.

Preisendorfer, R. W. & Mobley, C. D. Albedos and glitter patterns of a wind-roughened sea surface. 1986 Technical Symposium Southeast, 1986. International Society for Optics and Photonics, 58-65.

Rasera, M. D. F., Fl, Krusche, A. V., Richey, J. E., Ballester, M. V. & Victória, R. L. 2013. Spatial and temporal variability of pCO_2 and CO_2 efflux in seven Amazonian Rivers. *Biogeochemistry,* 116**,** 241-259.

Rasera, M. D. F. F., Ballester, M. V. R., Krusche, A. V., Salimon, C., Montebelo, L. A., Alin, S. R., Victoria, R. L. & Richey, J. E. 2008. Estimating the surface area of small rivers in the southwestern Amazon and their role in CO_2 outgassing. *Earth Interactions,* 12**,** 1-16.

Raymond, P. A., Bauer, J. E. & Cole, J. J. 2000. Atmospheric CO_2 evasion, dissolved inorganic carbon production, and net heterotrophy in the York River estuary. *Limnology and Oceanography,* 45**,** 1707-1717.

Raymond, P. A., Caraco, N. F. & Cole, J. J. 1997. Carbon dioxide concentration and atmospheric flux in the Hudson River. *Estuaries,* 20**,** 381-390.

Raymond, P. A., Hartmann, J., Lauerwald, R., Sobek, S., Mcdonald, C., Hoover, M., Butman, D., Striegl, R., Mayorga, E., Humborg, C., Kortelainen, P., Durr, H., Meybeck, M., Ciais, P. & Guth, P. 2013. Global carbon dioxide emissions from inland waters. *Nature,* 503**,** 355-359.

Rebsdorf, A., Thyssen, N. & Erlandsen, M. 1991. Regional and temporal variation in pH, alkalinity and carbon dioxide in Danish streams, related to soil type and land use. *Freshwater Biology,* 25**,** 419-435.

Reidenbach, M., Limm, M., Hondzo, M. & Stacey, M. 2010. Effects of bed roughness on boundary layer mixing and mass flux across the sediment-water interface. *Water Resources Research,* 46.

Rennermalm, A. K., Smith, L. C., Chu, V. W., Forster, R. R., Box, J. E. & Hagedorn, B. 2012. Proglacial river stage, discharge, and temperature datasets from the Akuliarusiarsuup Kuua River northern tributary, Southwest Greenland, 2008–2011. *Earth Systsem Science Data,* 4**,** 1-12.

Richey, J. E., Melack, J. M., Aufdenkampe, A. K., Ballester, V. M. & Hess, L. L. 2002. Outgassing from Amazonian rivers and wetlands as a large tropical source of atmospheric CO_2. *Nature,* 416**,** 617-620.

Rignot, E., Velicogna, I., Van Den Broeke, M., Monaghan, A. & Lenaerts, J. 2011. Acceleration of the contribution of the Greenland and Antarctic ice sheets to sea level rise. *Geophysical Research Letters,* 38.

Rock, L. & Mayer, B. 2007. Isotope hydrology of the Oldman River basin, southern Alberta, Canada. *Hydrological Processes,* 21**,** 3301-3315.

Rodgers, P., Soulsby, C., Petry, J., Malcolm, I., Gibbins, C. & Dunn, S. 2004. Groundwater–surface-water interactions in a braided river: a tracer-based assessment. *Hydrological Processes,* 18**,** 1315-1332.

Romanovsky, V., Burgess, M., Smith, S., Yoshikawa, K. & Brown, J. 2002. Permafrost temperature records: Indicators of climate change. *Eos, Transactions American Geophysical Union,* 83**,** 589-594.

Rose, S. & Long, A. 1989. Dissolved inorganic carbon in the Tucson basin aquifer. *Ground Water,* 27**,** 43-49.

Russell, A. J. 2007. Controls on the sedimentology of an ice-contact jökulhlaup-dominated delta, Kangerlussuaq, west Greenland. *Sedimentary Geology,* 193**,** 131-148.

Ryu, J.-S. & Jacobson, A. D. 2012. CO_2 evasion from the Greenland Ice Sheet: A new carbon-climate feedback. *Chemical Geology,* 320–321**,** 80-95.

Sand-Jensen, K. & Staehr, P. A. 2012. CO_2 dynamics along Danish lowland streams: water–air gradients, piston velocities and evasion rates. *Biogeochemistry,* 111**,** 615-628.

Sayles, F. L. & Eck, C. 2009. An autonomous instrument for time series analysis of TCO_2 from oceanographic moorings. *Deep Sea Research Part I: Oceanographic Research Papers,* 56**,** 1590-1603.

Schaefer, K., Zhang, T., Bruhwiler, L. & Barrett, A. P. 2011. Amount and timing of permafrost carbon release in response to climate warming. *Tellus B,* 63**,** 165-180.

Schuur, E., Mcguire, A., Schädel, C., Grosse, G., Harden, J., Hayes, D., Hugelius, G., Koven, C., Kuhry, P. & Lawrence, D. 2015. Climate change and the permafrost carbon feedback. *Nature,* 520**,** 171-179.

Schuur, E. A., Bockheim, J., Canadell, J. G., Euskirchen, E., Field, C. B., Goryachkin, S. V., Hagemann, S., Kuhry, P., Lafleur, P. M. & Lee, H. 2008. Vulnerability of permafrost carbon to climate change: implications for the global carbon cycle. *BioScience,* 58**,** 701-714.

Sharp, M., Parkes, J., Cragg, B., Fairchild, I. J., Lamb, H. & Tranter, M. 1999. Widespread bacterial populations at glacier beds and their relationship to rock weathering and carbon cycling. *Geology,* 27**,** 107-110.

Shiklomanov, N. I. & Nelson, F. E. 1999. Analytic representation of the active layer thickness field, Kuparuk River Basin, Alaska. *Ecological Modelling,* 123**,** 105-125.

Shin, W.-J., Lee, K.-S., Park, Y., Lee, D. & Yu, E.-J. 2015. Tracing anthropogenic DIC in urban streams based on isotopic and geochemical tracers. *Environmental Earth Sciences,* 74**,** 2707-2717.

Singer, G. A., Fasching, C., Wilhelm, L., Niggemann, J., Steier, P., Dittmar, T. & Battin, T. J. 2012. Biogeochemically diverse organic matter in Alpine glaciers and its downstream fate. *Nature Geoscience,* 5**,** 710-714.

Skidmore, M. L., Foght, J. M. & Sharp, M. J. 2000. Microbial life beneath a high Arctic glacier. *Applied and Environmental Microbiology,* 66**,** 3214-3220.

Smart, G. M. 1999. Turbulent velocity profiles and boundary shear in gravel bed rivers. *Journal of Hydraulic Engineering,* 125**,** 106-116.

Smiley, C. R., Kamenos, N. A, Hoey, T. B., & Ellam, R. M. 2016. Glacial runoff and tidal action drive physical and isotopic composition of Fjord Kangerlussuaq, West Greenland. *Hydrological Processes.* In Review.

Sobek, S., Tranvik, L. J., Prairie, Y. T., Kortelainen, P. & Cole, J. J. 2007. Patterns and regulation of dissolved organic carbon: An analysis of 7,500 widely distributed lakes. *Limnology and Oceanography,* 52**,** 1208-1219.

Sommerfeld, R. A., Massman, W. J. & Musselman, R. C. 1996. Diffusional flux of CO_2 through snow: Spatial and temporal variability among alpine-subalpine sites.

Soulsby, C., Helliwell, R. C., Ferrier, R. C., Jenkins, A. & Harriman, R. 1997. Seasonal snowpack influence on the hydrology of a sub-arctic catchment in Scotland. *Journal of Hydrology,* 192**,** 17-32.

Spencer, R. G., Guo, W., Raymond, P. A., Dittmar, T., Hood, E., Fellman, J. & Stubbins, A. 2014. Source and biolability of ancient dissolved organic matter in glacier and lake ecosystems on the Tibetan Plateau. *Geochimica et Cosmochimica Acta,* 142**,** 64-74.

Spencer, R. G., Mann, P. J., Dittmar, T., Eglinton, T. I., Mcintyre, C., Holmes, R. M., Zimov, N. & Stubbins, A. 2015. Detecting the signature of permafrost thaw in Arctic rivers. *Geophysical Research Letters,* 42**,** 2830-2835.

Storms, J. E. A., De Winter, I. L., Overeem, I., Drijkoningen, G. G. & Lykke-Andersen, H. 2012. The Holocene sedimentary history of the Kangerlussuaq Fjord-valley fill, West Greenland. *Quaternary Science Reviews,* 35**,** 29-50.

Striegl, R. G., Dornblaser, M. M., Mcdonald, C. P., Rover, J. R. & Stets, E. G. 2012. Carbon dioxide and methane emissions from the Yukon River system. *Global Biogeochemical Cycles,* 26.

Stubbins, A., Hood, E., Raymond, P. A., Aiken, G. R., Sleighter, R. L., Hernes, P. J., Butman, D., Hatcher, P. G., Striegl, R. G., Schuster, P., Abdulla, H. a. N., Vermilyea, A. W., Scott, D. T. & Spencer, R. G. M. 2012. Anthropogenic aerosols as a source of ancient dissolved organic matter in glaciers. *Nature Geoscience,* 5**,** 198-201.

Stuiver, M. & Polach, H. A. 1977. Discussion; reporting of C-14 data. *Radiocarbon,* 19**,** 355-363.

Stumm, W. & Morgan, J. 1996. Aquatic chemistry, chemical equilibra and rates in natural waters. *Environmental Science and Technology Series*.

Tarnocai, C., Canadell, J. G., Schuur, E. a. G., Kuhry, P., Mazhitova, G. & Zimov, S. 2009. Soil organic carbon pools in the northern circumpolar permafrost region. *Global Biogeochemical Cycles,* 23.

Telmer, K. & Veizer, J. 1999. Carbon fluxes, pCO_2 and substrate weathering in a large northern river basin, Canada: carbon isotope perspectives. *Chemical Geology,* 159**,** 61-86.

Ten Brink, N. W. & Weidick, A. 1974. Greenland ice sheet history since the last glaciation. *Quaternary Research,* 4**,** 429-440.

Thackston, E. L. & Dawson, J. W. 2001. Recalibration of a Reaeration Equation. *Journal of Environmental Engineering,* 127**,** 317-321.

Thomas, A. & Raiswell, R. 1984. Solute acquisition in glacial melt waters. II. Argentiere (French Alps): Bulk melt waters with open-system characteristics. *Journal of Glaciology,* 30**,** 44-48.

Tobias, C. & Böhlke, J. K. 2011. Biological and geochemical controls on diel dissolved inorganic carbon cycling in a low-order agricultural stream: Implications for reach scales and beyond. *Chemical Geology,* 283**,** 18-30.

Tranvik, L. J., Downing, J. A., Cotner, J. B., Loiselle, S. A., Striegl, R. G., Ballatore, T. J., Dillon, P., Finlay, K., Fortino, K. & Knoll, L. B. 2009. Lakes and reservoirs as regulators of carbon cycling and climate. *Limnology and Oceanography,* 54**,** 2298-2314.

Tweed, S., Leblanc, M., Bass, A., Harrington, G. A., Munksgaard, N. & Bird, M. I. 2015. Leaky savannas: the significance of lateral carbon fluxes in the seasonal tropics. *Hydrological Processes*.

Vachon, D., Prairie, Y. T. & Cole, J. J. 2010. The relationship between near-surface turbulence and gas transfer velocity in freshwater systems and its implications for floating chamber measurements of gas exchange. *Limnology and oceanography,* 55**,** 1723.

Van As, D., Hubbard, A. L., Hasholt, B., Mikkelsen, A. B., Van Den Broeke, M. R. & Fausto, R. S. 2012. Large surface meltwater discharge from the Kangerlussuaq sector of the Greenland ice sheet during the record-warm year 2010 explained by detailed energy balance observations. *The Cryosphere,* 6**,** 199-209.

Van Der Laan, S., Karstens, U., Neubert, R., Van Der Laan‐Luijkx, I. & Meijer, H. 2010. Observation‐based estimates of fossil fuel‐derived CO_2 emissions in the Netherlands using $\Delta\,^{14}C$, CO and ^{222}Radon. *Tellus B,* 62**,** 389-402.

Van Tatenhove, F. G. & Olesen, O. B. 1994. Ground temperature and related permafrost characteristics in West Greenland. *Permafrost and Periglacial Processes,* 5**,** 199-215.

Vihermaa, L. E., Waldron, S., Garnett, M. H. & Newton, J. 2014. Old carbon contributes to aquatic emissions of carbon dioxide in the Amazon. *Biogeosciences,* 11**,** 3635-3645.

Vitousek, P. M., Mooney, H. A., Lubchenco, J. & Melillo, J. M. 1997. Human domination of Earth's ecosystems. *Science,* 277**,** 494-499.

Vogel, J. (ed.) 1993. *Variability of Carbon Isotope Fractionation during Photosynthesis,* San Diego: Academic Press.

Vonk, J. E. & Gustafsson, O. 2013. Permafrost-carbon complexities. *Nature Geoscience,* 6**,** 675-676.

Vonk, J. E., Mann, P. J., Davydov, S., Davydova, A., Spencer, R. G., Schade, J., Sobczak, W. V., Zimov, N., Zimov, S. & Bulygina, E. 2013. High biolability of ancient permafrost carbon upon thaw. *Geophysical Research Letters,* 40**,** 2689-2693.

Wachniew, P. 2006. Isotopic composition of dissolved inorganic carbon in a large polluted river: The Vistula, Poland. *Chemical Geology,* 233**,** 293-308.

Wadham, J., De'ath, R., Monteiro, F., Tranter, M., Ridgwell, A., Raiswell, R. & Tulaczyk, S. 2013. The potential role of the Antarctic Ice Sheet in global biogeochemical cycles. *Earth and Environmental Science Transactions of the Royal Society of Edinburgh,* 104**,** 55-67.

Waldron, S., Marian Scott, E., Vihermaa, L. E. & Newton, J. 2014. Quantifying precision and accuracy of measurements of dissolved inorganic carbon stable isotopic composition using continuous-flow isotope-ratio mass spectrometry. *Rapid Communications in Mass Spectrometry,* 28**,** 1117-1126.

Waldron, S., Scott, E. M. & Soulsby, C. 2007. Stable isotope analysis reveals lower-order river dissolved inorganic carbon pools are highly dynamic. *Environmental science & technology,* 41**,** 6156-6162.

Waldron, S., Watson‐Craik, I. A., Hall, A. J. & Fallick, A. E. 1998. The carbon and hydrogen stable isotope composition of bacteriogenic methane: A laboratory study using a landfill inoculum. *Geomicrobiology Journal,* 15**,** 157-169.

Wallin, M. B., Öquist, M. G., Buffam, I., Billett, M. F., Nisell, J. & Bishop, K. H. 2011. Spatiotemporal variability of the gas transfer coefficient (KCO_2) in boreal streams: Implications for large scale estimates of CO_2 evasion. *Global Biogeochemical Cycles,* 25.

Wallroth, T., Lokrantz, H. & Rimsa, A. 2010. The Greenland Analogue Project (GAP). Literature review of hydrogeology/hydrogeochemistry. Swedish Nuclear Fuel and Waste Management Co., Stockholm (Sweden).

Walsh, C. J., Roy, A. H., Feminella, J. W., Cottingham, P. D., Groffman, P. M. & Morgan Ii, R. P. 2005. The urban stream syndrome: current knowledge and the search for a cure. *Journal of the North American Benthological Society,* 24**,** 706-723.

Wang, J., Han, H. & Zhang, S. 2014. Carbon dioxide flux in the ablation area of Koxkar glacier, western Tien Shan, China. *Annals of Glaciology,* 55**,** 231-238.

Wang, X., Song, C., Wang, J., Miao, Y., Mao, R. & Song, Y. 2013. Carbon release from Sphagnum peat during thawing in a montane area in China. *Atmospheric Environment,* 75**,** 77-82.

Wanninkhof, R. 1992. Relationship between wind speed and gas exchange over the ocean. *Journal of Geophysical Research: Oceans,* 97**,** 7373-7382.

Wanninkhof, R. & Mcgillis, W. R. 1999. A cubic relationship between air-sea CO_2 exchange and wind speed. *Geophysical Research Letters,* 26**,** 1889-1892.

Waterman, D. M., Liu, X., Motta, D. & García, M. H. 2016. Analytical Lagrangian Model of Sediment Oxygen Demand and Reaeration Flux Coevolution in Streams. *Journal of Environmental Engineering***,** 04016028.

Wiebe, R. & Gaddy, V. 1940. The solubility of carbon dioxide in water at various temperatures from 12 to 40 and at pressures to 500 atmospheres. critical phenomena*. *Journal of the American Chemical Society,* 62**,** 815-817.

Wilkinson, R. 1984. A method for evaluating statistical errors associated with logarithmic velocity profiles. *Geo-marine letters,* 3**,** 49-52.

Willemse, N. W. 2002. *Holocene sedimentation history of the shallow Kangerlussuaq lakes, west Greenland,* Danish Polar Center.

Worrall, F. & Burt, T. P. 2010. Has the composition of fluvial DOC changed? Spatiotemporal patterns in the DOC-color relationship. *Global Biogeochemical Cycles,* 24.

Yang, C., Telmer, K. & Veizer, J. 1996. Chemical dynamics of the "St. Lawrence" riverine system: δD_{H2O}, $\delta^{18}O_{H2O}$, $\delta^{13}C_{DIC}$, $\delta^{34}S_{sulfate}$, and dissolved $^{87}Sr/^{86}Sr$. *Geochimica et Cosmochimica Acta,* 60**,** 851-866.

Yates, K. K., Dufore, C., Smiley, N., Jackson, C. & Halley, R. B. 2007. Diurnal variation of oxygen and carbonate system parameters in Tampa Bay and Florida Bay. *Marine Chemistry,* 104**,** 110-124.

Zalasiewicz, J., Williams, M., Haywood, A. & Ellis, M. 2011. The Anthropocene: a new epoch of geological time? *Philosophical Transactions of the Royal Society of London A: Mathematical, Physical and Engineering Sciences,* 369**,** 835-841.

Zappa, C. J., Mcgillis, W. R., Raymond, P. A., Edson, J. B., Hintsa, E. J., Zemmelink, H. J., Dacey, J. W. & Ho, D. T. 2007. Environmental turbulent mixing controls on air-water gas exchange in marine and aquatic systems. *Geophysical Research Letters,* 34.